Altered hippocampal fast oscillations and GABAergic circuits in neuregulin 1 over-expressing mice

---

Wiebke Nissen

Thesis submitted for the degree of
Doctor of Philosophy at the University of Oxford



Lincoln College
University of Oxford
Hilary Term 2012

Für Charlotte

Abstract

Altered hippocampal fast oscillations and GABAergic circuits in neuregulin 1 over-expressing mice

Wiebke Nissen
Lincoln College, University of Oxford
Thesis submitted for the degree of *Doctor of Philosophy* in Hilary Term 2012

Neuregulin 1 (NRG1) is a growth factor implicated in neurodevelopment and postnatal maintenance of synaptic circuits. Its gene has been associated with schizophrenia, and the expression of the type I isoform (NRG1tyI) is increased in patients' brains. Earlier behavioural phenotyping of mice over-expressing NRG1tyI revealed impairment in hippocampus-dependent spatial working memory. This present work investigates the effects of increased NRG1tyI expression on hippocampal network functioning in these mice.

Fast network oscillations, specifically at gamma frequencies, were studied in CA3 hippocampal slices in a carbachol model using cellular and extracellular microelectrode recording techniques. The peak frequency of field potential oscillations was significantly reduced in slices from NRG1tyI mice compared to wild-type littermates. In addition, NRG1tyI mouse slices were more prone to develop epileptiform activity. During rhythmic activity, the balance of phasic excitation and inhibition was significantly altered in principal cells of NRG1tyI mice. Inhibitory synaptic input was more sustained, while excitatory synaptic currents were kinetically unchanged but larger and more variable in amplitude. Together, these data suggest altered functioning of the GABAergic inhibitory circuits that generate and maintain gamma oscillations. Because parvalbumin-expressing (PV+) interneurons are a major target of NRG1 signalling, the inhibition from PV+ interneurons to pyramidal cells was examined next. Channelrhodopsin-2-mediated photostimulation of PV+ cell axons failed to show changes in GABAergic inhibition of CA3 pyramidal cells in NRG1tyI mice. However, synaptic miniature glutamatergic neurotransmission was reduced in identified PV+ basket cells (BCs) and axo-axonic cells (AACs) but not in pyramidal cells. The change was expressed postsynaptically, affecting NMDA receptor- but not AMPA receptor-mediated currents.

The data suggest that NRG1tyI over-expression results in alterations in PV+ interneuron types, particularly at the glutamatergic synapses that excite these cells. These changes and the altered gamma oscillations are already evident in late adolescence — before the age at which cognitive deficits are detectable.

Declaration

The work described in this thesis was carried out at the Department of Pharmacology, University of Oxford, between October 2008 and November 2011 under the supervision of Dr Karri Lamsa and the co-supervision of Prof. Ole Paulsen (Neuronal Oscillations Group, Department of Physiology, Development and Neuroscience, University of Cambridge). The research presented in this thesis is my own original work, with the exceptions outlines below.

Dr Andras Szabo provided assistance with anatomical and immunohistochemical procedures in all parts of the thesis. He also contributed to the cell visualisations and laminar axon profile analysis in Chapter 5 as outlined in Table A4. The data is incorporated in Figures 5.1, 5.2, A1 and A2 and Table 5.1.

Chapter 5 contains data of two perisomatic-targeting interneurons and one pyramidal cell recorded by Ms Linda Avena (M.Sc. Neuroscience, University of Oxford) and one perisomatic-targeting interneuron recorded by Mr Matthew Prior (FHS, University of Oxford). The physiological and anatomical analyses were performed by myself.

The immunocytochemical reactions shown in Figure 4.2C were prepared and performed by Dr Peter Magill (Medical Research Council, Anatomical Neuropharmacology Unit, Oxford). However, the evaluation (images and cell counting) was done by myself.

Figures 1.3 and 1.4 in the Introduction are adapted, with permission, from Dr Inga Deakin's DPhil thesis, submitted in Trinity Term 2009 at the University of Oxford.

No part of this thesis has been submitted for any other examination.

Approximate word count: 50,000

Acknowledgements

I would like to express my gratitude to all the people who have guided and accompanied me during this adventure.

First and foremost, this project would not have progressed without the advice, encouragement and help from my principal supervisor, Karri Lamsa, and my co-supervisor, Ole Paulsen. Karri guided me through every valley and peak of this DPhil, and I am very grateful for his patience, constant support and infectious enthusiasm. Ole set the initial path for this research and was always available for discussions, advice and inspirations, even after the Neuronal Oscillations Group moved to Cambridge. I offer my sincere thanks to you both for your genuine interest in my scientific and personal development, not just during my DPhil but also in the preceding year.

I would also like to thank Paul Harrison for offering to collaborate on the NRG1tyI project and for his continued interest in my work. Also, this project would not have been considered if Inga Deakin had not spotted the hippocampal dysfunction in NRG1tyI mice. Inga's previous work set a valuable and solid background. Thank you!

The enthusiasm for science and collaboration that I experienced in the Oxford Neuroscience Community is exceptional. In particular, our close collaboration with Peter Somogyi and the MRC Anatomical Neuropharmacology Unit has facilitated my project in so many different ways – not only through outstanding technical support but also from the many scientific discussions. I am particularly grateful to Peter Magill for his ideas and for sharing several invaluable mouse strains with me.

I would also like to thank Denise (BSB) and her team, Bev and her team (Psychology), as well as Liz with her team (MRC ANU) for taking great care of the furry stars of my project.

I am grateful to Iris Oren for sharing the analysis programme for gamma oscillations with me, and also to Norbert Hajos, Jozsef Csicsvari and Joseph Raimondo for their helpful suggestions and time. The success in the optogenetics investigation was attributable to the invaluable support and advice from Tommas Ellender, Liz Norman, Dennis Kaetzel, Colin Akerman, Michael Kohl, Louise Upton and Michael Craig. Thank you everyone! For all the help in histology, I am grateful to Andras Szabo who taught me the "dos and don'ts" of immunohistochemical evaluation, and helped me in all anatomical aspects of my project. Without the antibodies and technical advice of Kristina Detzner, Wendy Tynan, Peter Magill, Ben Micklem and David Roberts, I would have not managed to complete the study. Beata Godlewska's expertise got me started on the genotyping, and Chris Barkus patiently advised me on statistics – thank you both! I would also like to thank all members of the NOG as well as Colin Akerman and his group for many fun and very insightful journal club discussions.

Finally, Michael Field has been a star in the last stretch of this adventure with invaluable help in editing and formatting this thesis! Last but not least, I am grateful to the Department of Pharmacology, the MRC, Lincoln College, The Guarantors of Brain and the Vice Chancellors' Fund of the University of Oxford for supporting me in my work.

My time in Oxford would have not been so much fun without Kristina, Henrike, Tommas, Michelle, George, Anne, Claudia, Petrina, Michiel, Nancy, Rob, Andrea, Victoria, Nisha, my Lincoln library buddies and other dear friends! Thank you for reminding me there is a world away from the laboratory. Finally, a huge thank you to my dear friend Wendy: your friendship and encouragement throughout the DPhil meant the world to me!

My love goes to my parents, my brother and Jasmin, my grandma and my soulmate Sanni for believing in me when I did not. There are no words to express the gratitude I feel for your patience, your endless support and love throughout this time.

Contents

1 Introduction 1
1.1 The neurobiology of neuregulin 1 1
1.1.1 The NRG1 gene and its proteins 2
1.1.2 Brain area and cell type-specific expression of NRG1 4
1.1.3 NRG1 signalling through ErbB receptors 5
1.1.4 Functions of NRG1 in the nervous system 7
1.1.5 The neurobiology of schizophrenia and the implication of NRG1 10
1.2 The hippocampus: structure and connectivity 13
1.2.1 Signal transmission in the hippocampus 13
1.2.2 Ontogenetic development of the hippocampal circuitry 15
1.2.3 The cytoarchitecture of area CA3 18
1.2.3.1 Perisomatic inhibition 23
1.3 Hippocampal gamma oscillations 28
1.3.1 Hippocampal gamma rhythm *in vivo* 28
1.3.2 Hippocampal gamma rhythm *in vitro* 29
1.3.3 Gamma oscillations in encoding information 33
1.3.4 Gamma oscillations in schizophrenia 35
1.4 Context of this study 37
1.4.1 Previous findings in NRG1 type I over-expressing mice 37
1.4.2 Aims of this research 40
2 Methods 42
2.1 Transgenic mice 42
2.1.1 NRG1tyI over-expressing mice 42
2.1.2 PV-Cre and R26R-eYFP mice 43
2.1.3 Lhx6-eGFP mice 44
2.2 Phenotyping and genotyping NRG1tyI mice 44
2.2.1 DNA extraction 45
2.2.2 Amplification of transgene-specific sequences and gel electrophoresis 45
2.3 Hippocampal slice preparation and storage 46

2.4 Electrophysiological recordings 48
2.4.1 Carbachol-induced gamma oscillations: Simultaneous field potential and single cell recordings 50
2.4.2 Light-evoked IPSCs in CA3 pyramidal cells 52
2.4.3 Whole-cell recordings from CA3 Lhx6-eGFP+ cells 53
2.5 *In vivo* injection of AAV2-mediated ChR2-eYFP constructs 55
2.6 Data analysis and statistics 56
2.6.1 Field potential oscillations, cell firing properties and synaptic currents 56
2.6.2 Light-evoked inhibitory postsynaptic currents 60
2.6.3 Miniature excitatory postsynaptic currents 62
2.6.4 Statistical analyses 63
2.7 Anatomical processing and evaluation 64
2.7.1 Tissue fixation and re-sectioning 64
2.7.1.1 Perfusion-fixed brains 65
2.7.1.2 Fixation of acute slices 65
2.7.2 Cell visualisations 66
2.7.2.1 Cell reconstructions and laminar analysis 66
2.7.3 Immunohistochemistry 67
3 *In vitro* cholinergically induced synchronised network activity is altered in NRG1tyI mice 72
3.1 Introduction 72
3.2 Results 73
3.2.1 CCh-induced gamma-frequency field oscillations are significantly slower in NRG1tyI mice 73
3.2.2 Reduced threshold for epileptiform activity in NRG1tyI mice 77
3.2.3 Unaltered intrinsic properties but altered rhythmic inhibition of pyramidal cells during oscillatory network activity in NRG1tyI mice 79
3.2.3.1 CA3 pyramidal cell spike-coupling to gamma oscillation cycles is unchanged in NRG1tyI mice 80
3.2.3.2 Synaptic input to pyramidal cells is altered in NRG1tyI mice during gamma oscillations 84
3.3 Discussion 90
3.3.1 CCh-induced rhythmic network activity 91
3.3.2 Altered CCh-induced network activity in NRG1tyI mice 93
3.3.3 Mechanisms underlying altered network activity in NRG1tyI mice 95
3.3.3.1 Possible interaction between NRG1 and AChR signalling? 96

3.3.3.2 Field power of gamma oscillations 98
3.3.4 Epileptiform discharges in NRG1tyI mice 100
3.3.5 Could altered gamma oscillation underlie the cognitive deficits in NRG1tyI mice? 101
3.4 Figures 103
4 Synaptic inhibition of CA3 pyramidal cells by PV+ interneurons is unchanged in NRG1tyI mice 108
4.1 Introduction 108
4.2 Alternative methodological approaches 109
4.3 Results 111
4.3.1 Setting the scene: selective activation of PV+ axons using optogenetics 111
4.3.1.1 PV expression pattern in hippocampus of NRG1tyI mice is similar to WT 111
4.3.1.2 Cre recombinase-dependent ChR2-eYFP expression selective to PV neurons in mid-ventral hippocampus 111
4.3.1.3 Optically evoked ChR2-activated synaptic GABAergic currents in CA3 pyramidal cells 115
4.3.1.4 Minimal optical stimulation 117
4.3.2 PV+ axon-mediated IPSCs have similar properties in PV-Cre and NRG1tyI/PV-Cre mice 120
4.4 Discussion 124
4.4.1 PV+ expression in NRG1tyI mice 125
4.4.2 ChR2-mediated selective stimulation of PV+ cell axons 126
4.4.3 Unchanged PV^{+} mediated inhibition of pyramidal cells in NRG1tyI mice 128
4.4.4 Perspective 130
4.5 Figures 131
5 Impairment of NMDA receptor-mediated spontaneous excitatory transmission in PV+ PTIs of NRG1tyI mice 138
5.1 Introduction 138
5.2 The search for a suitable reporter mouse 142
5.3 Results 144
5.3.1 Anatomical identification of cell types 144
5.3.1.1 Axo-dendritic structure of CA3 PTIs 145
5.3.2 Unaltered AMPAR- but smaller NMDAR-mediated mEPSCs in PTIs of NRG1tyI mice 151
5.3.3 Unchanged excitatory transmission at CA3 pyramidal cells of NRG1tyI mice 159

5.3.4 Cell type-specific properties of AMPAR- and NMDAR-mediated quantal synaptic activity 161
5.4 Discussion 164
5.4.1 Anatomical identification of Lhx6+ PTIs 165
5.4.1.1 Patching PTIs in slices from Lhx6-eGFP mice 165
5.4.1.2 Variability in axon arborisation of PTIs in area CA3 166
5.4.1.3 Recovering immunopositivity for PV 167
5.4.2 NMDAR-mediated postsynaptic currents in PTIs 167
5.4.3 Postsynaptic changes in glutamate receptor-mediated currents in PTIs of NRG1tyI mice 169
5.4.3.1 Interaction of NRG1 with NMDAR-mediated glutamatergic signalling 171
5.4.3.2 AMPAR-mediated glutamatergic signalling and presynaptic glutamate release 172
5.4.4 Glutamatergic signalling in pyramidal cells of NRG1tyI mice 174
5.4.5 Perspective 175
5.5 Figures 176
6 General discussion 182
6.1 Summary of findings 182
6.2 Functional implications of NMDAR hypofunction 183
6.2.1 Cognitive functions 183
6.2.2 Neuronal network function 185
6.2.3 Input and output function of PV+ interneurons 187
6.3 Neurobiological effects of NRG1tyI over-expression: Is there a link with the pathophysiology of schizophrenia? 190
6.4 Other mechanisms potentially contributing to changed network function in NRG1tyI mice 192
6.5 Future directions 195
6.6 Final conclusions 198
7 Appendix 199
Tables 199
Figures 207
8 References 216

Abbreviations

AAC	axo-axonic cell
AAV2	adeno-associated virus serotype 2
ACh(R)	acetylcholine (receptor)
ACSF	artificial cerebrospinal fluid
AIS	axon initial segment
AMPA(R)	α-amino-3-hydroxy-5-methylisoxazole-4-propionic acid (receptor)
ANOVA	analysis of variance
AP5	(2*R*)-amino-5-phosphonopentanoic acid
BC	basket cell
CA	cornu ammonis
CB1R	cannabinoid receptor 1
CCh	carbachol
CCK	cholecystokinin
CGE	caudal ganglionic eminences
ChR2	channelrhodopsin-2
CR	calretinin
CV	coefficient of variation
DG	dentate gyrus
DIO	double-floxed inverted open reading frame
EC	entorhinal cortex
E_{Cl}	equilibrium potential for chloride
$E_{GABA\text{-}A}$	reversal potential for GABA-A receptor-mediated IPSCs
EGF	epidermal growth factor
eGFP	enhanced green fluorescent protein
eYFP	enhanced yellow fluorescent protein
EPSC	excitatory postsynaptic current
(f)EPSP	(field) excitatory postsynaptic potential
GABA	gamma-aminobutyric acid
IPSC	inhibitory postsynaptic current
ISI	interspike interval
kainateRs	kainate receptors
LGE	lateral ganglionic eminences
Lhx6	LIM homeobox 6
LTP	long-term potentiation
mAChR	metabotropic acetylcholine receptor
mEPSC	miniature excitatory postsynaptic current
mIPSC	miniature inhibitory postsynaptic current
MES	minimal electrical stimulation

MGE	medial ganglionic eminences
MOS	minimal optical stimulation
nAChR	nicotinic acetylcholine receptor
NBQX	1,2,3,4-Tetrahydro-6-nitro-2,3-dioxo-benzo[f]quinoxaline-7-sulfonamide
NGS	normal goat serum
NHS	normal horse serum
Nkx2.1	NK2 homeobox 1 (transcription factor and product of the *Nkx2.1* gene)
NMDA(R)	*N*-methyl-D-aspartate (receptor)
nNOS	neuronal nitric oxide synthase
NPY	neuropeptide Y
NRG1tyI	neuregulin 1 type I isoform
O-LM	oriens-lacunosum moleculare
PB	phosphate buffer
PBS	phosphate buffered saline
PSC	postsynaptic current
PTI	perisomatic-targeting interneuron
PV	parvalbumin
Q_e	phasic excitatory charge transfer
Q_i	phasic inhibitory charge transfer
SEM	standard error of the mean
SNP	single nucleotide polymorphism
s.o./p./l./r./l.-m.	stratum oriens/pyramidale/lucidum/radiatum/lacunosum-moleculare
SOM	somatostatin
str.	stratum
TBS-Tx	Tris-buffered saline with 0.3% Triton X-100
TTX	tetrodotoxin
uIPSC	unitary inhibitory postsynaptic current
R_{access}	access resistance, calculated from current step in voltage-clamp mode
R_{input}	input resistance
V_m	membrane voltage
V_h	holding voltage
WT	wild-type

1 Introduction

Sensory perception, motor control, cognitive function, and memory – even love and resentment – are inextricably reliant on the physiological functioning of brain circuits. A myriad of factors work together to establish and maintain these supremely complex neuronal circuits. One important factor is the signalling protein neuregulin 1 (NRG1). Research efforts continue to unravel NRG1's complex involvement in the biology of the developing and mature brain, particularly since its genetic linkage to schizophrenia was established. The function of NRG1 in the hippocampus is of particular interest, as this brain area is implicated in schizophrenia. Although hippocampal dysfunction may well underlie the cognitive impairment from which schizophrenic patients suffer, currently available medication does not target this aspect of the disorder efficiently.

To set the context for this study on NRG1's impact on hippocampal circuit functioning, I first review the neurobiology of NRG1 and its involvement in schizophrenia. Next, I briefly describe the structure of the hippocampus and its connectivity, with particular focus on the CA3 area. I then introduce hippocampal oscillations, in particular those at gamma frequency, and explain their putative role in cognitive processing. Finally, I review previous findings in NRG1 type I over-expressing mice — the strain that has been in the focus of this study.

1.1 The neurobiology of neuregulin 1

Variants of the NRG1 protein were independently discovered for three different properties. First, a factor named 'ARIA' (acetylcholine receptor-inducing activity) was

found to induce the synthesis of acetylcholine receptors (AChRs) in cultured chicken muscle cells (Usdin & Fischbach, 1986). Second, another factor ('neu', 'heregulin') was discovered to be a ligand for the oncogenic ErbB2 receptor, and, third, a 'glial growth factor' could promote the proliferation of Schwann cells (reviewed in Falls, 2003). When it became clear that these proteins were encoded by the same NRG1 gene, the alternative names were combined to the common name 'neuregulin' (Falls, 2003; Harrison & Law, 2006).

1.1.1 The NRG1 gene and its proteins

A family of four genes (NRG1–4) encodes neuregulin proteins. They share an epidermal growth factor (EGF)-like domain that activates ErbB receptor tyrosine kinases (see Section 1.1.3). Of the four NRGs, NRG1 (encoded on human chromosome 8p13) is the best characterised (reviewed in Falls, 2003; Harrison & Law, 2006; Mei & Xiong, 2008). The biology of NRG1 proteins is complex, because multiple promoters and alternative splicing give rise to over 30 different human NRG1 isoforms with a number of distinct domains (Figure 1.1).

(1) Alternative promoters determine which 5' exon is transcribed. The N-terminal sequences differ in length and classify the 'type' of NRG1. In humans, six different NRG1 types have been identified (type I–VI) while only three (I–III) are recognised in rodents (Steinthorsdottir et al., 2004). The protein domain structure of the three common NRG1 types (I-III) is well conserved in human, rat and mouse (Steinthorsdottir et al., 2004). Type III contains a lipophilic cysteine-rich domain (CRD) and an N-terminal transmembrane domain (TMn), in addition to the C-terminal transmembrane domain (TMc) that is common to all NRG1

isoforms. Therefore, type III NRG1 proteins pass through the membrane twice, so remain membrane-bound even after cleavage (see below).

(2) The Immunglobulin (Ig) domain, encoded by two exons, characterises the 'Ig-NRG1s' (type I, II and human-specific type IV and V) and enables binding to proteoglycans at the cell surface and in the extracellular matrix. This may be associated with protein localisation (reviewed in Falls, 2003).

(3) The 'EGF-like' domain is common to all NRG1 types, and has variants α, β and γ. The β variant is reported to be more prevalent in the brain (Wen et al., 1994), and to have higher affinity to ErbB receptors (Jones et al., 1999) and greater potency in neurons (Liu et al., 2001) compared with the α form.

(4) Some NRG1 types contain a variable linker that connects the EGF-like domain with the TMc domain. Others have a terminal 'stalk' ('3' in Figure 1.1) at this point. Notably, these are soluble isoforms because they lack the TMc domain. (The same is true for γ-EGF variants.)

(5) The C-terminal cytoplasmic tail ('c'-part), encoded by three exons, is common to all membrane-bound NRG1 isoforms, and may terminate with a carboxy tail of 'a'-form (more common in the nervous system) or a 'b'-form.

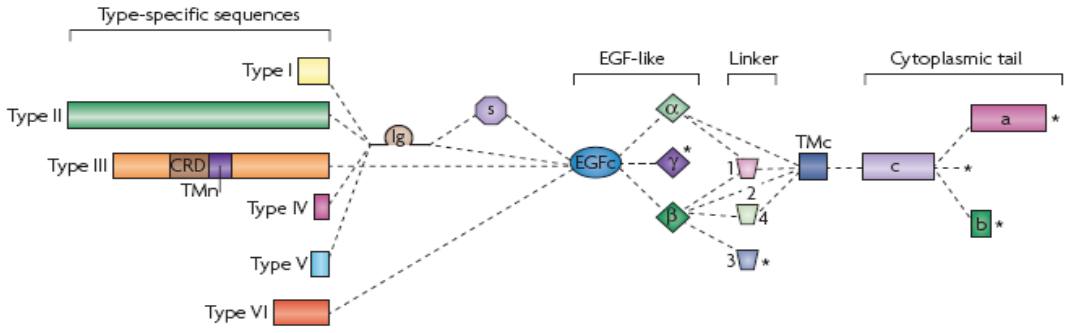


Figure 1.1 NRG1 isoforms arising from different promoter use and alternative splicing.
CRD, cystein-rich domain; TMn, N-terminal transmembrane domain; Ig, immunoglobulin domain; EGFc, core epidermal growth factor domain; TMc, C-terminal transmembrane domain. Adapted with permission (Nature Publishing Group) from Mei & Xiong (2008).

1.1.2 Brain area and cell type-specific expression of NRG1

Expression of NRG1 mRNA and protein has been reported in the neocortex, hippocampus, cerebellum and several brainstem nuclei (e.g. medial septum) in adult human (Law et al., 2004) and rodent brain (Chen et al., 1994; Corfas et al., 1995; Eilam et al., 1998; Kerber et al., 2003; Woo et al., 2007). In the hippocampus, NRG1 is mainly expressed in pyramidal cells of areas CA2, CA3, subiculum and parahippocampal gyrus, but less in dentate gyrus (DG) and CA1 (Corfas et al., 1995; Law et al., 2004; but see Eilam et al., 1998). The latter is interesting because ErbB4 (NRG1's receptor) is prominently expressed in CA1. This suggests pre-synaptic localisation of the signalling molecule NRG1 (in CA3) and post-synaptic location of its receptor ErbB4 (in CA1) (Huang et al., 2000).

However, some findings regarding NRG1 expression are conflicting. For instance, the expression of cortical NRG1 mRNA may (Chen et al., 1994; Law et al., 2004) or may not (Corfas et al., 1995; Kerber et al., 2003) be lamina-specific. The inconsistency in these findings might be attributable to differences in ribonucleotide probes (in situ hybridisation) or antibodies (immunohistochemistry) used in the studies, as well as to differences in animal species and age. As most studies have employed a universal NRG1 probe or antibody, little is known about isoform-specific expression. The few studies that utilised type-specific ribonucleotide probes (Kerber et al., 2003; Woo et al., 2007) observed NRG1 types I and II expressed in forebrain (possibly lamina-specific) and hippocampus of adult rats. In addition to isoform diversity, NRG1 expression is also reported to vary throughout development (Chen et al., 1994; Meyer et al., 1997), and may continue to vary in the adult brain, particularly because neuronal activity enhances NRG1 expression (Eilam et al., 1998). Some NRG1 types may be expressed at higher levels in pre-, peri- and neonatal hippocampus compared to adult brain (Meyer et

al., 1997), whereas the expression of NRG2 only increases postnatally (Talmage & Role, 2004).

At the cellular level, NRG1 is primarily, but not solely, expressed in pyramidal cells of adult hippocampus and neocortex (Chen et al., 1994; Kerber et al., 2003; Law et al., 2004). Some glial and possibly some interneuron expression has also been reported, but co-labelling with suitable neurochemical markers to identify interneuron types has not been performed. Subcellularly, NRG1 was found to localise to somatodendritic compartments, but it was also detected in fibre tracts and neuropil, thus implicating a presynaptic localisation of NRG1 (Law et al., 2004).

1.1.3 NRG1 signalling through ErbB receptors

NRG1 proteins are initially membrane-bound (by the common TMc domain, Figure 1.1), but they can be cleaved between the EGF-like- and the TMc domains by activity of cell-surface metalloproteases (reviewed in Falls, 2003; Mei & Xiong, 2008). Neuronal activity appears to regulate the processing of the membrane-anchored NRG1 precursors (Ozaki et al., 2004). Proteolytic cleavage gives rise to soluble N-terminal fragments containing the Ig and EGF domains (type I, II, IV, V), or, in case of type III, membrane-bound N-terminal fragments with a CRD domain. Thus, NRG1 may 'forward' signal in a paracrine (soluble N-terminal fragments) or juxtacrine fashion (membrane-bound N-terminal fragments) (Falls, 2003). In addition, the remaining C-terminal NRG1 fragment may initiate 'backward' (reverse) signalling in the NRG1-expressing cell (Bao et al., 2003; Falls, 2003).

NRG1 binds to ErbB3 and ERbB4 receptors via its EGF-like domain. Upon binding of NRG1, ErbB receptors form heterodimers (also with the co-receptor ErbB2) or homodimers (only ErbB4), which in turn triggers auto-phosphorylation of C-terminal

tyrosine residues and thereby activates various signalling cascades (reviewed in Mei & Xiong, 2008). The ErbB4 receptor is the primary receptor in neurons, while ErbB3 receptor expression has also been reported in glial cells (Gerecke et al., 2001). The ErbB4 receptor has different splice variants (yielding different types of intracellular domain), but it is currently unclear which contribute to signalling in hippocampal neurons (Neddens et al., 2011).

The neuronal expression pattern of ErbB4 receptors has been a matter of some debate (see Neddens et al., 2011), but recent immunohistochemical studies have shown that hippocampal ErbB4 co-localises with GABA (gamma-aminobutyric acid)-containing interneurons and not with pyramidal cells (Vullhorst et al., 2009; Fazzari et al., 2010). This was confirmed in frontal cortex of various animal species (mouse, rat, monkey and human) (Yau et al., 2003; Neddens et al., 2011). Similarly, ErbB4 mRNA expression is present in fast-spiking interneurons but absent in pyramidal cells of mouse hippocampus and frontal cortex (Vullhorst et al., 2009; Neddens et al., 2011). In general, ErbB4 is co-expressed with cholecystokinin (CCK), parvalbumin (PV), neuronal nitric oxide synthase (nNOS) and calretinin (CR) and, to a lesser extent, with calbindin and somatostatin (SOM) (Yau et al., 2003; Fazzari et al., 2010; Neddens & Buonanno, 2010). In hippocampi of adult mice, 54% of CCK-containing (CCK+) cells, 42% of PV+ cells and 39% of nNOS+ cells express ErbB4 with few differences between hippocampal subregions (Neddens & Buonanno, 2010). This suggests that ErbB4 expression may be concentrated in specific interneuron types (Section 1.2.3). In mouse somatosensory cortex, Fazzari and colleagues (2010) reported that ErbB4 strongly localises to PV+ interneurons with morphological characteristics of axo-axonic cells (AACs) and basket cells (BCs). Subcellularly, ErbB4 expression has been identified at presynaptic terminals (Woo et al., 2007; Fazzari et al., 2010; but see

Chapter 4) and postsynaptic densities of interneurons (Garcia et al., 2000; Huang et al., 2000; Vullhorst et al., 2009; Fazzari et al., 2010). Various GABAergic interneuron types, including perisomatic-targeting interneurons (PTIs), may be subject to modulation by NRG1/ErbB4 signalling (reviewed further in Chapters 4 and 5).

1.1.4 Functions of NRG1 in the nervous system

NRG1/ErbB4 signalling is implicated in a wide range of processes, both during development and throughout adult life. Genetic ablation of NRG1, either total (knockout of NRG1-EGF domain) or of selected isoforms (Ig-NRG or CRD-NRG), has demonstrated its essential role in the development of heart, breast and nervous system. Homozygous NRG1 knockouts are not viable due to developmental abnormalities (Meyer and Birchmeier, 1995; Kramer et al., 1996; Stefansson et al., 2002; review by Falls, 2003). To elucidate the role of NRG1 in the nervous system, both genetic mouse models (heterozygous mutants; Deakin et al., 2009) and acute application of exogenous NRG1 peptides have been employed. These studies have revealed that NRG1's effects on the nervous system are pleiotropic. During development, NRG1 controls neuronal differentiation, migration and axon guidance. It promotes glial development, neuron-glial signalling and assists in synapse formation. Importantly, it also has a role in mature brain, as suggested by its continued expression throughout life (Section 1.1.2). Generally, postnatal NRG1/ErbB4 signalling is reported to interfere with glutamatergic, GABAergic, dopaminergic (Kwon et al., 2008; Neddens et al., 2009) and cholinergic neurotransmission, and may modulate activity-dependent synaptic plasticity (see Chapters 3 to 5). As an illustration of the diversity of NRG1 function, Table 1.1 categorises its roles in the immature and mature nervous system, and lists many of the relevant key discoveries pertaining to NRG1/ErbB4 signalling in the neocortex and

Table 1.1 Pleiotropic functions of NRG1 in the immature and mature nervous system

Function	Key reference	Findings
(A) Immature nervous system		
Neuronal specification	Liu et al., 2005	NRG1 stimulates proliferation of embryonic neural progenitor cells
Neuronal migration	Flames et al., 2004	NRG1 isoforms (expressed in developing cortex) are short- and long-range chemoattractants for medial ganglionic eminence explants; ablation of ErbB4 decreases postnatal cortical interneuron density
	Lopez-Bendito et al., 2006	NRG1 type III creates a permissive corridor for thalamocortical development; soluble Ig-NRG1 serves as long-range chemoattractant to cortex
Glial development and differentiation	reviewed in: Mei & Xiong, 2008; Newbern & Birchmeier, 2010	NRG1 promotes differentiation of neural progenitor cells towards glial cell fate and stimulates their proliferation; NRG1 stimulates proliferation and maturation of glia cells (Schwann cells, oligodendrocytes) and promotes survival (oligodendrocytes, astrocytes)
Neuron-glia signalling & myelination	Michailov et al., 2004	NRG1 type III is essential for myelination in PNS: over-expression of NRG1 type III (not I) increases thickness of myelin sheath in PNS
	Brinkmann et al., 2008	NRG1 type I and III over-expression causes hypermyelination in neocortex
Dendritic growth and maturation	Gerecke et al., 2004	NRG1 stimulates neurite outgrowth in cultured hippocampal neurons
	Barros et al.,2009	Increased NRG1 promotes and loss of ErbB2/B4 impairs dendritic spine maturation in cultured hippocampal neurons
Synapse formation and maturation	Li et al., 2007	NRG1/ErbB4 controls activity-dependent maturation and spine stability of excitatory synapses in CA1 hippocampus; over-expression of ErbB4 selectively increases AMPAR-mediated transmission
	Fazzari et al., 2010	NRG1 promotes GABAergic synapotgenesis; ablation of ErbB4 in interneurons reduced frequency of mEPSCs in hippocampal interneurons but not in pyramidal cells
	Ting et al., 2011	NRG1 increases number and size of postsynaptic densities (PSD-95 puncta) as well as the frequency and amplitude of mEPSCs in GABAergic interneurons

Table 1.1 continued

Function	Key reference	Findings
(B) Mature nervous system		
Regulation of neurotransmitter receptors		
1) nAChRs	Liu et al., 2001	Acute exposure to NRG1 increases nAChRs in GABAergic cells
	Chang & Fischbach, 2006	NRG1 acutely decreases nAChRs in CA1 interneurons
	discussed further in Chapter 3	
2) GABA-A receptors	Okada & Corfas, 2004	Lasting exposure to NRG1 selectively downregulates α subunits in cultured hippocampal cells
	discussed in detail in Chapter 4	
3) ionotropic glutamate receptors (AMPARs; NMDARs)	Ozaki et al., 1997	Lasting exposure to NRG1 induces expression of NR2C subunit in cultured cerebellar granule cells
	discussed in detail in Chapter 5	
Modulation of synaptic transmission	Woo et al., 2007	GABAergic transmission: NRG1 stimulates depolarisation-induced GABA release in prefrontal cortex
	Gu et al., 2005	Glutamatergic transmission: NRG1 reduces NMDAR-mediated currents in frontal cortex pyramidal cells
	discussed further in Chapters 4 and 5	
Modulation of synaptic plasticity	Kwon et al., 2005; Kwon et al., 2008	NRG1 reverses LTP at Schaffer collateral-CA1 synapses through dopamine receptors
	Bjarnadottir et al., 2007	$NRG1^{+/-}$ mice show impaired theta-burst hippocampal LTP but this is rescued by acute NRG1 (unless if in excess, e.g. high NRG1 concentrations, then LTP is reduced again). See comment by Role & Talmage, 2007.

The classification of NRG1 functions is based on Table 1 in Harrison & Law (2006). AMPARs, α-amino-3-hydroxy-5-methylisoxazole-4-propionic acid receptors; LTP, long-term potentiation; nAChRs, nicotinic acetylcholine receptors; NMDARs, *N*-methyl-D-aspartate receptors; mEPSCs, miniature excitatory postsynaptic currents; PNS, peripheral nervous system.

hippocampus. More extensive reviews can be found in Falls (2003), Harrison & Law (2006), Mai & Xiong (2008), Buonanno (2010) and Rico & Marin (2011).

Importantly, the outcome of NRG1 studies can depend, to a significant extent, on the particular experimental design. Such factors include: use of acute versus genomic intervention; species, age and developmental stage; brain region; and tissue preparation technique (*in vitro* studies). In addition, the biological complexity of NRG1 isoforms and isoform-specific signalling (Meyer et al., 1997) is likely to contribute to the diversity of NRG1 effects. Different isoforms are likely to have distinct functions in the adult brain, but this complexity is, as yet, poorly understood as few studies have worked with selected NRG1 isoforms (Ozaki et al., 1997; Bjarnadottir et al., 2007; Deakin et al., 2012).

1.1.5 The neurobiology of schizophrenia and the implication of NRG1

Several genes have been associated with schizophrenia including catechol-O-methyl transferase (COMT), dysbindin (DTNBP1), disrupted-in-schizophrenia 1 (DISC1), GRM3, encoding metabotropic glutamate receptor-3 (mGluR3), as well as NRG1 (Harrison & Weinberger, 2005; Kleinman et al., 2011). Overall, it is suggested that multiple 'risk genes' (as well as gene/environment interactions) contribute to the disorder, each of small effect (Harrison & Law, 2006). The clinical symptoms profile is complex, characterised as having positive (hallucinations, delusions) and negative symptoms (social withdrawal, affective flattening), as well as cognitive impairment (Harrison, 2004). Schizophrenia is believed to be a neurodevelopmental disorder (Rapoport et al., 2005) that is a manifestation of network dysfunctions in several brain areas, specifically within the hippocampus and prefrontal cortex and their connectivity (Uhlhaas & Singer, 2010).

The dopaminergic neurotransmitter system has been implicated in the neuropathology of schizophrenia (reviewed in Guillin et al., 2007), but malfunctions here may be secondary to changes in other neurotransmitter systems. The finding that misuse of ketamine and other *N*-methyl-D-aspartate receptor (NMDAR) antagonists causes psychotic symptoms has boosted the idea that the glutamatergic system and NMDARs might contribute to the pathophysiology (Olney & Farber, 1995; Coyle et al., 2003; Stone et al., 2007). Specifically, NMDARs on GABAergic interneurons are proposed to be dysfunctional in schizophrenia, and ample evidence implicates dysregulation of GABAergic signalling in its pathophysiology (reviewed in Lewis et al., 2011; Gonzalez-Burgos & Lewis, 2012). Post-mortem brain examinations have revealed reduced expression of enzymes implicated in GABA synthesis (GAD67 enzyme, the 67 kDa isoform of glutamate decarboxylase) and uptake (Volk et al., 2000; Volk et al., 2001). Furthermore, expression of PV, a neurochemical marker for some interneurons, is impaired in prefrontal cortex of schizophrenic patients (Hashimoto et al., 2003; Lewis et al., 2012). A distinct subtype of PV-expressing interneurons may be particularly affected in the disorder (Woo et al., 1998). I will discuss this in greater detail in Chapter 6. Importantly, impaired GABAergic inhibition might be the cause of over-activity in other neurotransmitter systems, and thereby result in excessive dopamine signalling — typical of the positive schizophrenia symptoms.

The NRG1 gene has been genetically associated with schizophrenia since a study of the Icelandic DNA repository in 2002: single nucleotide polymorphisms (SNPs) in the 5' region of the NRG1 gene on chromosome 8p showed statistical linkage to schizophrenia (Stefansson et al., 2002). Although subsequent association studies have had mixed results, overall the evidence supports an association of NRG1 with schizophrenia (reviewed in Harrison & Law, 2006) and has grown for particular NRG1

isoforms (see below; Law et al., 2006; Tan et al., 2007; Keri et al., 2009) and for other members of the NRG gene family (NRG3; Kao et al., 2010). NRG1's receptor, ErbB4 has also been genetically linked with an increased risk of schizophrenia (Walsh et al., 2008). Furthermore, biological mechanisms of NRG1/ErbB4 signalling hint at its potential involvement in the pathophysiology of schizophrenia (see Chapter 6; Banerjee et al., 2010; Buonanno, 2010; Rico & Marin, 2011).

Interestingly, most SNPs are located in the non-coding region of the NRG1 gene, therefore expression levels rather than NRG1 protein function itself is likely to be altered in schizophrenia (Harrison and Weinberger, 2005; Harrison and Law, 2006). Postmortem studies of NRG1 gene expression in schizophrenic patients reported increased expression of NRG1 type I in brain tissue (Harrison and Law, 2006; Bertram et al., 2007; Parlapani et al., 2010). Specifically, NRG1 type I (but not II or III) mRNA expression was increased in prefrontal cortex (Hashimoto et al., 2004) and hippocampus (Law et al., 2006; Parlapani et al., 2010). NRG1 protein levels were also found to be increased in the prefrontal cortex of schizophrenic patients (Chong et al., 2008) but the 'pan-NRG1' antibodies could not distinguish type-specific changes. NRG1 protein levels detected by antibodies against the 'a'-type cytoplasmic tail were not altered in the prefrontal cortex of schizophrenic subjects (Hahn et al., 2006).

In conclusion, schizophrenia has most consistently been associated with increased NRG1 type I expression, although other NRG isoforms/proteins may also be involved (Law et al., 2006).

1.2 The hippocampus: structure and connectivity

1.2.1 Signal transmission in the hippocampus

The hippocampus and related brain regions form a functional unit that is called the 'hippocampal formation' (Amaral & Witter, 1989). It comprises of the DG, the 'hippocampus proper' (Cornu Ammonis, CA; subfields: CA1–3), the subiculum, the pre- and parasubiculum and the entorhinal cortex (EC). The term hippocampus often refers to the DG and the 'hippocampus proper'. The principal cells in the 'hippocampus proper' are glutamatergic pyramidal cells that are arranged in a compact layer (the str. pyramidale), but likely form a heterogeneous, functionally distinct cell population (Mizuseki et al., 2011; Slomianka et al., 2011). The principal cells in the different subregions of the hippocampal formation are connected via an excitatory feedforward glutamatergic synapse loop that ensures a unidirectional flow of information; granule cells of the DG receive inputs predominantly from the EC through the perforant path and send mossy fibre projections to area CA3. The CA3, in turn, sends collaterals to area CA1. Pyramidal cells in CA1 project to the subiculum, which targets back to the EC. CA1 pyramidal cells also project directly to the deep layers (in particular layer V) of the EC, although this projection is suggested to be relatively weak compared with the hippocampal connection of CA1 neurons via subicular pyramidal cells (Swanson et al., 1978; Amaral & Witter, 1989). In addition to the trisynaptic pathway (DG-CA3-CA1-subiculum), the hippocampus also has a shorter monosynaptic pathway, in which projections from layer III of the EC relay information to CA1 ('temporoammonic pathway'), whose neurons project back to layer V of the EC (Nakashiba et al., 2008).

Most of the projections are organised in a highly topographic manner, often in the transverse as well as septo-temporal plane (reviewed in Somogyi, 2010).

The signal that is sent via the multisynaptic feedforward loop is processed, en route, in local circuits of each hippocampal subregion. Information processing in the hippocampus involves both the separation and the completion of input patterns to contrast and restore inputs, respectively (reviewed in McNaughton & Morris, 1987; Lisman, 1999; Bischofsberger et al., 2006 Andersen et al., 2007). Unique local circuit and synapse dynamics contribute to the different ways of information processing: the DG is proposed to amplify contrasts between more dissimilar input patterns (by performing pattern separation, McNaughton & Morris, 1987), whereas the CA3 network is suited to restore incomplete input patterns (see below). Area CA1, on the other hand, may serve to compare the input from EC layer III with the output from CA3 (match-mismatch detection), and also to convey information back to the cortex (Lisman, 1999; Andersen et al., 2007). The autoassociative memory function of area CA3 may be attributable to its strong recurrent excitatory connectivity: in certain conditions, for instance when an animal is at a particular place, mossy fibre synapses activate a distinct ensemble of CA3 pyramidal cells (‘conditional detonators’, see Bischofsberger et al., 2006). Additional information about the memory context (e.g. details of the environment) may be received from the EC via the perforant pathway, biasing individual CA3 pyramidal cells to subthreshold depolarisation (Lisman, 1999). Repeated visits of the animal at the same place (in the same environment) will potentiate CA3–CA3 synapses of this activated pyramidal cell assembly. During memory retrieval in a modified environment, previously potentiated CA3–CA3 synapses help complete a partial cue (represented in a subset of active pyramidal

neurons) by spreading the activity across to those other pyramidal cells that were part of the originally encoded activity pattern (complete memory).

Importantly, each hippocampal subregion comprises complex local inhibitory microcircuits that organise the activity of pyramidal cell assemblies. Inhibitory interneurons are the primary elements of these unique local microcircuits. They express glutamic acid decarboxylase (GAD) and release GABA as their primary transmitter. Interneurons are a consortium of highly specialized neuron types that differ in their anatomical, neurochemical and functional features (Section 1.2.3; Freund & Buzsaki, 1996). Together, this population of interneurons serves to control the spatio-temporal pattern of pyramidal cell activity by inhibition (reviewed in Somogyi, 2010).

1.2.2 Ontogenetic development of the hippocampal circuitry

Correct wiring of neuronal circuits is critical for physiological function. Therefore, knowledge of the development of the hippocampal circuitry, in particular the GABAergic system, is a prerequisite to understanding hippocampal function. Three main developmental stages during embryonic and early postnatal life may be distinguished (Flames & Marin, 2005; Danglot et al., 2006; Ramamoorthi & Lin, 2011):

1. Proliferation and differentiation of hippocampal neurons

Pyramidal cells are derived from the ventricular zone of the dorsal telencephalon, while interneurons originate from the subpallium (ventral telencephalon). During development, the subpallium is subdivided into lateral, medial and caudal ganglionic eminences (LGE, MGE, CGE) and the preoptic area. All these regions express common transcription factors (e.g. Mash1, Dlx) which stimulate the GABAergic phenotype (reviewed in Danglot et al., 2006). The expression of other

transcription factors is region-specific, depends on developmental stage, and is likely to determine the interneuron subtype specification and, ultimately, give rise to the diverse interneuron population (Butt et al., 2005; Miyoshi et al., 2007; Batista-Brito & Fishell, 2009). For example, transcription factor Nkx2.1, expressed in MGE, defines cortical interneurons that later express PV or SOM. In contrast, cortical interneurons from the CGE postnatally express CCK, CR, VIP or neuropeptide Y (NPY) (Lopez-Bendito et al., 2004; Xu et al., 2004; Morozov et al., 2009). Dysfunction of these early developmental processes might result in inappropriate numbers and/or subtypes of neurons.

2. Neuronal migration

Pyramidal cells migrate radially across relatively short distances from the ventricular zone towards the pial surface. In contrast, GABAergic neurons travel further, from subpallial ganglionic eminences to their cortical targets. They then settle into cortical layers through radial migration in an inside-out manner, such that the youngest neurons are closest to surface (reviewed in Danglot et al., 2006). GABAergic neurons that arrive in the hippocampal marginal zone (later str. radiatum) translocate to other layers during early postnatal days. Multiple short- and long-range chemoattractants (among them, NRG1) and chemorepellents play a pivotal role in the tangential and radial migration (Flames et al., 2004; Lopez-Bendito et al., 2006).

3. Morphological maturation and synaptogenesis

Morphological maturation of interneurons occurs progressively, over an extended (3–4 week) postnatal period, once cells have reached their final destinations.

During maturation, synapses develop, and distinct interneuron types acquire their neurochemical properties. Interestingly, different interneuron types (Section 1.2.3) mature at different stages (e.g. AACs mature later than BCs; Howard et al., 2005). Strikingly, GABAergic synapses occur on GABAergic interneurons *before* glutamatergic synapses on GABAergic interneurons (Gozlan & Ben-Ari, 2003). For example, in the DG, the first GABAergic synapses in Lhx6-containing PTIs occur around P3 (Sauer & Bartos, 2010). At this stage, GABA signalling is still excitatory in these cells (up to ~P10), due to the late expression of the K^+/Cl^- co-transporter KCC2 (Ben-Ari, 2002). Hippocampal principal cells are only innervated later, but in the same sequence as GABAergic interneurons (first GABAergic, then glutamatergic synapses).

Synaptogenesis initially requires activity-independent mechanisms, such as cell–cell recognition (e.g. mediated by Neuroligin-2/Neurexin at inhibitory synapses; Varoqueaux et al., 2004), but later on, activity-dependent mechanisms become critical. Endogenous neuronal activity, possibly driven by GABA, promotes further synapse formation and maturation, morphogenesis and interneuron type-specific expression of neuropeptides and voltage-gated channels. Neuronal activity may be conveyed by brain-derived neurotrophic factor (BDNF), because its synthesis and release is dependent on neuronal activity, and it promotes GABAergic synaptogenesis (reviewed in Danglot et al., 2006). BDNF is also involved in the formation of excitatory synapses on hippocampal fast-spiking PV+ interneurons, as confirmed by PV-selective knockout of TrkB receptors (Zheng et al., 2011). NRG1/ErbB4 signalling may have similar functions given its activity-dependent expression (Eilam et al., 1998) and processing (Ozaki et al., 2004). As outlined above, it has recently been implicated in the formation and maturation of

synapses, particularly in PV+ interneurons (Fazzari et al., 2010; Ting et al., 2011). In conclusion, correct synapse development in the early postnatal weeks is crucial to achieve the correct balance between excitation and inhibition in the mature circuit.

1.2.3 The cytoarchitecture of area CA3

The CA3 region is central to generating hippocampal gamma oscillations (Section 1.3) and is the focus of this study. It is subdivided into regions CA3c (within hilus), CA3b and CA3a (closest to CA2). All subregions consist of distinct strata that are visible in a transverse hippocampal sections: large pyramidal cell somata are located in the dense str. pyramidale, which may be further subdivided into a more compact, superficial part and a less compact, deeper part (Slomianka et al., 2011). The apical dendrites of pyramidal cells extend through str. lucidum and str. radiatum to str. lacunosum-moleculare where they branch extensively. Basal dendrites extend into the lower str. oriens towards the alveus (Ishizuka et al., 1995).

Excitatory connectivity in area CA3

There are four major glutamatergic input pathways to CA3 pyramidal cells (reviewed in Somogyi, 2010):

(1) DG granule cells project to CA3 pyramidal cells via glutamatergic mossy fibres. They predominately target proximal pyramidal cell dendrites, a laminar area visible as str. lucidum in area CA3.

(2) Perforant pathway inputs from medial and lateral EC layer II are primarily received on distal CA3 pyramidal cell dendrites in the str. lacunosum-moleculare. Some CA3 pyramidal cells (those closest to the DG) may, however, not receive perforant path inputs.

(3) Associational fibres connect CA3 pyramidal cells recurrently within the same brain hemisphere. Their glutamatergic synapses are primarily located in the str. radiatum and str. oriens. As mentioned above, recurrent connections in the CA3 network enable input integration.

(4) Contralateral CA3 areas are connected through commissural fibres. Importantly, synapses of commissural inputs are likely to differ from associational fibre synapses in both molecular and functional aspects (Shinohara et al., 2008; Kohl et al., 2011).

CA3 interneurons may also be excited by all four glutamatergic afferent pathways, but the weight of afferent-specific input likely varies between interneuron types (see below and Chapter 5). When an interneuron is excited by an extrinsic afferent input (e.g. an input originating from another functional area), it elicits 'feedforward' inhibition (reviewed in Buzsaki, 2006). For example, neurogliaform cells in area CA1 extend their dendrites mainly in str. lacunosum-moleculare and receive input from the perforant pathway (e.g. from pyramidal cells in layer II of the EC). In the CA1 circuit, these cells thus mediate 'pure' feedforward inhibition (Alger & Nicoll, 1982; Capogna, 2011). In contrast, interneurons that receive excitatory input predominantly from local pyramidal cells mediate 'feedback' inhibition. Oriens-lacunosum moleculare (O-LM) interneurons are a classical sample of the latter as their dendrites ramify mainly in str. oriens where local pyramidal cells axons arborise (Blasco-Ibanez & Freund, 1995). Most hippocampal GABAergic interneuron types contribute to feedforward as well as feedback inhibition; only some cell types, as illustrated in the samples above, are specialized to one of these logical operations. In line with this, GABAergic interneurons

show laminar differences in their dendritic arborisation, and not all interneurons have dendritic trees that span all layers (Gulyas et al., 1999; Somogyi & Klausberger, 2005).

In addition to the cortical glutamatergic inputs, area CA3 receives a variety of signals from subcortical areas. These include cholinergic inputs from the medial septum, noradrenergic projections from the locus coreuleus in the brainstem, serotonergic inputs from midbrain raphe nuclei (Freund & Buzsaki, 1996) as well as modulation by endocannabinoids produced within the hippocampus itself (Hajos et al., 2000). These neuromodulatory signals affect both pyramidal cells and distinct interneuron types, depending on the expression of receptors (Armstrong & Soltesz, 2012). For example, the direct action of ACh on pyramidal cells is excitatory, producing depolarisation (Fisahn et al., 2002). This is mediated through activation of postsynaptic muscarinic AChRs (mAChRs), predominantly subtype M1, which initiate signalling cascades to reduce various potassium conductances (Fisahn et al., 2002). Some interneurons, like CCK-containing BCs, are also sensitive to ACh. CCK-positive BCs express muscarinic (M1 and M3) and nicotinic (α4 or α7 subunit-containing) AChRs, and cholinergic activation alters their firing patterns and rates (Ceo-del Rio et al., 2010; Ceo-del Rio et al., 2011). Chapter 3 expands on the cholinergic modulation of CA3 pyramidal cells and interneurons.

Inhibitory connectivity in area CA3

Inhibitory connectivity is complex. Diverse interneuron types can be classified in terms of their neurodevelopmental origin (see above) and their anatomical, neurochemical and functional features. This multi-parameter classification is useful for identifying distinct subpopulations and understanding their division of labour in hippocampal function (Freund & Katona, 2007; Armstrong & Soltesz, 2012). The population of GABAergic interneurons that serves area CA3 appears to be as diverse as

in area CA1, but their classification and brain-state-specific behaviour has not been as well investigated as for CA1 interneurons (Klausberger & Somogyi, 2008; Somogyi, 2010).

Anatomical classification

Hippocampal interneurons target pyramidal cells in a domain-specific manner. Axon arborisation is an instructive classification criterion, because it reveals which postsynaptic cell domain interneurons primarily target to. Interneurons whose axons predominately innervate pyramidal cell somata and proximal dendrites (BCs; Freund & Buzsaki, 1996), or pyramidal cell axon initial segments (AACs; Somogyi, 1977; Somogyi et al., 1983) are suited to control pyramidal cell output (Miles et al., 1996). In addition to these types of PTIs, there are numerous types of dendritic-targeting interneurons. These regulate the excitatory dendritic input to pyramidal cells in a layer-specific manner, and can suppress the generation of postsynaptic calcium-dependent spikes, thereby effectively controlling input–output transformation in pyramidal cells (Miles et al., 1996; Lovett-Barron et al., 2012). In area CA3, mossy-fibre-associated cells selectively control glutamatergic input from the DG (Vida & Frotscher, 2000), whereas interneurons with predominant axon arbor in str. lacunosum-moleculare (O-LM-like cells in CA3; Gulyas et al., 1993a) could be involved in feedback inhibition in the area. In general, feedback inhibition is mediated by interneurons that receive excitatory input mainly from local pyramidal cells and serves as a regulatory mechanism to decrease the output of active pyramidal cells in the same area (which recruit the inhibition in the first place, hence termed ‘feedback’). Dendritic-targeting interneurons that arborise in the str. radiatum and str. oriens are ideally suited to control recurrent fibre input. NPY-releasing interneurons such as ivy cells and bistratified cells (but note that existence of the latter in CA3 is not proven; Somogyi, 2010) may exert

inhibitory effects on CA3 pyramidal cells by suppressing glutamate release via presynaptic Y2 receptors (McQuinston & Colmers, 1996).

A third pattern of interneuron connectivity targets other interneurons, and may be ideally suited to synchronise interneuronal output. Certain interneurons specifically target other inhibitory cells, and are hence called 'interneuron-selective interneurons' (Acsady et al., 1996; Gulyas et al., 1996). Such connections can also be projective as was demonstrated in a subset of hippocampo-septal interneurons, which relay information from the hippocampus to the medial septum. These cells appear to be interneuron selective, targeting GABAergic pacemaker neurons in the medial septum as well as other hippocampo-septal cells (Toth et al., 1993; Gulyas et al., 2003). They were suggested to control septo-hippocampal disinhibition (Toth et al., 1993).

Neurochemical classification

Neuronal structure is not always a sufficient criterion to distinguish different types of interneurons. For example, two types of BCs have very similar axon arborisations but vary in their neurochemical expression profile, either expressing PV, or cannabinoid receptor 1 (CB1R) and CCK (Glickfeld & Scanziani, 2006; Szabo et al., 2010). In general, distinct hippocampal interneuron types express mutually exclusive calcium binding proteins (PV, Calbindin and CR) and/or characteristic combinations of neuropeptides (e.g. NPY, SOM, CCK, vasoactive intestinal polypeptide) (Somogyi & Klausberger, 2005). Although the expression of calcium-binding proteins is mutually exclusive between interneuron populations, PV (for example) is expressed in four structurally different interneuron types (BC, AAC, bistratified cell and O-LM interneurons; Somogyi, 2010). Therefore, unambiguous classification requires interneuron morphology together with neurochemical identification.

Functional classification

Finally, interneurons differ in their intrinsic electrophysiological properties (e.g. membrane properties; firing pattern; synapse dynamics; reviewed in Freund & Katona, 2007; Armstrong & Soltezs, 2012) as well as in their temporal firing characteristics during defined brain states (Klausberger et al., 2003; Klausberger et al., 2004). Using PTIs as an example, I now outline how distinct functional characteristics contribute to the functional diversity of interneurons.

1.2.3.1 Perisomatic inhibition

Perisomatic inhibition is provided by PV+ AACs (also known as chandelier cells) and two types of BCs that express either PV or CB1R (and CCK), but not both (Somogyi & Klausberger, 2005). In area CA1, PV+ BCs synapse more on pyramidal cell somata while CB1R+ BC may preferentially contact proximal dendritic domains (Foldy et al., 2010). PV+ BCs, CB1R+ BCs and AACs differ in three main properties: synaptic inputs, intrinsic membrane properties and GABAergic synapse kinetics/dynamics (Howard et al. 2005; Freund & Katona, 2007; Armstrong & Soltezs, 2012 for reviews). In this regard, area CA3 has not been extensively investigated; most of our knowledge stems from evidence obtained in area CA1.

Synaptic input

All three PTI types have spineless dendrites that vertically span all hippocampal layers (Gulyas et al., 1999 but see Li et al., 1992). Glutamatergic input to CA1 PV+ interneurons is richer (Gulyas et al., 1999) and stronger than into CB1R+ BCs (Glickfeld & Scanziani, 2006), but there may be differences between axons from distinct afferent cell populations (Szabadics & Soltezs, 2009). I will discuss this together with postsynaptic receptor-type expression patterns further in Chapter 5.

Glutamatergic synapses of CA1 PV+ and CB1R+ BCs also vary in their dynamics, with stronger short-term depression of excitatory inputs to CB1R+ BCs (Glickfeld & Scanziani, 2006). In addition to the glutamatergic input, PTIs also receive GABAergic inputs either from local interneurons in area CA3 or from external GABAergic afferents (e.g. neurons in the medial septum) (Freund & Antal, 1988; Freund, 1989; Toth et al., 1997; Bartos et al., 2002). Interestingly, GABAergic input is stronger in CB1R+ BCs than in PV+ BCs (Freund & Katona, 2007).

Intrinsic functional properties

PV+ PTIs differ in their passive membrane properties. PV+ BCs have shorter membrane time constants than dendritic-targeting PV+ bistratified cells (Buhl et al., 1996) or CB1R+ BCs (Glickfeld & Scanziani, 2006). Together with strong glutamatergic innervation, fast time constants make PV+ BCs temporally precise followers of pyramidal cell input. The less accurate CB1R+ BCs are better suited to integration of (feedforward and feedback) inputs (Glickfeld & Scanziani, 2006; Freund & Katona, 2007). In line with this, CB1R+ BCs are also more susceptible to subcortical neuromodulation than PV+ BCs and AACs, and they express various relevant receptors (serotonergic 5-HT_3 receptor, cholinergic M1-, M3-type mAChRs, α4 or α7 subunit-containing nAChRs, intracellular estrogen receptor, presynaptic CB1 receptor). Taken together, CB1R+ BCs are probably important for integrating slow-conducting subcortical afferent inputs. Nevertheless, PV+ BCs also express some modulatory receptors (μ opioid receptor, M1- and M2-type mAChRs, CCK receptor), as do AACs (M2-type mAChR; Hajos et al., 1998), which serve to modify their input–output function (Glickfeld & Scanziani, 2006; Freund & Katona, 2007 for review).

Firing and synaptic output

PV+ BCs and AACs are fast-spiking interneurons that exhibit little spike frequency adaptation (Freund & Buzsaki, 1996). In contrast, CB1R+ BCs are regular-spiking neurons (Pawelzik et al., 2002; Ascoli et al., 2008; Szabo et al., 2010). The fast-spiking phenotype is associated with the voltage-gated potassium channel Kv3.1 (Du et al., 1996). Differences in their spiking properties were also observed during spontaneous hippocampal rhythms in anaesthetised animals (Klausberger et al., 2003; Klausberger et al., 2005). With regards to GABA output, synapses differ in their efficiency of GABA release: CA1 PV+ BCs release GABA with high temporal precision (due to tight coupling of release machinery with P/Q-type calcium channels), whereas release from CB1R+ BCs is more asynchronous (Hefft & Jonas, 2005). It is noteworthy that neuromodulators may differentially control GABA release from both types of BCs (see above; Freund & Katona, 2007). Finally, postsynaptic sites (e.g. GABA-A receptor subunit composition and chloride regulation) may differ between GABAergic terminals of different interneuron types (Armstrong & Soltesz, 2012). Heteropentameric GABA-A receptors often contain two α, two ß and one γ subunit of different composition depending on the brain region (reviewed in Nyiri et al., 2001). Interestingly, the α2 subunit has been more frequently associated with AAC synapses than with somatic synapses on hippocampal pyramidal cells (Nusser et al., 1996). Similarly, the α2 subunit content is shown to be higher in PV-negative synapses, probably established by CCK+ BCs, than in PV-expressing synapses (Nyiri et al., 2001). In contrast, PV+ BCs preferably synapse on α1 subunit-containing receptors (Klausberger et al., 2002). Thus, the two types of BCs may act via distinct GABA-A receptor populations. The subunit composition of GABA-A receptors conveys unique physiological and pharmacological properties. For example, GABA-A receptors

containing α1 subunits show a higher affinity for the benzodiazepine zolpidem compared to α2-containing GABA-A receptors (reviewed in Nyiri et al., 2001). In fact, in CA1 pyramidal cells, zolpidem was shown to potentiate synaptic responses from fast-spiking BCs, likely expressing PV, but not regular-spiking BCs (likely PV−; Thomson et al., 2000). Distinct α subunits of the GABA-A receptors also mediate different effects of the benzodiazepine diazepam (reviewed in Nyiri et al., 2001): The sedative and amnesic action of diazepam has been attributed to α1 subunit-containing receptors, implying a role for PV+ BCs in mnemotic processes. In contrast, the anxiolytic action of diazepam has been associated with α2 subunit-containing receptors, specifically at synapses of CB1+ BCs. The latter is consistent with the anxiolytic effects of CCK as well as of cannabinoid agonists (Freund & Katona, 2007). Interestingly, α2 subunit-containing GABA-A receptors are reported to have a higher affinity to GABA than α1 subunit-containing GABA-A receptors, and experiments on recombinant GABA-A receptors suggest that the α2 subunit may convey faster rise times and slower decay kinetics than α1 subunit-containing GABA-A receptors (Lavoie et al., 1997). Miniature inhibitory postsynaptic currents (mIPSCs) were found to decay more slowly in CA1 hippocampal neurons from α1 knockout mice compared to those from wild-type (WT) mice (Goldstein et al., 2002).

All PTIs are characterised by vast divergence, and often make multiple contacts on a single pyramidal cell (Gulyas et al., 1993a; Miles et al., 1996): in area CA1, a single PV+ BC was estimated to contact more than 1500 pyramidal neurons and 60 other PV+ interneurons (Sik et al., 1995). Mutual interconnectivity, through synaptic and electric connections (somatodendritic gap junctions, Fukuda & Kosaka, 2000; Bartos et al., 2001; Bartos et al., 2002), allows PV+ interneurons (in particular PV+ BCs) to synchronise their firing output. This ensures that BCs exert spatiotemporal

control over the activity of a large ensemble of pyramidal cells (Cobb et al., 1997; Pouille & Scanziani, 2001). This makes them suited to shape temporal oscillatory patterns (see below). Interestingly, AACs target an equally impressive number of pyramidal cells (1 AAC to ~1200 CA1 pyramidal cells; Howard et al., 2005), but not interneurons. Further, it is not known if they are coupled through gap-junctions (Howard et al., 2005). Strikingly, AACs may exert excitatory effects on postsynaptic pyramidal cells due to a shift in the local chloride reversal potential in axon initial segments (AISs; Szabadics et al., 2006; Woodruff et al., 2009 but see Glickfeld et al., 2009). Taken together, it appears that AACs may control pyramidal cell output by shunting concurrent excitatory inputs, whereas PV+ BCs may serve to synchronise pyramidal cell output by hyperpolarising inhibition (Cobb et al., 1995).

1.3 Hippocampal gamma oscillations

Adult brain networks generate a broad spectrum of oscillations. Distinct frequency bands have long been shown to represent different behavioural states (reviewed in Buzsaki, 2006). Theta oscillations (4–10 Hz) with superimposed fast rhythmic activity in the gamma band (~25–140 Hz) are associated with awake, attentive behaviour as well as with rapid eye movement (REM) sleep. Cognitive functions, such as working memory, memory encoding and memory retrieval are linked with these neural oscillations (reviewed in Engel et al., 2001; Fries, 2005; Lisman, 2005).

1.3.1 Hippocampal gamma rhythm *in vivo*

In awake, behaving rats, hippocampal gamma-frequency oscillations occur most prominently when nested in theta frequency epochs (Bragin et al., 1995; Csicsvari et al., 2003). Two independent circuits are proposed to produce hippocampal gamma oscillations. One is located within area CA3; the other is in the EC (Bragin et al., 1995; Csicsvari et al., 2003). Gamma oscillations also occur in CA1 but they lag those in CA3, which suggests that the activity is propagated from CA3 to CA1 (Csicsvari et al., 2003). In addition, area CA1 receives direct input from layer III of the medial EC via the perforant pathway (Charpak et al., 1995; Colgin et al., 2009). It was recently proposed that the two sources produce gamma oscillations at slightly different frequencies. Faster gamma oscillations (>80 Hz) recorded in CA1 were found to be coherent with gamma activity in medial EC, while slower (25–80 Hz) oscillations in CA1 were coherent with CA3 gamma activity (Colgin et al., 2009). Oscillations in area CA3 show phase reversal at the border of str. pyramidale and str. radiatum, and are associated with an extracellular current source in the str. pyramidale. Correspondingly,

current sinks are found in strata radiatum and oriens (Csicsvari et al., 2003), where excitatory glutamatergic synapses are located.

Buzsaki and colleagues (1983) suggested that synchronous excitatory and inhibitory postsynaptic potentials in hippocampal pyramidal cell populations underlie the oscillatory activity. *In vivo* studies revealed that the firing of CA3 pyramidal cells and interneurons is indeed coupled to ongoing gamma oscillations. Pyramidal cell activity has been shown to precede interneuronal firing (Csicsvari et al., 2003), which supports the idea that, mechanistically, CA3 pyramidal cells recruit interneurons (see below). Interestingly, pyramidal cells do not fire in every gamma cycle (Csicsvari et al., 2003; Senior et al., 2008), unlike some interneuron types as has been observed in anaesthetised rats (Tukker et al., 2007; Lasztoczi et al., 2011). The coupling of interneuron firing to gamma oscillations depends on the interneuron type. For instance, in area CA1, bistratified cell firing was strongly modulated by gamma oscillations, while O-LM cells were not observed to be gamma-modulated (Tukker et al., 2007).

1.3.2 Hippocampal gamma rhythm *in vitro*

To study the cellular mechanisms underlying the generation and maintenance of gamma oscillations, *in vitro* preparations are instructive, because they offer controlled conditions and enable visually-guided recordings from individual neurons. Due to the unique lamellar structure of the hippocampus (Andersen et al., 1969; Andersen et al., 2000), hippocampal slices contain much of the *in vivo* connectivity. The compact laminar arrangement of pyramidal cells and the density of synaptic connections also allow recordings of reliable extracellular signals. Persistent oscillatory activity in area CA3 can be induced by various pharmacological or electrical means, each of which tonically excites the network (reviewed in Bartos et al., 2007).

Firstly, the cholinergic agonist carbachol (CCh, 5–200 μM) triggers oscillations in the gamma-frequency range in rodent hippocampal slices (Fisahn et al., 1998; Gulyas et al., 2010). CCh-induced gamma oscillations require AMPA (α-amino-3-hydroxy-5-methylisoxazole-4-propionic acid) receptor- and GABA-A receptor-mediated transmission (Fisahn et al., 1998).

Secondly, gamma oscillations may be induced by kainate (Hajos et al., 2000; Fisahn et al., 2004; Gloveli et al., 2005; Kehrer et al., 2007). Kainate-induced oscillations in area CA3 are maintained in the absence of AMPA receptor (AMPAR)-mediated transmission but blocked by the GABA-A receptor antagonist bicuculline (Fisahn et al., 2004).

Thirdly, tonic activation of metabotropic glutamate receptors (mGluRs) also induces gamma oscillations. They are resistant to AMPAR blockade but susceptible to bicuculline (Whittington et al., 1995; Palhalmi et al., 2004).

Finally, elevated extracellular potassium (LeBeau et al., 2002) and high-frequency stimulation (Whittington et al., 1995; Sohal et al., 2009) also provide means to trigger oscillatory activity in the hippocampal network.

The differential sensitivity of gamma oscillations to AMPAR blockers is suggested to result from the differential localisation of receptors on the cellular components that activate the network (Bartos et al., 2007). Sufficiently strong tonic activation of interneurons (by kainate or mGluR agonists) makes the inhibitory neuron network independent of phasic excitation. In contrast, CCh is reported to preferentially excite pyramidal cells (rather than interneurons), rendering the network dependent on both phasic excitation and inhibition (Fisahn et al., 2002).

Importantly, *in vitro* gamma oscillations share many properties of *in vivo* gamma oscillations (see above). CCh-induced gamma oscillations were shown to reverse phase in str. lucidum (Mann et al., 2005), and current source density analysis revealed alternating current sinks and sources in str. pyramidale and str. radiatum (Mann et al., 2005), similar to the findings *in vivo* (Csicsvari et al., 2003). Further, cell firing patterns in CCh-induced oscillations resemble those observed *in vivo* (Csicsvari et al., 2003) with pyramidal cell firing preceding interneuronal activity (Hajos et al., 2004; Mann et al., 2005; Oren et al., 2006).

Mechanistically, hippocampal gamma oscillations are suggested to arise either from mutual inhibition of interneurons (interneuron network gamma, ING, model; Whittington et al., 1995; Vida et al., 2006) or from recurrent inhibition of pyramidal cells (pyramidal interneuron network gamma, PING, model; Traub et al., 1997; Oren et al., 2006). The ING model proposes that reciprocally connected interneurons synchronise each other through mutual inhibition when tonic excitation is provided. In contrast, the PING model directly involves pyramidal cells and suggests that recurrent feedback between excitatory and inhibitory neurons gives rise to rhythmic synaptic excitation of the interneuron network (Whittington et al., 2000; Tiesinga & Sejnowski, 2009). Experimental evidence favours the latter as the major underlying mechanism for gamma oscillations in the CA3 hippocampus: pyramidal cells fire before interneurons (Csicsvari et al., 2003; Hajos et al., 2004; Oren et al., 2006); reciprocal inhibition may not be essential for maintaining hippocampal oscillations *in vivo* (Wulff et al., 2009); and interfering with phasic excitation of interneurons alters hippocampal gamma oscillations *in vivo* and *in vitro* (Chapter 6; Fuchs et al., 2007; Korotkova et al., 2010; Carlen et al., 2012). Besides the importance of phasic excitation for gamma oscillations

in area CA3, tonic excitation and inhibition of interneurons is also reported to modulate gamma oscillation frequency (Mann & Mody, 2010; Chapter 6).

Perisomatic-targeting inhibition has been strongly implicated in the generation of gamma oscillations (Mann et al., 2005; Oren et al., 2006; Gulyas et al., 2010). Indeed, PV+ BCs are strongly phase coupled with gamma cycles *in vitro*, and fire in nearly every cycle (Hajos et al., 2004; Oren et al., 2006; Gulyas et al., 2010). The firing of PV+ BCs and AACs was also reported to be moderately coupled to the ascending phase of gamma cycles *in vivo* (Tukker et al., 2007). Fast-spiking interneurons in CA1 are observed to resonate at low gamma (rather than theta) frequency, and fire preferentially at gamma input frequencies, unlike pyramidal cells and O-LM interneurons (Pike et al., 2000). Recent *in vivo* studies also demonstrated that selective activation of PV+ interneurons (albeit not selective for PTIs) induces cortical gamma rhythm, whereas this was suppressed when PV+ interneurons were silenced (Cardin et al., 2009; Sohal et al., 2009). Other interneuron types, such as CCK+ BCs, may have modulatory roles; their contributions might vary in relation to subcortical inputs (Armstrong & Soltezs, 2012; Chapter 6).

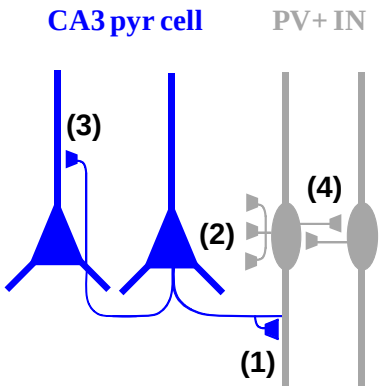


Figure 1.2 Recurrent feedback inhibition.

Synapses between pyramidal cells (blue) and PV+ PTIs (grey) involved in gamma oscillations according to recurrent feedback inhibition. Excitatory glutamatergic synapses (1) and (3), inhibitory GABAergic synapses (2) and (4).

In summary, a recurrent feedback inhibition loop between pyramidal cells and PV+ PTIs is thought to establish gamma oscillations in area CA3 (Oren et al., 2006; Bartos et al., 2007): CA3 pyramidal cells excite PV+ PTIs via glutamatergic synapses (**1** in Figure 1.2), which in turn provide phasic GABAergic feedback inhibition to pyramidal cells (**2**). This is propagated across the population because of strong recurrent connections between pyramidal cells (**3**) and reciprocal inhibition (possibly enhanced by gap-junction-coupling) between PV+ interneurons (**4**).

1.3.3 Gamma oscillations in encoding information

The hippocampus is associated with the formation of memory, and network oscillations are believed to be fundamental to this process.

Representations of life events (especially those with a spatial component) are encoded 'in the combined firing rate and spike timing of glutamatergic pyramidal cells' (Somogyi, 2010). Network oscillations (e.g. synchronised activity of neuron populations) organise the timing and extent of principal cells firing (Buzsaki, 2010). Oscillatory cycles probably provide distinct time windows of excitability that allow the interaction of active pyramidal cells, for example, those that respond to the same external stimulus (but encode different aspects of the stimulus). Pyramidal cells only undergo synaptic plasticity (long-term potentiation) when excitatory inputs occur within a critical time window (spike-timing-dependent plasticity; Markram et al., 1997; Bi and Poo, 1998). The length of a gamma cycle (~20–40 ms) might be that required to achieve 'binding' of active pyramidal cells by synaptic plasticity. Indeed, Fries (2005) suggested that neurons communicate through coherence: cells that do not fire within the temporal window set by a given gamma cycle will be segregated from the active ensemble. This might include cells that are silenced by dendritic inhibition. Cells that are synchronised

in a given gamma cycle likely represent the same event (or indeed, spatial location). Analogous, subsequent gamma cycles, each consisting of different active pyramidal cell ensembles, might encode a complete memory trace (or sequence of a spatial track). Thus, gamma activity may provide a temporal reference for active pyramidal cell assemblies (Lisman, 2005; Colgin & Moser, 2010). It has been proposed that the order in which pyramidal-cell ensembles are active (i.e. the temporal sequence of a memory trace) is encoded by slower theta cycles (4–10 Hz) that serve as an absolute phase reference for pyramidal cell spiking (O'Keefe, 1993; Lisman, 2005). In fact, the activity of pyramidal cell ensembles correlates with the spatial location of an animal ('place cells', O'Keefe & Nadel, 1978), and they fire at theta frequencies when the animal is in the preferred location (Buzsaki et al., 1983). In rodents, theta–gamma coupling is enhanced when spatial information is remembered correctly (Moran & Hong, 2011).

From the neuronal coherence theory (Fries, 2005), it follows that gamma oscillations (and the coupling to theta oscillations) may also be play a pivotal role in facilitating communication between brain areas (Colgin & Moser, 2010). Indeed, gamma coherence between area CA1 and medial EC is proposed to facilitate memory encoding, whereas coherence between area CA3 and CA1 might be related to memory retrieval (Colgin et al., 2009; Colgin & Moser, 2010). Theta and gamma oscillations are also implicated in the transient storage of information: 'working memory' (Jensen & Lisman, 1996; Colgin & Moser, 2010). Working memory is thought to involve several brain areas. Human neuroimaging strongly implicates the prefrontal cortex in working memory (Goldman-Rakic, 1995), whereas rodent studies have suggested hippocampal involvement (Castner et al., 2004). Of note, working memory in rodents is not identical to the human concept of 'online' storage of information, it is evaluated in 'win-shift

tasks', and may be better described as short-term habituation (Baddeley, 2010; Sanderson & Bannermann, 2012).

Generally, rodent studies investigating the function of spatial memory distinguish between spatial working memory and spatial reference memory (Olton & Papas, 1979). Recent studies with knockout mice have revealed that these two forms of spatial memory involve distinct cellular and network processes (Fuchs et al., 2007; Korotkova et al., 2010). Of interest, working memory (but not reference memory) was associated with PV+ interneurons (Murray et al., 2011), in line with their pivotal role in gamma oscillations.

1.3.4 Gamma oscillations in schizophrenia

Schizophrenia is associated with impaired gamma-band activity during working memory processes (reviewed in Gonzalez-Burgos et al., 2010; Uhlhaas & Singer, 2010). For instance, EEG recordings in schizophrenic patients showed reduced prefrontal gamma-band activity during cognitive tasks (Cho et al., 2006). Despite some contradictory results (Moran & Hong, 2011), the general consensus is that the gamma frequency component is reduced during impaired cognitive function (Uhlhaas & Singer, 2010; Moran & Hong, 2011). However, oscillations in other frequency bands have also been reported to be abnormal in the disorder (reviewed in Moran & Hong, 2011) so the details of dysfunction may be a lot more complex than originally assumed. Oscillations in different frequency ranges may also interact differently in schizophrenia, and indeed, theta–gamma coupling was proposed to be altered in the disorder (Lisman & Buzsaki, 2008). Of particular interest, the synchrony between hippocampal and prefrontal cortex networks might be dysfunctional in schizophrenic patients (Uhlhaas & Singer, 2010). In agreement with this, the oscillatory phase-locking of medial prefrontal cortex neurons to

hippocampal theta rhythm was impaired in a mouse model of schizophrenia during a spatial working-memory-related task (Df(16)$A^{+/-}$ mice; Sigurdsson et al., 2010).

From the above explanations, it follows that interfering with oscillations or mechanisms of oscillogenesis is likely to result in deficits in cognitive tasks. This might be the underlying mechanism for the cognitive impairment — specifically, the decline in working memory — that has been reported in patients with schizophrenia (Park & Holzman, 1992; Burglen et al., 2004; Heinrichs, 2005). This aspect of the disorder is not well targeted by current medication, even though cognitive dysfunction is the best indicator of long-term outcome for patients (Green, 1996). Altered PV+ interneuron functioning and GABAergic signalling, both implicated in the pathophysiology of schizophrenia (see above), might give rise to the altered neuronal rhythms and the cognitive deficits.

1.4 Context of this study

1.4.1 Previous findings in NRG1 type I over-expressing mice

In light of the evidence for enhanced NRG1 levels in schizophrenia, particularly of type I NRG1 (Section 1.1.5), it may be more informative to elucidate the neuropathological changes that develop from increased rather than reduced NRG1 expression (hypomorphic NRG1 mice; reviewed in Deakin et al., 2009) or (transient) acute exposure to NRG1 protein. Two strains of NRG1 type I (NRG1tyI) over-expressing mice have been created (Michailov et al., 2004; Kato et al., 2010) but the biological effects of isoform-specific (type I) upregulation have not been thoroughly investigated.

One recently reported strain (Kato et al., 2010) over-expresses NRG1 type I β (tagged with GFP) ubiquitously under the EF1α promoter. This gives rise to significant over-expression (~4.3 fold increase in mRNA) in the cerebral cortex, striatum and hippocampus. These mice showed some behavioural traits often implicated in schizophrenia, such as hyperactivity and reduced social interaction, but the neurobiological effects of NRG1 over-expression on hippocampal network functioning have not been investigated (Kato et al., 2010).

In the second strain, over-expression of the NRG1 type I β1a isoform (Figure 1.1) is selectively driven in neurons under the Thy 1.2 promoter (Michailov et al, 2004). This strain was selected for the present study, as this mimics the increased NRG1 type I expression reported in the hippocampus of human schizophrenic patients (Law et al., 2006). This strain had previously been phenotypically characterised by Dr Inga Deakin at the Department of Psychiatry, University of Oxford (Deakin, 2009; Deakin et al.,

2009; Deakin et al., 2012). This initial characterisation revealed evidence of profound hippocampus-related behavioural changes that initiated the present study. I now outline the most relevant findings.

The Thy 1.2 promoter used in the transgene construct (Michailov et al., 2004) drives strong expression specifically in neurons from postnatal day 6–10 (Caroni, 1997). Indeed, NRG1tyI mRNA was found to be approximately 5-fold higher in brains of 1-month-old NRG1tyI mice (P25; Brinkmann et al., 2008) and 8–10-fold higher in hippocampus of 2.5–4-month-old transgenic mice, relative to littermates (Deakin, 2009), but the precise time of onset of NRG1tyI over-expression has not been determined. Over-expression occurs predominantly in the hippocampus and the deeper layers of the cortex (Figure 1.3), and in some midbrain nuclei but not in cerebellum or striatum. *In situ* hybridisation staining patterns are indicative of expression in pyramidal neurons (Figure 1.3), but unavailability of commercial NRG1-isoform-specific antibodies prevented detailed immunocytochemical analysis of cell type-specific expression. The pan-NRG1 antibody (Santa Cruz Biotechnology, Santa Cruz, CA, USA) used by Brinkmann and colleagues (2008) confirmed general over-expression of NRG1 protein in brain. The expression of other NRG1 types (II and III) mRNA is not affected in the hippocampus (Deakin et al., 2012).

Behaviourally, heterozygous NRG1tyI over-expressing mice develop a movement-related tremor, which is apparent at around P21, and might be related to increased axon myelination in the central nervous system (Brinkmann et al., 2008) or NRG1tyI over-expression in deeper brain nuclei (Deakin et al., 2012). Furthermore, NRG1tyI mice were impaired in prepulse inhibition at 3 months (although their baseline

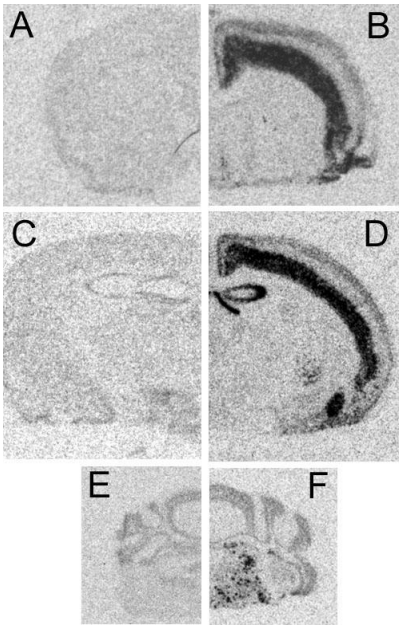


Figure 1.3 Over-expression of NRG1 type I mRNA.

In situ hybridisation confirms over-expression of NRG1 type I mRNA in deep cortical layers and the hippocampus (B,D) but not in the cerebellum (F) of a 3-month-old NRG1tyI (B,D,F) but not a WT (A,C,E) mouse. Adapted from Deakin et al. (2012; Supplementary Figure 1).

acoustic startle response was increased; Deakin et al., 2009), and became hyperactive when older (12 months; Deakin et al., 2012). The overall phenotype is complex and not always consistent with what would be expected from the behaviour of hypomorphic NRG1 mice if a linear effect of NRG1/ErbB4 signalling was assumed (Deakin et al., 2009; Deakin et al., 2012). The key finding relevant to this present study was the selective impairment of hippocampus-dependent spatial working memory (Deakin et al., 2012). Interestingly, this impairment occurred in 10-month-old NRG1tyI mice (both male and female; Deakin, 2009), whereas 3–4-month-old mice were unaffected in the same rewarded alternation task (spatial non-matching-to-place T-maze task). Importantly, short-term memory was selectively impaired, because spatial reference memory was unaltered in mice of both age groups (appetite Y-maze task; Deakin et al., 2012).

Despite this age-emergent cognitive deficit, basal synaptic transmission and long-term plasticity at the CA3–CA1 Schaffer collateral synapse were not altered in mice of either age group (Deakin et al., 2012). However, evoked field excitatory postsynaptic potentials (fEPSPs) in area CA1 of 10–14-month-old NRG1tyI mice often presented evidence of polysynaptic activity or after-discharge, particularly after theta burst stimulation of Schaffer collaterals (Figure 1.4). This occurred more often in NRG1tyI mice than in WT mice, and more often in 10–14-month-old mice than in 2.5–5-month-old mice (Deakin, 2009). This finding, together with the age-emergent and specific impairment of working memory, motivated the present investigation into hippocampal network functioning.

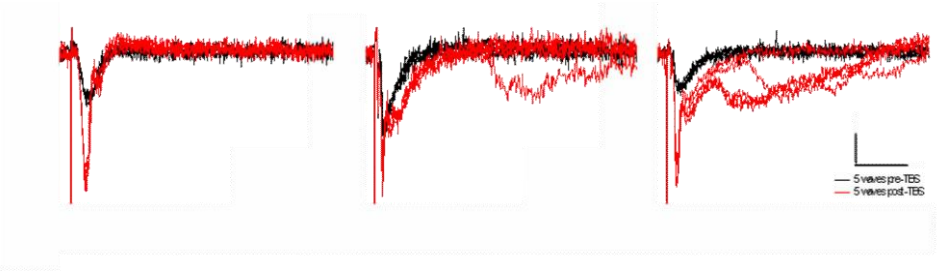


Figure 1.4 Field EPSPs with after-discharges in NRG1tyI mouse slices.
Representative traces of field EPSPs (fEPSPs) from 3 hippocampal slices showing stimulus-evoked after-dischange in NRG1tyI mouse slices. Each sample contains 5 superimposed fEPSPs, either pre-theta burst stimulation (TBS), black, or post-TBS, red. TBS was applied to induce long-term potentiation in the CA3–CA1 Schaffer collateral synapses. Some slices show normal potentiation of the fEPSP (left), but the majority of slices also contained delayed negative deflections in the late phase of the fEPSPs (50–100 ms after stimulus), either occasionally (middle) or frequently (right). They often (but not solely) occurred after TBS. Scalebars, 20 ms and 0.5 mV. Adapted with permission from Deakin, 2009.

1.4.2 Aims of this research

The overall aim of this research was to identify if, and how, postnatal NRG1 type I over-expression causes neurobiological changes in the CA3 hippocampal network that parallel the reported cognitive deficit (Deakin et al., 2012). In light of the specific spatial working memory deficit in NRG1tyI mice, and the suggested role of gamma

oscillations in working memory, alterations in gamma-frequency oscillations and GABAergic interneurons were hypothesised (Figure 1.5).

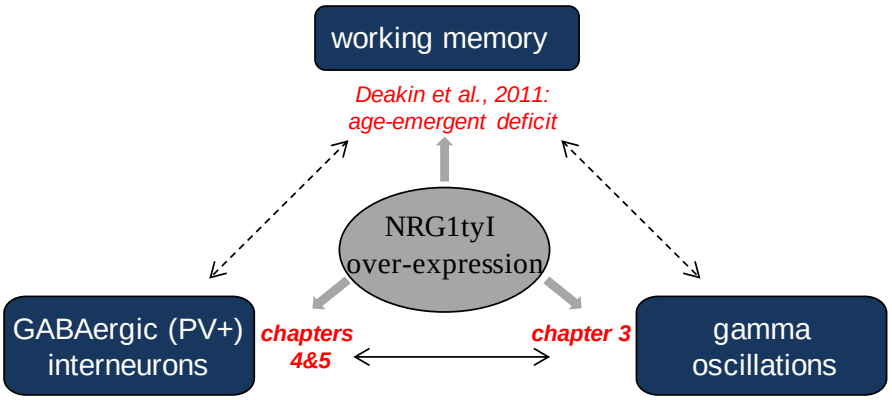


Figure 1.5 Schematic illustrating the context and overall aim of the thesis.

Chapter 3 aims to establish if NRG1tyI over-expression alters gamma oscillations in CA3 hippocampus *in vitro* compared to WT mice. The differential contribution of the excitatory and inhibitory elements to gamma oscillations is examined in both genotypes. I provide evidence for altered function of inhibitory circuits during oscillations, and proceed to investigate the underlying synaptic processes in Chapters 4 and 5. Gamma oscillations in area CA3 are postulated to result from a recurrent inhibitory feedback loop between CA3 pyramidal cells and PV+ interneurons. Thus, the work reported in Chapter 4 aims to provide an insight into whether NRG1tyI over-expression interferes with the functioning of the inhibitory synapse between PV+ PTIs and CA3 pyramidal cells. For this, I employ non-invasive selective light-activation of PV+ interneurons by channelrhodopsin-2 (ChR2). Chapter 5 aims to dissect whether NRG1tyI over-expression alters the excitatory input to identified PV+ PTIs and to principal cells. Specifically, miniature excitatory neurotransmission mediated by both AMPARs and NMDARs in identified BCs, AACs and pyramidal cells of NRG1tyI mice was compared to those in control mice. Finally, in Chapter 6, I discuss how the findings could relate to the behavioural phenotype of NRG1tyI mice and to schizophrenia.

2 Methods

2.1 Transgenic mice

Animal care and experimental procedures were carried out in compliance with the UK Home Office Animals (Scientific Procedures) Act (1986) and following the guidelines of the ethical code of the University of Oxford. Mice were housed in groups of 2–6 animals or individually (adult males), and had *ad libitum* access to food and water. They were kept on a 12h/12h dark-light cycle at a temperature of 22 ± 1°C with 60−70% air humidity.

2.1.1 NRG1tyI over-expressing mice

Mice over-expressing NRG1 type I β1a isoform (NRG1tyI mice) were originally generated by microinjecting a DNA construct consisting of a murine *NRG1 type I* transgene under a Thy 1.2 promoter into fertilized mouse oocytes (Figure 4 and Supplemental Material of Michailov et al., 2004). The NRG1 transgene was derived from PCR-amplified cDNA (Michailov et al., 2004). Injected oocytes were implanted into female mice, which became the founders of the transgenic NRG1tyI line. In collaboration with Prof. Paul Harrison (Dept. of Psychiatry, Oxford), heterozygous male NRG1tyI mice from the original founder line (line 1, IgBC) were generously donated by Prof. Klaus Nave (Max-Planck-Institute for Molecular Medicine, Göttingen, Germany) and backcrossed with WT C57BL/6J female mice (Harlan, UK). All experiments on NRG1tyI mice in this study were performed on heterozygous transgenic mice and their WT littermates, obtained from at least the seventh generation of backcrossing.

The Thy 1.2 promoter that drives the expression of the NRG1 transgene is described to induce neuron-selective expression from postnatal day 6–10 (Caroni, 1997). NRG1 type I mRNA was determined to be 8 to 10-fold higher in hippocampus of 2.5- to 4-month-old transgenic mice, compared to age-matched littermates (Deakin, 2009). Previous phenotypic characterisation of NRG1tyI mice is described in Section 1.4.1 of the Introduction. Because there was no sex difference in the impairment of spatial working memory (Deakin, 2009), I examined and pooled data from mice of both sexes throughout the study.

2.1.2 PV-Cre and R26R-eYFP mice

Homozygous PV-Cre mice were originally generated by Hippenmeyer et al. (2005) and obtained from The Jackson Laboratory (Bar Harbor, ME, USA; strain name: B6;129P2-*Pvalb*$^{tm1(cre)Arbr}$/J; stock number 008069). Homozygous female PV-Cre mice were crossbred with heterozygous male NRG1tyI mice. NRG1tyI$^{+/-}$ PV-Cre$^{+/-}$ offspring (NRG1tyI/PV-Cre) of both sexes and PV-Cre$^{+/-}$ littermates (PV-Cre) were injected with adeno-associated virus serotype 2 (AAV2) that carried DNA constructs (Section 2.5) for optical stimulation experiments (Chapter 4). Homozygous PV-Cre mice were also crossbred with homozygous R26R-eYFP (enhanced yellow fluorescent protein) mice (MRC National Institute for Medical Research, London, UK; Srinivas et al., 2001). Mice of this litter (PV-Cre$^{+/-}$ R26R-eYFP$^{+/-}$; PV-Cre/R26R-eYFP) were kindly donated by Dr Peter Magill (MRC Anatomical Neuropharmacology Unit, Oxford) for evaluation of the specificity of Cre recombinase expression in PV-Cre mice (Chapter 4), and for further crossbreeding with heterozygous NRG1tyI mice (NRG1tyI$^{+/-}$ PV-Cre$^{+/-}$ R26R-eYFP$^{+/-}$). These mice were used for preliminary experiments (Chapter 5).

2.1.3 Lhx6-eGFP mice

Lhx6-eGFP transgenic mice (LIM homeobox protein 6 – enhanced green fluorescent protein) were originally obtained from the Mutant Mouse Regional Resource Center (MMRRC at The Jackson Laboratory, Bar Harbor, ME, USA; strain name: Tg(Lhx6-EGFP)BP221Gsat/Mmmh; code: 000246-MU) and kindly donated by Dr Peter Magill (MRC, Oxford). In these mice, eGFP expression is driven by the regulatory sequence of the Lhx6 gene, which is active in hippocampal interneurons expressing PV+, SM+, CR+ or NPY+ (further described in Section 5.2). Female heterozygous Lhx6-eGFP mice were crossbred with male heterozygous NRG1tyI mice, and the offspring, NRG1tyI$^{+/-}$ Lhx6-eGFP$^{+/-}$ (NRG1tyI/Lhx6) mice were used in the study of glutamatergic excitatory transmission in interneurons (Chapter 5).

2.2 Phenotyping and genotyping NRG1tyI mice

Heterozygous NRG1tyI mice develop a movement-related tremor that is apparent at the age of weaning (Michailov et al., 2004; Deakin et al., 2009). To confirm that mice with a tremor phenotype over-expressed the NRG1 type I transgene, 44 randomly selected weaned mice were genotyped by PCR with primers specific for the transgene, as detailed below. There was 100% correlation between observed phenotype and detected genotype (19 ‘shaking’ NRG1tyI over-expressing; 25 ‘non-shaking’ WT mice). This confirmed that the tremor was a reliable behavioural trait to distinguish NRG1tyI mice from WT littermates, in line with previous findings (Deakin, 2009). Therefore, all remaining animals were only phenotyped. To minimise the risk of misidentification, two researchers independently determined the phenotype of each mouse on the day of the experiment.

2.2.1 DNA extraction

DNA was extracted from ear or tail biopsies using the Nucleon Hard Tissue Genomic DNA Extraction Kit (GE Healthcare, Amersham, UK) according to the manufacturer's instructions. In brief, tissue samples (~25 mg) were manually diced and digested in a 350 µL solution of detergent ('Reagent B') with 18 µL proteinase K overnight at 50°C. Sodium perchlorate and chloroform were then added to the lysate to remove protein and phospholipid contaminants. Protein-binding Nucleon Resin was applied to separate the organic (protein-containing) phase and the aqueous (DNA) phase. From the upper aqueous phase, DNA was precipitated with cold absolute ethanol by centrifugation (4,000 ×*g*, 5 min) and the DNA pellet was washed repeatedly in 70% ethanol, air-dried and finally resuspended in nuclease-free water (10 µL). The concentration of extracted DNA (ng/µL) and purity (absorbance ratio A_{260}/A_{280}) was estimated with an ND-1000 spectrophotometer (NanoDrop, Wilmington, DE, USA). For subsequent PCR, DNA samples were diluted in nuclease-free water to ~300 ng/µL.

2.2.2 Amplification of transgene-specific sequences and gel electrophoresis

Genotyping PCR was performed on the extracted DNA using PuReTaq Ready-To-Go PCR beads (GE Healthcare). These PCR beads contained Taq DNA polymerase, deoxyribonucleotide triphosphates (dNTPs), $MgCl_2$ and buffer. Forward and reverse primer (125 ng each, at 100 ng/µl), DNA (~600 ng) and nuclease-free water (to 25 µL) were added to the beads. The PCR protocol is given in Table 2.1. The primer pair (Michailov et al., 2004; synthesised by Eurofins, Ebersberg, Germany) amplifies a transgene-specific, 850 bp product:

Forward: 5'- TGG CAA AGG ACC TTA GGC AGT GT -3'

Reverse: 5'- CTG GTA GAG CTC CTC CGC TTC -3'

Table 2.1 PCR protocol

Step	Temperature	Duration
1. Heat activation (DNA polymerase)	95°C	3 min
2. ×30 cycles:		
a. Denaturation	94°C	30 sec
b. Annealing	65°C	30 sec
c. Extension	72°C	1 min
3. Final extension	72°C	20 min
4. Hold	4°C	unlimited

Agarose gels (2%) for electrophoresis of PCR products were prepared by dissolving agarose (8 g) in 1 M TEA buffer (400 mL; composed of 0.1 mM triethanolamine, 20 mM ethylenediaminetetraacetic acid and 2 mM dithiothreitol, pH 7.4) at 98 °C, and then adding ethidium bromide (40 µL). Set gels were covered with 1× TEA. DNA samples (10 µL) were mixed with Loading Dye (2 µL; NEB, Ipswich, MA, USA) and loaded into preformed wells with one lane for markers (123 bp Ladder, Sigma-Aldrich, Gillingham, UK). Following electrophoresis (100 V), bands were visualised under UV by fluorescent ethidium bromide bound to the separated DNA fragments. The presence of a ~850 bp band confirmed that the mouse genomic DNA contained the NRG1 transgene. A negative control (lack of genomic DNA) was included in each PCR experiment.

2.3 Hippocampal slice preparation and storage

Acute hippocampal slices (250–400 µm) used in all electrophysiology experiments of this study were prepared in a standardised way. Mice were terminally anaesthetized by intraperitoneal injection of pentobarbitone sodium (20% w/v, dosage ~0.2 mg/g; Pharmasol, Andover, UK) and sacrificed when the breathing had slowed

down (~1 breath per second) and the response to stimulation of the limb withdrawal reflex had ceased. Mice were decapitated and the brain was rapidly removed and placed in oxygenated (95% O_2, 5% CO_2), ice-cold (0–4°C) cutting solution (Table 2.2). The cerebellum and olfactory bulb were cut with a scalpel and discarded. Hemispheres were separated, and a small part of the dorsal neocortex was cut to create a smooth, plane surface onto which hemispheres were glued to a microtome plate using cyanoacrylate adhesive. Both hemispheres were used throughout the study, and they were cut simultaneously. Horizontal brain slices (250–400 µm) were cut using a HM650V vibrating microtome (Carl Zeiss AG, Oberkochen, Germany). Slice thickness was adjusted according to requirements: 400 µm thick slices were cut to ensure sufficiently intact recurrent connectivity for the study of network oscillatory activity (Chapter 3); thinner slices of 250 µm maximised the yield of the relevant hippocampal area from Lhx6-eGFP reporter mouse brains. To optimise neuron survival in thicker tissue, particularly of metabolically demanding fast-spiking interneurons (Kann et al., 2011; Whittaker et al., 2011), the solution used in the preparation of 400 µm-thick slices was modified (Oren et al., 2006; Table 2.2). Once cut, slices were trimmed of subcortical areas and immersed in oxygenated cutting solution at 32°C for 10–15 min to allow metabolic recovery. Following recovery, slices were transferred to an interface storage chamber that contained oxygenated Earle's balanced salt solution (in mM, 117.24 NaCl, 5.33 KCl, 1.01 $NaH_2PO_4 \cdot H_2O$, 26.19 $NAHCO_3$, 5.56 D-glucose; Invitrogen, Paisley, UK) supplemented with 3 mM $MgCl_2$, 1 mM $CaCl_2$ and 27 mM glucose (Table 2.2), at room temperature (20–25°C). For thicker slices (400 µm) used in the study of gamma oscillations, the interface storage chamber was filled with preheated (~32°C) recording solution (artificial cerebrospinal fluid, ACSF); this was allowed to cool to room temperature once slices were transferred to the interface chamber. The solution was

oxygenated (95% O_2, 5% CO_2) and stirred to ensure even oxygen supply (Hajos & Mody, 2009; Hajos et al., 2009). Slices were stored for at least 60 min before starting experiments. Chemicals were purchased from Fisher Scientific (Loughborough, UK), Invitrogen, Sigma–Aldrich (Gillingham, UK) or VWR International (Lutterworth, UK).

Table 2.2 Solutions for preparation and storage of hippocampal slices

Solution type	Study of gamma oscillations (Chapter 3)		Study of neurotransmission in absence of rhythmic activity (Chapters 4 & 5)	
Cutting solution	Sucrose	252 mM	Sucrose	75 mM
	NaCl	-	NaCl	87 mM
	KCl	2.5 mM	KCl	2.5 mM
	$MgCl_2$	5 mM	$MgCl_2$	7 mM
	$CaCl_2$	0.5 mM	$CaCl_2$	0.5 mM
	NaH_2PO_4	1.25 mM	NaH_2PO_4	1.25 mM
	$NaHCO_3$	26 mM	$NaHCO_3$	25 mM
	Glucose	10 mM	Glucose	20 mM
Storage chamber solution	Recording solution (ACSF) preheated to ~32°C		EBSS supplemented with	
			$MgCl_2$	3 mM
			$CaCl_2$	1 mM
			Glucose	27 mM
Recording solution (ACSF)	NaCl		119 mM	
	KCl		2.5 mM	
	$MgSO_4$		1.3 mM	
	$CaCl_2$		2.5 mM	
	NaH_2PO_4		1.25 mM	
	$NaHCO_3$		25 mM	
	Glucose		11 mM	

All solutions were adjusted to pH 7.2 and equilibrated with 95% O_2, 5% CO_2.
ACSF, artificial cerebrospinal fluid; EBSS: Earle's balanced salt solution.

2.4 Electrophysiological recordings

All recordings in hippocampal slices were performed in a submerged recording chamber (Luigs & Neumann, Ratingen, Germany), mounted on the stage of a BX51WI

upright microscope (Olympus, Southend, UK). The chamber was continuously superfused with oxygenated (95% O_2, 5% CO_2) ACSF in a pump-driven circuit (Watson–Marlow, Falmouth, UK) at variable flow rates (~5–8 mL/min). Drugs were dissolved in ACSF as required (Table 2.3). Hippocampal strata and cells were visualised digitally using a 20× immersion objective with 2–4 zoom (i.e. up to 80× magnification) and infrared differential interference contrast (DIC; Stuart et al., 1993) in combination with a CCD camera (Till Photonics, Gräfelfing, Germany). Electrodes were made from borosilicate glass capillaries (GC150F-10, Harvard Apparatus, Edenbridge, UK) pulled in a P-97 horizontal microelectrode puller (model, Sutter Instrument Co., Novato, CA, USA). Data were recorded with a Multiclamp 700B amplifier (Molecular Devices, Sunnyvale, CA, USA). Recordings were low-pass filtered at 2 kHz using the built-in Bessel filter, digitized at 10 kHz with a Digidata 1400 and acquired with pClamp10 software (Molecular Devices). Whole-cell access was established following formation of a gigaseal (>1 GΩ) between pipette tip and cell membrane. Recordings were started ~5–10 min after break-in to enable diffusion of intracellular solution in the soma and proximal calibre dendrites. During all whole-cell recordings, cells were filled with neurobiotin (Vector Laboratories, Burlingame, CA, USA) for *post hoc* anatomical analysis. Series resistance was not compensated for during voltage-clamp recordings but monitored throughout the recording by applying 50 ms long 10 mV test pulses. Access and input resistance were derived from currents in response to the test pulses according to Ohm's law (Ogden, 1994). Recordings in which access resistance (R_{access}) changed by >20% during the course of the experiment were excluded from analysis. Voltage measurements were not corrected for liquid–liquid junction potential error (except in Figure 4.4).

Table 2.3 Drugs used in this study

Drug	Supplier	Biological Activity	Stock solution	Final concentration
Carbamoylcholine chloride (carbachol, CCh)	Sigma–Aldrich, Gillingham, UK	AChR agonist	20 mM in ddH_2O	5-20 µM
1,2,3,4-Tetrahydro-6-nitro-2,3-dioxo-benzo[f]quinoxaline-7-sulfonamide (NBQX) disodium salt	Ascent Scientific, Cambridge, UK	AMPAR / kainateR antagonist	10–25 mM in ddH_2O	10-25 µM
DL-2-amino-5-phosphonopentanoic acid (AP5)	Ascent Scientific	NMDAR antagonist	100 mM in 100 mM NaOH (in ddH_2O)	100 µM
CGP55845	Tocris Bioscience, Bristol, UK	GABA-B receptor antagonist	1 mM in DMSO	1 µM
Picrotoxin	Tocris Bioscience	GABA-A receptor antagonist	100 mM in DMSO or 50 mM in ethanol	100 µM
Tetrodotoxin (TTX)	Tocris Bioscience	selective inhibitor of Na^+ channel	1 mM in ddH_2O	1 µM

ddH_2O, double-distilled water; DMSO, dimethylsulfoxide

2.4.1 Carbachol-induced gamma oscillations: Simultaneous field potential and single cell recordings

Hippocampal slices from NRG1tyI mice (1–2 months and 3–6 months old) and WT littermates were used for the study of carbachol (CCh)-induced gamma oscillations. The *in vitro* model of cholinergically-induced gamma oscillations (originally described in an interface chamber; Fisahn et al., 1998) was introduced to a submerged recording chamber. Rhythmic field activity, induced upon application of 5–20 µM CCh, was recorded extracellularly in the CA3b/c area of the hippocampus using an ACSF-filled pipette (3–5 MΩ) placed at the border of str. pyramidale and str. oriens. Peak frequencies of gamma oscillations were found to be stable (for over 50 min, Figures

3.1B and 3.2B) in submerged conditions with high flow rates (~8 mL/min) and by optimising the laminar flow with a metal insert (Hajos et al., 2009). The temperature in the submerged recording chamber was maintained between 28 and 32°C (Fisahn et al., 2009; Gulyas et al., 2010). Recordings (~60 s) were taken for analysis of gamma activity at least 5 min after induction with CCh.

Cellular firing from individual neurons was detected using a second, ACSF-filled pipette (4–8 MΩ) placed in the str. pyramidale of area CA3b/c in close proximity to the field pipette. Escape currents underlying the generation of action potentials were recorded in a loose-patch (seal resistance 0.5–1.0 GΩ) configuration in voltage-clamp mode for ~60 s.

Postsynaptic currents (PSCs) were recorded in a separate set of pyramidal cells to those used for cell firing in the hippocampal CA3b/c area. Pipettes (4–8 MΩ) were filled with intracellular solution containing (in mM): 145 K-Gluconate, 25 HEPES, 10 KOH, 8 NaCl, 2 Mg-ATP, 0.2 GTP, 0.2 EGTA, 5 QX-314 Br [*N*-(2,6-dimethylphenylcarbamoylmethyl) triethylammonium bromide] and 0.2–0.3% neurobiotin (295 mOsm/L, pH 7.1). Membrane voltage (V_m) was measured in current-clamp mode at the beginning of the experiment (Section 3.2.3.2) and was not corrected for liquid-liquid junction potential error. Cells were clamped at the calculated reversal potential for IPSCs (−72 mV) to record compound EPSCs, and at the estimated reversal potential for EPSCs (0–30 mV) to record compound IPSCs. The reversal potential for GABA-A receptor-mediated IPSCs ($E_{GABA\text{-}A}$) was assumed to be close to the equilibrium potential for chloride (E_{Cl}). E_{Cl} was calculated according to the Nernst equation (Ogden, 1994). It should be noted, however, that GABA-A receptors are also permeable for bicarbonate anions (HCO_3^-) in addition to chloride ions, with a permeability ratio of approximately 0.2 to 0.3 in vertebrate neurons (Kaila et al., 1993).

GABA-A receptor-mediated HCO_3^- efflux has a mildly depolarising effect on the cell, and therefore, in physiological conditions in rat neocortical neurons, HCO_3^- caused an up to 9 mV positive shift in E_{GABA-A} compared to E_{Cl} (Kaila & Voipio, 1987; Kaila et al., 1993).

2.4.2 Light-evoked IPSCs in CA3 pyramidal cells

The study reported in Chapter 4 was carried out on 350 µm thick hippocampal slices from 5–9-week-old NRG1tyI/PV-Cre mice and PV-Cre littermates (Section 2.1.2) that had previously been injected with viral ChR2-eYFP constructs (for *in vivo* injections see Section 2.5). During slice preparation and storage, light was minimised to avoid photoactivation of ChR2. Prior to storage in the interface chamber, slices were swiftly screened for ChR2-eYFP-transfected neurons using appropriate eYFP filter sets (L5, Leica, Wetzlar, Germany; or #41028, Chroma, Bellows Falls, VT, USA) and CCD cameras (ORCA-ER, Hamamatsu Photonics K.K., Iwata, Japan; or VX55, TILL Photonics). Slices that contained a dense tangle of eYFP+ axons in area CA3 were stored in the interface chamber and subsequently used for whole-cell recording of CA3 pyramidal cells in combination with optical stimulation of PV+ cell axons (Chapter 4). Somata inside the str. pyramidale or at the border to str. oriens were patched under DIC optics using glass pipettes (4–8 MΩ). The intracellular solution contained (in mM): 145 K-Gluconate, 25 HEPES, 10 KOH, 8 NaCl, 2 Mg-ATP, 0.2 GTP, 0.2 EGTA, 5 QX-314, 0.2–0.3% neurobiotin (295 mOsm/L, pH 7.1). It ensured physiological chloride conditions and enabled comparison with recordings of compound IPSCs during rhythmic activity (Section 2.4.1). Excitatory transmission was pharmacologically blocked by NBQX (25 µM) and DL-AP5 (100 µM). Cells were initially clamped between −40 and −10 mV while setting up the minimal optical stimulation (MOS; Section 4.3.1.4). For extended recording of MOS-elicited IPSC properties (20–30

sweeps; Section 4.3.2), cells were voltage-clamped at −10 to 0 mV to ensure a stronger driving force for chloride. For current-voltage plots (Figure 4.4), cells were clamped at a series of voltages (−10 mV to −110 mV), and the peak amplitudes of MOS-elicited IPSCs were measured in 3–5 stimulation cycles.

ChR2 (excitation range 450 ± 25 nm) was activated by blue laser light (473 nm) using a standard 'Endow GFP band-pass filter set' (#41017: excitation HQ470/40x, dichroic Q495LP, emission HQ525/50m; Chroma). A blue light spot of ~15–20 µm diameter (achieved by a 113 µm fibre light guide for laser–microscope coupling; Rapp OptoElectronic, Hamburg, Germany) was systematically moved along the str. pyramidale to a location that reliably elicited IPSCs in the postsynaptic recorded cell. During the MOS protocol, brief paired pulses of blue light (3 ms duration, 50 ms interpulse interval) were given at ~50–90% of maximum laser power (maximum laser unit output prior entry to optic fibre guide: 100 mW). Subsequently, the laser power was reduced to the minimum required for stable light activation of a minimal number of PV+ cell fibres (Section 4.3.1.4). Individual ChR2-eYFP+ neurons recorded in cell-attached current-clamp mode were confirmed to be firing action potentials when the excitation of ChR2 at the patched soma was strong enough to reach firing threshold (not shown but in line with Boyden et al., 2005; Sohal et al., 2009).

2.4.3 Whole-cell recordings from CA3 Lhx6-eGFP+ cells

Spontaneous miniature synaptic currents were recorded in *post hoc* identified PTIs in 250 µm horizontal slices of 1–2-month-old NRG1tyI/Lhx6 mice and of heterozygous Lhx6 littermates (Section 2.1.3; Chapter 5). Lhx6-eGFP-expressing cell somata in or close to the str. pyramidale were visualised with epifluorescence (Olympus BX51WI with Chroma Endow GFP filter set) and patched in whole-cell mode (guided using DIC

microscopy). Cell somata were mostly located in subregions CA3c and b (except L200711 which was in CA3a; Figure A1 in the Appendix). For whole-cell patching, pipettes (6–8 MΩ) were filled with (in mM) 145 Cs-Methanesulfonate, 20 HEPES, 10 CsOH, 8 NaCl, 0.2 CsOH-EGTA, 2 Mg-ATP, 0.3 GTP-Na, 5 QX-314, 0.2-0.3% neurobiotin (295 mOsm/L, pH 7.2). Cs-based intracellular solutions achieve more stable recordings by blocking K^+ currents. Inhibitory transmission was pharmacologically blocked with picrotoxin (100 µM) and CGP55845 (1 µM), while the generation of action potentials was blocked by tetrodotoxin (TTX; 1 µM). Recorded cells were initially voltage-clamped at −65 mV. After blocking AMPARs and kainate receptors (kainateRs) by NBQX (25 µM), cells were clamped at +40 mV for recording of NMDAR-mediated miniature EPSCs (mEPSCs), once the holding current had stabilised. At the end of the recording, DL-AP5 (100 µM) was applied to verify that mEPSCs were mediated by NMDARs (Section 5.3.2). Continuous recordings of 3 min were interleaved with 10 mV voltage steps to monitor R_{access}. Recordings in which R_{access} changed by >30% between voltage-clamping at −65 mV and at +40 mV were excluded from analysis, in order to enable comparison of NMDA/AMPA receptor-mediated currents. Cells were usually recorded in whole-cell mode for ~15–20 min before the pipette was carefully retracted. To allow diffusion of neurobiotin and help restore endogenous expression of cytosolic marker proteins (e.g. eGFP and PV), slices were kept in a submerged chamber for ~30−45 min prior to fixation. CA3 pyramidal cells were recorded inside the str. pyramidale, either in Lhx6-expressing mice (NRG1tyI/Lhx6 and Lhx6 mice) or in non-reporter NRG1tyI and WT mice (Table A5).

2.5 *In vivo* injection of AAV2-mediated ChR2-eYFP constructs

AAV2 particles were stereotactically injected into mid-ventral CA3 hippocampus of heterozygous NRG1tyI/PV-Cre and PV-Cre mice. Injections were either uni- or bilateral. The AAV2 particle suspension (titre: ~4 x 10^{12} per mL) carrying fusion genes for ChR2 and eYFP (Figure 4.3; Boyden et al., 2005) were produced by Vector Core Services, Gene Therapy Centre Virus, University of North Carolina, USA. AAV2 was chosen because it is known to transfect neurons but not astroglia (Bartlett et al., 1998). For *in vivo* delivery of virus to Cre-expressing PV interneurons, 3–6-week-old mice were anesthetized with 2–4% isoflurane at 1–1.5 per min. The depth of anaesthesia was monitored throughout the procedure, and peri-operative analgesia was administered (buprenorphine 0.1 mg/kg; Vetergesic, Alstoe Animal Health, York, UK). A small craniotomy was made, 2.7 mm caudal and 2.75 mm lateral from Bregma. A 33-gauge needle attached to a Hamilton Microlitre Syringe (UK) was placed 3.4 to 2.6 mm below the brain surface. In each hemisphere, 400–450 nL of virus suspension was delivered at a rate of 80 nL/min through a pump-driven syringe (Ultra Microsyringe pump /Micro4 controller; World Precision Instruments, Sarasota, FL, USA). Injections were distributed such that ~100–150 nl of virus suspension was injected at each of three dorso-ventral locations, ~0.4 mm apart: two minutes after injection at the lowest site, the needle was retracted by 0.4 mm for another injection, and then again by 0.4 mm for a third injection. After the third injection, the needle was retracted by 0.2 mm and, following another 2 min wait, slowly retracted fully. The pauses between injections were to ensure that virus settled and diffused at the selected injection sites. Staggered injections served to increase transfection along the horizontal brain axis and thus maximise the yield of horizontal brain slices. Finally, the scalp incision was sutured, and fluids in anaesthetised mice were replaced by subcutaneous injection of glucose

saline (in sterile water). If necessary, analgesics (e.g. buprenorphine) were administered post-operatively to aid recovery. Injected mice recovered for 10–21 days prior preparation of slices to allow good transfection and viral ChR2-eYFP expression.

2.6 Data analysis and statistics

2.6.1 Field potential oscillations, cell firing properties and synaptic currents

Off-line data analysis was performed with Igor Pro software ver. 6.05 (Wavemetrics, Portland, OR, USA) as described in Oren et al. (2006). Firstly, recordings were digitally filtered with a bidirectional DSP filter (ftp://ftp.wavemetrics.net/IgorPro/User_Contributions/DSPFilters.ipf.zip). Field recordings were low-pass filtered (200 Hz), and extracellular unit recordings and whole-cell recordings were high-pass filtered (1 Hz), to eliminate slow fluctuations in holding currents. The power of the field oscillations was measured by power spectral density (PSD) analysis of ~60 s recordings. For this, the discrete fast Fourier transform was calculated on a sliding window of 8192 points (~1.5 s), with consecutive windows overlapping by 50%. To minimise end effects, the windows were multiplied by a Hanning window prior to calculating the fast Fourier transform. The oscillatory power was evaluated as the area under the PSD curve between 10 and 40 Hz. These limits were chosen to account for the low oscillation frequency in CA3 networks of NRG1tyI mice (lowest detected peak frequency: 13.4 Hz).

The box plots in Figures 3.1B, C and 3.2B, C represent the data with statistical values. This presentation is suitable for data that are not normally distributed: the lower boundary of the box indicates the 25^{th} percentile, the line within the box marks the median, and the upper boundary indicates the 75^{th} percentile. The whiskers (error bars) below and above the box illustrate the 10^{th} and 90^{th} percentiles and the dots represent 5^{th}

and 95th percentiles. However, at least nine data points are needed to compute 5th, 10th, 90th and 95th percentiles. (Occasionally, there are no data points beyond the 10th and 90th percentile due to computational limitations.) The box plots in Figures 3.1B, C and 3.2B, C present data obtained from analysis of the *first* ~60 s of the recording taken in each slice (these varied between 5 and 70 min after initial exposure to CCh). Percentile calculations were carried out either in Sigma Plot ver. 10 (Systat Software, Chicago, IL, USA) (Figures 3.1B, C, 3.2B, C), or in Excel ('percentile command', Office 2007, Microsoft) (Figures 3.4D, 3.5D, F). The percentile plots in Figures 3.5D and 3.5F represent the mean of the data distribution at every 5th percentile. In contrast, the data distribution shown in Figure 3.4D did not appear to be normal (Shapiro–Wilk test, $p<0.05$), therefore the median of all data points was calculated for every 5th percentile.

For analysis of the phase-coupling of events (e.g. cell firing, synaptic current peak) to ongoing field potential oscillation, the field recording was transformed by Morlet wavelet. The Morlet transform enables analysis of signals whose frequencies vary in time, such as non-sinusoidal *in vitro* gamma frequency oscillations. Morlet transform can be used to define the phase of events. The relevant Igor Pro procedures were kindly provided by Dr Iris Oren (Institute of Neurology, UCL, UK) and are described in detail in Oren et al. (2006). Briefly, the magnitude component of the Morlet wavelet transform was examined between 10 and 45 Hz, and the maximum magnitude was found for each time point. The corresponding frequency was identified, and the oscillation phase determined on the basis of this dominant frequency. The phase was defined as −180°, associated with the minimum of the oscillation, to completion of a full cycle at the following minimum, +180° (see Figure 1F in Oren et al., 2006). Cycle-averaged field oscillations for graphical representation (Figure 3.4F) and cycle-

averaged PSCs for a baseline estimate (see below) were obtained by summing recordings over cycles and normalising to the number of cycles.

The waveform of the field potential oscillations was analysed in two ways. Firstly, the coefficient of variation (CV) of the magnitude of the field oscillation was calculated for each experiment from the SD of the maximum wavelet magnitude over the entire 60 s long, 200 Hz low-pass filtered recording (Section 3.2.1). Secondly, the occurrence of population spikes was probed in 60 s long, band-pass filtered (500 Hz–1 kHz) recordings by simple threshold analysis (detection of negative deflections exceeding an amplitude threshold) (Figure 3.4A). To avoid possible biasing of data, thresholds were not set to absolute values by visual inspection (as in Oren et al., 2010) but normalised to the mean wavelet magnitude of each recording ($1/6^{th}$ of the mean magnitude). This threshold criterion was verified to detect prominent downward deflections but not noise in each recording.

Event times for cell firing were defined as the times at which the spikes crossed a custom-set current threshold that was chosen by visual inspection of traces to exceed the noise level; this absolute threshold varied between recordings. Firing rate was defined as the total number of events divided by the length of the recording (~60 s). Interspike interval (ISI) is the difference between consecutive event times. Event phases are the wavelet phases of the ongoing field potential oscillation at the times of the events; each phase can be represented as a unit vector pointing in the direction of the phase angle. The mean event phase is given by the direction of the summation vector *R*. The normalised length of the vector, *r* ($r = R \div$ number of events), is a measure of the strength of the phase-coupling of events.

The phasic excitatory and inhibitory charge transfers (Q_e and Q_i, respectively) were computed as the mean areas between baseline values and the recorded currents per

oscillatory cycle. Following the procedure described by Oren et al. (2006), the baseline value was initially estimated by calculating the cycle-averaged event for a 30 s recording (see above). The minimum (or maximum) value for each cycle-averaged IPSC (or EPSC) was used as the initial baseline estimate. This estimate was refined in 0.1 s long windows over the entire recording by calculating the mean of all values that exceeded the initial estimate in each window. This value was used as the baseline for the 0.1 s window. If no values exceeding the initial estimate were found, the baseline estimate was incrementally adjusted (positively for IPSCs, negatively for EPSCs) until a value was found. The ratio of mean Q_e to mean Q_i was calculated for each cell (Figure 3.5C).

For analysis of PSC amplitudes and kinetics, events in 30 s recording periods were detected as the peak current per cycle of the oscillation (Oren et al., 2006). Detection was limited to compound PSC events whose peak current occurred within the oscillatory cycle (search region from cycle start point to cycle end point), and which had 20–80% rise times >0.2 ms and half-amplitude decay times >0.5 ms, to reduce detection of artefacts. With these limitations, the frequency of detected PSC events was lower than the peak frequency of the field gamma, and is therefore not reported here. Each PSC amplitude was calculated as the difference between the value at event start and the peak value per cycle. The event start was defined as the time at the local minimum (for IPSCs) or the local maximum (for EPSCs) of the band-pass-filtered (10–45 Hz) current recording preceding the peak. Medians (rather than the means) of individual recordings are reported and were used for statistical evaluation to reduce errors resulting from event misdetection. Similarly, the IPSC/EPSC amplitude ratio was calculated for each cell based on median PSC amplitudes. The CV of the PSC amplitudes was calculated from the SD of all amplitudes detected in a 30 s recording.

The kinetics of the synaptic events can provide information about the extent of the synchronisation of individual events during the compound PSC: 20–80% rise time and half-amplitude decay time were analysed for all detected events (threshold 1 pA) and repeated for prominent events (those exceeding the median amplitude of all PSC events in that particular recording), to account for noise in small amplitude events. Both analyses showed a similar trend and statistical significance. The data presented here (Figure 3.5) are based on all events. Rise times were defined as the time difference between time points corresponding to 20% and 80% of the event amplitude on the rising phase of the event. Half-amplitude decay times correspond to the time difference between the time of the peak value per cycle and the time point corresponding to 50% of the event peak amplitude on the decay phase of the event. Values from individual recordings are reported as medians to reduce errors caused by misdetections in these automated procedures.

2.6.2 Light-evoked inhibitory postsynaptic currents

Minimal optical stimulation was verified by off-line analysis in Clampfit ver. 10.2 (pClamp 10, Molecular Devices): For all laser powers applied, the peak amplitude of the first light-evoked IPSC was quantified as the difference between a 10 ms baseline reading before optical stimulation and the mean value in a ~1 ms window around the peak of the first IPSC. Peak amplitudes were plotted against laser power (e.g. Figure 4.5A). Local and absolute peaks in light-evoked IPSCs with discontinuous rising phases were analysed separately following visual inspection (black and green dots in Figure 4.5A). Where off-line analysis verified that optical stimulation elicited minimal responses (e.g. photoactivation was limited to a single or a few PV+ cell fibres; detailed in Section 4.3.1.4), IPSCs elicited by this laser power were further analysed for kinetics and amplitude with a custom-written Igor Pro procedure. IPSCs of 20–30 sweeps were

analysed in each recording. Traces were digitally low-passed filtered at 1 kHz and analysed automatically, but with visual verification of each individual trace to exclude unstable baseline or spontaneous activity. Peak amplitudes of the first light-evoked IPSC were calculated as the detected peak subtracted by the mean of a 15 ms pre-stimulus baseline. Where the peak amplitude was larger than failure threshold (> 3 SD of baseline), the onset of the response was determined as the local minimum preceding the IPSC peak. Latency is the delay between the start of the laser pulse and onset of the IPSC. Kinetic parameters were analysed as follows: 20–80% rise time is the difference between time points corresponding to 20% and 80% of the event amplitude on the rising phase of the IPSC; half-amplitude decay time is the time from peak to 50% amplitude. Analysis of decay tau time was performed for all events in which a mono-exponential function could be fitted to the event decay (Figure 4.5B.v). The mono-exponential curve was fitted between the event peak and the decay end (i.e. the time point at which baseline is reached, or the IPSC amplitude has dropped by at least 90%). Analysis of paired-pulse ratio (2^{nd} IPSC peak amplitude ÷ 1^{st} IPSC peak amplitude) was limited to sweeps in which the paired (second) IPSC peak amplitude was larger than 3 SD of pre-pulse baseline (calculated 5 ms prior to the second light pulse). For comparison between genotypes, medians were calculated from individual experiments. Recordings were excluded if R_{access} changed by >20% or if anatomical identification revealed that the recorded cell was not a pyramidal cell.

For the current-voltage plot in Figure 4.4C, peak IPSC amplitudes of individual traces were plotted as a function of the voltage holding potential. Voltage measurements were corrected for liquid-liquid junction potential (−11.7 mV, calculated with Clampex's Junction Potential Calculator software, JPCalc; Barry, 1994). Approximate

reversal potentials were determined from x-axis intercepts of linear regressions fitted to the data (SigmaPlot).

2.6.3 Miniature excitatory postsynaptic currents

Miniature EPSCs were automatically analysed in Clampfit 10.2 (pClamp 10, see above). Recordings of 120 s duration were band-pass filtered (4 Hz–6 kHz), and synaptic events were detected with an amplitude threshold-crossing algorithm. Optimal criteria for threshold detection at both voltage-clamping potentials (−65 mV and +40 mV) were carefully evaluated in three randomly chosen experiments in which pharmacological blocking of AMPARs / kainateRs and, subsequently, NMDARs allowed the evaluation of event misdetection at −65 mV and +40 mV. At −65 mV, fast negative-going mEPSCs were reliably detected as those below −5 pA (amplitude threshold; baseline = 0 pA), lasting between 0.5 and 100 ms (event duration). To avoid erroneous double detection of a single event, the noise rejection threshold for event detection was set at 0.5 ms. Slower NMDAR-miniature events at +40 mV were detected as those above +7 pA for 0.8–200 ms (noise rejection threshold 0.8 ms). The higher latter amplitude threshold reflects the higher noise level at +40 mV, likely due to activation of voltage-gated ion channels. For comparison, I repeated the analysis with a 5 pA threshold (see additional analysis in Section 5.3.2). Because noise levels at each voltage were similar throughout all recordings, the same detection criteria were employed for analysis of mEPSCs in different cell types (BCs, AACs, pyramidal cell) in both genotypes.

Detected events were analysed in peak amplitude and area (area between the data trace and the baseline during a single event). For area, all sample amplitudes within the event were summed, and the result was multiplied by the sampling interval (area units:

pA·ms; pClamp 10). Current kinetics (rise time, decay time) could not be reliably determined by automatic screening of mEPSCs because noise in traces severely affected kinetic measurements in small amplitude events. Comparisons between experiments were conducted on median amplitude and area values from individual experiments.

2.6.4 Statistical analyses

For CCh-induced gamma oscillations, circular statistics were used to determine the phase coupling of events: Events were deemed significantly phase-coupled if the Rayleigh probability of R was <0.05. Calculation of the Rayleigh probability is described in Oren et al. (2006). Statistical significance of linear variables was examined for absolute values or medians obtained from individual experiments of both genotypes (NRG1tyI and non-NRG1tyI mice). The values were imported into SPSS ver. 18.0 (IBM, Endicott, New York, USA), inspected for normality (p>0.05, Shapiro–Wilk test) and for homogeneity of variance (p>0.05, Levene's test). For normal distributions, significance between NRG1tyI (NRG1tyI; NRG1tyI/PV-Cre; NRG1tyI/Lhx6) and non-NRG1tyI (e.g. WT; PV-Cre; Lhx6) groups was tested using independent samples t tests. For samples lacking normal distribution, non-parametric two-independent sample tests were utilised to compare distributions across groups (Mann–Whitney U-Test). To correlate variables from non-normal distributions, I used Spearman's rank correlation (correlation coefficients are noted in the text). Interactions of between-subject factors were detected with two-tailed analyses of variance (ANOVAs), even in those cases where the data lacked normality and/or equal variance (Figures 3.1, 3.2 and 5.6; Tables 5.3 and A1). This statistical approach is in accordance with Glass and colleagues (1972) who suggest that the F statistic controls the Type I error rate well under conditions of non-normality (Glass et al., 1972). It may also be justified because, firstly, data transformations could often not correct many of the violations and, secondly, non-

parametric tests would not detect interactions of between-subject factors but would involve multiple testing to investigate the given factors that might cause inflation of Type 1 errors. Differences between repeated measures (such as percentiles, Figures 3.4D, 3.5D, F; Table 3.1) were tested with a 'repeated measures ANOVA' which is preferred over a multivariate procedure for small sample sizes (Field, 2009). In cases where the assumption of sphericity had been violated (Mauchly's test), the degrees of freedom were corrected using Greenhouse–Geisser estimates of sphericity (Field, 2009). Significant overall effects or interactions of between-subject factors revealed by ANOVA (p<0.05) were further explored by subsequent simple main effect analysis or *post hoc* Bonferroni-corrected pairwise comparison.

To evaluate the effect of the introduced over-expressed gene NRG1tyI on the properties of field potential oscillations (Chapter 3), statistical comparisons were carried out at two levels: slices (1–4 slices per mouse) and mice (using the mean value of all slices per mouse). In young mice (1–2 months), both analyses yielded similar results (Table A2), but in old mice (3–6 months), the difference in peak oscillatory frequency was only significant at the slice level, not mice (Table A2), probably because of low n number of old animals. To compare the probability of epileptiform discharges in NRG1tyI mice with the probability that they occur in the WT network, I employed Fisher's Exact test.

2.7 Anatomical processing and evaluation

2.7.1 Tissue fixation and re-sectioning

Fixative contained 4% paraformaldehyde and 0.2% picric acid in 0.1 M phosphate buffer (PB, pH 7.4). In some cases, 0.05% glutaraldehyde was added immediately prior use to complement the fixation by paraformaldehyde and picric acid. Glutaraldehyde is

a bifunctional aldehyde that stabilises proteins more effectively than formaldehyde. It is known to rapidly cross-link distant amino acids of protein molecules, but it penetrates tissues only slowly and may not always be ideal for subsequent immunohistochemical staining (because of unsaturated aldehyde groups that may link amine-containing groups of antibodies; Kiernan, 1981).

2.7.1.1 Perfusion-fixed brains

The two immunocytochemical evaluations in Section 4.3.1 were carried out on sections obtained from perfusion-fixed brains. For this, mice were deeply anaesthetised with pentobarbitone sodium and sacrificed by cardiac perfusion: ~50 mL of 0.1 M phosphate buffered saline (PBS), followed by ~100 mL of fixative. Whole brains were removed, and post-fixed for ~2 hours, then thoroughly washed in 0.1 M PB. For dissection, either both hemispheres (evaluation of PV-Cre/R26R-eYFP mice) or right hemispheres (evaluation of NRG1tyI mice) were embedded in 20% gelatine and fixed for 1.5 h (fixative plus 0.05% glutaraldehyde) and sectioned coronally (50–70 µm; VT1000S vibrating microtome, Leica) in 0.1 M PB. At least five hippocampal sections along the dorso-ventral axis were randomly chosen for immunohistochemistry (Section 2.7.3).

2.7.1.2 Fixation of acute slices

To visualise neurobiotin-labelled neurons, acute slices (250–400 µm) were fixed overnight at 4°C in fixative solution containing glutaraldehyde (as above). Slices were then thoroughly washed in 0.1 M PB, and stored in PB supplemented with 0.05% sodium azide at 4°C. For resectioning, slices were embedded in 20% gelatine and fixed for 1 h. The base of the gelatine block was glued to a microtome plate using

cyanoacrylate adhesive, and embedded slices were re-sectioned at 50–60 µm thickness with a Leica VT1000S vibrating microtome in 0.1 M PB.

2.7.2 Cell visualisations

All sections obtained from a re-sectioned slice were washed in TBS-Tx buffer [50 mM Tris-buffered saline (TBS; pH 7.4) with 0.3% Triton X-100] and incubated overnight with streptavidin conjugated to either Alexa Fluor 488, Cy3, or Alexa Fluor 647 (Table 2.5). The next day, sections were washed in TBS-Tx, mounted in Vectashield (H-1000, Vector Laboratories) and examined with a DM5000 B epifluorescent microscope (Leica) using an appropriate filter set (L5, Y3 or Y5; Leica) and an ORCA-ER CCD camera (Hamamatsu).

2.7.2.1 Cell reconstructions and laminar analysis

PTIs recorded in Lhx6 mice (Chapter 5) were reconstructed digitally to unambiguously determine the axon distribution across all CA3 strata. Depending on how much streptavidin-Cy3-visualised axon each section contained, one to four sections per cell were digitally photographed using an AxioImager Z1 epifluorescence microscopy (Carl Zeiss AG) with a 43HE filter set, 20× objective and AxioVision software (ver. 4.7.1). Stacks (optical thickness ~1.2 µm) were assembled through the entire 50 to 60 µm thick sections, and collapsed to two-dimensional images using ImageJ software (ver. 1.45; http://rsbweb.nih.gov/ij/) by maximal projection. Images were inverted to show the cell on white background, and neurites were traced semi-automatically by NeuronJ (ImageJ plug-in) at a set line thickness (3 pixels). Dendrites and axons were distinguished by microscopic examination. For presentation (Chapter 5 and Figure A1), one to three reconstructed sections were digitally aligned in GIMP software (ver. 2.6.11; http://www.gimp.org/) using dendrites, main axons and

hippocampal strata as reference features. Laminar borders were determined in one section (either containing the soma or the majority of axon) in epifluorescent images (AxioImager Z1, 43HE filter set, 5× magnification), and verified by landmarks at 20× magnification. The borders of the str. pyramidale illustrate the compact arrangement of pyramidal cell somata, but note that individual pyramidal cells in area CA3 may be loosely located outside the str. pyramidale (more so than in area CA1).

To quantify the distribution of axon across different laminae in putative BCs (Section 5.3.1.1), the visualised axon lines in individual sections were expressed as pixel numbers (Szabo et al, 2012). Because the axon line thickness was fixed in the reconstructed image, the pixel count approximately represents the proportion of axon in each layer of the two-dimensional image. Pixel numbers were calculated for horizontal 'bins': the str. pyramidale and str. lucidum are represented by one bin each, while the str. radiatum and str. oriens were divided into three equal-depth bins to account for the variability in axon arborisation within them. For the computation of axon pixels across laminae, visualised sections were digitally straightened such that the layers were oriented horizontally (GTKMorph programme, GIMP).

Pixels in similar laminar bins were summed from two or three sections in each cell (section with majority of axon; Table A4). For the purpose of normalisation, the sum of all pixels across all bins was set at 1.0 for each cell. The histograms in Figure 5.1B represent the mean ± SEM (standard error of the mean) of the normalised laminar distribution of axon pixels across all putative BCs (Szabo et al. 2012).

2.7.3 Immunohistochemistry

Immunohistochemistry was performed on free-floating sections. Selected sections were washed in TBS-Tx, then blocked in 20% normal horse serum (NHS, Vector

Laboratories; or normal goat serum, NGS, depending on the species in which the secondary antibody was raised) in TBS-Tx for at least 1 h at room temperature, and then incubated with the relevant primary antibodies (Table 2.4) for 48 h at 4°C. Appropriate fluorochrome-conjugated secondary antibodies (Table 2.5) were applied overnight at 4°C, after thorough washing (3× 20 min in TBS-Tx) to remove unbound primary antibody. The next day, after another thorough wash in TBS-Tx (3× 20 min), sections were mounted in Vectashield under coverslips.

With this protocol, three different batches of mouse antibody against Cre recombinase (Table 2.4) failed to elicit satisfactory staining, either in fixed hippocampal slices or fixation-perfused brain sections.

For immunoreactivity to Ankyrin-G, slices were pre-treated with pepsin (0.2 mg/mL in 0.2 M HCl) at 37°C for 5 min to improve antigen retrieval (Szabo et al., 2010). After washing in 0.1 mM PB, slices were treated with glycine (0.1 M in TBS-Tx) for 30 min at room temperature to reduce background staining. Slices were blocked in normal goat serum (NGS; 10% in TBS-Tx) and incubated in relevant primary (mouse anti-Ankyrin-G; Table 2.4), then secondary antibody (DyLight 649-conjugated goat anti-mouse IgG; Table 2.5) as described above. Despite pretreatment, Ankyrin-G staining was only sparse in some sections, and tended to be more successful inside the section rather than at its surface. This might be because fixation of the inner tissue was less effective, likely protecting antigen sites of Ankyrin-G from cross-linking. Therefore, immunoreactivity to Ankyrin-G was often tested on several sections per slice.

Immunoreactivity was evaluated at 40× or higher magnification, using either an Axio Imager Z1 microscope with ApoTome ‘structured illumination’ resolution enhancer (Carl Zeiss AG) and AxioVision software, or an LSM710 confocal laser-

scanning microscope (sequential multitrack single channel operation mode; Carl Zeiss AG) with Zen2008 software. In the latter, only one laser was applied to the section at one time. No cross-talk between channels was found under our conditions (see Nissen et al., 2010). When indicated, digital micrographs were constructed from z-stacks with ImageJ software. Micrographs were adjusted in brightness and contrast, but not otherwise manipulated. Immunoreactivity was declared 'negative' when fluorescence was not detected in relevant parts of the neurobiotin-filled cell in an area where similar parts of unfilled cells were immunopositive. Immunonegativity to CB1R was confirmed on at least two (but up to five) separate regions with successful antibody staining. Immunoreactivity was considered inconclusive ('not tested') if antibody staining was insufficient at the tissue depth of Streptavidin-Cy3-visualised axon (e.g. Ankyrin-G; Section 5.3.1.1); or if at least two researchers could, independently, not make a clear decision on immunoreactivity. Immunoreactivity to Ankyrin-G was declared 'positive' if at least three close appositions between Streptavidin-Cy3-visualised rows of axon boutons and Ankyrin-G-containing AIS were observed by two independent researchers.

For the semi-quantitative evaluation of PV and Cre co-expression in PV-Cre/R26R-eGFP mice (Section 4.3.1.2), stack images across the entire slice thickness of area CA3 (of the mid-ventral or dorsal hippocampus) were taken in two 50–70 µm sections with the AxioImager Z1epifluorescence microscope (Carl Zeiss AG) using appropriate filter sets (38HE and 43HE), 40× oil immersion objective and AxioVision software. All PV+ and eYFP+ somata were counted in the str. oriens, str. pyramidale and str. lucidum and the lower third of the str. radiatum in all CA3 subfields on z-projected greyscale images (ImageJ; Figure 4.2).

Table 2.4 Primary antibodies

Antigen	Species	Type[a]	Supplier (URL)	Product code	Dilution[b]
Ankyrin-G	Mouse	M	NeuroMab (neuromab.ucdavis.edu)	75-416	1:500
Ankyrin-G	Mouse	M	Santa Cruz Biotech (www.scbt.com)	sc-12719	1:100
CB1R	Guinea pig	P	Frontier Science (www.frontier-science.co.jp)	Cb1-GP-Af530-1	1:1000
Cre	Mouse	M	Millipore (www.millipore.com)	MAB3120	1:500
GFP[c]	Chicken	P	Aves (www.aveslab.com)	GFP-1020	1:500
PV	Rabbit	P	Swant (www.swant.com)	PV-28 or PV-25	1:1000
PV	Guinea pig	P	Synaptic Systems (www.sysy.com)	195004	1:2000

[a] M: monoclonal; P: polyclonal

[b] Dilutions in TBS-Tx containing 1% NHS (or NGS)

[c] Primary antibody against GFP was used to enhance transgenic or virally-mediated eYFP fluorescence in fixed tissue.

Table 2.5 Streptavidin conjugates and secondary antibodies

Conjugate	Species	Supplier (URL)	Product code	Dilution[a]
Secondary Antibodies				
Alexa 488	Goat anti-Chicken	Invitrogen (http://www.invitrogen.com)	A-11039	1:500
DyLight 488	Donkey anti-Guinea pig	Jackson (http://www.jacksonimmuno.com)	706-485-148 (discontinued)	1:500
AMCA	Donkey anti-Rabbit	Jackson	715-155-152	1:500
Cy3	Donkey anti-Mouse	Jackson	715-165-151	1:400
Cy5	Donkey anti-Rabbit	Jackson	711-175-152 (discontinued)	1:250
Cy5	Donkey anti-Guinea pig	Jackson	706-175-148 (discontinued)	1:250
DyLight 649	Goat anti-Mouse	Thermo (http://www.thermofisher.com)	35515	1:250
Streptavidin Conjugates				
Alexa 488		Invitrogen (http://www.invitrogen.com)	S-32354	1:1000
Cy3		Caltag (http://www.caltagmedsystems.co.uk)	SA1010	1:2000
Alexa 647		Invitrogen http://www.invitrogen.com	S-32357	1:1500 – 1:5000

[a] Dilutions in TBS-Tx containing 1% NHS (or NGS)

3 *In vitro* cholinergically induced synchronised network activity is altered in NRG1tyI mice

3.1 Introduction

NRG1 type I over-expressing (NRG1tyI) mice exhibit a selective age-emergent impairment of hippocampus-dependent working memory (Introduction 1.4.1; Deakin et al., 2012). This suggests that NRG1 over-expression causes pathological changes in hippocampal neuronal circuits. In this chapter, I explore synchronised network activity patterns, because they have been proposed to underlie cognitive processing (Engel et al., 2001; Fries, 2005). In particular, synchronised activity at the gamma range (~25–140 Hz; Colgin & Moser, 2010) in the CA3 area of the hippocampus may represent the network correlate of neuronal processes that encode and/or retrieve working memory (see Introduction 1.3.3; Buzsaki et al., 1983; Engel et al., 2001; Csicsvari et al., 2003; Jensen, 2006; Lisman & Buzsaki, 2008; Colgin & Moser, 2010).

As NRG1 is a strong schizophrenia susceptibility gene (Stefansson et al., 2002; Li et al., 2006; Keri et al., 2009), it is intriguing that both cognitive capacity and gamma-frequency oscillations are impaired in schizophrenic patients (Spencer et al., 2003; Lewis & Gonzalez-Burgos, 2006; Uhlhaas & Singer, 2010): cognitive impairment, specifically a decline in working memory, is at the core of schizophrenia (Park & Holzman, 1992; Heinrichs, 2005), and cortical gamma oscillations are typically *reduced* in amplitude in schizophrenic patients during working memory tasks (reviewed in Uhlhaas & Singer, 2010). Therefore, the question arises as to whether NRG1tyI over-expression affects hippocampal gamma oscillations in parallel to the described cognitive deficit.

To study hippocampal gamma oscillations, I applied a cholinergic model of ongoing field potential oscillations (Fisahn et al., 1998) in a submerged recording chamber (Hajos et al., 2009). This is a well-established *in vitro* model of robust gamma-frequency oscillations, which enables the experimenter to study the neuronal circuits that contribute to the generation and maintenance of these oscillations in the hippocampus (Hajos et al., 2004; Mann et al., 2005; Oren et al., 2006).

I studied cholinergically induced network activity in transverse hippocampal slices prepared from NRG1tyI mice and WT littermates. As outlined above (Introduction 1.4.1), age is a crucial parameter in the performance of NRG1tyI mice in behavioural tests of working memory: 10-month-old but not 3- to 4-month-old transgenic mice showed significant impairment in hippocampus-dependent spatial working memory (Deakin et al., 2012). Based on these findings, I investigated gamma-frequency oscillations in slices from mice of two different age groups, 3–6 months and 1–2 months of age, to find out if neuropathological changes preceded the apparent decline in working memory.

3.2 Results

3.2.1 CCh-induced gamma-frequency field oscillations are significantly slower in NRG1tyI mice

First, I investigated the rhythmic network activity in 3–6-month-old mice. Cholinergic activation (5–20 μM carbachol, CCh) successfully induced robust field potential oscillations in the CA3 area of hippocampal slices (Figure 3.1A). Following at least 5 min of bathing in CCh, one-minute extracellular recordings in str. pyramidale were analysed by power spectrum density to identify the frequency components and

field power. Oscillations in slices of wild-type (WT) mice (*n*=19 slices from 9 mice) showed a mean peak frequency of 26.3 ± 1.1 Hz (Figure 3.1B). This is consistent with various reports of *in vitro* CCh-induced network activity in CA3 hippocampus (Mann et al., 2005; Oren et al., 2006; Fisahn et al., 2009; Hajos et al., 2009; Gulyas et al., 2010). Slices from NRG1tyI mice (*n*=14 slices in 8 mice) also exhibited lasting oscillations in the presence of CCh (Figure 3.1A), but, importantly, these were at a significantly lower mean peak frequency (22.0 ± 0.9 Hz; *p*=0.005, independent samples t test; Figure 3.1B). This shift to lower frequencies was apparent at all times that local field potential oscillations were probed following exposure to CCh (Figure 3.1B right). Statistical analysis revealed a significant overall effect of genotype on the peak frequency ($F_{(1,55)}$=19.163, *p*<0.001, two-way ANOVA) but no significant main effect of time ($F_{(3,55)}$=0.664, *p*=0.578) and no overall interaction between the two factors ($F_{(3,55)}$=0.531, *p*=0.663), confirming the stability of oscillation frequency within genotype over time. Simple main effect analysis further confirmed that the peak frequency was significantly different at the first three time points (10 min: $F_{(1,55)}$=8.757, *p*=0.005; 10–30 min: $F_{(1,55)}$=6.073, *p*=0.017; 30–50 min: $F_{(1,55)}$=6.401, *p*=0.014) but not at >50 min in CCh, presumably due to low numbers ($F_{(1,55)}$=1.394, *p*=0.243; see Table A1). Taken together, this shows that increased NRG1tyI expression changes the functioning of the CA3 neuronal circuit elements responsible for oscillatory activity. Importantly, these results demonstrate that the neuronal circuitry that underlies gamma oscillations is already affected in NRG1tyI mice of pre-symptomatic age, i.e. before the behavioural deficit is apparent (10 months; Deakin et al., 2012).

Mean oscillatory power (the area under the power spectral density curve 10–40 Hz, see Figure 3.1A) varied highly between slices: 62.84 ± 7.97 μV^2/Hz (mean ± SEM) across WT mice slices (median 58.60 μV^2/Hz, *n*=19), and 141.45 ± 41.33 μV^2/Hz

across slices from NRG1tyI mice (median 65.23 μV^2/Hz, n=14; Figure 3.1C). Distributions of peak power across all slices tended to be larger in some slices from NRG1tyI mice at this age, although this was not statistically significant when comparing the field power of the first recording in every slice (one measurement per slice between 5–70 min after bathing in CCh*;* p=0.291, Mann–Whitney U test; 3–6 months old). There was, however, a significant overall effect of genotype in the field power of recordings in WT and NRG1tyI mouse slices over the different time points at which oscillations were probed (significant overall effect of genotype: $F_{(1,55)}$=15.296, p<0.001, see Table A1). Note, however, that this latter statistical analysis consists of repeated measures in some but not all slices, which might result in statistical significance given the high variability in field power (see Table A1). This overall effect of genotype was due to significantly higher peak oscillatory power in NRG1tyI slices at all time windows except the last (10 min: $F_{(1,55)}$=4.416, p=0.040; 10-30 min: $F_{(1,55)}$=4.785, p=0.033; 30-50 min: $F_{(1,55)}$=7.180, p=0.010; >50 min: $F_{(1,55)}$=1.450, p=0.234, simple main effect analysis).

Given the pronounced change in gamma oscillations in 3–6-month-old transgenic mice, the question arises as to how much earlier (relative to behavioural symptoms) changes in hippocampal network functioning might be detected. Is a qualitatively similar change in CCh-induced oscillations also apparent in younger mice? Surprisingly, field potential recordings in 1–2-month-old mice revealed a similar profile: across all slices, the CA3 network of transgenic mice oscillated at significantly lower peak frequencies (22.1 ± 0.6 Hz, median 23.19 Hz; n=21 slices from 10 mice) than that of WT mice (26.2 ± 0.6 Hz, median 25.64 Hz; n=27 slices from 17 mice; p<0.001, Mann–Whitney U test; Figure 3.2B). The effect was also significant when statistical comparisons were performed at the level of mice, by calculating the mean

oscillation frequency value across all slices taken per mouse (p<0.001, independent samples t test; Table A2). In contrast, in old mice, the comparison of mean peak frequencies on the level of mice failed to reach statistical significance (see Table A2). This is likely due to the greater contribution of two outlying WT mice in which oscillations were only probed in one slice each and each oscillated at an unusually low peak frequency. As in slices from old mice, the peak frequencies in young NRG1tyI mouse slices were significantly lower, over all times that oscillations were probed, following exposure to CCh (Figure 3.2B right; overall effect of genotype: $F_{(1,87)}$=49.820, p<0.001, two-way ANOVA, for details see Table A1). In addition, there was a main effect of time ($F_{(3,87)}$=3.026, p=0.034) but no interaction between the two factors ($F_{(3,87)}$=1.035, p=0.381). The main effect on time may be attributable to the significant difference in the oscillatory frequencies in slices from NRG1tyI mice over time ($F_{(3,87)}$=2.850, p=0.042, simple main effect analysis), while oscillation frequencies in WT mouse slices were stable over time ($F_{(3,87)}$=0.956, p=0.417, simple main effect analysis).

Similarly to the results in older mice (3–6 months), mean oscillatory power in 1–2-month-old mice also tended to be larger across all slices from NRG1tyI mice (245.36 ± 65.45 μV^2/Hz, median 158.33 μV^2/Hz, n=21; WT: 140.16 ± 23.35 μV^2/Hz, median 106.96 μV^2/Hz, n=27; p=0.167, Mann–Whitney U test; Figure 3.2C). Interestingly, field power drifted during long experiments in slices from NRG1tyI mice (Figure 3.2C right), and two-way ANOVA revealed a significant overall effect of genotype ($F_{(1,87)}$=29.848, p<0.001) as well as time ($F_{(3,87)}$=3.894, p=0.012), and a significant interaction between the two factors ($F_{(3,87)}$=5.122, p=0.003). Again, the overall effect of time on field power may be attributed to NRG1tyI mouse slices ($F_{(3,87)}$=8.747, p<0.001, simple main effect analysis), but not to WT mouse slices ($F_{(3,87)}$=0.098, p=0.961). In fact, the oscillatory

power was significantly larger in NRG1tyI slices after 30 min in CCh (10 min: $F_{(1,87)}$=3.254, p=0.075; 10-30 min: $F_{(1,87)}$=0.933, p=0.337; 30-50 min: $F_{(1,87)}$=4.356, p=0.040; >50 min: $F_{(1,87)}$=28.099, p<0.001, simple main effect analyses).

Having identified a tendency to larger power, I next explored whether cycle-to-cycle oscillation amplitude was more stable in slices from young NRG1tyI mice than from age-matched WT littermates. For this, I employed Morlet wavelet transform of oscillatory cycles (Methods 2.6.1 and Section 3.2.3.1). I analysed the variability of the maximum of the wavelet transform magnitude at each time point across 60 s long recordings (maximum wavelet magnitude; Oren et al., 2006) and calculated the CV from the SD of the maximum wavelet magnitude for all recordings from young slices (WT: n=27 slices, NRG1tyI: n=21 slices). The maximum wavelet magnitude fluctuated similarly over time in both genotypes, and the CV indicated no significant difference between the groups (WT: 29.29 ± 0.43%; NRG1tyI: 29.69 ± 0.91%; p=0.689, independent samples t test). Thus, cycle-to-cycle amplitudes in slices from NRG1tyI mice varied to the same degree as those in slices from WT mice.

To summarise, CCh-induced synchronised network oscillations were similarly altered in NRG1tyI mice of 3–6 months and 1–2 months and significantly slower at both pre-symptomatic ages. Mean oscillatory power was highly variable, with a tendency to being larger across transgenic slices of *older* mice (3–6 months), while there was a gradual increase in power with time of exposure to CCh in slices from *younger* NRG1tyI mice (1–2 month old).

3.2.2 Reduced threshold for epileptiform activity in NRG1tyI mice

In addition to the changes in oscillatory network activity, I noticed that slices from NRG1tyI mice (of both age groups) were more prone to develop epileptiform activity in

the presence of CCh. Epileptiform discharges resemble short interictal-like bursts and/or longer-lasting (>1s) ictal-type episodes (Rutecki & Yang, 1998; Avoli, 2001; Dzhala & Staley, 2003). These occurred immediately following wash-in of CCh but not at baseline, i.e. not in the absence of CCh (Figure 3.3A.i). In a few NRG1tyI slices (Table A3), interictal-like population discharges developed from robust gamma oscillations following >30 min of field recording (Figure 3.3A.ii).

Overall, for both genotypes, epileptiform discharges occurred more often when the CA3 network was excited by higher CCh concentration (20 vs 5 µM in older mice; 10 vs 5 µM in young mice; Figure 3.3B). Consequently, CCh concentration was reduced to 5 µM in further experiments, to achieve better stability of gamma oscillations.

Interestingly, the incidences of epileptiform bursts at high CCh concentrations were similar between younger and older animals, thus indicating that age did not significantly contribute to this CA3 network phenomenon. When pooling the results from both age groups (10–20 µM CCh), 82% (32/39) of slices from nearly all NRG1tyI mice (13/14) presented CCh-induced epileptiform activity, either immediately or developing over time. In comparison, only 27% (10/37) of slices from only one third (6/17) of all WT mice showed epileptiform activity at some stage of recording (Fisher's exact test, $p<0.001$; Figure 3.3C, Table A3). At 5 µM CCh, none of the 17 WT slices (from 10 WT mice) developed epileptiform activity as observed by field potential recordings, while 27% (8/30) of slices from more than half (6/11) of NRG1tyI mice became epileptic at some point (Fisher's exact test, $p=0.038$).

The higher susceptibility for epileptiform activity in NRG1tyI mice points to an altered balance of excitation/inhibition in the hippocampal network of transgenic mice as young as one month old. This might indicate that CA3 pyramidal cells of NRG1tyI mice are more easily excited by muscarinic ACh receptor activation which could elicit

hyper-synchronous pyramidal cell firing and epileptiform discharges in the network (Fisahn et al., 2002; Poulsen et al., 2002). An imbalance of excitation/inhibition could also result from increased CA3 pyramidal cell recurrent connectivity and/or aberrant GABAergic signalling. In a series of experiments, I investigated whether principal cell functioning or the rhythmic synaptic input to pyramidal cells is altered in NRG1tyI mice during CCh-induced oscillations.

3.2.3 Unaltered intrinsic properties but altered rhythmic inhibition of pyramidal cells during oscillatory network activity in NRG1tyI mice

A candidate mechanism for the generation and maintenance of CCh-induced gamma oscillations is the synaptic feedback circuitry between pyramidal cells and specific interneurons (Introduction 1.3.2): In CA3 hippocampus, pyramidal cells signal to local pyramidal cells and PTIs; the latter provide feedback, via phasic GABAergic inhibition, to pyramidal cells and other interneurons. Both elements of this signalling loop determine the temporal properties of the oscillatory cycles (Mann et al., 2005; Oren et al., 2006; Bartos et al., 2007). The rate and temporal precision of CA3 pyramidal cell output can influence the timing and strength of the feedback inhibition, which in turn governs pyramidal cell output. Although the frequency and magnitude of *in vitro* gamma oscillations are primarily set by the kinetics and strength of perisomatic inhibition (Oren et al., 2010), a change in pyramidal cell firing, for example by modulation of axonal excitability, could potentially modulate gamma oscillations (Traub et al., 2000). Indeed, loss of rhythmic pyramidal cell firing (resulting from blockade of a voltage-gated K^+ current, the 'M-current') was shown to alter gamma oscillation amplitude, although not its frequency (Leao et al., 2009). Unreliable or irregular pyramidal cell firing could also explain the propensity to epileptiform activity in NRG1tyI mice; it has also been associated with the occurrence of fast ripples in

epileptic hippocampus (Foffani et al., 2007). Therefore, I decided to first study pyramidal cell firing in NRG1tyI mice during rhythmic network activity.

The above data indicated that neurobiological changes of the CA3 hippocampal circuit were already present in NRG1tyI mice as young as 4 weeks, and did not appear to further alter with age in my experimental conditions. Consequently, I focused on studying the hippocampal network of younger mice (~1–2 months) for the remainder of this investigation.

3.2.3.1 CA3 pyramidal cell spike-coupling to gamma oscillation cycles is unchanged in NRG1tyI mice

Synchronised discharges of pyramidal cell populations are often visible in field potential traces as spike-like downward deflections at the trough of the oscillation cycle (Hajos et al., 2004). With larger ensembles of local pyramidal cells discharging synchronously during oscillation cycles, more spikes are visible in field potential traces. Intriguingly, the field potential waveform of NRG1tyI recordings appeared to be sharper and more 'pointed'. Indeed, the power spectral densities often appeared to consist of a second harmonic (not quantified), which probably reflects the less sinusoidal nature of oscillations in NRG1tyI mice (Figure 3.2A). Taken together, it emerged that NRG1tyI field potential recordings might consist of more population spikes. I analysed the occurrence of prominent population spikes per 100 oscillation cycles (Figure 3.4A). Spikes were defined as events more negative than 1/6 of the mean wavelet magnitude; this threshold was carefully evaluated in a subset of recordings to ensure reliable detection of visually verified population spikes and to minimise false positive detection. Employing a relative threshold (rather than a fixed threshold for all recordings) takes the variability of the mean oscillation magnitude between samples into account without biasing the data (see Methods 2.6.1; Oren et al., 2010). The number of downward

deflections per 100 cycles varied greatly between genotypes (WT: 1 to 85%; NRG1tyI: 0 to 80%), thus indicating a contribution from other, undetermined factor(s) to the population spikes (e.g. recording subfield in area CA3; origin of slice along the dorso-ventral hippocampal axis). Importantly, the distribution of detected spikes across all slices did not differ between the genotypes (WT: median 15.56%, *n*=27 slices; NRG1tyI: median 21.24%, *n*=21; *p*=0.959, Mann–Whitney U test; Figure 3.4A). Even though NRG1tyI recordings were not indicative of more synchronised population discharges in this analysis, individual CA3 pyramidal cell output in the transgenic mouse might still be altered (firing rate and/or temporal precision).

To probe action potential firing of individual cells, loose cell-attached voltage clamp recordings were made from putative pyramidal neurons (*n*=11 in 8 slices from NRG1tyI mice; *n*=10 in 8 slices from WT mice) in parallel with field recordings. A second ACSF-filled pipette was placed in CA3 str. pyramidale in close proximity to the field pipette, and current deflections (in voltage-clamp mode) were recorded for approximately one minute (Methods 2.4.1; Figure 3.4B).

In line with earlier field potential recordings, in this subset of data (*n*=8 slices for each genotype), gamma oscillations were again significantly slower across all transgenic slices compared to WT (WT: 25.0 ± 0.8 Hz, *n*=8 slices; NRG1tyI: 19.2 ± 1.2 Hz, *n*=8; *p*=0.001, independent samples t test on slice level; for statistical comparison see Table A2). Moreover, the distribution of field power was significantly higher in NRG1tyI in this subset of slices (median 274.74 μV^2/Hz, *n*=8 slices vs WT: median 86.87 μV^2/Hz, *n*=8 slices; p=0.012 Mann–Whitney U test). This is probably due to the fact that cell firing was usually recorded >30 min after the initiation of gamma oscillations, and (as mentioned above) the power in young slices gradually increased after 30 min (see Chapter 3.2.1 and Figure 3.2B).

Four parameters of pyramidal cell firing were analysed: firing rate, interspike interval (ISI), coupling strength of the firing to the oscillation, and phase of firing relative to the field potential oscillation cycle. For analysis of the latter two, oscillatory cycles were transformed by Morlet wavelet using automated custom-written Igor Pro procedures kindly provided by Dr Iris Oren (Institute of Neurology, UCL, UK; see Methods 2.6.1). The wavelet transform was used to define the phase of cell firing. Analysis revealed that none of the four parameters differed between the groups:

Firstly, cells located inside the str. pyramidale of NRG1tyI mice fired spontaneously during gamma oscillation, with a similar rate to that of CA3 str. pyramidale cells of WT mice (Figure 3.4C, NRG1tyI: 2.5 ± 0.3 Hz, n=11; WT: 2.0 ± 0.4 Hz, n=10; p=0.432, independent samples t test).

Secondly, there was no significant clustering of spikes over the recording period. In Figure 3.4D, to account for the apparent non-normal occurrence of ISI in individual cells, the data of individual cells (dots) are presented as percentiles; and, to account for the variability of ISIs between cells, the median (rather than mean) of every 5^{th} percentile is plotted in the percentile curves. Repeated measures ANOVA with genotype and percentile as fixed factors revealed no overall interaction between the two factors ($F_{(1.291,24.521)}$=0.257; p=0.677, Greenhouse–Geisser correction of sphericity), and no main effect of genotype ($F_{(1,19)}$=0.758; p=0.395) but a significant main effect of percentile as expected ($F_{(1.291, 24.521)}$=24.478; p<0.001, Greenhouse–Geisser correction). The distributions of median ISIs were also not significantly different between genotypes (p=0.398, Mann–Whitney U test) but cells in NRG1tyI mice tended to fire action potentials at slightly shorter intervals (median of all 50^{th} percentile ISIs: 306.95 ms, n=11) than WT cells (414.68 ms, n=10; dashed lines in Figure 3.4D). Given the lower oscillation frequency in NRG1tyI mice, this indicates that in transgenic mice pyramidal

cells firing occurred over more oscillatory cycles: on average, NRG1tyI cells fired every sixth oscillation cycle, assuming an average cycle length of 50 ms (field peak frequency ~20 Hz), whereas WT cells fired only every tenth cycle (average cycle length ~40 ms, frequency ~25 Hz). Firing in consecutive cycles (ISI < 100 ms) only occurred in less than 5% of all events (Figure 3.4D). Moreover, burst firing was not observed in either genotype, not even in those cells that were recorded in slices that later presented epileptiform bursts (WT: 1 of 8 slices; NRG1tyI: 3 of 8 slices).

Thirdly, the firing of most (but not all) cells was significantly phase-coupled to the gamma oscillations (Rayleigh probability <0.05, see Methods 2.6.4: 7 of 10 cells in WT; 10 of 11 cells in NRG1tyI). The strength of their phase-coupling (r_{AP}) to the ongoing oscillation did not significantly vary between genotypes (Figure 3.4E, WT: r_{AP}=0.33 ± 0.05, *n*=7; NRG1tyI: r_{AP}=0.43 ± 0.08, *n*=10; *p*=0.348, independent samples t test).

Lastly, significantly coupled cells of both genotypes fired preferentially at the start of the gamma cycle, near the minimum of the field oscillation cycle, as illustrated in Figure 3.4F (WT: 111.57 ± 14.58°, *n*=7; NRG1tyI: 113.60 ± 6.79°, *n*=10; *p*=0.902, independent samples t test).

Phase-coupling strength has been reported to vary with oscillation power (Oren et al., 2006). Indeed, there was a positive correlation between phase-coupling strength and overall field power in WT conditions (ρ=0.821, *p*=0.023, Spearman's correlation, *n*=7; Figure 3.4G). However, phase-coupling strength of NRG1tyI cells did not correlate with field power, despite the significantly larger field power in transgenic slices (ρ=−0.164, *p*=0.651, Spearman's correlation, *n*=10).

The finding that pyramidal cell firing is unaltered in 1–2 month-old NRG1tyI mice is consistent with our previous report on cell firing of CA3 pyramidal cells in older

mice (3−6 months, Deakin et al., 2012). In summary, the data indicate that CA3 pyramidal cell output during CCh-induced gamma oscillation in NRG1tyI mice is as efficient and temporally precise as in WT mice.

3.2.3.2 Synaptic input to pyramidal cells is altered in NRG1tyI mice during gamma oscillations

Next, I studied synaptic inputs in CA3 pyramidal cells during the cholinergically induced network activity. These inputs are compound postsynaptic currents, and their kinetics are mainly determined by the temporal synchronisation of individual afferent synapses (although postsynaptic receptor subunit composition at individual synapses also contributes to the compound kinetics). Synaptic input analysis was performed for two reasons: firstly, the slower gamma field oscillations in transgenic mice suggest that altered inhibitory compound current kinetics might give rise to more sustained oscillatory cycles (Fisahn et al., 1998; Oren et al., 2010); and secondly, the higher occurrence of epileptiform bursts in slices from NRG1tyI mice indicates an imbalance of excitation and inhibition, which might be reflected in an altered ratio of excitatory and inhibitory synaptic events in individual pyramidal cells.

Postsynaptic currents (PSCs) were recorded in a new set of CA3b/c str. pyramidal cells (independent of the firing properties presented above). Cells inside or close to str. pyramidale were patched under visual guidance (DIC infra-red microscopy) and recorded in whole-cell voltage-clamp mode. Cells were filled with neurobiotin and anatomically identified *post hoc* as pyramidal cells, based on the presence of characteristic mushroom-like spines on dendrites, characteristic dendritic trees and triangular-shaped somata located near or within str. pyramidale (Figure 3.5A).

Field and whole-cell recordings were performed simultaneously with two electrodes (Figure 3.5B). Data were collected at various time points after initiation of

gamma oscillations (>5 min up to 55 min). In line with the above findings, gamma oscillations in this subset had significantly lower peak frequencies, and were significantly larger in power (WT: *n*=11 slices; NRG1tyI: *n*=7; see Table A2). In total, 13 cells in 11 slices were recorded from 9 WT mice, and 8 cells in 7 slices were recorded from 5 NRG1tyI mice. In 2 of 21 cells, neurobiotin labelling was unsuccessful, but the cells were included in the PSC analysis because their PSC properties did not differ from anatomically identified pyramidal cells. For clarity, all these cells are referred to as pyramidal cells. Access resistance ranged between 14.3 to 17.9 MΩ in neurons of WT mice (*n*=12) and 12.5 to 18.3 MΩ in cells of NRG1tyI mice (*n*=7; *p*=0.308; note: R_{access} was not noted in one WT and one NRG1tyI mouse cell).

In the presence of carbachol (5–10 μM), CA3 pyramidal cells were similarly depolarised in slices from WT and NRG1tyI mice, as determined by V_m in current clamp mode (WT: V_m = −48 ± 2 mV, *n*=12; NRG1tyI: V_m= −47 ± 2 mV, *n*=7; *p*=0.730, independent samples t test; note: V_m was not noted in one WT cell and one NRG1tyI cell). This finding indicates that activation of mAChRs excited pyramidal cells in NRG1tyI mice to the same degree as cells of WT littermates. Neurons were voltage-clamped at the calculated reversal potential for GABA-A receptor-mediated IPSCs (−72 mV; 8 mM chloride in the intracellular filling solution, uncorrected liquid-liquid junction potential) to record compound EPSCs. Compound IPSCs were recorded at the estimated reversal potential for EPSCs (0 to +30 mV of the uncorrected potential). To shed light onto the apparent imbalance of excitation and inhibition in the CA3 network, I analysed mean Q_e and Q_i per oscillatory cycle in CA3 pyramidal cells (following Oren et al., 2006, see Methods 2.6.1). The mean Q_e tended to be larger in cells of NRG1tyI mice (Q_e=1.05 ± 0.23 pC, *n*=8 cells) than in those of WT mice (Q_e=0.59 ± 0.07 pC, *n*=13 cells), although this did not quite reach statistical significance (p=0.06, Mann–

Whitney test; Figure 3.5C left). In contrast, analysis of mean Q_i revealed no difference between pyramidal cells of each genotype (WT: Q_i=0.87 ± 0.13 pC, *n*=13 cells vs. NRG1tyI: Q_i=0.91 ± 0.12 pC, *n*=8 cells; p=0.874, independent samples t test; Figure 3.5C middle). The balance of excitation and inhibition was further investigated by comparing the Q_e/Q_i ratio in each cell. Importantly, there was a significant difference in the Q_e/Q_i ratio between pyramidal cells in NRG1tyI (Q_e/Q_i=1.15 ± 0.15 pC, *n*=8 cells) and those in WT mice (Q_e/Q_i=0.76 ± 0.07 pC, *n*=13 cells; *p*=0.019, independent samples t test). As illustrated in Figure 3.5C (right), excitation exceeded inhibition in the majority of principal cells recorded in NRG1tyI mice, whereas in most pyramidal cells in WT mice the inhibitory input dominated over the excitatory one, in line with previous reports (Oren et al., 2006; Atallah & Scanziani, 2009, see discussion below). To explore whether the difference in the charge transfer resulted from larger or more sustained compound currents, peak compound current amplitudes as well as rise (20–80%) and decay (half amplitude decay) kinetics were analysed next. Custom-written Igor Pro procedures for detection and analysis of PSC parameters (Methods 2.6.1) were kindly made available by Dr Iris Oren. Median values were taken from individual experiments to minimise the effects of outliers. Compound IPSCs received by CA3 pyramidal cells during gamma cycles were of similar median amplitudes in both groups [WT: 51.49 ± 8.12 pA (mean ± SEM); NRG1tyI: 53.51 ± 7.22 pA; statistical comparisons in Table 3.1]. Mean percentile plots (mean of the distributions at every 5^{th} percentile) were also not shifted between groups (Figure 3.5D; note: the data appeared to be normally distributed, therefore the mean, not median, of all data is presented). Furthermore, genotype was not found to have a significant overall effect on the IPSC amplitude ($F_{(1,19)}$=0.33, *p*=0.858, repeated measures ANOVA) unlike percentile ($F_{(1.065,20.238)}$=74.152, *p*<0.001, see Table 3.1 for details). There was no interaction

between the two factors ($F_{(1.065,20.238)}$=0.096, p=0.776). In contrast, genotype had a significant overall effect on compound EPSC amplitude ($F_{(1,19)}$=4.749, p=0.042, repeated measures ANOVA; Figure 3.5D). Interestingly, the interaction between genotype and percentile (main effect of percentile: $F_{(1.209,22.978)}$=53.228, p<0.001) was also close to significance ($F_{(1.209, 22.978)}$=3.818, p=0.056), and simple main effect analysis revealed a significant difference between genotypes in some percentiles larger than the median (65^{th}, 70^{th}, 75^{th}, 80^{th}, 85^{th} and 100^{th}, p<0.05, pairwise comparison with Bonferroni correction). The distributions of median EPSC amplitudes between genotypes did not reach statistical significance [WT: −35.70 ± 3.67 pA (mean ± SEM); NRG1tyI: −54.78 ± 10.76 pA; p=0.06, independent samples t test, Table 3.1]. Note that two NRG1tyI pyramidal cells received very large median compound EPSC amplitudes.

Plots of median EPSC amplitude against median IPSC amplitude showed that in the majority of WT cells (10 of 13), median IPSC amplitudes were larger than EPSC amplitudes (IPSC/EPSC ratio >1; Figure 3.5E). In contrast, only 3 of 8 NRG1tyI mouse cells had an IPSC/EPSC amplitude ratio >1. In the remaining 5 cells, the median compound excitatory phasic input was equal to or larger than the median compound inhibitory phasic input. Although comparison of median IPSC/EPSC amplitude ratios in all cells failed to reach statistical significance (p=0.082, Mann–Whitney U test), the data, taken together, are in line with the finding of increased Q_e/Q_i ratios in transgenic pyramidal cells during CCh-induced gamma oscillations.

Table 3.1 Statistical analyses of PSC properties in NRG1tyI and WT pyramidal cells

	Repeated measures ANOVA with fixed factors genotype (WT, NRG1tyI) and percentile (20, every 5th) (F- and *p*-values)			**T test significance** (*p*-values)
Property	**Genotype**	**Percentile**	**Interaction**	**Medians**
IPSC amplitude (pA)	$F_{(1, 19)}$=0.330 *p*=0.858	$F_{(1.065, 20.238)}$=74.152 *p*<0.001***	$F_{(1.065, 20.238)}$=0.096 *p*=0.776	0.867
EPSC amplitude (pA)	$F_{(1, 19)}$=4.749 *p*=0.042*	$F_{(1.209, 22.978)}$=53.228 *p*<0.001***	$F_{(1.209, 22.978)}$=3.818 *p*=0.056	0.06
IPSC rise time (ms)	$F_{(1, 19)}$=0.005 *p*=0.942	$F_{(2.128, 40.423)}$=558.923 *p*<0.001***	$F_{(2.128, 40.423)}$=2.789 *p*=0.070	0.272
IPSC half decay time (ms)	$F_{(1, 19)}$=2.171 *p*=0.157	$F_{(1.006, 19.122)}$=32.663 *p*<0.001***	$F_{(1.006, 19.122)}$=0.771 *p*=0.392	0.001**
EPSC rise time (ms)	$F_{(1, 19)}$=0.922 *p*=0.349	$F_{(1.444, 27.434)}$=859.688 *p*<0.001***	$F_{(1.444, 27.434)}$=0.477 *p*=0.564	0.237
EPSC half decay time (ms)	$F_{(1, 19)}$=1.117 *p*=0.304	$F_{(1.012, 19.225)}$=42.212 *p*<0.001***	$F_{(1.012, 19.225)}$=0.564 *p*=0.464	0.348

NRG1tyI: *n*=8; WT: *n*=13. Distributions across 20 percentiles (every 5th percentile) were compared with repeated measures ANOVAs. In those cases where the assumption of sphericity was violated, a Greenhouse–Geisser correction was applied (see Methods). Independently, medians were compared with independent samples t tests. * p<0.05; ** p<0.01; *** p<0.001

Overall, compound EPSCs of recordings from NRG1tyI mouse cells exhibited significantly larger cycle-to-cycle amplitude fluctuations than those from WT [WT:62.52 ± 5.13% (mean CV ± SEM), median 57.93%, *n*=13 cells; NRG1tyI: 68.29 ± 4.47%, median 64.24%, *n*=8; *p*=0.03, Mann–Whitney U test]. There was considerable variability of compound EPSC amplitudes in both genotypes (>60%). In contrast, IPSC amplitudes fluctuated less in both genotypes, and showed no significant difference between groups according to the CVs of IPSC amplitudes (WT: 49.87 ± 1.23%, median 49.33%; NRG1tyI: 51.88 ± 1.82%, median 50.46%; *p*=0.352, independent samples t test). This is in line with the earlier finding that cycle-to-cycle field amplitude fluctuations were similar between transgenic and WT mice (Section 3.2.1), because the waveform of the field potential primarily reflects inhibitory currents in local pyramidal cells (Oren et al., 2010). Taken together, the finding that the amplitudes of compound EPSCs but not IPSCs were larger and more variable agrees with the overall increased

excitation/inhibition ratio in principal cells of NRG1tyI mice after cholinergic activation. This may also predispose the transgenic network to epileptiform discharge.

Lastly, I investigated the kinetics of compound synaptic events as they reflect the temporal synchronisation of afferent synaptic fibres. Importantly, median compound inhibitory currents in pyramidal neurons of NRG1tyI mice took significantely longer to decay from IPSC peaks to half amplitudes [decay times 10.34 ± 0.53 ms (mean ± SEM)] compared to WT (7.96 ± 0.31 ms; p=0.001). Across all percentiles, decay times tended to be longer in cells of NRG1tyI mice as illustrated in the prominent right-shift of the percentile plot (Figure 3.5F) but the effect of genotype did not reach statistical significance ($F_{(1,19)}$=2.171, p=0.157, repeated measures ANOVA, see Table 3.1). In contrast, median IPSC rise times [WT: 5.57 ± 0.30 ms (mean ± SEM); NRG1tyI: 5.04 ± 0.32 ms; p=0.272, independent samples t test) as well as median EPSC rise times (WT: 3.35± 0.17 ms; NRG1tyI: 3.75 ± 0.33 ms; p=0.237, independent samples t test) and median EPSC decay times (WT: 6.70± 0.31 ms; NRG1tyI: 7.24 ± 0.51 ms; p=0.348, independent samples t test) were unchanged. Percentile plots of EPSC rise and decay times and IPSC rise times also confirm no further difference in the compound current shape between genotypes (Figure 3.5F): Genotype did not have a significant overall effect on any of these three parameters (unlike percentile), and there was no significant interaction between the factors (repeated measures ANOVA, see Table 3.1). This highlights the fact that the difference in inhibitory decay times is unlikely to have resulted from variable electronic (dendritic) filtering (McBain and Dingledine, 1992), particularly as inhibitory currents during CCh-induced oscillations are likely to be predominately received at the soma (Mann et al., 2005). Note, however, that some EPSCs in the NRG1tyI cells tended to have longer decay times as indicated by the milder slope of the percentile plot (Figure 3.5F bottom right). To determine whether

larger amplitude EPSCs had a longer decay, I plotted median EPSC amplitudes against median EPSC half-amplitude decay times for the individual experiments. However, no significant correlation was found (NRG1tyI: ρ=0.238, *p*=0.570, *n*=8; WT: ρ=0.115, *p*=0.707, *n*=13, Spearman's correlation; Figure 3.5F bottom right).

The selective effect on IPSC decay time was confirmed by analysing only prominent PSC events (defined as those that exceeded the median of all PSC amplitudes in individual experiments). This higher threshold should eliminate possible misdetections of noise as small events in the previous analysis. Overall, this analysis yielded the same result: median IPSC decay times but not median IPSC rise times, nor EPSC kinetics proved to be significantly different between genotypes (data not shown).

In summary, compared with WT, compound inhibitory currents in NRG1tyI mouse pyramidal cells were no larger in amplitude but decayed significantly slower. The slower IPSC kinetics are reflected in the slower field oscillations, because the sum of perisomatic inhibitory currents constitute most of the field response (Mann et al. 2005; Oren et al., 2010). Together with larger, more variable (but kinetically unchanged) compound excitatory currents in NRG1tyI pyramidal cells, these findings are in agreement with the finding of the altered balance of excitation and inhibition in the NRG1tyI network.

3.3 Discussion

The work described in this chapter aimed at exploring whether neurobiological changes related to cognitive processing occur in the hippocampal network of NRG1tyI mice. Employing an *in vitro* model of gamma oscillations, I studied CCh-induced synchronised network activity in the CA3 area of NRG1tyI mice and WT littermates.

The principal results may be summarised as:

1. The peak frequency of CCh-induced field oscillations was significantly lower in NRG1tyI mouse slices than in age-matched WT mouse slices. This difference was significant in mice as young as one month.
2. The CA3 hippocampal network of NRG1tyI mice had a higher tendency to develop epileptiform activity upon exposure to CCh than that of WT. The increased incidence was already present in 1–2-month-old NRG1tyI mice and did not deteriorate with age.
3. Individual CA3 pyramidal cell firing during CCh-induced rhythmic gamma oscillation in NRG1tyI mice was as efficient and temporally precise as in WT.
4. During CCh-induced rhythmic activation, the ratio of excitatory to inhibitory charge transferred in an oscillatory cycle was significantly larger in pyramidal cells of NRG1tyI mice than in those of WT mice. Overall larger and more variably amplitude compound excitatory inputs may have contributed to this. Inhibitory synaptic inputs to CA3 pyramidal cells were unaltered in amplitude but decayed more slowly in cells of NRG1tyI mice.

All these changes in the CA3 hippocampal network of NRG1tyI mice occur prior to any detectable cognitive deficits (10 months, Deakin et al., 2012).

3.3.1 CCh-induced rhythmic network activity

Application of carbachol by superfusion evoked field potential oscillations in the CA3 network of WT mice with peak frequencies (25–30 Hz) that correspond to the lower range of gamma frequency oscillations observed *in vivo* (~25-140 Hz; Colgin et al., 2009). The lower band (<30 Hz) is sometimes also referred to as the ‘β2 range’ (Whittington, 2008). Despite the low frequency, the mechanisms underlying the

generation and maintenance of oscillations are likely to be similar to *in vivo* gamma oscillation because the rate and temporal features of pyramidal cell firing resemble those of *in vivo* gamma oscillations (Csicsvari et al., 2003; Senior et al., 2008). Furthermore, all aspects of the field potential oscillation induced here (e.g. field peak frequency, field power, stability of oscillations) are consistent with previous *in vitro* studies on CCh-induced gamma oscillations in CA3 hippocampus (Mann et al., 2005; Oren et al., 2006; Fisahn et al., 2009; Hajos et al., 2009; Gulyas et al., 2010). The frequency of CCh-induced oscillations has been reported to be linearly dependent on the temperature of the recording bath (Ecker et al., 2001; Dickinson et al., 2003; Fisahn et al., 2009; Gulyas et al., 2010) so it may be expected that higher recording temperatures would have increased the oscillation frequency. Sub-physiological recording temperatures were chosen deliberately to reduce the metabolic rate in high energy demanding fast-spiking interneurons (Gulyas et al., 2006; Whittaker et al., 2011), and to achieve clearer and more stable oscillatory activity in the submerged recording chamber (Dickinson et al., 2003; Gulyas et al., 2010). Similar recording temperatures (~30°C) elicited similar peak frequencies (25–30 Hz) in a kainate-induced oscillation paradigm (Fisahn et al., 2009). Notably, in the present experimental set-up, field potential oscillations in WT mouse slices were stable in both frequency and power, from within 5 min of immersion in CCh and throughout the recording period (Figures 3.1B,C and 3.2B,C; Table A1). This contrasts with previous observations (Gulyas et al., 2010; Heistek et al., 2010 but see Hajos et al., 2009).

With regards to the underlying synaptic currents in CA3 pyramidal cells, compound excitation and inhibition have been reported to fluctuate in balance during each oscillatory cycle: the inhibitory charge was found to be ~4× larger than the excitatory charge (Oren et al., 2006), and the amplitude of the *in vitro* and *in vivo*

recorded inhibitory conductance was ~4–5× larger than the excitatory conductance (see Figures 2E & 5E in Atallah & Scanziani, 2009). In contrast, in the present study, the median IPSC amplitude was on average only ~1.4× larger than the median EPSC amplitude in WT pyramidal cells. Similarly, the median inhibitory charge was on average ~1.5× larger than the median excitatory charge. While the Q_e values reported here are consistent with a previous report (Oren et al., 2006: Q_e=0.56 ± 0.063 pC; here: Q_i=0.59 ± 0.07 pC), Qi values varied significantly (Oren et al., 2006: Qi=3.2 ± 0.30 pC; here: Q_i=0.87 ± 0.13 pC). The difference in the IPSC/EPSC ratio might partially stem from different recording conditions, in particular a difference in the electrochemical driving force for GABA-A receptor-mediated chloride currents. In fact, both previous studies, Oren et al. (2006) and Atallah & Scanziani (2009), used a lower Cl^- concentration (3 mM vs 8 mM) in the intracellular filling solution, which is likely to result in a stronger (by ~26 mV according to Nernst equation; see Methods 2.4.1) electrochemical driving force for IPSCs when recorded at the estimated reversal potential for EPSCs, 0 mV. As a consequence, the IPSC/EPSC ratios reported in this study might be smaller, but importantly, as outlined above, the synaptic mechanisms underlying the generation of oscillations are still likely to be similar.

3.3.2 Altered CCh-induced network activity in NRG1tyI mice

Field potential oscillations in slices from NRG1tyI mice were of markedly lower frequency than those in slices from WT mice. Peak frequencies ranged in the beta/ lower gamma frequency band (~13–30 Hz). However, individual pyramidal cells fired as efficiently (i.e. similar firing rate) and with the same temporal accuracy as pyramidal cells of WT mice and consistent with previous reports (Fisahn et al., 1998; Oren et al., 2006; Gulyas et al., 2010). Thus the principal mechanisms underlying the generation of oscillations in the hippocampal network of transgenic mice are likely to be similar to

those in WT mice. Field oscillatory power tended to be larger in slices from NRG1tyI mice but was also more variable across slices, making interpretation more difficult (see Section 3.3.3.2).

To the best my knowledge, the effects of postnatal Nrg1tyI over-expression on gamma oscillations has not previously been explored, either *in vitro* or *in vivo*. Acute application of NRG1β peptide has been shown to increase the power of kainate-induced gamma oscillations in area CA3 without modulating oscillation frequency (Fisahn et al., 2009). However, short- (=acute) and long-term (=genomic) effects of NRG1 may be quite distinct. For example, the length of exposure to soluble NRG1 was shown to influence the direction of postsynaptic receptor expression: Fischbach and colleagues reported an increase in nAChR expression and synaptic currents following 2–4 days of treatment with NRG1 peptide (Liu et al., 2001), but a decrease in nAChR-mediated currents upon immediate exposure to the same NRG1 peptide (Chang & Fischbach, 2006). Moreover, NRG1 domains other than the core receptor-binding EGF-like domain could also elicit variable effects (Harrison & Law, 2006): the N-terminal Ig-type I domain as well as the "1" stalk of the full length NRG1 protein expressed in the NRG1tyI mice are likely to influence extracellular matrix binding and protein localisation. This might affect the network differently to the 'core NRG1β' peptide (the EGF-like domain; Fisahn et al., 2009). Indeed, core NRG1 and full length NRG1 were observed to elicit slightly different effects (Abe et al., 2011). In agreement with this, behavioural phenotypes of various NRG1 hypomorphic mice differed (even exhibiting opposite effects), depending on which NRG1 isoform and protein domain was targeted for genetic manipulation (reviewed in Deakin et al., 2009). Lastly, kainate and carbachol induce gamma oscillations by different tonic excitation mechanisms (Bartos et al., 2007). Interestingly, carbachol-induced oscillations (unlike kainate-induced

oscillations) are *not* affected by acute NRG1 treatment (Fisahn et al., 2009). I applied the cholinergic model of gamma oscillations because activation of mAChRs is believed to best reflect *in vivo* conditions (Fisahn et al., 1998), by mimicking elevated ACh levels during exploratory behaviour at which *in vivo* gamma oscillations occur (Hajos & Paulsen, 2009).

3.3.3 Mechanisms underlying altered network activity in NRG1tyI mice

Aberrant NRG1tyI signalling altered the excitation/inhibition balance in the hippocampal network. Larger and more variable (cycle-to-cycle amplitude variability) compound excitatory inputs in CA3 pyramidal cells in NRG1tyI mice tended to transfer more charge per oscillatory cycle. This strongly suggests that excitation is dysfunctional in the NRG1tyI network after cholinergic activation, and unable to recruit a balanced degree of inhibition. Increased excitation, unbalanced by inhibition, is likely to underlie the greater susceptibility to epileptiform discharges in the transgenic CA3 network (in the presence of CCh). Epileptiform activity also indicates hyper-synchronous pyramidal cell firing. Yet, during gamma activity, the absolute rate and pattern of pyramidal cell firing was not observed to be altered, even though firing tended to occur more frequently *per oscillatory cycle* in transgenic mice (Section 3.2.3.1). Greater excitation of pyramidal cells is unlikely to have resulted from cholinergic activation, because V_m was similar for the two genotypes (Section 3.2.3.2). It is therefore unlikely that NRG1 over-expression would have increased AChR density in pyramidal cells, as has been reported at the neuromuscular junction (Martinou et al., 1991) and in cultured GABAergic cells (Liu et al., 2001) following acute NRG1 treatment. Aberrant NRG1 signalling could modify synaptic connectivity between pyramidal cells, although this should be mediated through ErbB receptor isoforms (e.g. ErbB2/3 in pyramidal cells,

Gerecke et al., 2001) other than ErbB4 (Yau et al., 2003; Vullhorst et al., 2009; Fazzari et al., 2010). I will examine excitatory synapses in pyramidal cells further in Chapter 5.

Importantly, the altered excitation/inhibition ratio further illustrates that inhibition is not able to counterbalance the increased excitation in NRG1tyI mice. It thus appears that the recurrent inhibitory feedback loop, which plays a major role in the generation of gamma oscillations (Introduction 1.3.2) and efficiently balances phasic excitation in physiological networks, may be dysfunctional in the transgenic network. In fact, the findings of prolonged field oscillation cycles and phasic inhibitory compound currents argue for a malfunction of the inhibitory component of the feedback loop. GABAergic inhibitory synapses from PV-expressing PTIs (BCs and AACs) to CA3 pyramidal cells are of primary interest because their current kinetics pace the CA3 hippocampal network (Mann et al., 2005; Atallah & Scanziani, 2009; Gulyas et al., 2010; Oren et al, 2010). Prolonging synaptic GABAergic current kinetics pharmacologically (GABA-A receptor modulation) effectively modulates the frequency of CCh-induced gamma oscillations (Fisahn et al., 1998; Heistek et al., 2010). In addition, PV+ interneurons are likely targets of aberrant NRG1 signalling because they strongly express ErbB4 receptors (Vullhorst et al., 2009; Fazzari et al., 2010), and their synaptic development and maturation is controlled by NRG1/ErbB4 signalling (Fazzari et al., 2010; Ting et al., 2011). Taken together, altered kinetics of synaptic inhibition from PV+ cells might well contribute to the slower gamma oscillation frequency observed in NRG1tyI mice. The dynamics of inhibitory GABAergic synapses, from PV+ PTIs to CA3 pyramidal cells, are examined further in Chapter 4.

3.3.3.1 Possible interaction between NRG1 and AChR signalling?

The original NRG1 report described its effects on cholinergic transmission at the neuromuscular junction (Usdin & Fischbach, 1986). Acute treatment with NRG1 has

also been reported to increase ACh-induced inward currents in hippocampal GABAergic neurons by inducing α7 subunit-containing postsynaptic nAChRs (Liu et al., 2001; Zhong et al., 2008), so the question arises as to whether NRG1 over-expression renders PV+ interneurons (in particular those that generate gamma oscillations) more sensitive to cholinergic agonists. In this case, increased tonic AChR-mediated excitation would drive CA3 PV+ interneurons more intensively and strengthen their output to principal cells in NRG1tyI mice. This might contribute to the sustained compound inhibition in pyramidal cells of NRG1tyI mice.

Although interneuronal firing was not monitored during rhythmic oscillations (lack of suitable PV+ reporter mice, see Chapters 4 and 5), several observations argue against a contribution of increased AChR levels to the slower oscillations. Firstly, CCh is an agonist of both mAChRs and nAChRs, but tonic activation of mAChRs is thought to predominate in the induction of *in vitro* oscillations (Fisahn et al., 2002), whereas NRG1 primarily affects nAChR-, but not mAChR-mediated currents (in str. radiatum CA1 interneurons, Chang & Fischbach, 2006). A synergistic effect of CCh and NRG1 is unlikely, particularly because CCh probably triggers synchronised network activity primarily by stimulating pyramidal cells rather than interneurons (Fisahn et al., 1998; Fisahn et al., 2002). Importantly, I found that pyramidal cells in WT and NRG1tyI mice were similarly depolarised by CCh (see above). Secondly, PV+ axon terminals express mAChRs (M_2-type; Freund & Katona, 2007; Szabo et al., 2010) not nAChRs (but see Krenz et al., 2001) but there is no evidence that NRG1 can alter interneuron output through mAChRs. Thirdly, even if NRG1 did affect GABA release from PV+ interneurons through mAChRs, application of CCh has been shown to decrease GABA release from PV-containing fast-spiking BCs (Gulyas et al., 2010; Szabo et al., 2010). Therefore, a potentially enhanced effect of CCh by NRG1 would be expected to reduce,

not increase, GABA release. On its own, this would not be expected to prolong compound IPSCs. Taken together, the postulation that the slower oscillations in NRG1tyI mice result from altered levels of AChRs is not supported by the experimental evidence. In addition, the fact that fEPSP after-discharges were observed in slices from NRG1tyI mice independently of CCh (see Introduction 1.4.1) implies that NRG1 over-expression changes the hippocampal network through AChR-independent pathways. In Chapters 4 and 5, I examine the synaptic mechanisms of the inhibitory feedback loop involved in gamma oscillations.

3.3.3.2 Field power of gamma oscillations

While NRG1tyI over-expression robustly affected oscillation frequency, changes in field power were more variable across the slices, and these are more difficult to interpret. Overall, there was a trend to larger field power in slices from transgenic mice; this became significant in slices from young transgenic mice after 30 min exposure to CCh (Figure 3.2C). In general, biological systems might be expected to have more energy at lower frequencies (red noise). Earlier studies on CCh-induced gamma oscillations have also reported negative correlations between frequency and power (Ecker et al., 2001; Buzsaki & Draguhn, 2004; Oren et al., 2006).

Many factors might account for the variability of field power between individual experiments, including technical issues, such as the survival of fast spiking PV+ interneurons during the preparation of acute slices. Due to their high metabolic demands, PV+ BCs are more dependent on the respiratory chain function than pyramidal cells (Buzsaki et al., 2007; Whittaker et al., 2011). In fact, BCs contain higher levels of cytochrome *c* oxidase and more mitochondria than pyramidal cells (Gulyas et al., 2006). Given the primary role of BCs in gamma oscillations, any compromise of their survival during acute slice preparation will decrease *in vitro* field

oscillation power. Slices from older mice are more vulnerable (Vreugdenhil & Toescu, 2005). Despite optimised slicing conditions, including the use of sucrose/ NaCl cutting solution to reduce ATP consumption by $Na^+/K^-{}^+$ATPases (see Methods 2.3; Hajos et al., 2009), the average field power was lower in WT slices from old mice than in those from young mice. Also, variability in the depth of the field-recording electrode within the 400 µm thick slice could account for differences in detected gamma power. Deeper recording sites might access a more intact network with consequently higher amplitudes of gamma oscillation (Kann et al., 2011). Finally, the amplitude of oscillations has been reported to increase with increasing CCh concentration (Fisahn et al., 1998). This might, at least in part, explain the variability in power I detected across slices, as different CCh concentrations (5–20 µM) were used to drive the network.

The reason for the increase in field power with time in CCh (in young NRG1tyI mice) is unclear; however, it occurred independent of CCh concentration, and it did not correlate with the likelihood of developing epileptiform discharges in any of the slices (data not shown). Technical reasons, such as changes in local extracellular space volume and increase in tissue resistance with time, could be contributory factors, although none of these can account for the difference between genotypes. Alternatively, NRG1 might trigger plasticity-induced processes during CCh-induced gamma oscillations, possibly by a delayed effect on AChRs (see above), but this remains to be investigated.

The more pronounced effect on oscillatory frequency rather than field power in NRG1 over-expression was unexpected, because in schizophrenic patients cortical gamma oscillations are typically *reduced* in amplitude (reviewed in Gonzalez-Burgos et al., 2010; Uhlhaas & Singer, 2010). However, one study has reported that the frequency of visual stimuli-evoked gamma oscillations were lower in schizophrenic patients than

in healthy individuals (Spencer et al., 2004). This raises the question as to whether NRG1tyI mice are, in fact, a face-valid model of schizophrenia (see Chapter 6; Deakin et al., 2012). On the other hand, many animal models related to schizophrenia show inconsistent changes in gamma-band oscillations: either increased (Pinault, 2008; Roopun et al., 2008) or decreased (Cunningham et al., 2006; Zhang et al., 2008; further discussed in Chapter 6). In fact, gamma oscillation changes are likely to be brain-region-specific (Roopun et al., 2008), and NRG1 over-expression may modulate gamma oscillations in other cortices differently.

3.3.4 Epileptiform discharges in NRG1tyI mice

Slices from NRG1tyI mice were more prone to develop epileptiform bursts in the presence of CCh, in line with the altered excitation/inhibition ratio in the CA3 network. Interestingly, impaired output of fast-spiking interneurons has been causally linked with the occurrence of epileptiform seizures (Lau et al., 2000; Ogiwara et al., 2007), thus justifying the focus on PV+ interneurons in Chapter 4. Others have reported that loss of dendritic inhibition reduces seizure threshold, while perisomatic inhibition prevents continuous epileptiform activity (Cossart et al., 2001). From this, one could hypothesise that epileptiform activity occurs in NRG1tyI mouse slices in which dendritic inhibition is too compromised (e.g. severed by the slicing procedure) to compensate for the impaired perisomatic inhibition.

Interestingly, NRG1/ErbB4 signalling has recently been associated with epilepsy (Li et al., 2012; Tan et al., 2012). However, in contrast to my data, deficient rather than augmented signalling through ErbB4 receptors led to epileptiform discharges in ErbB4$^{-/-}$ mice (Fisahn et al., 2009). In addition, acute application of exogenous NRG1 was found to be neuroprotective, reducing generalised seizures in control but not in transgenic

mice whose PV+ cells were deficient in ErbB4 (Li et al., 2012; Tan et al., 2012). Again, acute and chronically enhanced NRG1 signalling might act differently on the network. Interestingly, mRNA expression of NPY, a protein with anti-epileptic function (Sorensen et al., 2009) and a marker for some dendritic-targeting interneurons in CA1 hippocampus (Klausberger et al., 2004; Fuentealba et al., 2008), was reported to be upregulated in NRG1tyI mice (Deakin, 2009). Whether this reflects increased expression in individual cells or increased numbers of NPY+ interneurons is unclear. It is also unknown if this is a primary or secondary effect on the observed network behaviour: upregulation of NPY+ interneurons might compensate for dysfunction in other interneurons types.

3.3.5 Could altered gamma oscillation underlie the cognitive deficits in NRG1tyI mice?

The significant change in gamma oscillation peak frequency was independent of age, and it occurred in mice as young as one month old. This was surprising because significant cognitive defects were not evident until 10 months (Deakin et al., 2012). This apparent temporal discrepancy might reflect the greater sensitivity of the *in vitro* oscillation model (subtle cellular changes in the neuronal network might arise before physiological information processing is significantly compromised). It is conceivable that cognitive impairment only emerges in NRG1tyI mice when additional (possibly age-related) factors have compounded the existing altered gamma oscillation in area CA3. Besides hippocampal gamma oscillations, persistent cortical up/down state activity and neuronal communication between brain regions are also implicated in intact working memory (Introduction 1.3.3; Moran & Huang, 2011). It is possible that these only deteriorate in adult NRG1tyI mice, and thus only then give rise to spatial working memory deficiency (see Chapter 6). However, it is also possible that the alterations in

gamma oscillations observed here are, in fact, not related to the cognitive deficit observed in old NRG1tyI mice. Note that *in vitro* gamma oscillations were not studied in 10-month-old mice because a network deficit was already detected in pre-symptomatic, younger mice. It was therefore deemed unnecessary to repeat the study in older mice, especially given the additional costs and time required to breed and maintain mice to that age.

The late emergence of cognitive defects conflicts with the observation that cognitive impairment in human schizophrenic patients is often present before (or at) the first psychotic episode during adolescence (Rund et al., 2004). Hence, NRG1tyI mice might not be a sufficiently accurate model of schizophrenia (lacking face validity, as discussed in Deakin et al., 2012), although they still do provide a suitable tool to further our understanding of the neurobiology of NRG1/ErbB4 signalling.

Figure 3.1 CCh-induced oscillations in 3–6-month-old WT and NRG1tyI mice.

(A) Sample traces (low-pass filtered at 200 Hz) of the cholinergically-induced field potential oscillations recorded in the CA3 pyramidal cell layer, in a slice from a 4.5-month-old WT mouse (left), and in a 3-month-old NRG1tyI mouse slice (right). Below: Comparison of the corresponding power spectral densities (PSD) demonstrated lower peak frequency in NRG1tyI mouse slices. Power was sampled as the area under the power spectral density curve between 10 and 40 Hz.

(B) Box plots of all recordings in slices from older mice (3–6 months) show that peak frequencies were consistently lower in slices from NRG1tyI mice compared to WT. The whiskers indicate the 90^{th} and 10^{th} percentile of the data; dots represent the 5^{th} and 95^{th} percentile (if data points available); dashed lines represent the mean. The plot on the left summarises the frequencies obtained from the first ~60 s recording in every slice (between 5 and 70 min after bathing in CCh). Right: Lower peak frequencies were observed at all times that gamma oscillations were probed (see Table A1). Note that the number of slices varies in each time window because field potential oscillations were not always probed repeatedly in every slice but at variable 1–3 time points per slice.

(C) The field power of oscillations in the CA3 network tended to be larger in slices from transgenic mice compared to WT, but this did not reach statistical significance in the left plot which summarises the field power of the first recording in each slice (p=0.291, Mann–Whitney U test). Genotype did, however, have an overall significant effect on the field power across the different time windows at which oscillations were probed (right plot, see Table A1). Note, however, that the right plot incorporates repeated measures in some but not all slices. *p<0.05, ** p<0.01; n refers to the number of slices.

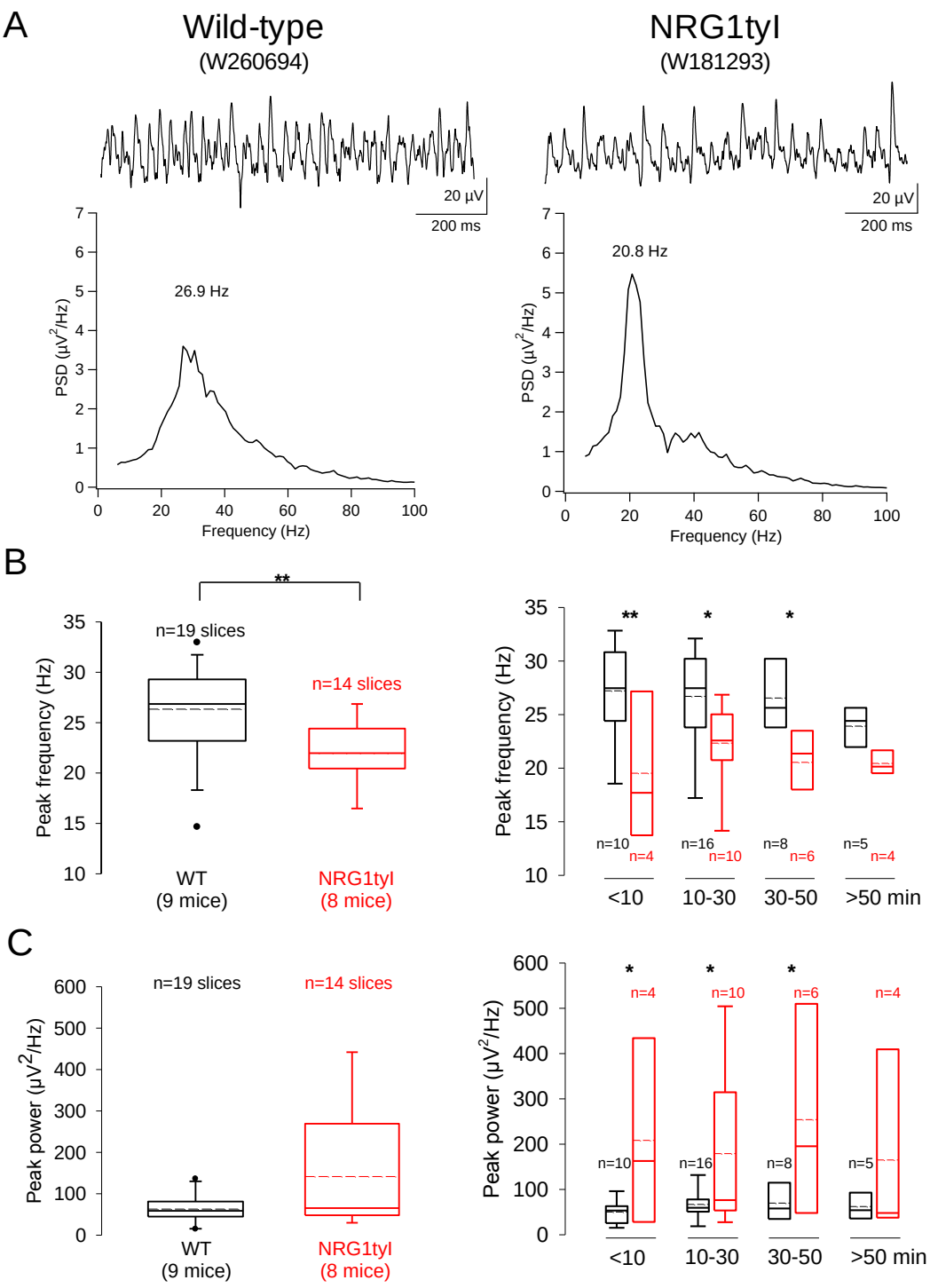

A
Wild-type
(W260694)
NRG1tyI
(W181293)
20 µV
200 ms
26.9 Hz
20.8 Hz
PSD (µV²/Hz)
Frequency (Hz)
B
Peak frequency (Hz)
n=19 slices
n=14 slices
WT
(9 mice)
NRG1tyI
(8 mice)
**
*
n=10
n=4
n=16
n=10
n=8
n=6
n=5
n=4
<10
10-30
30-50
>50 min
C
Peak power (µV²/Hz)

Figure 3.1

Figure 3.2 CCh-induced oscillations in 1–2-month-old WT and NRG1tyI mice.

(A) Sample traces (low-pass filtered at 200 Hz) illustrating gamma oscillations recorded in a slice of a 1-month-old WT (left) and a 1-month-old NRG1tyI mouse (right). The corresponding power spectral densities (PSD) confirm lower mean peak oscillatory frequency in slices from transgenic mice. Note the second harmonic (around 40 Hz) in the PSD of the recording in the NRG1tyI mouse slice, indicating a less sinusoidal oscillation (Section 3.2.3.1).

(B) Summary box plots (left) present significant difference in the frequencies of the *first* ~60 s long recordings taken in every slice (between 5 and 70 min after bathing in CCh). Right: Genotype had an overall significant effect on peak frequencies across all times at which gamma oscillations were probed (see Table A1). Note: the number of slices varies in each time window because oscillations were not always probed repeatedly in every slice but at 1–3 variable time points per slice.

(C) Box plots of field powers (left) summarising the field oscillatory power of the first recordings taken in every slice (5–70 min after bathing in CCh). Note the variability across slices. The difference between genotypes fails to reach statistical significance (p=0.167, Mann–Whitney U test). However, the plot on the right reveals that peak gamma power increased to significantly larger values in recordings from transgenic mice after 30 min in CCh (compared to slices from WT mice, p<0.05, see text and Table A1 for statistical analyses). Box plot whiskers, outliers and mean as in Fig 3.1. *p<0.05, **p<0.01, ***p<0.001; n refers to the number of slices.

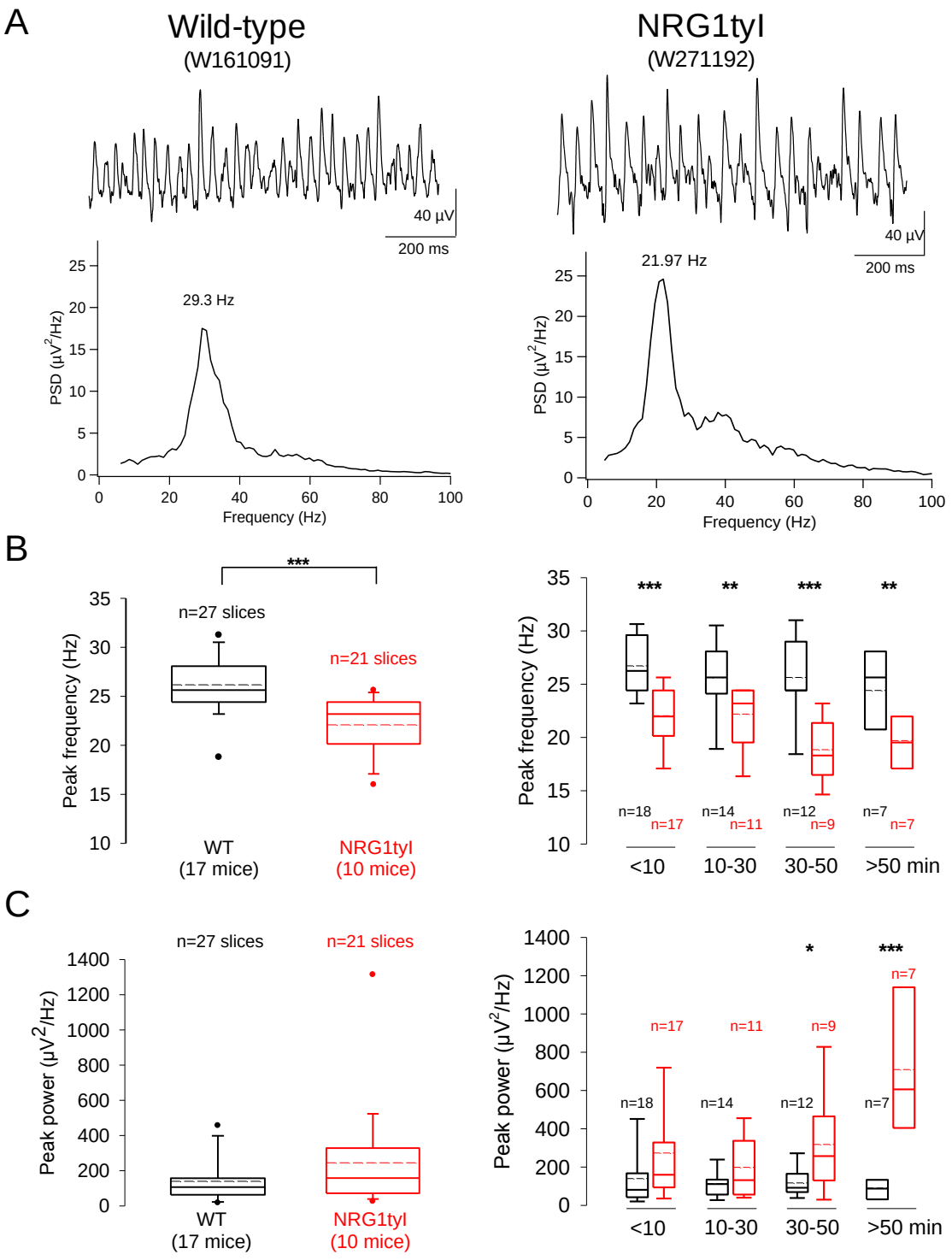

A
Wild-type
(W161091)
NRG1tyI
(W271192)
40 µV
200 ms
29.3 Hz
21.97 Hz
PSD (µV²/Hz)
Frequency (Hz)
B
***
n=27 slices
n=21 slices
Peak frequency (Hz)
WT
(17 mice)
NRG1tyI
(10 mice)
**
n=18
n=17
n=14
n=11
n=12
n=9
n=7
<10
10-30
30-50
>50 min
C
Peak power (µV²/Hz)
*

Figure 3.2

Figure 3.3 Slices from NRG1tyI mice are more prone to epileptiform activity.

(A) A.i: Sample field potential traces during baseline (top) and following application of 20 μM Carbachol (bottom) in a NRG1tyI mouse slice: In this experiment cholinergic activation immediately evoked interictal and ictal epileptiform field potential discharges. A.ii: Slice from another NRG1tyI animal in which interictal-like population discharges occurred occasionally during ongoing gamma oscillations after prolonged exposure to CCh (>80 min of 10 μM CCh).

(B) Epileptiform discharges were more frequent when slices were exposed to a higher concentration of CCh (10 μM in slices from young mice, 20 μM for old mice).

(C) Pie charts of all slices recorded in WT (white) and NRG1tyI (red) mice illustrate the percentage of slices in which bath-application of 10–20 μM CCh resulted in robust gamma oscillations (solid), immediate field epileptiform activity (single-lined) or initial gamma oscillations that gradually developed epileptiform discharges during prolonged exposure of CCh (at least 30 min but up to 80 min; crossed). C.ii: The incidence of epileptiform events was lower when CCh concentration was reduced to 5 μM CCh but still more than 25% of slices from NRG1tyI mice displayed epileptiform activity either immediately or during prolonged exposure to CCh.

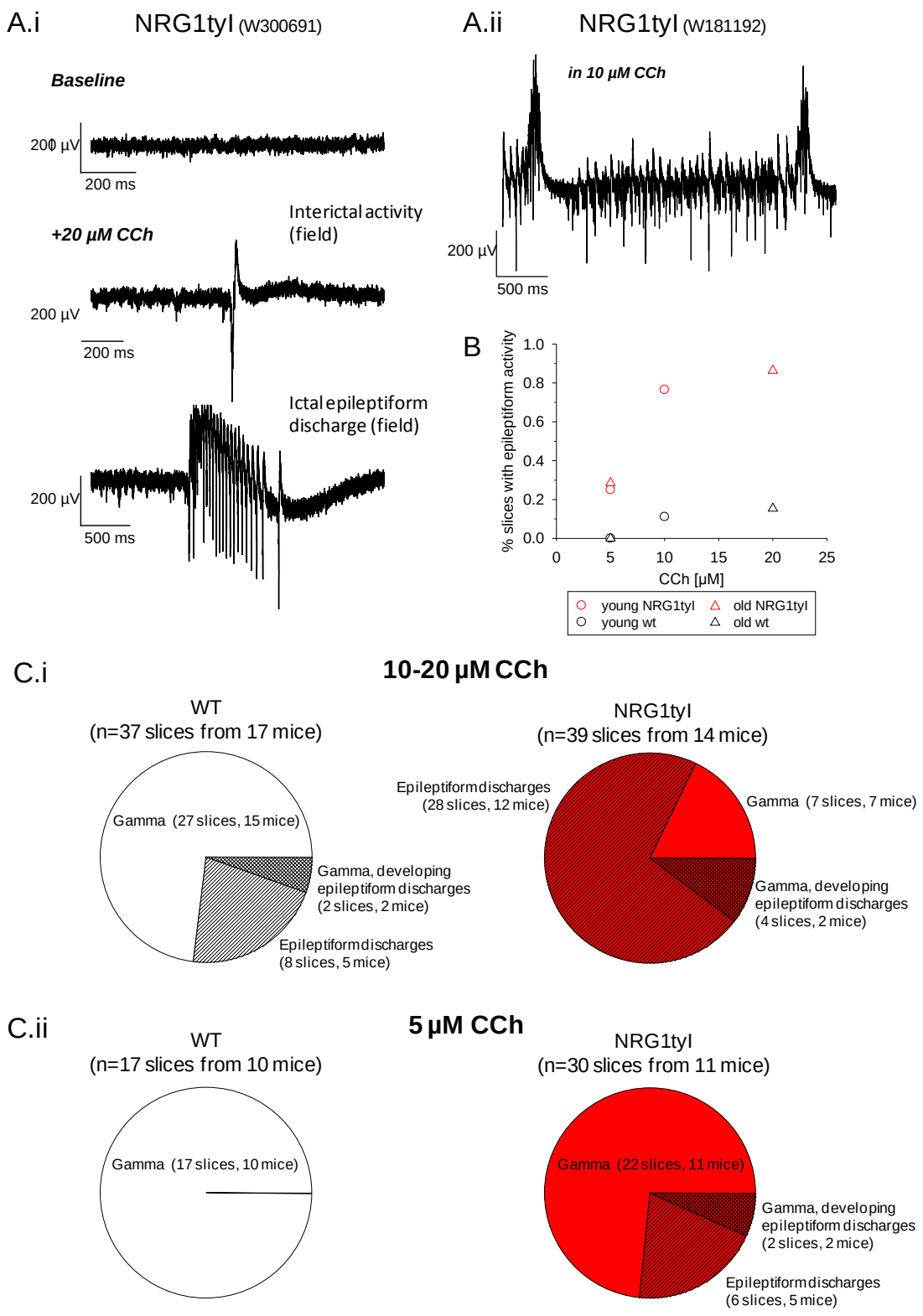

A.i
NRG1tyI (W300691)
Baseline
200 µV
200 ms
+20 µM CCh
Interictal activity (field)
200 µV
200 ms
Ictal epileptiform discharge (field)
200 µV
500 ms
A.ii
NRG1tyI (W181192)
in 10 µM CCh
200 µV
500 ms
B
% slices with epileptiform activity
1.0
0.8
0.6
0.4
0.2
0.0
0
5
10
15
20
25
CCh [µM]
young NRG1tyI
old NRG1tyI
young wt
old wt
C.i
10-20 µM CCh
WT
(n=37 slices from 17 mice)
Gamma (27 slices, 15 mice)
Gamma, developing epileptiform discharges (2 slices, 2 mice)
Epileptiform discharges (8 slices, 5 mice)
NRG1tyI
(n=39 slices from 14 mice)
Epileptiform discharges (28 slices, 12 mice)
Gamma (7 slices, 7 mice)
Gamma, developing epileptiform discharges (4 slices, 2 mice)
C.ii
5 µM CCh
WT
(n=17 slices from 10 mice)
Gamma (17 slices, 10 mice)
NRG1tyI
(n=30 slices from 11 mice)
Gamma (22 slices, 11 mice)
Gamma, developing epileptiform discharges (2 slices, 2 mice)
Epileptiform discharges (6 slices, 5 mice)

Figure 3.3

Figure 3.4 CA3 pyramidal cell firing during gamma oscillations.

(A) Representative 1 kHz high-pass filtered field potential recordings from slices of a WT (left) and a NRG1tyI mouse (right). Downward deflecting spike-like components were detected (arrows) by a simple threshold (dashed line) (Section 3.2.3.1). The number of detected population spikes per 100 cycles did not differ between genotypes across all slices (Mann–Whitney U test) but note the great variability between recordings (right trace).

(B) Simultaneous field potential and cell-attached recording inside str. pyramidale in CA3 hippocampus (left). Representative extracellular field (black) and superimposed cell-attached recordings (blue) in slices obtained from 1-month-old mice (right). Pyramidal cell firing was recorded as current deflections in a voltage-clamped pipette in loose cell-attached mode. Current deflections are truncated.

(C) Histogram comparing the mean firing rate (Hz) of all sampled cells in WT (white) and transgenic mice (red) with scatter plots corresponding to firing rates of individual cells. Statistical analysis revealed no difference between groups (p=0.432, independent samples t test). Error bars represent ± SEM.

(D) Comparison of inter-spike intervals (ISIs) between the two groups (NRG1tyI in red). Median ISIs of individual cells are shown as dots; lines represent the medians of every 5^{th} percentile across all cells per genotype (note, ISI distributions are non-parametric). The dotted area is enlarged (right) to show that cells of NRG1tyI mice tended to fire action potentials at slightly shorter median intervals than WT, but there was no overall significant effect of genotype across all percentiles (repeated measures ANOVA) nor a significant difference between median ISIs (Mann–Whitney U test, see text for details).

(E) Histogram and scatter plots of the strength of cell firing coupling to the field oscillation cycle. The average vector length ($0 > r_firing < 1$) was not different between genotypes (p=0.348, independent samples t test). Only significantly coupled cells (Rayleigh p<0.05) are plotted. Error bars represent ± SEM.

(F) Distributions of the mean angles (degrees) at which significantly coupled cells (7 cells in 6 WT mice, white; 10 cells in 6 NRG1tyI mice, red) fired relative to the low-pass filtered field signal. There was no difference between groups (p=0.902, independent samples t test). A representative cycle-averaged field oscillation is shown for illustration of phase definition.

(G) Phase-coupling strength correlates to oscillatory power in WT slices (white dots, ρ=0.821, p=0.023) but not in NRG1tyI mice (red dots).

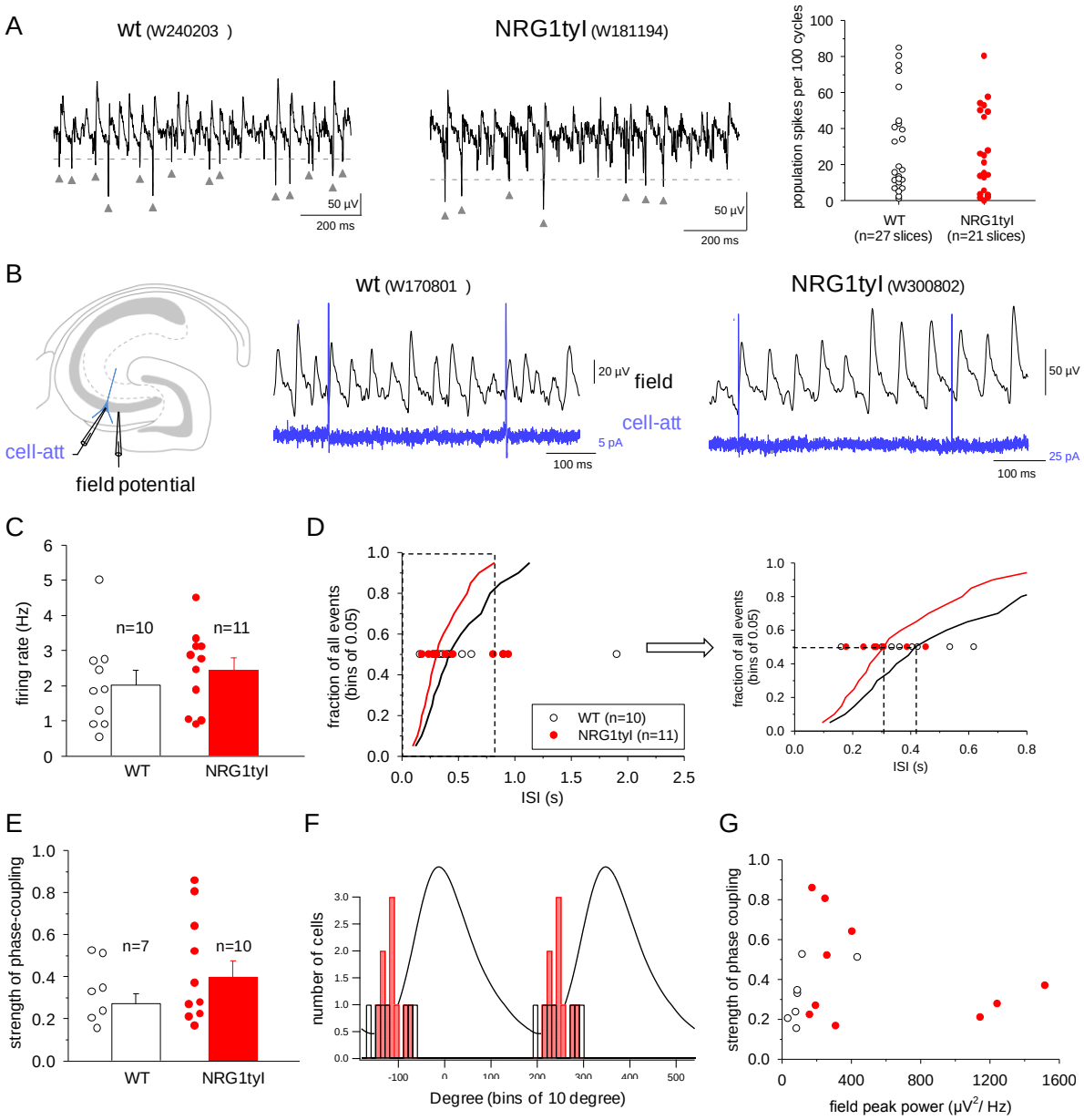

A
wt (W240203)
NRG1tyl (W181194)
50 µV
200 ms
population spikes per 100 cycles
WT
(n=27 slices)
NRG1tyl
(n=21 slices)
B
wt (W170801)
NRG1tyl (W300802)
cell-att
field potential
20 µV
field
cell-att
5 pA
100 ms
50 µV
25 pA
C
firing rate (Hz)
n=10
n=11
WT
NRG1tyl
D
fraction of all events
(bins of 0.05)
WT (n=10)
NRG1tyl (n=11)
ISI (s)
E
strength of phase-coupling
n=7
n=10
F
number of cells
Degree (bins of 10 degree)
G
strength of phase coupling
field peak power (µV²/ Hz)

Figure 3.4

Figure 3.5 Synaptic currents in CA3 pyramidal cells during gamma cycles.

(A) Neurobiotin-filled WT pyramidal cell with characteristic somatodendritic morpholgy (left). Stack image produced with structured illumination microscopy; scalebar 100 µm. High-magnification confocal stack image of dendrites with characteristic mushroom-like spines in also shown (right); scalebar 5 µm.

(B) Representative recordings of GABAergic inhibitory (green) and excitatory glutamatergic (blue) synaptic currents in CA3 pyramidal cells in slices from WT (left) and NRG1tyI mouse (right). The black traces show the corresponding low-pass filtered (200 Hz) extracellular field potential oscillations.

(C) Histogram and scatter plots of the mean phasic excitatory (Q_e, left) and inhibitory charge (Q_i, middle) transferred in an oscillatory cycle, and Q_e,/Q_i ratios (right) in pyramidal cells from WT (white) and NRG1tyI (red) mice. The mean Q_e,/Q_i ratio was significantly different in principal cells of NRG1tyI mice compared to WT ($p=0.019$, independent samples t test). Histograms represent mean ± SEM.

(D, E) Analysis of compound PSC amplitudes.

(D) Percentile distribution plots of IPSC amplitudes (left) and EPSC amplitudes (right) in pyramidal cells of WT (black) and NRG1tyI (red) mice. Dots represent the median amplitude distributions across cells. For every 5^{th} percentile, the mean of all percentiles in each genotype was calculated and plotted. Genotype was found to have an overall significant effect on EPSC but not IPSC amplitudes over all percentiles (see text).

(E) Scatter plot illustrating that median compound IPSC amplitudes were larger than median compound EPSC amplitudes in 10 of 13 WT cells (white, IPSC/EPSC ratio >1), whereas in the majority of NRG1tyI cells (5 of 8) the median excitatory input was equal to or larger than median inhibitory input.

(F) Percentile distribution plots of IPSC (top) and EPSC (bottom) kinetics. Top: median IPSC rise times (20–80%, left) and IPSC decay times (half amplitude decay, right) in all recorded pyramidal cells are shown. Each lines represents the mean of every 5th percentile in each genotype. Genotype did not have an overall significant effect on IPSC rise times or decay times, but IPSC decay times were significantly different at individual percentiles (see text). Median IPSCs were shown to take significantly longer to decay to half amplitude in pyramidal cells of transgenic mice (10.34 ± 0.53 ms) than in pyramidal neurons of WT littermates (7.96 ± 0.31 ms; $p=0.001$). This is illustrated by the prominent right shift of the mean percentile curve. Far right: Scatter plots of median IPSC amplitude versus median IPSC decay time for individual experiments (WT, white; NRG1tyI, red). Bottom: Percentile distribution plots of EPSC rise times (left) and EPSC decay times (right) in all pyramidal cells recorded in both genotypes. Neither median rise times ($p=0.237$) nor median half amplitude decay times ($p= 0.348$) of the excitatory currents in pyramidal cells differed between genotypes. Furthermore, genotype had no overall significant effect on either parameter (see text). There was no clear correlation of median EPSC decay times to median EPSC amplitudes as the scatter plot demonstrates (far right; WT, white; NRG1tyI, red).

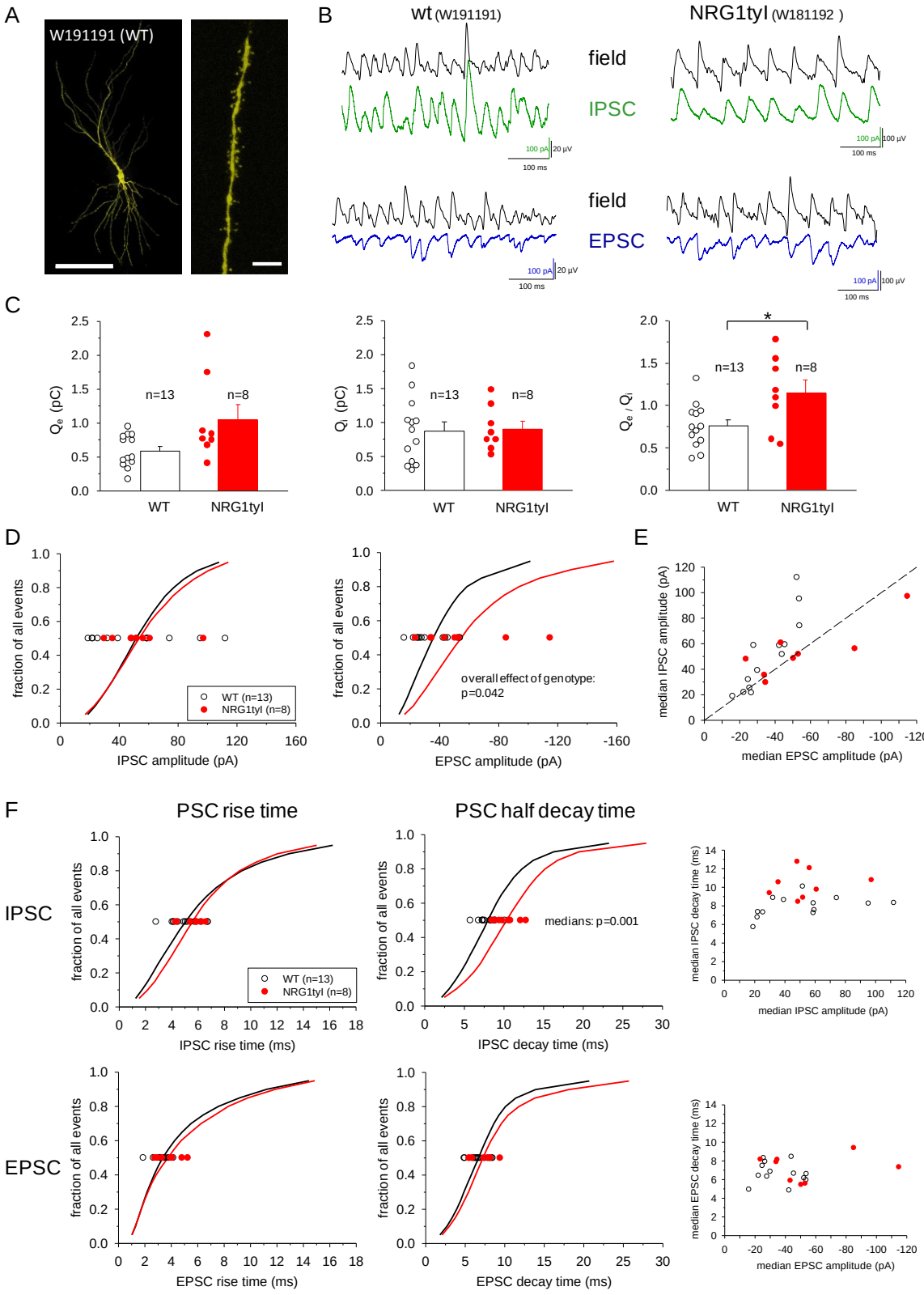

A
W191191 (WT)
B
wt (W191191)
NRG1tyI (W181192)
field
IPSC
field
EPSC
C
n=13
n=8
WT
NRG1tyI
D
fraction of all events
WT (n=13)
NRG1tyI (n=8)
IPSC amplitude (pA)
overall effect of genotype:
p=0.042
EPSC amplitude (pA)
E
median IPSC amplitude (pA)
median EPSC amplitude (pA)
F
PSC rise time
PSC half decay time
IPSC
medians: p=0.001
IPSC rise time (ms)
IPSC decay time (ms)
median IPSC decay time (ms)
median IPSC amplitude (pA)
EPSC
EPSC rise time (ms)
EPSC decay time (ms)
median EPSC decay time (ms)
median EPSC amplitude (pA)

Figure 3.5

4 Synaptic inhibition of CA3 pyramidal cells by PV+ interneurons is unchanged in NRG1tyI mice

4.1 Introduction

As discussed in Chapter 3, the frequency of CCh-induced oscillations is, to a great extent, determined by phasic GABAergic inputs to pyramidal cells. Temporal accuracy and efficiency of GABAergic synapses pace hippocampal pyramidal cells and set the frequency at which the CA3 network oscillates (Fisahn et al., 1998; Traub et al., 2000; Oren et al., 2006; Vida et al., 2006; Mann & Paulsen, 2007). Of all interneuron types, PV+ PTIs play a key role in generating *in vitro* gamma oscillations (Introduction 1.3.2). Malfunction of GABAergic synapses is therefore likely to have a major effect on oscillation frequency and power.

Both types of PV+ PTIs (PV+ BCs and AACs) are suited to control the firing output of pyramidal cells and could potentially contribute to the generation of gamma oscillations (Cobb et al., 1995; Miles et al., 1996). PV+ BCs are mutually connected and have ideal physiological properties to ensure reliable excitatory recruitment (Geiger et al., 1997; Hu et al., 2010) as well as efficient and synchronous GABA release (Hefft & Jonas, 2005); they are thus principally implicated in generating gamma oscillations (reviewed in Bartos et al., 2007). Their large divergence ensures spatiotemporal control of a large ensemble of pyramidal cells (Cobb et al., 1997). The role of AACs is less defined, but they may assist in generating field potential gamma activity given their equally large divergence to AIS of principal cells (Somogyi & Klausberger, 2005). It

should be noted, though, that GABA release from AACs has recently been suggested to contribute less to CCh-induced field gamma oscillations (Gulyas et al., 2010).

There is evidence in the literature that NRG1 signalling can directly affect GABAergic synapse function. For example, acute NRG1 treatment is reported to stimulate GABA release in prefrontal cortex (Woo et al., 2007; Wen et al., 2010). Wen and colleagues implicate presynaptic ErbB4 receptors at PV+ interneurons in mediating this regulatory effect. Acute application of NRG1 also interferes with the expression of GABA-A receptors, but, interestingly, the direction of interference differs between brain regions and cell types: in cultured cerebellar granule cells, NRG1 increased functional GABA-A receptors by inducing expression of the GABA-A receptor β1 subunit (Rieff et al., 1999). In contrast, acute NRG1 treatment of hippocampal slice cultures reduced expression of GABA-A receptor α subunits, without affecting glutamatergic receptors (Okada and Corfas, 2004). The latter study also reported a decrease in mIPSC amplitude but not frequency in CA1 pyramidal cells following acute treatment with NRG1 β1 peptide.

Given the role of phasic GABAergic transmission mediated by PV+ PTIs in gamma frequency oscillations, and the evidence that NRG1/ErbB4 signalling affects GABAergic transmission, I set out to study if postnatal NRG1tyI over-expression selectively alters the properties of these PV+ GABAergic synapses.

4.2 Alternative methodological approaches

To investigate synaptic connectivity between PV+ PTIs and CA3 pyramidal cells, alternative methodological approaches may be used: Recordings of mIPSCs may be suboptimal as they distinguish poorly between afferent interneuron types and the targeting domain of the releasing axon terminals. Similarly, extracellular electrical

stimulation of axons in str. pyramidale is unselective and, in addition to PV+ cell fibres, also activates axons of CB1R+/CCK+ BCs. Although the contribution of CB1R+/CCK+ cell fibres could be suppressed by applying CB1R agonists (Glickfeld et al., 2008), this does not overcome the fact that axons of several other interneuron types may ramify in the pyramidal layer (e.g. local axon clouds of GABAergic projection cells, see Klausberger & Somogyi, 2008). In addition, CB1R agonists would not fully block these fibres but would only suppress CB1R+/CCK+ BC-evoked IPSCs by about ~70% (Glickfeld et al., 2008; Murray et al., 2011). Recordings from connected cell pairs (presynaptic PTIs and postsynaptic CA3 pyramidal cells) would probably provide the most informative experimental configuration to reveal the physiological properties and characteristics of cell type-specific synapses (e.g. Maccaferri et al., 2000; Bartos et al., 2002; Gulyas et al., 2010; Szabo et al., 2010). However, this approach yields low success in CA3 hippocampus without a suitable fluorescent reporter mouse (e.g. PV-eGFP, Meyer et al., 2002; Nkx2.1Cre MADM, Woodruff et al., 2009).

In the absence of a suitable, commercially available reporter mouse (see Chapter 5), I instead employed a novel optogenetic technique that enables selective photostimulation of PV+ interneuron axons in str. pyramidale, and combined it with whole-cell recordings of inhibitory currents in *post hoc* anatomically identified CA3 pyramidal cells (Sohal et al., 2009; Cardin et al., 2010). The first part of this chapter describes the experimental prerequisites (PV expression, suitability of Cre-mouse lines) and how the technique was implemented in NRG1tyI mice crossed to PV-Cre mice. I propose that IPSCs elicited with minimal laser power have properties that resemble unitary IPSCs recorded from connected cell pairs (Petreanu et al., 2007). In the second part, I compare the IPSC properties in CA3 pyramidal cells of NRG1tyI mice and

control littermates, and demonstrate that PV+ inhibitory synapses fail to show evidence for malfunction pre-or postsynaptically in the transgenic mice.

4.3 Results

4.3.1 Setting the scene: selective activation of PV+ axons using optogenetics

4.3.1.1 PV expression pattern in hippocampus of NRG1tyI mice is similar to WT

Before embarking on a PV-dependent optogenetic investigation, it was important to determine the overall PV expression pattern in the hippocampus of NRG1tyI mice. I characterised immunoreactivity to PV in the hippocampal formation of perfusion-fixed NRG1tyI mice and compared it to that in WT mice (10–12 months old, *n*=3 for each genotype, Methods 2.7.1.1). The pattern of PV staining across the hippocampus did not grossly differ between genotypes (Figure 4.1). In particular, the CA3 area demonstrated similar cellular staining patterns of PV+ somata and axons within and near str. pyramidale, as well as of PV+ dendrites and axons in strata oriens and radiatum (higher magnification pictures in lower panel of Figure 4.1). This is in line with the unchanged PV+ cell density in various hippocampal subregions (hilus, CA2/3, CA1) that was reported previously in 15-month-old WT and NRG1tyI mice (Supplementary Table 3 in Deakin et al., 2012). Together, these results demonstrate that NRG1tyI over-expression neither interferes with the overall expression of PV nor significantly impacts on the gross anatomical appearance or number of PV+ neurons.

4.3.1.2 Cre recombinase-dependent ChR2-eYFP expression selective to PV neurons in mid-ventral hippocampus

Having verified that the cellular expression pattern of PV is not altered in NRG1tyI mice, it was essential to evaluate the specificity of hippocampal Cre

recombinase expression in the available PV-Cre mouse line (Methods 2.1.2) before crossbreeding it with NRG1tyI mice. To this end, PV-Cre mice were crossbred to mice of the common Cre-reporter line, R26R-eYFP (Methods 2.1.2; Srinivas et al., 2001). In the crossbred strain (PV-Cre/R26R-eYFP), expression of eYFP is driven by Cre recombinase and should be strictly dependent on PV expression. Thus, the eYFP signal should be restricted to PV+ cells (Figure 4.2). This approach was chosen due to technical difficulties with primary antibodies against Cre recombinase (Methods 2.7.3). Co-labelling of eYFP and PV immunoreactivities was evaluated in coronal hippocampal sections of perfusion-fixed mouse brains (n=2 mice, four and seven weeks old, Methods 2.7.1.1). PV+ and GFP+ somata were counted in stack epifluorescent images along the entire CA3 area (CA3c-a) of randomly chosen hippocampal sections (Methods 2.7.3). Of the eYFP+ somata counted across all three strata (oriens, pyramidale and lucidum/radiatum, total 139 cells), 96.2 ± 0.6% co-labelled with PV (Figure 4.2A). In each stratum, expression of Cre recombinase (as reported by eYFP) was virtually exclusive to PV+ cells, with 90–100% of all eYFP+ neurons immunopositive for PV (as visualised by AMCA fluorescence). However, not all PV+ somata (209 cells counted) expressed Cre recombinase: across all layers, only 64.0 ± 13.2% of PV+ somata in every layer were eYFP+ (Figure 4.2B). In contrast, an earlier report concluded that more than 90% of PV+ neurons co-express Cre recombinase in dorsal root ganglia (Hippenmeyer et al., 2005). This discrepancy may be due to region-specific differences. It is not known if Cre expression in the hippocampus of these mice is biased towards specific PV+ interneuron types, but it is noteworthy that Cre-mediated recombination was successful in most PV+ somata located inside str. pyramidale (76.3 ± 5.5%). Because the somata of PTIs are proposed to be often located within or near str. pyramidale (Freund & Buzsaki, 1996), it may be assumed that they also express Cre

recombinase. I concluded that the PV-Cre mouse line is suitable for experiments aimed at selectively activating axons of PV+ PTIs.

Because PV expression was not grossly altered in NRG1tyI mice, I could assume that PV is also a suitable promoter to drive the expression of Cre recombinase in NRG1tyI mice crossbred with PV-Cre mice ($NRG1tyI^{+/-}$ $PV\text{-}Cre^{+/-}$, 'NRG1tyI/PV-Cre'). AAV2 particles containing the Cre-dependent DNA construct ChR2-eYFP was stereotactically injected into the CA3 hippocampus of NRG1tyI/PV-Cre mice and PV-Cre littermates (see Method 2.5). Expression of this viral ChR2-eYFP recombinant gene is driven by a strong EF1α promoter, but, importantly, its open reading frame is flanked by two loxP sites that require Cre-dependent inversion prior gene expression (Figure 4.3A; Sohal et al., 2009). Two specific features of this approach are worth mentioning:

Firstly, hippocampal PV expression only starts postnatally (around P10; Nitsch et al., 1990; Bergmann et al., 1991). Therefore, AAV2 was delivered to 3–6-week-old mice to ensure sufficient expression of Cre protein. This is particularly important because the NRG1tyI/PV-Cre mice were heterozygous for Cre recombinase, and as such produced lower levels of Cre protein than homozygous PV-Cre mice (Hippenmeyer et al., 2005). In 3–6-week-old heterozygote mice, Cre protein levels were found to be sufficient to achieve inversion and recombination of viral ChR2-eYFP DNA construct, thereby leading to its expression (Figure 4.3C).

Secondly, the mid-ventral hippocampus was selected for stereotactic injection, because brain slices used in the study of CCh-induced oscillation primarily focussed on this area (Chapter 3).

Preliminary stereotactic injections of fluorescent beads into six PV-Cre mice determined the ideal coordinates of mid-ventral CA3 hippocampus of 3–6-week-old mice: −2.7 mm caudal and 2.75 mm lateral from Bregma, and 3.4–2.6 mm ventral to the

brain surface (Figure 4.3B). Using these coordinates, the CA3 hippocampi of 33 mice [18 PV-Cre (6 homozygotes, 12 heterozygotes), and 15 NRG1tyI/PV-Cre] were successfully injected, either uni- or bilaterally. Injected mice were allowed to recover for at least 10 days (up to 21) to ensure good transfection and viral ChR2-eYFP expression. This protocol led to selective expression of ChR2-eYFP in PV+ cells of area CA3: horizontal brain slices prepared from 5–9 week old injected mice contained a dense tangle of ChR2-eYFP+ axons in the CA3 hippocampus (Figure 4.3C, AAV2-injected NRG1tyI/PV-Cre mouse). Expression of ChR2-eYFP occurred predominantly within str. pyramidale as well as at the border of and within str. oriens of CA3b/c. Neighbouring areas, such as str. radiatum of CA3 and the granule layer of the DG, were generally transfected to a lesser extent and only contained sparse ChR2-eYFP+ axons.

Importantly, ChR2-eYFP+ somata and neurites proved immunopositive to PV (Figure 4.3D), thus confirming both the absence of transcriptional leakiness of the viral construct, as well as PV cell type-specific expression of Cre protein (Figure 4.2A). However, not all PV+ somata and dendrites were positive for ChR2-eYFP (asterisks in Figure 4.3D), likely because these cells did not express Cre recombinase (Figure 4.2B), or because they had not been transfected with virus. It is noteworthy that ChR2-eYFP+ somata often appeared weaker than ChR2-eYFP− somata in their immunoreactivity for PV, possibly because Cre expression lowers PV immunoreactivity.

In analysis of subcellular expression, ChR2-eYFP fluorescence in acute slices was primarily observed in axons. Preferred axonal expression of this particular ChR2 construct has also been observed by others (Kohl et al., 2011, but see Boyden et al., 2005). More recently developed ChR2 constructs localise more specifically to the somatodendritic compartment (Lewis et al., 2009). Here, only few ChR2-eYFP+ somata and dendrites were observed amid the very dense ChR2-eYFP+ network in acute slices,

and somatic fluorescence was more prominent in layers other than str. pyramidale. In acute slices, somatic fluorescence within str. pyramidale was presumably masked by the overwhelming fluorescence of the dense PV+ axon network, and optical resolution (epifluorescence using a 20× immersion objective with 2–4× zoom) was a likely limiting factor in visualising somata located deeper within the 350 µm slices. In thinner (70 µm) sections and with higher magnification, ChR2-eYFP fluorescence was also visible in somata and dendrites (Figure 4.3C).

Based on visual comparison, there was no striking difference in the extent of virus transfection, or in cellular/subcellular expression of ChR2-eYFP between the genotypes (PV-Cre and NRG1tyI/PV-Cre). This is in line with the finding that hippocampal expression of PV is not altered (above), and suggests that NRG1tyI over-expression does not interfere with PV-dependent expression of Cre recombinase or virus uptake.

4.3.1.3 Optically evoked ChR2-activated synaptic GABAergic currents in CA3 pyramidal cells

Successful expression of ChR2 in PV+ interneurons enabled selective optical stimulation of PV+ cell axons to study their synaptic properties in CA3 pyramidal cells. I characterised the properties of PV+ cell-mediated synaptic GABAergic currents. For this, horizontal hippocampal slices from 5–9-week-old AAC2 injected NRG1tyI/PV-Cre mice and PV-Cre littermates were prepared and screened for eYFP fluorescence (Methods 2.4.2). In slices exhibiting eYFP expression, postsynaptic pyramidal cell somata inside str. pyramidale or at the border to str. oriens were patched in whole-cell mode. A low chloride (8 mM NaCl) intracellular solution was used to maintain physiological conditions, and cells were voltage clamped at −10 mV or 0 mV to ensure a strong chloride driving force for inhibitory currents. Excitatory transmission mediated through AMPARs/kainateRs and NMDARs was pharmacologically blocked (25 µM

NBQX, 100 µM AP5). During whole-cell voltage-clamp recordings, neurons were filled with neurobiotin for *post hoc* anatomical identification of pyramidal cells (Figure 4.4A). Brief paired pulses of blue light (473 nm; pulse duration 3 ms with 50 ms interpulse interval; max laser power 100 mW) at least 200 µm from the patched soma were used to excite ChR2 (Boyden et al., 2005). The laser spot size was decreased to ~15–20 µm diameter (113 µm fibre light guide; Methods 2.4.2) and focussed inside str. pyramidale to preferentially activate PV+ axon originating from PTIs (Figure 4.4A).

Photostimulation evoked reliable and reproducible IPSCs in pyramidal cells of both genotypes (Figure 4.4B). Synaptic currents occurred with short latencies (2.96–7.50 ms) that depended on the strength of ChR2 excitation and presumably on the level of ChR2 expression in addition to synaptic delay time [5.15 ± 0.18 ms (mean ± SEM), *n*=34 pyramidal cells for both genotypes]. These results are in line with latencies reported in optical stimulation of cortical glutamatergic synapses (Petreanu et al., 2007). I ensured that IPSCs did not result from optically triggered (direct) release of GABA from PV+ axon terminals but required sodium action potentials and were blocked by 1 µM TTX (tested independently in 6 cells, 3 of which were NRG1tyI/PV-Cre; Figure 4.4E). Synaptic currents were concluded to be of GABAergic nature for two reasons. Firstly, IPSCs reversed at holding potentials of ~−74 mV (liquid-liquid junction potential correction of −11.7 mV, *n*=4 cells; Figure 4.4C), which is close to the calculated reversal potential for chloride (E_{Cl}=−72 mV; Kaila et al., 1993)[1]. Secondly,

[1] Yet, the fact that the recorded $E_{GABA\text{-}A}$ value was a few millivolts more negative than the calculated value of E_{Cl} was unexpected (see Methods). It could, for instance, theoretically result from activity-driven interstitial space reduction and consecutive extracellular Cl^- accumulation (rather than K^+ which is readily permeant across cell membranes, and hence its concentration is well buffered) during repetitive light-activation of GABA-A receptors (Autere et al. 1999). Interestingly, it has recently also been suggested that the inward-rectifying voltage-dependent chloride channel ClC2 could specifically mediate the efflux of Cl^- from the postsynaptic cell during membrane hyperpolarisations (e.g. during voltage-clamping to −90 mV, when I–V curve is recorded). Such a postsynaptic microdomain has been reported to be specific to GABAergic synapses from PV+ cells (Foldy et al. 2011).

IPSCs were blocked by 100 μM picrotoxin (tested independently in 8 cells, 4 of which in NRG1tyI/PV-Cre; Figure 4.4D). Finally, IPSCs were likely to originate from activation of PV+ PTIs, not only because the blue light spot was focussed inside str. pyramidale, but also because synaptic currents were depressed following a second presynaptic axon activation evoked 50 ms after the first (Figure 4.4B). Paired-pulse depression is characteristic of hippocampal PV+ PTI–pyramidal cell signalling (Kraushaar & Jonas, 2000; Bartos et al., 2002; Szabo et al., 2010), unlike signalling by PV+ bistratified and PV+ O-LM interneurons that is less paired-pulse modulated, at least in area CA1 of rat hippocampus (Maccaferri et al., 2000).

It is important to note that optical stimulation was similarly successful and reliable in NRG1tyI/PV-Cre mice (Figure 4.4B right trace), and IPSCs showed a similar pharmacological profile to those in recorded cells from PV-Cre mice (blocked by TTX and picrotoxin). Hence, it may be concluded that optical stimulation of PV+ axons is appropriate for quantitative analysis of the properties of PV+ PTI–CA3 pyramidal cell synapses.

4.3.1.4 Minimal optical stimulation

To enable comparative analysis of the properties of PV+ PTI–CA3 pyramidal cell synapses in the two different genotypes, I employed minimal optical stimulation (MOS) to restrict light activation to a few PV+ fibres, ideally a single fibre (Figure 4.5A). Its implementation was analogous to that of minimal electrical stimulation (MES), which is often used to study monosynaptic glutamatergic connections (e.g. Kneisler & Dingledine, 1995a,b) and sometimes GABAergic synapses (MacIver, 2009). However, the great advantage of MOS over MES is its fibre selectivity: it is restricted to PV+ fibres. Here, MOS was used to evoke PV+ cell-mediated IPSCs that resemble unitary responses of connected cell pairs. Unitary responses are often characterised to compare

strength, type (facilitating or depressing) and current kinetics of defined synapses (Maccaferri et al., 2000; Bartos et al., 2002; Szabo et al., 2010).

The MOS protocol was implemented as follows. The position of the laser light spot (using ~50-90% of maximal laser output power) was systematically moved along and within str. pyramidale until a location was found that consistently elicited IPSCs in the postsynaptic whole-cell recorded cell (voltage-clamped between −40 and −10 mV). The laser power was then reduced until excitation of ChR2 was not strong enough to elicit an action potential in the presynaptic axon (Figure 4.5A). Next, the minimal laser power to reliably elicit action potentials in the presynaptic ChR2+ axon and evoke IPSCs in the whole-cell voltage-clamped postsynaptic neuron was determined by stepwise adjusting the laser power (~0.2–0.5% increases in power). At a certain level, fast kinetics IPSCs with monophasic rise characteristics were evoked in the postsynaptic neuron, reflecting the presynaptic ChR2+ axon switching from being silent to firing action potentials. The critical laser power at which IPSCs were evoked in postsynaptic neurons varied between neurons (30–90% of maximum laser power; ~100 mW before entering the 113 µm thick optic fibre), but importantly the switch from no IPSC to stable IPSC occurred over just few increments. The IPSCs elicited at this critical laser power are most likely the result of the activity of a single axon for the following reasons:

Firstly, occasional failures probably result from sub-threshold excitation of ChR2 in a single axon. It is unlikely that ChR2 excitation would fail to reach firing threshold simultaneously in multiple axons (unless they express the same level of ChR2 proteins, and run in the same focal plane of the 20 µm light spot; but see discussion). Secondly, latencies of successfully evoked IPSCs showed very little temporal jitter in individual experiments [see sample recording in Figure 4.5B.ii, latency 6.24 ± 0.48 ms (mean ±

SD)]. Thirdly, IPSCs are characterised by monophasic rise times with little variability [Figure 4.5B.iv, 20–80% rise time: 1.00 ± 0.09 ms (mean ± SD)]. Finally, further increases in laser power often gave rise to IPSCs with discontinuous rising phases (Figure 4.5A, green dots indicate the peak amplitude of the delayed second current). This presumably reflects presynaptic activation of more than one PV+ axon with different spike delays (or consecutive activation of the same PV+ axon), resulting in temporal summation of slightly desynchronised IPSCs (Petreanu et al., 2007). It is likely that higher laser powers excite ChR2+ axons at different depths in the tissue because light scattering is greater.

In each recording, the step from no IPSC to a prominent IPSC was verified over a range of at least 10 incremental laser intensities, and the incremental stimulation protocol was often run twice to verify that minimum laser power was used. In some cases, slightly higher laser powers were needed in the second run to elicit an IPSC and avoid failures. This might result from continuous desensitisation of ChR2, which has been reported to be ~30 s (Petreanu et al., 2007), because sweeps of paired pulses were given every 10 s in this protocol.

In summary, MOS demonstrated to be a suitable technique for photoactivation of (most likely) a single ChR2+ fibre. Once the critical laser power had been established in each recording, 20–30 sweeps (6 sweeps per min) of light-evoked IPSCs were recorded in postsynaptic neurons clamped at −10 mV or 0 mV. Recordings in which optical stimulation failed to elicit a first IPSC (example in Figure 4.5B.i) were not included in the analysis. Figure 4.5B illustrates the properties of typical IPSCs recorded with MOS in a pyramidal cell from a NRG1tyI/PV-Cre mouse, and confirms that such IPSCs qualitatively resemble unitary IPSCs recorded from connected PV+ interneuron–CA3 pyramidal cell pairs with low latency jitter (Figure 4.5B.ii), stable peak amplitudes

(Figure 4.5B.iii), fast kinetics (20-80% rise time, half-amplitude decay time, decay tau; Figure 4.5B.iv-v) and typical paired-pulse depression (Figure 4.5B.vi) (Bartos et al., 2002; Szabo et al., 2010).

4.3.2 PV+ axon-mediated IPSCs have similar properties in PV-Cre and NRG1tyI/PV-Cre mice

Properties of MOS-elicited IPSCs were analysed by using a custom-written Igor Pro procedure (Methods 2.6.2) on 20–30 sweeps per whole-cell recording. For comparison across all cells, I used median rather than mean values to account for possible misdetection in the automated procedure. In total, I compared median IPSC properties of 18 cells from 11 successfully injected PV-Cre mice with those of 16 cells from 12 injected NRG1tyI/PV-Cre mice. Most cells (27 of 34) were successfully labelled with neurobiotin and anatomically verified as pyramidal cells based on their somatodendritic structure and the presence of mushroom-like spines on their apical and basal dendrites. In the remaining 7 cells (5 PV-Cre, 2 NRG1tyI/PV-Cre), labelling with neurobiotin was not successful but they were included in the analysis because their intrinsic and IPSC properties did not differ from the anatomically identified pyramidal cells. One further cell (PV-Cre) was morphologically identified as an interneuron and therefore excluded from the analysis.

First, I compared the intrinsic properties of CA3 pyramidal cells between genotypes. Neither the resting membrane potential nor the input resistance was significantly different in cells from NRG1tyI mice compared to those in PV-Cre mice [resting membrane potential: PV-Cre: −56.83 ± 1.72 mV, n=18; NRG1tyI/PV-Cre: −59.38 ± 2.11 mV, n=16; p=0.354, independent samples t test. Input resistance: NRG1tyI/PV-Cre: 81.88 ± 7.30 MΩ (mean ± SEM), n=16 cells; PV-Cre: 89.00 ± 4.49 MΩ, n=18; p=0.062, Mann–Whitney U test]. This is important because different input

resistances could alter the apparent kinetics and amplitude of synaptic currents, as measured from the soma. Access resistance in whole-cell recordings ranged between 11.7 and 16.9 MΩ in pyramidal cells (*n*=18) of PV-Cre mice. This was similar to pyramidal cells in NRG1tyI/PV-Cre mice (11.3 to 17.6 MΩ, *n*=16; *p*=0.625, independent samples t test), thereby allowing comparison of current kinetics between the genotypes.

MOS evoked IPSCs within ~5 ms after the onset of laser light, with no difference observed between genotypes [latency in PV-Cre: 4.94 ± 0.27 ms (mean ± SEM), *n*=18 cells; NRG1tyI/PV-Cre: 5.38 ± 0.21 ms, *n*=16 cells; *p*=0.220, independent samples t test). This implies that neither the generation of action potentials in PV+ axons nor the efficiency of transmitter release at GABAergic synapses of PV+ axons was influenced by NRG1tyI over-expression.

Next, I compared the strength of inhibitory synapses between PV+ axons and CA3 pyramidal cells (IPSC peak amplitudes), their current kinetics and paired-pulse ratios between genotypes. Together, these properties shed light on potential changes at pre- or postsynaptic loci of the synaptic connection, and any changes might (at least partly) account for the longer oscillatory cycles in NRG1tyI mice. However, none of the parameters analysed was significantly altered in 2-month-old NRG1tyI/PV-Cre mice (Figures 4.6 and 4.7, Table 4.1). It is worth noting, however, that median IPSC amplitudes were variable between experiments in both groups (Figure 4.6A, <20–160 pA in PV-Cre; up to 190 pA in NRG1tyI/PV-Cre). This variability in IPSC amplitudes might be due to activation of different presynaptic PV+ interneuron types, as unitary IPSCs originating from AACs have been reported to have larger peak amplitudes than unitary IPSCs mediated by fast spiking BCs in hippocampus (Szabo et al., 2010).

Table 4.1 Comparison of IPSC properties across genotypes

Property	Genotype (number of cells recorded)	Mean ± SEM (or medians) across all cells	Statistical test	Significance (*p*-values)
1st IPSC peak amplitude (pA)	PV-Cre (18)	60.22 ± 9.50 (median 44.35)	Mann–Whitney U test	0.654
	NRG1tyI/PV-Cre (16)	67.64 ± 12.96 (median 42.97)		
20-80% rise time (ms)	PV-Cre (18)	0.95 ± 0.09 (median 0.85)	Mann–Whitney U test	0.202
	NRG1tyI/PV-Cre (16)	1.08 ± 0.09 (median 0.97)		
half-amplitude decay time (ms)	PV-Cre (18)	9.59 ± 0.61	Independent samples t test	0.296
	NRG1tyI/PV-Cre (15)	10.50 ± 0.59		
decay tau (ms)	PV-Cre (18)	13.83 ± 0.79	Independent samples t test	0.085
	NRG1tyI/PV-Cre (15)	16.26 ± 1.16		
paired-pulse ratio	PV-Cre (18)	0.66 ± 0.04	Independent samples t test	0.120
	NRG1tyI/PV-Cre (16)	0.55 ± 0.06		

Comparisons are based on median parameters of individual cells. Medians are reported in addition to mean ± SEM for non-normal distributions. Note that half-amplitude decay time and decay tau could not be determined in one NRG1tyI transgenic pyramidal cell because of spontaneous activity and noise.

To examine this further, the kinetics parameter and paired-pulse ratios in relation to the median IPSC amplitudes were plotted for each recording (Figure 4.7). This also did not reveal a clear difference between genotypes in the distribution of parameters across the range of peak amplitudes (although there may have been too few IPSCs with median peak amplitudes >100 pA to infer a difference in decay kinetics). Rise and decay times of light-evoked IPSCs were not significantly different in NRG1tyI mice. Thus, it appears unlikely that changes in decay kinetics of PV+ cell-mediated IPSCs could explain the 30% longer decay of compound inhibitory currents during CCh-induced gamma oscillations (WT: 7.96 ± 0.31 ms; NRGtyI: 10.34 ± 0.53 ms).

Finally, the paired-pulse ratio revealed no difference between groups, and transmission at PV+ interneuron–pyramidal cell synapses also showed paired-pulse depression in NRG1tyI mice (Table 4.1). However, the mean success rate of eliciting a second IPSC by photostimulation (50 ms after a first IPSC) varied hugely across cells (PV-Cre: 20–100%, *n*=18 cells; NRG1tyI/PV-Cre: 10–100%, *n*=16). This is likely to have resulted from a failure to generate a second action potential in the presynaptic axon rather than a failure of vesicle release at the synapse, because connected PTI–pyramidal cell pairs show synaptic depression (by ~30–40%) but not complete failure of the second presynaptic stimulus (Kraushaar & Jonas, 2000; Bartos et al., 2002; Szabo et al., 2010). Repeated optical stimulation (within 50 ms) may not always be successful, due to desensitisation of ChR2 (recovery can take up to 30 s; Petreanu et al., 2007). On the other hand, paired pulses occasionally elicited second IPSCs larger than the first, in some but not all experiments (2^{nd} IPSC peak amplitude > 1^{st} IPSC peak amplitude; this was not further analysed). This might have resulted from optical recruitment of a second ChR2+ axon. It is conceivable that the first light pulse excited one ChR2+ axon strongly enough to reach firing threshold, but simultaneously depolarised a second presynaptic ChR2+ axon (possibly slightly out of the focal plane of the laser spot) to sub-threshold levels, which thus only reached firing threshold when further ChR2-mediated depolarisation was induced by a second light pulse. This hypothesis remains to be investigated, but since paired-pulse facilitation was only seen occasionally, I report here the median value of the paired-pulse ratios across all sweeps from each experiment.

In conclusion, MOS reveals no significant differences in GABAergic inhibition mediated by PV+ axons to CA3 pyramidal cells in ~1–2-month-old NRG1tyI transgenic mice, when compared to PV-Cre littermates.

4.4 Discussion

In this chapter I have explored potential changes in PV+ axon-mediated synaptic transmission to CA3 pyramidal cells in NRG1tyI mice. Alterations in this synapse function was hypothesised earlier to prolong CCh-induced gamma oscillation cycles, either by increasing decay times of individual IPSCs or by decreasing the probability of fast and reliable GABA release during rhythmic oscillation (see Chapter 3.2). To address the function of PV+ GABAergic synapses, I adapted and established a selective optogenetic stimulation approach (Sohal et al., 2009) and obtained the following results:

1. There was no detectable change in hippocampal PV expression in NRG1tyI mice. PV-dependent Cre recombinase expression could therefore be employed to establish selective expression of light-sensitive ChR2 in PV+ cells in the hippocampus of NRG1tyI mice and littermates.
2. Cre recombinase-dependent ChR2 expression was successfully established in mid-ventral hippocampus of NRG1tyI (NRG1tyI/PV-Cre) mice and of control (PV-Cre) littermates. Strong expression was detected predominantly in str. pyramidale and at the border to str. oriens, and was selective to PV+ neurons.
3. GABAergic transmission evoked by optical stimulation of ChR2 in CA3 pyramidal cells was blocked by TTX, thereby excluding direct optical activation of PV+ axon terminals. The properties of IPSCs elicited with MOS, analogous to MES, resembled unitary IPSCs reported at PV+ BC–CA3 pyramidal cell synapses.
4. NRG1tyI over-expression is not associated with changes in PV+ axon-mediated GABAergic transmission to CA3 pyramidal cells. This was verified in 1–2-month-old mice, that is, the same age as that when compound IPSCs during gamma oscillations were altered in NRG1tyI mice (Chapter 3).

4.4.1 PV+ expression in NRG1tyI mice

Hippocampal PV+ immunoreactivity patterns revealed no gross morphological differences between NRG1tyI and WT mice, and the overall extent of ChR2-eYFP expression in virus-injected mice was also not observed to differ between the two genotypes. These findings are consistent with a previous semi-quantitative estimation of hippocampal PV+ cell density that reported no change in NRG1tyI mice (Deakin et al., 2012). Together, these data provide the first evidence that enhanced NRG1tyI expression does not detectably alter the number of PV-expressing cells in 10–15-month-old mice (immunoreactivity and semiquantitative PV+ cell density). Yet, one has to be cautious in the interpretation of these results, because immunocytochemical studies fail to detect quantitative changes in the expression level of PV (Lewis et al., 2005). It is important to bear this in mind, in light of the link between NRG1 and schizophrenia, because PV mRNA levels rather than overall PV-containing cell density are reported to be decreased in schizophrenic patients (Woo et al., 1997; Reynolds et al., 2001; Beasley et al., 2002; Hashimoto et al., 2003).

Interestingly, reduced expression of PV is linked to impaired GABA metabolism, affecting synthesis and re-uptake of GABA in prefrontal cortex (Volk et al., 2000; Volk et al., 2001; review in Lewis et al., 2005). Because the physiological evidence here suggests that GABAergic signalling from PV+ interneurons to CA3 pyramidal cells is unaffected by NRG1 over-expression, one might tentatively conclude that PV+ levels might also be unchanged. However, the proposed function of PV as a calcium buffer (Caillard et al., 2000; Zucker & Regehr, 2002) relates more to regulating synapse dynamics, especially multiple pulse facilitation, than the synaptic properties of single IPSCs (Vreudgenhil et al., 2003; Eggermann & Jonas, 2012). As a result, the single- or paired-pulse evoked IPSCs that I recorded probably did not involve PV, and thus I

cannot infer that NRG1 over-expression changes PV expression levels. On the other hand, it is likely that PV levels impact persistent neuronal activities, such as gamma oscillations. Indeed, PV deficiency has been modelled (Volman et al., 2011) and shown (Vreudgenhil et al., 2003) to affect gamma oscillations: a cortical circuit model predicts that a reduction in PV-expressing cell number or PV levels reduces both oscillation power and frequency (Volman et al., 2011). Yet, genomic PV deficiency has been shown to increase the field power without affecting the frequency in area CA3 when tested in kainate-induced gamma oscillations (Vreudgenhil et al., 2003). Taken together, reduced PV levels influence the short-term dynamics of inhibitory synapses (beyond paired-pulse facilitation) and thus, if present, could contribute to the slower field potential oscillations in NRG1tyI mice.

Further, I cannot exclude the possibility of alterations of PV+ cell density in other brain regions. In fact, in mice that over-express NRG1tyI under the ubiquitous EF1α promoter, immunoreactivity for PV is elevated in protein extracts from frontal cortex but not from hippocampus (Kato et al., 2010). A region-specific alteration of PV mRNA levels was also reported in tissue from some schizophrenic patients (Hashimoto et al., 2003).

4.4.2 ChR2-mediated selective stimulation of PV+ cell axons

Optical stimulation of PV+ axons was successfully established, and the technique enables efficient screening of the function of PV+ synapses on CA3 pyramidal cells. Evoked IPSCs were monosynaptic and of GABAergic nature as expected. I provide evidence that IPSCs were mediated by PV+ axons of perisomatic-, not dendritic-targeting interneurons because synapses showed characteristic paired-pulse depression, not facilitation (Maccaferri et al., 2000; Szabo et al., 2010).

It is noteworthy that IPSC amplitudes showed some variability between stimulation cycles (Figure 4.4D and E). Sweep-to-sweep variability of IPSC peak amplitude has also been reported in recordings from connected BC–pyramidal cell pairs (Kraushaar & Jonas, 2000; Bartos et al., 2002; Szabo et al., 2010), and are likely to result from probabilistic transmitter release of GABAergic synapses. Unlike most pyramidal cells, which contact hippocampal interneurons through a single synapse (Gulyas et al., 1993b), GABAergic neurons usually signal to their target cells through multiple synaptic contacts (Hajos & Paulsen, 2009). This, together with the high release probability of individual GABAergic boutons, explains the absence of failures in single interneuron connections (Kraushaar & Jonas, 2000). Typically, BCs innervate CA3 pyramidal cells through 2–3 synaptic contacts (Miles et al., 1996; Biro et al., 2006).

Although the MOS approach was suited to screening synapse function of PV+ PTIs, a technical drawback with this particular ChR2 gene construct is its predominant expression in axon. Selected expression of ChR2 in the somatodendritic compartment (Lewis et al., 2009) would have made paired recordings (from presynaptic eYFP+ cells to CA3 pyramidal cells) successful, as originally endeavoured. This could have enabled *post hoc* anatomical identification, and also unambiguously establish that photostimulation of eYFP+ somata evokes unitary IPSCs akin to electrical stimulation of the presynaptic neuron (e.g. kinetics and PPD). Without *post hoc* anatomical identification, the presynaptic PV+ interneuron type remains unconfirmed, because physiological properties are only indicative but not sufficient for unambiguous identification of PV+ BCs and AACs. As outlined above, the range of GABA conductances (Figure 4.4C) and median IPSC amplitudes (Figures 4.6 and 4.7) are likely to reflect optical activation of either BCs or AACs. Unitary IPSCs from AACs have been shown to have larger IPSC peak amplitudes and longer decay kinetics than

those from PV+ fast-spiking BCs in area CA3 (Szabo et al., 2010), but distinct populations of IPSC amplitudes could not be distinguished in histograms (Figure 4.6). It is possible that MOS activated more than one presynaptic cell axon in some experiments. In addition, axon arbours of some cells may have been compromised during the preparation of slices, leading to smaller amplitude IPSCs. Therefore, the results on postsynaptic IPSC amplitude should be interpreted with caution.

Finally, the use of MOS makes it likely (but not certain) that subsequent optical stimulation (10 s interval) repeatedly activates the same fibre, and only one. It is conceivable that subsequent stimulation cycles activate different fibres, each giving rise to IPSCs that resemble uIPSCs. Because ChR2 takes ~30 s to recover from desensitisation (Petreanu et al., 2007), repeated stimulation of a previously activated ChR2+ fibre may result in it failing to reach threshold in the second run, while built-up of depolarisation in a second fibre (possibly slightly out of focus) might only then reach its threshold. As outlined above, the latter situation might also contribute to the great variability in the success rate in eliciting a second IPSC 50 ms after the first (Section 4.3.2). Paired recordings indicate that PV+ synapses are usually very reliable due to expression of P/Q-type voltage-gates calcium channels in the active zone of terminals (Hefft & Jonas, 2005; Glickfeld & Scanziani, 2006).

4.4.3 Unchanged PV+ mediated inhibition of pyramidal cells in NRG1tyI mice

My results do not provide evidence that NRG1tyI over-expression affects GABAergic signalling from PV+ PTIs to CA3 pyramidal cells, neither presynaptically (PPR) nor postsynaptically (IPSC amplitude and kinetics). IPSC current kinetics were not significantly changed in postsynaptic pyramidal cells, suggesting that NRG1tyI

over-expression does not alter postsynaptic GABA-A receptor subunit expression (α1, α2, β2 and γ2) in these synapses (see Introduction).

These findings were unexpected for three reasons: firstly, PV+ perisomatic GABAergic synapse kinetics primarily determine gamma oscillation frequency; secondly, ErbB4 expression has been reported in PV+ presynaptic terminals (Woo et al., 2007; Fazzari et al., 2010 but see below); and thirdly, prolonged treatment with NRG1 (2–9 days *in vitro*) modulates expression of postsynaptic GABA-A receptor subunits in hippocampal and cerebellar cultures (Rieff et al., 1999; Okada and Corfas, 2004). In addition, it has been reported that bath application of NRG1 faciliates evoked GABA release in prefrontal cortical slices through ErbB4 receptors (Woo et al., 2007; Wen et al., 2010), while genomic ablation of interneuronal ErbB4 reduces the frequency of mIPSCs in CA1 pyramidal cells (Fazzari et al., 2010).

As discussed in Chapter 3, the apparently conflicting results might be attributable to the duration of increased NRG1 signalling during experiments (acute versus genomic/chronic). In addition, there might be region-specific differences of NRG1/ErbB4 signalling (e.g. region-specific signalling cascades), assuming that effects were mainly mediated through ErbB4 receptors. Further, I cannot exclude the possibility that pooling IPSCs mediated by two different presynaptic interneuron types, either PV+ BCs or AACs, might mask subtle cell type-specific effects of NRG1tyI over-expression. Interestingly, the evidence for presynaptic expression of ErbB4 (Woo et al., 2007; Krivosheya et al., 2008; Fazzari et al., 2010) was challenged by recent results in rodent hippocampus where immunoreactivity for ErbB4 was not detected on PV+ axon terminals (Vullhorst et al., 2009; Neddens et al., 2011). The authors suggested that previous use of non-specific binding of polyclonal antisera against ErbB4 may have led to incorrect immunohistological interpretation (Neddens et al., 2011).

These authors generated and employed more specific antibodies against intra- and extracellular domains of the ErbB4 receptor for their studies. Importantly, my data are consistent with this later evidence that ErbB4 receptors are not expressed at presynaptic PV+ terminals in mouse area CA3, since presynaptic GABA release was not altered by NRG1tyI over-expression (unaltered paired pulse ratio). My results are also in line with the recent finding by Abe et al. (2011), who studied pharmacologically isolated IPSCs (elicited by electrical stimulation) in layer V pyramidal cells of mouse pups that were exposed to subcutaneous administration of NRG1β1 peptide (the core EGF domain). Such longer-term but sub-chronic NRG1 administration was also not found to change monosynaptic IPSC amplitudes or paired pulses, or miniature IPSCs (amplitude, frequency), although it should be noted that Abe et al. tested GABAergic synapses at particularly early postnatal age (P11–P12), when GABAergic transmission is still subject to developmental changes (Ben-Ari et al., 1997).

4.4.4 Perspective

While this work was in progress, evidence accummulated that ErbB4 expression occurred predominately at postsynaptic locations of GABAergic interneurons, particularly in PV+ but also CR+ and CCK+ interneurons (Krivosheya et al., 2008; Vullhorst et al., 2009; Fazzari et al., 2010; Neddens et al., 2011). This raised the question as to whether NRG1tyI over-expression could, alternatively, modify network inhibition by altering the excitatory glutamatergic drive of PV+ PTIs. Impaired recruitment of PV+ BCs (and/or AACs) might be expected to reduce inhibitory precision and efficiency in NRG1tyI mice and thus modulate gamma oscillations (Volman et al., 2011; Zheng et al., 2011).

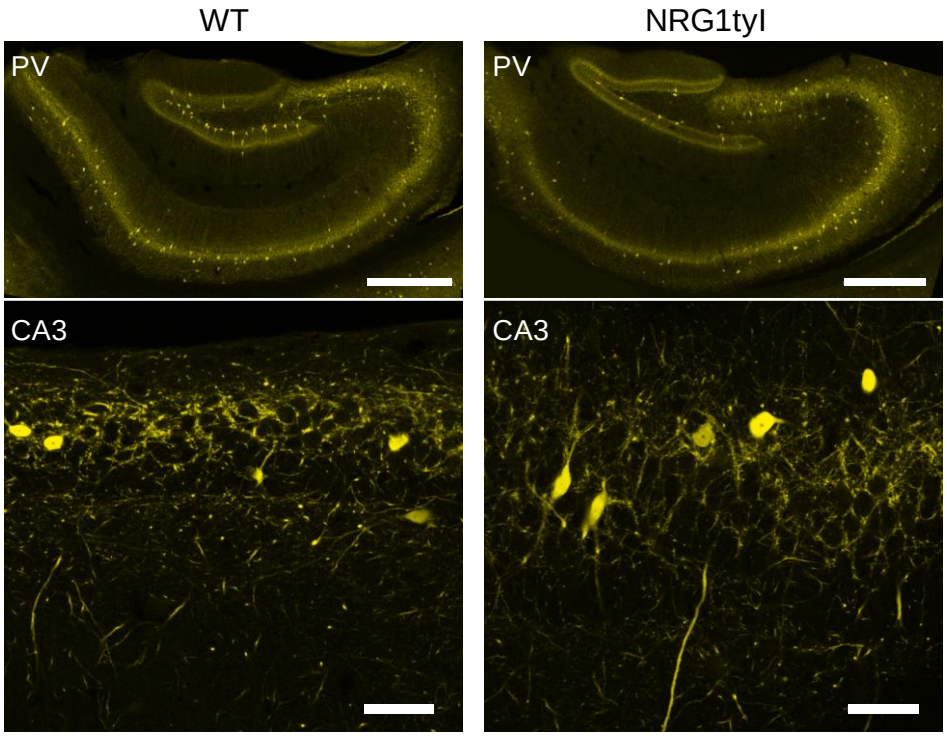


Figure 4.1 Overall pattern of PV immunoreactivity in the hippocampus is unchanged in NRG1tyI mice.

PV immunostaining in hippocampus of a 10-month-old WT and 12-month-old NRG1tyI mouse (top), and higher magnification view of CA3 (bottom), showing cellular staining in CA3 somata within and near str. pyramidale, as well as in dendrites and axons. Scalebars 500 µm (top panel), 50 µm (lower panel). Orthogonal projections of image stacks taken with confocal laser-scanning microscopy at 5× or 20× magnification are shown. PV immunoreactivity was visualised with Alexa Fluor 488. The figure (recoloured) was first published in Deakin et al. (2011) as Supplementary Figure 5.

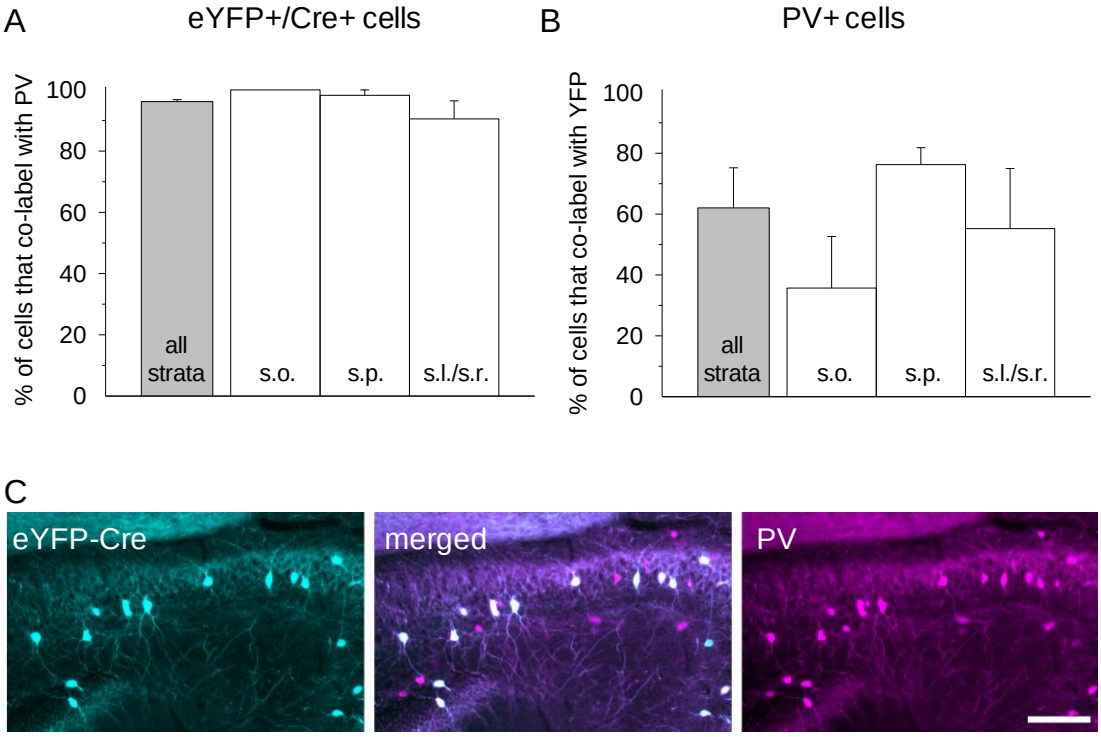


Figure 4.2 Cre recombinase expression is selective to PV+ neurons in the PV-Cre mouse.

Expression of Cre recombinase is reported here by eYFP fluorescence in PV-Cre/R26R-eYFP mice.

(A) Of all eYFP+ somata counted across CA3 hippocampus, 96% co-labelled with PV (grey bar). This was consistent across the different layers in CA3, with >80% of all eYFP+ somata also immunoreactive for PV (white bars). s.o., str. oriens; s.p., str. pyramidale; s.l. str. lucidum; s.o., str. radiatum.

(B) Cre recombinase is not expressed in all immunolabelled PV+ neurons: only 64% of PV+ somata in CA3 co-stained with eYFP. Note the difference between strata: 75% PV+ somata within str. pyramidale expressed eYFP, probably including PTIs.

(C) Enhanced YFP fluorescence (false-colour cyan, left) in area CA3 reports Cre expression, and overlaps extensively with immunolabelling for PV (false-colour mangenta, right), indicating the specificity of Cre expression (merged, middle). Note, eYFP fluorescence was further enhanced with immunoreaction to GFP primary antibody and visualised with Alexa Fluor 488-conjugated secondary antibody; PV was visualised with immunoreaction and secondary antibody fluorescence at AMCA. Z-stacked epifluorescence images were taken from a 50 µm thick section. Scalebar 100 µm.

Figure 4.3 Selective virus-mediated expression of ChR2 and eYFP in PV+ neurons in mid-ventral hippocampus.

(A) The injected AAV2 contained a double-floxed inverted open reading frame (DIO) encoding ChR2-eYFP fusion protein. Protein expression was driven by a strong *EF-1α* (elongation factor-1α) promoter. ITR: inverted terminal repeat, WPRE: woodchuck hepatitis B post-transcriptional regulatory element (to increase gene expression). Adapted from Kohl et al., 2011.

(B) Site of bilateral injection into mid-ventral CA3 hippocampus. Three injections were made along the dorsoventral axis to increase the transfection along the horizontal brain axis for *ex vivo* purposes (the most ventral site is illustrated here).

(C) Epifluorescent image taken at 5× magnification from a 70 µm fixed section. Enhanced YFP-tagged ChR2 expression was evident around the injection site in mid-ventral CA3 hippocampus, here shown in a horizontal section from an AAV2-injected NRG1tyI/PV-Cre mouse. Expression predominantly occurred in the subregion of CA3c/b inside str. pyramidale and at the border to str. oriens. Scalebar 250 µm.

(D) eYFP-tagged ChR2 distributes throughout the cell membrane (green, left), and co-localises with PV (yellow, right) in soma as well as neurites (see cell in the centre). Note that not all PV+ somata express eYFP-ChR2 (asterisks), presumably due to lack of Cre expression or unsuccessful viral transfection in these PV cells. PV was visualised with immunoreaction and secondary antibody fluorescence at Cy3. The endogenous fluorescence of eYFP-tagged ChR2 was *not* enhanced by immunoreaction in this image, but note that this image was taken in a 70 µm thick fixed section (not in a 350 µm thick acute slice where somatic fluorescence was more difficult to be identified; see text). Micrographs represent an orthogonal projection of stack images taken with structured illumination microscopy at 40× magnification. Scalebar 25 µm.

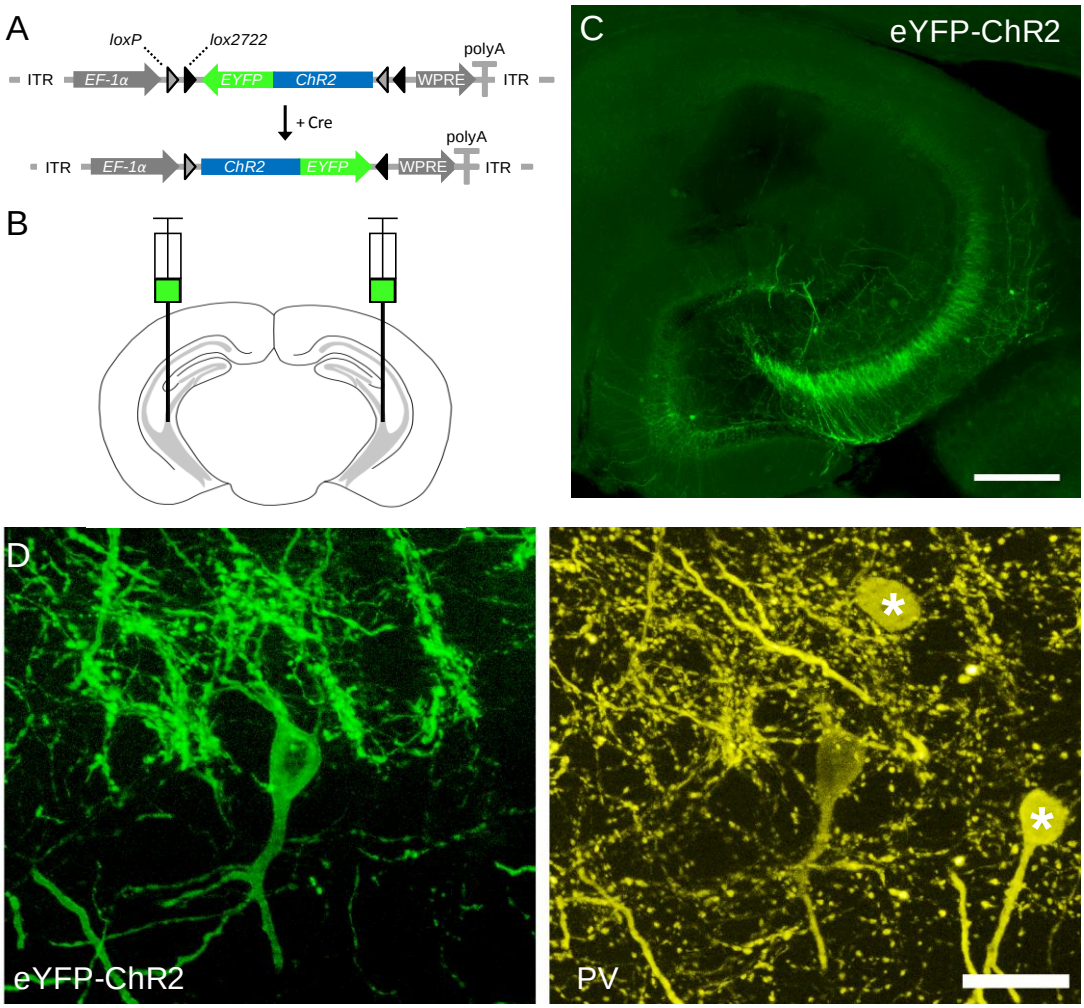

A
loxP
lox2722
polyA
ITR
EF-1α
EYFP
ChR2
WPRE
ITR
+ Cre
polyA
ITR
EF-1α
ChR2
EYFP
WPRE
ITR
B
C
eYFP-ChR2
D
eYFP-ChR2
PV

Figure 4.3

Figure 4.4 Properties of PV+ cell synapses to CA3 pyramidal cells studied by optical stimulation of ChR2.

(A) Experimental design. Layer-specific optical stimulation (473 nm) of ChR2-expressing PV+ cell axons arborising in CA3 str. pyramidale (s.p.), and simultaneous whole-cell voltage clamp recording from a postsynaptic CA3 pyramidal cell. The laser spot size was ~15–20 µm in diameter. Layers are indicated as s.o., str. oriens; s.l., str. lucidum. Below: neurobiotin-filled CA3 pyramidal cell (red) recorded in a virus-injected NRG1tyI/PV-Cre mouse (W081101, sample traces of this cell are shown in Figure 4.5), amongst a dense network of eYFP-ChR2-expressing fibres (green) within str. pyramidale (s.p.). Scalebar 50 µm. Inset: mushroom-like spiny dendrites (scalebar, 10 µm).

(B) Photostimulation evoked reliable and reproducible IPSCs in pyramidal cells of PV-Cre (left) and NRG1tyI/PV-Cre mice (right), using 3 ms long light pulses at 50 ms intervals (blue dots). The intracellular solution contained 8 mM chloride. Outward currents in cells clamped at −10 mV reversed when cells were clamped at −70 mV (V_h, holding voltage).

(C) IPSC evoked by photoexcitation of PV+ axons are reversed at V_h = −71 to −79 mV (corrected for liquid–liquid junction potential, −11.7 mV) which approximates the calculated E_{Cl}. This suggests synaptic currents were mediated through chloride-selective GABA receptors. Linear regressions were fitted to the data to determine the approximate reversal potential from the crossing of the fit with the x-axis (current=0 pA).

(D) Light-evoked IPSCs were blocked by wash-in of 100 µM picrotoxin (PiTx), confirming synaptic currents were primarily mediated through GABA-A receptors. Note continuous block of IPSCs even when laser power was at maximum. The example shown was recorded in a NRG1tyI/PV-Cre mouse. Blue dots represent 3 ms light pulses at 50 ms intervals.

(E) IPSCs were sensitive to 1 µM tetrodotoxin (TTX), confirming that presynaptic action potentials are required, and that synaptic currents did not result from direct optical activation of PV+ axon terminals. The example presented here was recorded in a PV-Cre mouse. Note continuous block of IPSCs even when laser power was maximum (to recruit as many fibres as possible).

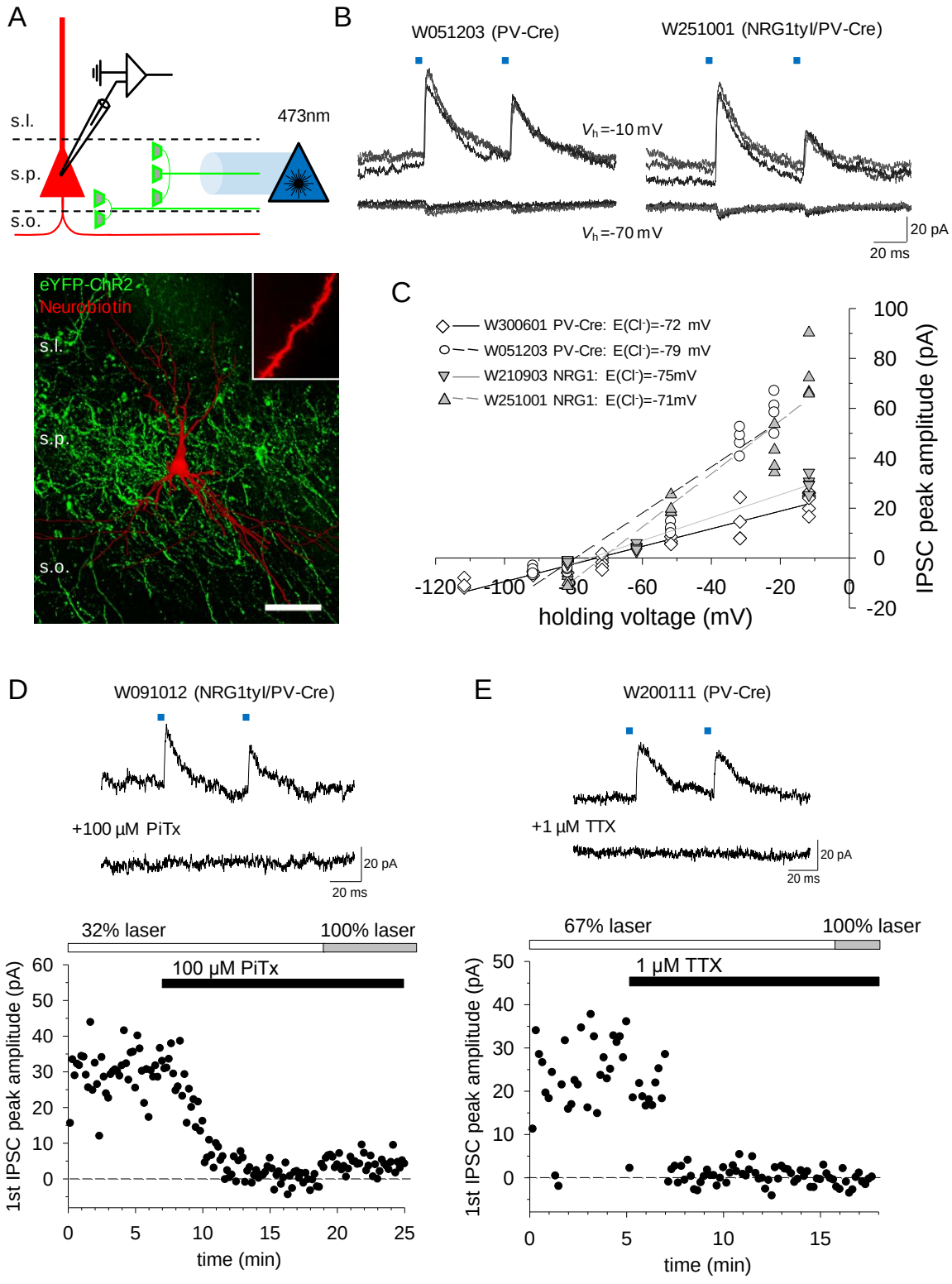

A
s.l.
s.p.
s.o.
473nm
B
W051203 (PV-Cre)
W251001 (NRG1tyI/PV-Cre)
V_h=-10 mV
V_h=-70 mV
20 pA
20 ms
eYFP-ChR2
Neurobiotin
s.l.
s.p.
s.o.
C
W300601 PV-Cre: E(Cl-)=-72 mV
W051203 PV-Cre: E(Cl-)=-79 mV
W210903 NRG1: E(Cl-)=-75mV
W251001 NRG1: E(Cl-)=-71mV
IPSC peak amplitude (pA)
holding voltage (mV)
D
W091012 (NRG1tyI/PV-Cre)
+100 µM PiTx
20 pA
20 ms
32% laser
100% laser
100 µM PiTx
1st IPSC peak amplitude (pA)
time (min)
E
W200111 (PV-Cre)
+1 µM TTX
20 pA
20 ms
67% laser
100% laser
1 µM TTX
1st IPSC peak amplitude (pA)
time (min)

Figure 4.4

Figure 4.5 Minimal intensity optical stimulation of PV+ cell axon.

(A) Gradual increase in laser stimulation power recruits individual PV+ cell axons in a step-wise manner. In this experiment, ~37% of maximum laser power elicited IPSCs in the CA3 pyramidal cell (W081101, NRG1tyI/PV-Cre; clamped at −40 mV, intracellular chloride: 8 mM). IPSCs evoked at this critical laser power (black dots) are characterised by monophasic rise and stable amplitude, and are therefore likely to represent one activated PV+ axon. When laser power was increased to 50% of maximum, a second IPSC with distinct delay (2^{nd} peak, green dot) was occasionally recruited. Note binary behaviour in the range of critical laser power (failures, open dots; successfully evoked IPSCs, black dots). Successfully activated PV+ cell axons are unlikely to show failure because each axon has several terminals with high release probability. Arrow indicates laser strength chosen in this experiment for prolonged recordings of IPSCs. Right: sample traces taken from the same experiment at indicated laser powers (blue dots represent 3 ms light pulses at 50 ms intervals; V_h, holding voltage).

(B) With critical laser power determined, cells were voltage-clamped at −10 or 0 mV to increase driving force, and IPSCs evoked by critical laser power were recorded (~30, every 10 s). (i) Paired light pulses (3 ms each at interval of 50 ms) elicited either paired IPSCs (black trace), or traces in which the second IPSC failed (blue trace), or both failed (red trace). Failures were not analysed. Inhibitory currents were characterised by (ii) low latency jitter, (iii) stable peak amplitude, (iv) fast 20–80% rise times, (v) fast half-amplitude decay times and (vi) paired-pulse depression. Inset to (v): decay tau was determined by fitting mono-exponential functions where feasible. Median values of each parameter were taken from each cell to enable comparative analysis across all cells.

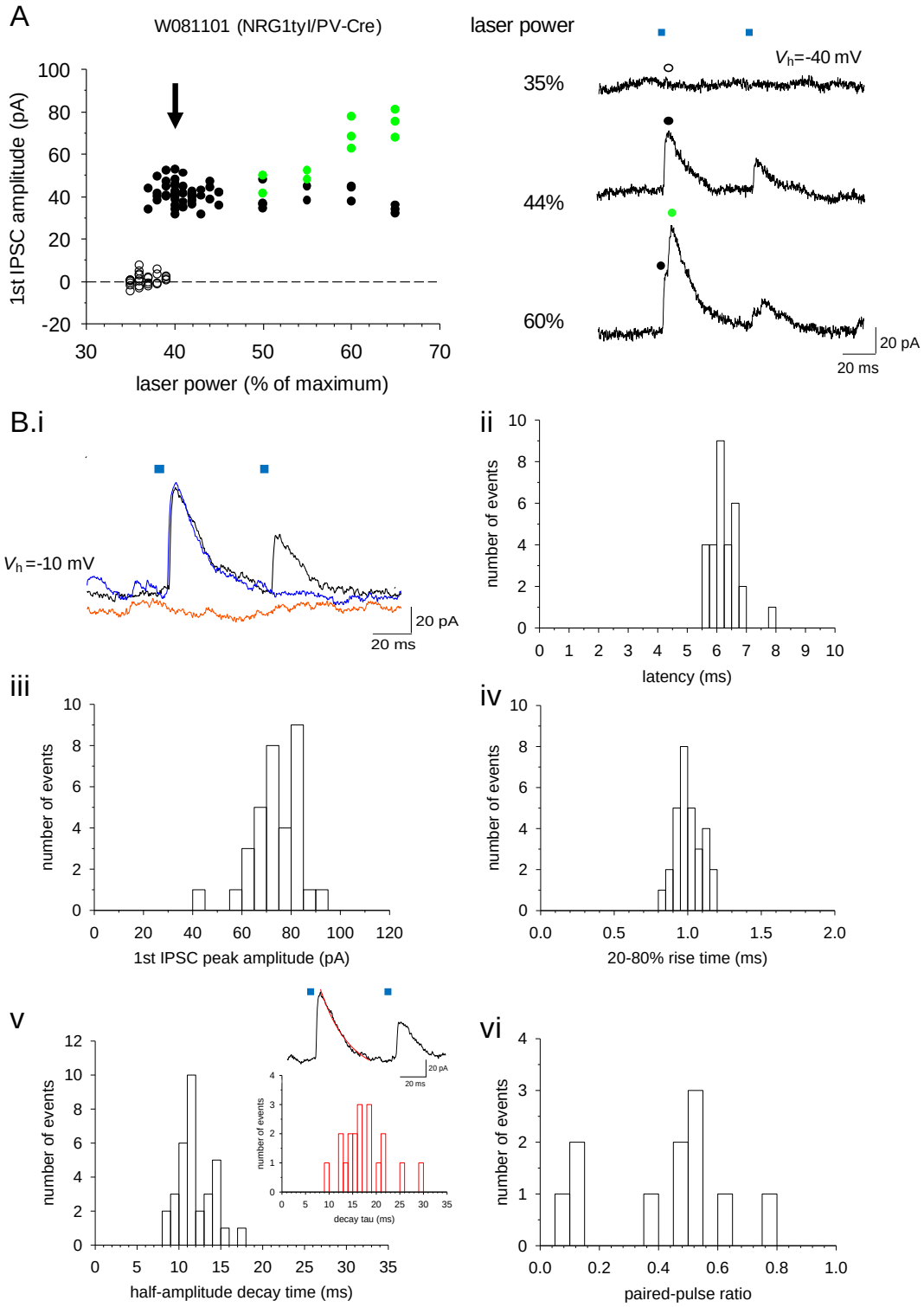

A
W081101 (NRG1tyI/PV-Cre)
1st IPSC amplitude (pA)
laser power (% of maximum)
laser power
V_h=-40 mV
35%
44%
60%
20 pA
20 ms
B.i
V_h =-10 mV
20 pA
20 ms
ii
number of events
latency (ms)
iii
number of events
1st IPSC peak amplitude (pA)
iv
number of events
20-80% rise time (ms)
v
number of events
half-amplitude decay time (ms)
decay tau (ms)
vi
number of events
paired-pulse ratio

Figure 4.5

Figure 4.6 Comparison of PV+ axon mediated IPSC properties between the two genotypes.

IPSCs were recorded from anatomically identified CA3 pyramidal cells voltage-clamped at −10 or 0 mV. PV-Cre, black; NRG1tyI/PV-Cre, red. There were no significant differences in (A) IPSC peak amplitude, (B) 20–80% rise time, (C) half-amplitude decay time, (D) decay tau or (E) paired-pulse ratio (all $p>0.05$, see Table 4.1). The histograms present medians of individual experiments. Note that half-amplitude decay time and decay tau could not be determined in one NRG1tyI transgenic pyramidal cell because of spontaneous activity and noise.

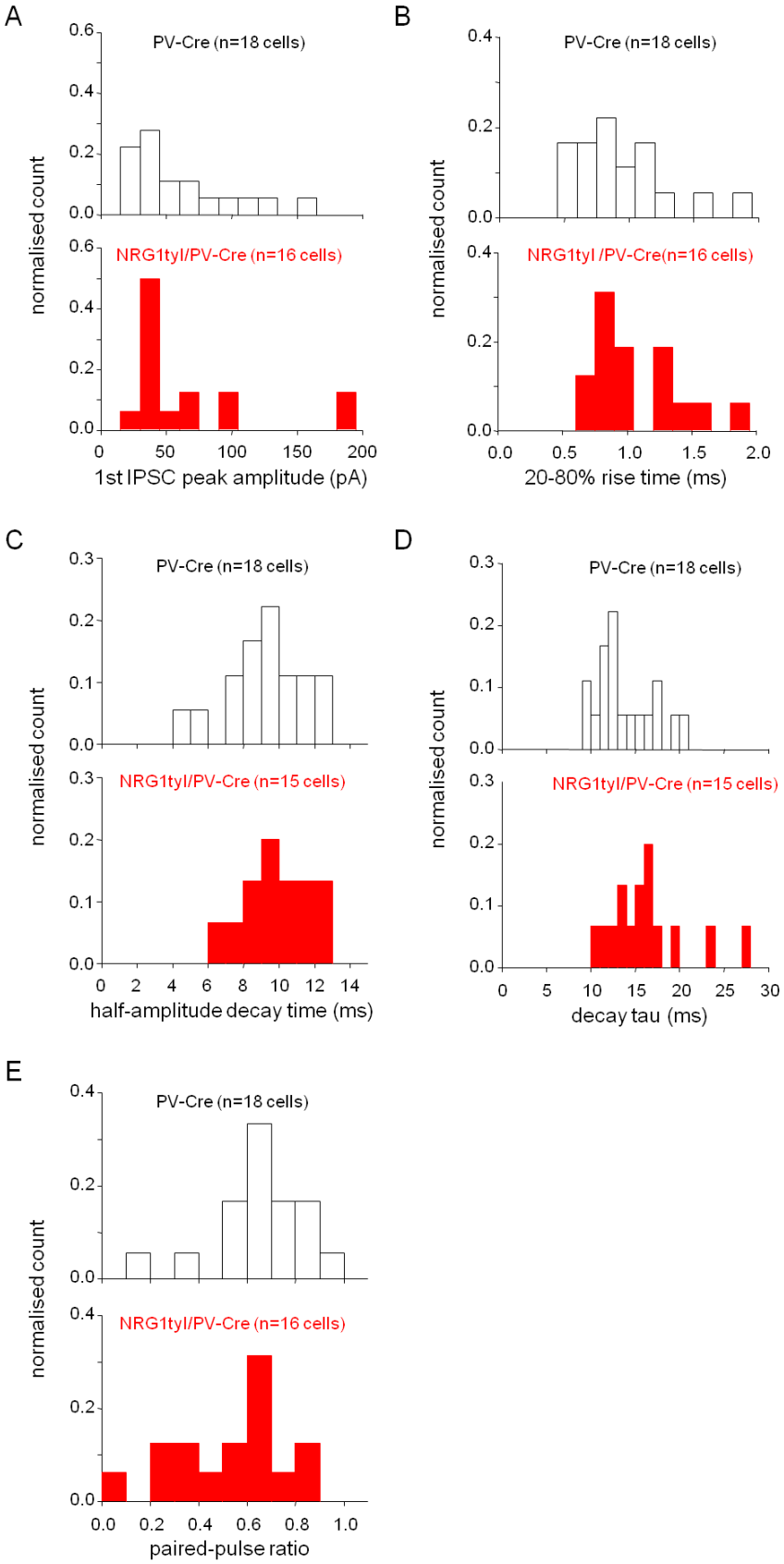

A
PV-Cre (n=18 cells)
NRG1tyI/PV-Cre (n=16 cells)
normalised count
1st IPSC peak amplitude (pA)
B
PV-Cre (n=18 cells)
NRG1tyI /PV-Cre(n=16 cells)
normalised count
20-80% rise time (ms)
C
PV-Cre (n=18 cells)
NRG1tyI/PV-Cre (n=15 cells)
normalised count
half-amplitude decay time (ms)
D
PV-Cre (n=18 cells)
NRG1tyI/PV-Cre (n=15 cells)
normalised count
decay tau (ms)
E
PV-Cre (n=18 cells)
NRG1tyI/PV-Cre (n=16 cells)
normalised count
paired-pulse ratio

Figure 4.6

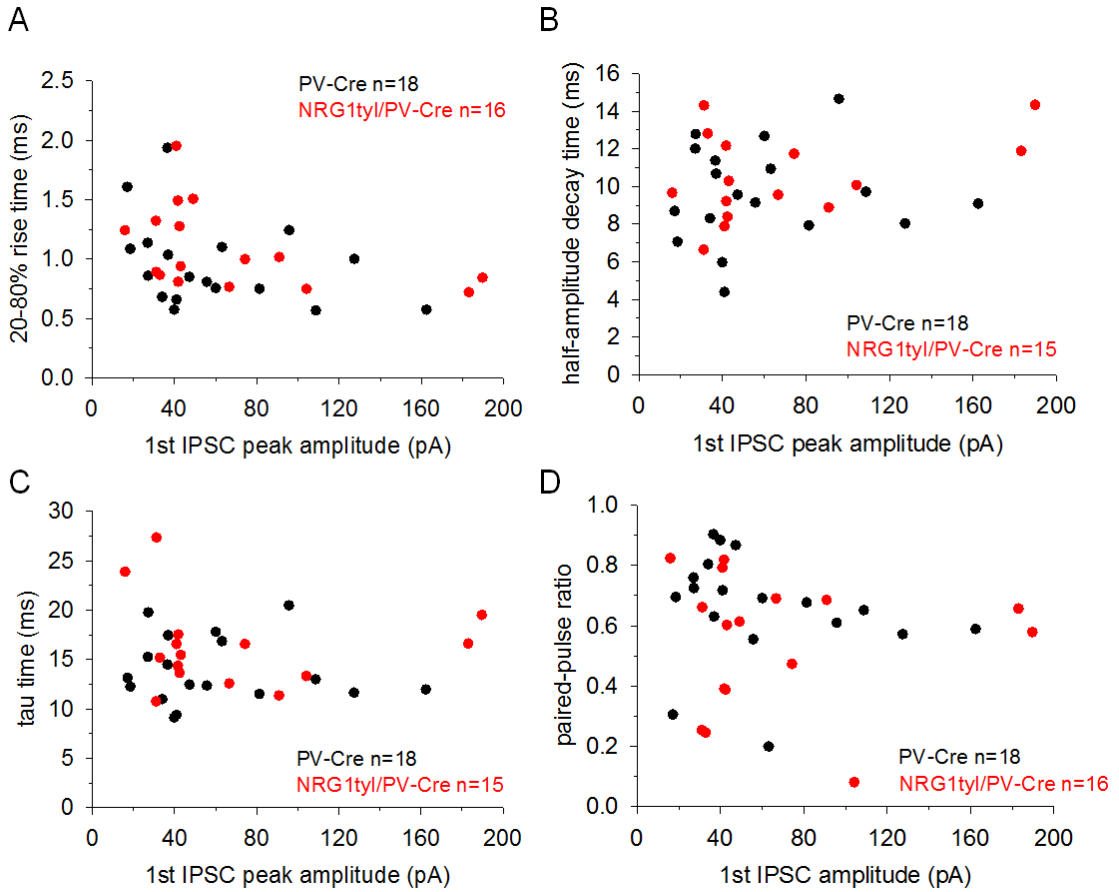


Figure 4.7 Scatter plots of IPSC properties in relation to median IPSC amplitudes.

The variability in IPSC amplitudes observed in both genotypes may result from activation of different presynaptic PV+ interneuron types (AAC vs. BCs, Szabo et al., 2010). To examine this further, the data of Figure 4.6 is presented as scatter plots of IPSC properties (20–80% rise time, half-amplitude decay time, decay tau and paired-pulse ratio) against median IPSC amplitudes of individual experiments. The scatter plots do not reveal a clear difference between genotypes in the distribution of parameters across the range of peak amplitudes, suggesting that increased NRG1tyI expression does not change CA3 PV+ cell mediated inhibition to pyramidal cells, independent of the presynaptic PV+ cell type.

5 Impairment of NMDA receptor-mediated spontaneous excitatory transmission in PV+ PTIs of NRG1tyI mice

5.1 Introduction

In the previous chapter I demonstrated that NRG1tyI over-expression fails to alter inhibitory input from PV+ GABAergic synapses to CA3 pyramidal cells. The inhibitory synapse of the feedback loop involved in generating gamma oscillations is therefore not likely to be affected by aberrant postnatal NRG1tyI expression. In this chapter, I explore the function of the glutamatergic synapses that drive these interneurons and the inhibitory feedback loop.

In a healthy CA3 hippocampal network, pyramidal cells excite PV+ interneurons through strong synapses that drive accurate spiking precision in these neurons (Miles et al., 1990; Gulyas et al., 1993b). Reduced or less synchronous excitatory recruitment of PV+ PTIs could be primary to slower compound IPSC kinetics. Indeed, such modulation has been shown to decrease gamma oscillations in mice whose PV+ interneurons lacked the BDNF receptor gene (Zheng et al, 2011), as well as in a computerised model (Volman et al., 2011). A large body of recent evidence suggests aberrant NRG1tyI expression could cause such a defect: Firstly, ErbB4 receptors are mainly expressed in somatodendritic compartments of some interneuron types, including PV+ interneurons (Huang et al., 2000; Vullhorst et al., 2009; Fazzari et al., 2010; Ting et al., 2011). Secondly, ablation of ErbB4 receptors from cortical interneurons has been reported to reduce miniature excitatory inputs to CA1 str. oriens

interneurons (Fazzari et al., 2010), although interneuron types were not further identified in that study. Following this line of evidence, one might expect NRG1tyI over-expression to result in stronger NRG1/ErbB4 signalling, thereby strenghtening interneuron recruitment, and indirectly causing stronger, longer lasting inhibitory outputs. However, as outlined earlier, research has revealed that the effects of NRG1 are diverse and do not linearly correlate with the level of NRG1 expression or signalling (Role and Talmage, 2007). Hence, increased NRG1 expression might not necessarily strengthen excitatory drive of PV+ interneurons. Thirdly, *reducing* the excitatory drive of PV+ interneurons by genetic knockout of AMPARs or NMDARs selectively in PV+ interneuron modulated hippocampal gamma oscillations, both *in vitro* (Fuchs et al., 2007) and *in vivo* (Belforte et al., 2010; Korotkova et al., 2010; Carlen et al., 2012). Finally, mice that had been pre-treated with the NMDAR antagonist MK-801 showed gamma oscillation changes similar to those in NRG1tyI mice: *in vitro* oscillations were larger in power and reduced in frequency (Kehrer et al., 2007). Taken together, altered excitatory drive of PV+ PTIs might, at least partially, underlie the prolonged gamma oscillation cycles and the altered excitation/inhibition balance in NRG1tyI mice.

As outlined in the introduction (Section 1.2.3), most principal cells and CA3 interneurons receive excitatory inputs from at least four different afferent cortical sources: mossy fibres specifically target proximal dendrites in the str. lucidum; the perforant pathway signals on distal dendrites in the str. lacunosum-moleculare; and associational (recurrent) fibres from ipsilateral area CA3 and commissural fibres from contralateral area CA3, both form synapses mainly in the str. radiatum and str. oriens. The dendritic distribution and synaptic density across laminae determines the relative strength of the inputs that different neuron types receive. For example, the strength of mossy fibre input to CA3 interneurons is interneuron type-specific. CA3 fast-spiking

BCs receive numerous but small excitatory inputs of low probability from connected mossy fibres (Szabadics & Soltesz, 2009).

Fast glutamatergic transmission in synapses on both CA3 pyramidal cells and interneurons is characteristically mediated by AMPARs/kainateRs and NMDARs (McBain & Dingledine, 1992; McBain & Dingledine, 1993; Weisskopf & Nicholl, 1995; Toth & McBain, 1998; Lei & McBain, 2002). In area CA3, synaptic AMPAR content is reported to be higher in some interneuron dendrites than in pyramidal cells (Baude et al., 1995). Kainate receptors were shown to contribute to postsynaptic excitation in some CA1 str. radiatum and str. L-M interneurons, but only in evoked not in spontaneous excitation (Wondolowski & Frerking, 2009). The NMDAR content and component is generally lower in many interneurons than in pyramidal cells in area CA1 (Sah et al., 1990; Nyiri et al., 2003). Nevertheless, mRNAs for the obligatory subunit GluN1 (NR1) and its complementary subunits GluN2A–D (NR2A–D) are expressed to different extents in different subsets of hippocampal interneurons (Monyer et al., 1994; Standaert et al., 1996). Of interest, GluN2D (the less $Mg2^{+}$-sensitive subunit isoform) has been implicated with BCs (Monyer et al., 1994), but direct, cell type-specific evidence is still missing.

Importantly, postsynaptic glutamate receptor types and their subunit compositions differ profoundly between hippocampal interneuron types (Catania et al., 1995; van Hooft et al., 2000; Blatow et al., 2005) as well as between distinct afferent inputs (Toth & McBain, 1998; Lei & McBain, 2002; Sambandan et al., 2010). Little is known about glutamatergic receptors and afferent-specific synapse compositions at identified PV+ PTIs in these areas. Some recent work on identified interneurons has shown that glutamatergic synapses on PV+ BCs in CA1 primarily consist of calcium-permeable AMPARs at Schaffer collateral synapses (Nissen et al., 2010), as do PTIs in the DG at

mossy fibre synapses (Koh et al., 1995; Geiger et al., 1997; Sambandan et al., 2010). Very little is known about NMDAR-mediated transmission in PTIs. In DG, BCs (albeit neurochemically unidentified) were not found to recruit NMDARs during spontaneous miniature excitation (Kneisler & Dingledine, 1995b) but in evoked stimulation (Kneisler & Dingledine, 1995a,b). In CA3, NMDA content at str. radiatum PV+ dendrites (of unidentified PV+ cell types) was reported to be low, with half of all synapses immunonegative for the NMDAR obligatory subunit GluN1 (Nyiri et al., 2003). Both findings suggest hippocampal BCs may contain low levels of NMDARs. However, NMDAR expression may be afferent-specific and its contribution to excitation of PTIs in DG is reported to be more prominent at mossy fibre synapses than at perforant path synapses (Sambandan et al., 2010). Similarly, mossy fibre synapses on unidentified str. lucidum interneurons (among which there may be BCs) exhibit a range of NMDARs that complement Ca^{2+}-impermeable AMPARs (Lei & McBain, 2002). In contrast, mossy fibre-pyramidal cell synapses contain only few NMDARs (Weisskopf & Nicholl, 1995).

In conclusion, the contribution of non-NMDA (AMPA/kainate) or NMDA postsynaptic receptors to neurotransmission can depend on the presynaptic input fibre and the postsynaptic interneuron type, as well as the pattern of afferent fibre activity (spontaneous miniature vs evoked; single vs repetitive).

To shed light on the synaptic coupling of pyramidal cells to PV+ PTIs in NRG1tyI mice and WT littermates, I studied miniature (TTX-insensitive) glutamatergic synaptic neurotransmission in these interneurons. Miniature EPSCs recorded in the absence action potentials represent responses elicited by spontaneous release of a single quantum with some heterogeneity between release sites (Bekkers et al., 1990). Furthermore, I explored the excitatory connectivity between CA3 pyramidal cells to

further elucidate the increased excitation/inhibition balance in NRG1tyI mice (Chapter 3). Because NMDAR function is implicated in the pathopysiology of schizophrenia, I discriminated AMPAR- and NMDAR-mediated neurotransmission by sequentially voltage-clamping whole-cell patch-clamped neurons at −65 mV and +40 mV, respectively, in combination with pharmacological blockage of AMPARs/kainateRs.

5.2 The search for a suitable reporter mouse

As mentioned in Chapter 4, recordings from PTIs generally yield low success because their somata are often located within the tightly packed hippocampal pyramidal layer (Freund & Buzsaki, 1996). Thus, most studies take advantage of suitable fluorescent reporter mice (e.g. PV-eGFP mice, Meyer et al., 2002). However, the commercially available GAD67-eGFP mouse strain (line 42; Jackson Laboratory, MA, USA; strain name: CB6-Tg(Gad1-EGFP)G42Zjh/J, strain code: 007677) which has been reported to express eGFP in PV-expressing interneurons in the neocortex (Chattopadhyaya et al., 2004), did not show detectable eGFP expression in the hippocampus of 3–6-week-old-mice (unpublished observation). The viral-delivery approach of Chapter 4 yielded eGFP-ChR2 expression mainly in axons rather than somatodendritic compartments of PV+ interneurons, so is also unsuitable for somatic recordings. I screened two other reporter lines.

The first were homozygous PV-Cre/R26R-eYFP mice (Methods 2.1.2) that express eYFP in PV-containing neurons, achieved by driving eYFP expression from the ubiquitous *Gt(ROSA)26sor* locus in a loxP/Cre-dependent manner (Srinivas et al., 2001). However, acute hippocampal slices from heterozygous mice crossbred with NRG1tyI (NRG1tyI/PV-Cre/R26R-eYFP) did not contain detectable eYFP signals at P22–P33, possibly due to weakening of the Rosa26 locus with postnatal age (Madisen

et al., 2010). Consequently, this approach was also not suitable for reporting PV expression in heterozygous 1-month-old mice. Stronger postnatal promoters (such as the novel, commercially available ai9 strain; Madisen et al., 2010) with loxP-restricted fluorescent reporter expression were not available at the time of this study.

The second examined transgenic mouse strain, LIM homeobox protein 6 (Lhx6)-eGFP transgenic mice, were locally available and well-suited for the purpose of my study (Methods 2.1.3). Here, eGFP expression is driven by the regulatory sequence of the Lhx6 gene, which is active in PV+ and some other interneurons. Specifically, Lhx6 is a transcription factor that is expressed in a subset of migrating cortical interneurons that later differentiate into PV+, SOM+, CR+ and NPY+ interneurons in the neocortex and hippocampus (Cobos et al., 2005; Cobos et al., 2006; Liodis et al., 2007). Approximately 90% of PV+ cells and ~92% of SOM+ cells co-express Lhx6 in hippocampus, whereas co-labelling with CR+ interneurons occurs to a smaller degree (~50% of CR+ cells, Liodis et al., 2007) and even less in the neocortex (~3–15% of NPY+ cells, ~2–5% of CR+ cells; Cobos et al., 2005; Cobos et al., 2006). Of particular interest, Lhx6 continues to be expressed in the same pattern postnatally and in adult mice (Cobos et al., 2005). Therefore, older Lhx6-eGFP mice (>1 month old) can serve as reporter mice for PV+, SOM+ and some CR+ interneurons types in hippocampus. Previous studies have employed heterozygous Lhx6-eGFP mice to study the postnatal development of PV+ PTIs in the DG (Sauer & Bartos, 2010), or the role of interneurons in the basal ganglia circuit (Gittis et al., 2010). Here, Lhx6-eGFP mice crossbred with NRG1tyI mice were used to increase the yield of PV+ interneurons in acute hippocampal slices. *Post hoc* anatomical identification was required to unequivocally distinguish PTIs from dendrite-targeting cell types (some of which are PV+ and SOM+) and interneuron-specific interneurons (CR+) in both genotypes.

5.3 Results

5.3.1 Anatomical identification of cell types

Lhx6-eGFP+ somata in or close to the str. pyramidale were patched along the entire dorso-ventral CA3 axis in Lhx6 or NRG1tyI/Lhx6 mice, and filled with neurobiotin for subsequent visualisation. In total, I recorded miniature EPSCs (mEPSCs) from 122 cells from 25 Lhx6 mice (2 $Lhx6^{+/+}$ mice, 23 $Lhx6^{+/-}$ mice) and 21 NRG1tyI/Lhx6 mice ($NRG1tyI^{+/-}$ × Lhx6 $^{+/-}$), along with 9 cells from 4 $NRG1tyI^{+/-}$ mice (no Lhx6-eGFP reporter gene). Mice were 3–10 weeks old to match the age of the mice in which altered CCh-induced gamma oscillations were observed. Of the 131 recorded cells, 90 were successfully and sufficiently labelled with neurobiotin for identification of cell type. In the remaining 41 recorded cells, labelling in axons was not successful or sufficient for unequivocal cell type identification. Based on axon arborisation across CA3 laminae, the absence of mushroom-like spine-bearing dendrites and multipolar soma shape, 74 cells were anatomically identified as CA3 interneurons. The majority of these (57 of 74 CA3 interneurons) had axons that arborised heavily in strata other than pyramidale (i.e. strata oriens, lucidum, radiatum and lacunosum-moleculare). This was expected because, as outlined above, Lhx6-containing cells co-express not only PV but also SOM, CR and NPY (Cobos et al., 2005; Cobos et al., 2006; Liodis et al., 2007), which are neurochemical markers of multiple cell types including dendrite-targeting (e.g. ivy cells: NPY+; bistratified cells, at least in CA1: PV+/SOM+/NPY+), perisomatic-targeting (e.g. BCs: PV+; AACs: PV+) and interneuron-specific interneurons (CR+). Because PTIs but not dendrite-targeting interneurons or interneuron-specific interneurons are primarily involved in the generation and maintenance of gamma oscillations (Introduction 1.3.2), these cells were not analysed

further, either anatomically or electrophysiologically. The remaining 17 of 74 recorded and successfully labelled CA3 interneurons had axons primarily arborising inside and close to str. pyramidale. These PTIs, 9 recorded in Lhx6 mice and 8 in NRG1tyI/Lhx6 or NRG1tyI mice, were carefully analysed for their anatomical, neurochemical and electrophysiological properties (Section 5.3.1.1 and Table 5.1). To strengthen the study, the analysis incorporated three additional PTIs recorded in Lhx6 mice by other group members (two by Linda Avena, M.Sc. Neuroscience and one by Matthew Prior, FHS, Department of Pharmacology).

The remaining 16 successfully labelled cells were anatomically identified as CA3 pyramidal cells based on the presence of characteristic mushroom-like spines on dendrites, their characteristic dendritic tree and triangular-shaped somata located near or within str. pyramidale (Section 5.3.3 and Figure 5.5A).

5.3.1.1 Axo-dendritic structure of CA3 PTIs

All 20 PTIs were digitally reconstructed from two to four 50–60 µm thick sections to unambiguously determine the axon distribution across all strata in each cell (sections that contained the majority of *in vitro* recovered axons were chosen; Methods 2.7.2.1 and Table A4 in the Appendix). Cell visualisations (Figures 5.1, 5.2 and A1) illustrate the variability in axon arborisation: the axonal arbour of some PTIs was more dense and concentrated in str. pyramidale, with axon collaterals inside str. lucidum (reminiscent of typical CA1 BCs; and similar to examples in Szabo et al., 2010 and Gulyas et al., 2010). Other PTIs arborised more heavily at the border of str. pyramidale and str. oriens, in addition to emitting axonal projections into str. lucidum and str. radiatum.

Given their postulated distinct roles in gamma oscillations (Bartos et al., 2007; Gulyas et al., 2010), I aimed to distinguish AACs from BCs using two principal criteria: firstly, their distinct axonal patterns inside the pyramidal cell layer (Nissen et al., 2010);

and secondly, the presence of close appositions of neurobiotin-filled AAC axon collaterals with Ankyrin-G-labelled initial segments. Ankyrin-G is a scaffolding protein that is abundant at the AIS of neurons and used as a marker for AIS (e.g. Szabo et al., 2010). Six of 20 PTIs had axons with prominent boutons forming radial rows that followed the AIS of pyramidal cells, typical of AAC (Somogyi, 1977; Somogyi et al., 1983). In five of these six cells, tight appositions of neurobiotin-filled boutons (visualized with Streptavidin-conjugated Cy3) to Ankyrin-G-labelled AIS were found on at least three separate Ankyrin-G-labelled AIS (Figure 5.2; Table 5.1). In one additional putative AAC, Ankyrin-G staining was not sufficient at the tissue depth of neurobiotin-labelled axon to determine immunoreactivity (tested independently in three 60 µm thick sections; Methods 2.7.3 for technical difficulties). Because of its vertical axon cartridges in the CA3 pyramidal cell layer and its prominent boutons, this cell was still classified as an AAC (W050712; Figure A1). In all, four cells from four Lhx6 mice and two cells from two NRG1tyI/Lhx6 mice were anatomically identified as AACs.

The remaining 14 PTIs did not have axon with radial bouton rows, but the majority of their axon collaterals were inside the pyramidal layer, often spreading into the neighbouring str. oriens or str. lucidum. To quantify the laminar distribution of axon in these 14 cells, the proportion of axon pixels across all strata was analysed in two-dimensional digital images of reconstructed cells (Methods 2.7.2.1). For pooling data, the counted axon pixels of individual cells were divided into horizontal bins as proportions, and pixels in similar laminar bins were summated (strata pyramidale and lucidum, 1 bin each; strata radiatum and oriens, 3 bins each). The average laminar distribution of axon across the 8 interneurons recorded in Lhx6 mice confirms that the majority of the *in vitro* recovered axon arborised inside str. pyramidale (42.7 ± 3.2% of normalized axon pixels, Figure 5.1B). The averaged distribution of axon over all

laminae was similar across six interneurons recorded in NRG1tyI/Lhx6 mice (46.1 ± 4.8% in str. pyramidale). This indicates that NRG1tyI over-expression did not grossly change the axon morphology of CA3 PTIs. Interestingly, in both genotypes, axon arborisation was biased more to the upper third of str. oriens than str. lucidum (see cell reconstructions and Figure 5.1B). It is not clear if this bias reflects *in vivo* axon arborisation, or an artefact associated with the cutting angle at which horizontal hippocampal slices were prepared. Recently published work on *in vitro* recorded CA3 PTIs has not elaborated on the variability in BC axon arborisation (Szabadics and Soltesz, 2009; Gulyas et al., 2010; Szabo et al., 2010). Five of the 14 PTIs were randomly selected to test immunoreactivity to Ankyrin-G (Methods 2.7.3 for technical difficulties). In two of these five cells, immunoreactivity to Ankyrin-G was successful at the tissue depth of neurobiotin-filled boutons, but in both cells tight appositions to Ankyrin-G-containing AIS could not be observed (Figure A2, Table 5.1). Hence, these two interneurons are unlikely to synapse onto AIS of CA3 pyramidal cells, so they are likely to be BCs. Despite the lack of electron microscopy evidence and systematic proof for the absence of immunoreactivity to Ankyrin-G, I propose the population of 14 interneurons to be classified as putative fast spiking BCs, given their axon arborisations concentrate inside str. pyramidale yet lack the prominent radial rows of boutons that characterise AACs.

All cells (with the exception of one AAC cell) were recorded from Lhx6-eGFP-containing somata in acute slices (Table 5.1). Given that the Lhx6-eGFP signal is primarily expressed in PV+ and SOM+ interneurons of the hippocampus (Liodis et al., 2007), and that PTIs express either PV or CCK (and CB1R) but not both or any other neurochemical markers (at least in area CA1; reviewed in Somogyi, 2010), it is likely

Table 5.1 Anatomically identified CA3 BCs and AACs

Cell code	Genotype	Recovered cell compartments	Immunoreactivity			
			GFP	PV	CB1R	Ankyrin-G
CB1R− putative BCs (n=14)						
W180511	Lhx6	ax	-		-	
W060712	Lhx6	ax, d, s	+	-	-	
W150712	Lhx6	ax	-		-	
L150711	Lhx6	ax, d, s	+	-	-	
L200711	Lhx6	ax (in CA3a)	+		-	
W240813	Lhx6	ax, d, s	+	-	-	n.t.
W250812	Lhx6	ax	-		-	-
M260812	Lhx6	ax	-		-	n.t.
W220612	NRG1tyI/Lhx6	ax	+		-	n.t.
W280612	NRG1tyI/Lhx6	ax, d, s	+	-	-	
W010713	NRG1tyI/Lhx6	ax, d, s	-	-	-	
W140711	NRG1tyI/Lhx6	ax	+		-	
W100813	NRG1tyI/Lhx6	ax, d, s	+	-	-	
W100815	NRG1tyI/Lhx6	ax, d, s	-	-	-	-
AACs (n=6)						
W120512	Lhx6	ax	-		-	+
W050712	Lhx6	ax, d, s	+	-	-	n.t.
W150713	Lhx6	ax, d, s	-	+ (faint)	-	+
W250713	Lhx6	ax, d, s	-	+	-	+
W220611	NRG1tyI/Lhx6	ax, d, s	+	+	-	+
W150812	NRG1tyI	ax, d, s	n.a.	+	-	+

GFP denotes the immunoreactivity of fixed tissue. Immunoreactivity for PV was never successful in axon of whole-cell recorded cells (see text), so it was not tested in cells in which the somatodendritic structure was lost. BC, basket cell; AAC, axo-axonic cell; AIS, axon initial segment; ax, axon; d, dendrites; s, soma; +, immunopositive; -, immunonegative; n.a., not applied (recorded in non-reporter mouse); n.t., not tested, e.g. insufficient Ankyrin-G staining at the tissue depth of neurobiotin-labelled axon, see text.

that all PTIs presented here are either PV+ AACs or PV+ (putative) BCs. To confirm the neurochemical properties of the interneurons, I tested the immunoreactivity of all 14 putative BCs and 6 AAC to GFP, PV and CB1R (Table 5.1): immunopositivity for both

GFP and PV could be shown in some but not all interneurons, probably because both markers are cytosolic proteins and subject to wash-out during 20 min somatic whole-cell recordings. Indeed, the somatic eGFP signal was lost within ~10 min of electrophysiological recording from the soma when the cytosol was diluted with intracellular solution. This confirmed that it was the targeted Lhx6-eGFP-containing soma that had been patched (rather than a nearby pyramidal cell). Interestingly, immunoreactivity for PV was recovered in somatodendritic compartments of most AACs but never in somata or dendrites of putative BCs (despite ~30–45 min slice recovery after recordings). Differences in the PV concentration in these two interneuron types might explain this finding if BCs contained less PV than AACs (but see discussion). Finally, it should be noted that immunoreactivity for PV was never observed in axons, not even in cells whose somata and dendrites were PV+. The reason for this is unclear, but our group has previously encountered this problem in whole-cell recordings of PV+ CA1 interneurons (unpublished observation). Thus, I did not routinely check immunoreactivity for PV in interneurons in which the somatodendritic structure had been lost after recording (Table 5.1). Unlike PV and GFP, CB1R is a membrane-bound protein and thus a more reliable marker as it cannot be easily washed out of the cell membrane. Importantly, immunoreactivity to CB1R was negative in axons of all PTIs, thereby confirming they were *not* CB1R-containing BCs (Glickfeld and Scanziani, 2006).

In conclusion, mEPSCs were recorded from 14 identified Lhx6-eGFP+, CB1R− PTIs that lacked prominent axon cartridges and are therefore referred to as putative BCs. Because CB1R and PV are mutually exclusive neurochemical markers for CA1 BCs (Somogyi & Klausberger, 2005), it is likely that these CB1R− putative BCs were in fact PV+ prior whole-cell recording. Furthermore, six Lhx6-eGFP+, CB1R− PTIs

were identified as AACs based on their axonal pattern and the presence of boutons in close apposition to Ankyrin-G-labelled AIS.

While axon morphology is an essential feature to distinguish interneuron types, dendritic morphology is of interest to understand possible excitatory inputs to CA3 PTIs. The *in vitro* recovered dendritic trees varied greatly in length and laminar extension between putative BCs and AACs: in some cells, dendrites extended only a couple of hundred micrometers into strata oriens, pyramidale and lucidum/ lower radiatum; in other putative BCs and most AACs, dendrites projected several hundred micrometers into str. lacunosum-moleculare or the hilus of DG (compare cell visualisations in Figures 5.1, 5.2 and A1; note these visualisations contain most of but not the complete *in vitro* recovered dendritic trees of all sections). Dendritic trees may have been more extensive *in vivo* but cut during *in vitro* slice preparation or re-sectioning, because, in CA1, dendrites of PV+ interneurons are reported to span all layers (Gulyas et al., 1999). Furthermore, dendritic trees are likely to vary depending on the CA3 subfield and dorso-ventral location in the hippocampus. I did not observe any gross morphological difference in the dendritic tree of either putative BCs or AACs between genotypes. Dendrites of both genotypes were often 'beaded', i.e. contained varicosities that possibly reflect the high density of mitochondria, typical of high-energy-demanding PV+ BCs (Gulyas et al., 1999; Gulyas et al., 2006). Whether AACs and BCs differ in their dendritic length and ramification in distant str. lacunosum-moleculare has been debated in CA1 (Li et al., 1992; Gulyas et al., 1999), but this was not studied here. In six cells, the somatodendritic compartment was not recovered following whole-cell recording. Because these cells received synaptic excitatory input, it is likely that the somato-dendritic structure was irreversibly damaged when retracting the patch pipette at the end of the whole-cell recording.

Given the variability of dendrite morphology, the input pathways of mEPSC to CA3 putative BCs and AACs cannot be unequivocally determined, but the majority of inputs presumably originated from the strata oriens, lucidum and radiatum. Inputs to str. lacunosum-moleculare may contribute to a minor degree, but, due to the large electrotonic distance, perforant pathway synapses at PTIs are most likely strongly affected by dendritic filtering, which also affected mEPSCs in str. radiatum interneurons (McBain & Dingledine, 1993).

5.3.2 Unaltered AMPAR- but smaller NMDAR-mediated mEPSCs in PTIs of NRG1tyI mice

Miniature EPSCs were recorded in whole-cell mode (intracellular solution: Cs-Methanesulfonate with 5 mM QX-314) in the presence of GABA-A and -B receptor blockers (picrotoxin, 100 µM; CGP-55845, 1 µM) and tetrodotoxin (1 µM). To discriminate spontaneous miniature events mediated by AMPARs/kainateRs and NMDARs, cells were first clamped at −65 mV, and mEPSCs were recorded for 3 min. AMPA/kainateRs were then blocked by NBQX (25 µM); this eliminated all mEPSCs at −65 mV in all putative BCs and AACs, thus verifying they were mediated by non-NMDARs (Figures 5.3A and D). Next, cells were voltage-clamped at +40 mV in the continuous presence of NBQX in order to record NMDAR-mediated mEPSCs for 3 min. In a subset of putative BCs and in one AAC (Table A4), AP5 (100 µM) was applied at the end of the recording to verify that mEPSCs at this potential were mediated solely by NMDARs (Figures 5.4A and D).

Recording conditions were similar for cells of both genotypes: access resistances for whole-cell recordings of putative BCs and AACs, assessed during voltage-clamp at −65 mV, ranged between 11 and 44 MΩ (Lhx6: 11−44 MΩ, n=12; NRG1tyI/Lhx6: 12–33 MΩ, n=8; p=0.347; Table 5.2). Input resistances in Lhx6+ putative BCs were similar

to those in NRG1tyI mice (median ~200 MΩ for both; Table 5.2). Median input resistances in AACs were also comparable (Lhx6: 187.02 MΩ, *n*=4; NRG1tyI/Lhx6: 145.41, *n*=2), but statistical comparison was not feasible due to low cell numbers. The finding of similar input resistances in putative BCs (and possibly AACs) in both genotypes provides the first evidence that NRG1tyI over-expression does not change the passive leak conductance of these interneurons. However, one has to be careful in this interpretation, because the use of Cs-based intracellular solution precludes the estimation of resting K^+ conductances. Consequently, intrinsic membrane properties such as resting membrane potential cannot be measured.

Miniature EPSCs were analysed in 120 s-long, band-pass filtered (4 Hz–6 kHz; Figures 5.3 and 5.4) recordings using automatic threshold detection (pCLAMP10 software, Molecular Devices, CA, USA). Criteria for threshold detection (amplitude/event duration) were carefully selected in a subset of cells to ensure reliable detection of visually verified events at each voltage potential and to minimise false positives (Methods 2.6.3). Note that the criteria for detection of NMDAR-mediated events differed slightly due to greater noise at this voltage. To ensure valid comparison between genotypes and cell types, NMDAR-independent or NMDAR-mediated mEPSCs were analysed with the same respective criteria across all cells. Pharmacological blockade of relevant glutamate receptors (AMPARs/kainateRs; NMDARs) significantly reduced the number of detected events (NBQX: by 82–100%, Figure 5.3D; AP5: by 96–100%, Figure 5.4D), ensuring minimal false positive detection at the chosen threshold settings. Detected events were automatically analysed for maximum current amplitudes and current integrals (area under the curve from onset to event end). The latter is indicative of the quantal charge of a single event. Together with mean frequency, these parameters provide characterisation of post- and presynaptic

efficacy. Current kinetics could not be reliably determined by this automated approach, because noise in the traces severely compromised measurement of time to peak and decay time. Consequently, and because the competitive antagonist NBQX does not discriminate between AMPAR and kainateR (unlike e.g. GYKI 53655, an AMPAR-selective antagonist), I cannot exclude the possibility that kainateRs contributed to mEPSCs, as has been described in some CA1 interneurons (Goldin et al., 2007). However, kainateRs would be expected to give rise to event kinetics slower than those observed in mEPSCs in putative BCs and AACs in this study (time to peak ~1 ms, see Figure 5.3A; Frerking et al., 1998; Cossart et al., 2002). For this reason, I refer to events recorded at −65 mV as 'AMPAR-mediated' events.

AMPAR-mediated mEPSCs

Miniature EPSCs recorded in putative BCs at −65 mV generally exhibited small but variable peak amplitudes (~10–120 pA; sample traces in Figure 5.3A). Occurrence histograms of all detected mEPSC amplitudes revealed skewed distributions in putative BCs of both genotypes (Figure 5.3B), which is in line with previous reports of mEPSCs in CA3 str. radiatum interneurons (McBain & Dingledine, 1993) and in CA3 pyramidal cells (McBain & Dingledine, 1992). Although dendritic filtering probably contributed to amplitude distribution by attenuating EPSCs from more distant inputs, event amplitudes were positively correlated to the time to peaks in two individual experiments (Lhx6: ρ=0.158, p<0.001, n=743 detected events, Spearman's correlation; NRG1tyI/Lhx6: ρ=0.115, p=0.01, n=499, Spearman's correlation, see insets in Figure 5.3B). Electrotonic attenuation would be expected to affect both measures equally, and give rise to a weak negative linear correlation (i.e. EPSCs of more distal dendritic origin tend to be smaller and exhibit slower time to peak; Rall, 1969). Therefore, dendritic filtering of AMPAR-mediated mEPSC is an unlikely contributory factor to explain the skewed

amplitude distribution in both genotypes. Instead, afferent pathway-specific differences in presynaptic quantal content, transmitter release mechanisms or in postsynaptic glutamate receptors (density and subunit compositions) might better explain the skewed distribution (discussed in McBain & Dingledine, 1993). Whatever the cause(s), the effect appeared to influence the distribution of mEPSC amplitudes equally when NRG1tyI was over-expressed. Dealing with non-normal distributions, I obtained median (rather than mean) values of mEPSC parameters (amplitude and area) from individual recordings for comparison across cell types. Table 5.2 provides an overview of the mean ± SEM and median values calculated from (median) parameters across cell types in both genotypes, and lists the *p*-values of appropriate statistical comparisons between genotypes. All statistical comparisons were repeated using *mean* values from individual recordings, but this revealed qualitatively similar statistical results.

Across all eight putative BCs recorded in Lhx6 mice, AMPAR-mediated mEPSCs were detected at variable frequencies (1.8–9.4 Hz; Figure 5.3C.i), and NRG1tyI over-expression did not significantly affect the range (2.5–8.6 Hz, n=6; p=0.796, Table 5.2). Furthermore, mEPSCs of both genotypes exhibited similar median amplitudes (p=0.689; Figure 5.3C.ii) and median areas (p=0.487; Figure 5.3C.iii), thus showing that NRG1tyI over-expression does not significantly alter miniature AMPAR-mediated synaptic transmission, neither pre- nor postsynaptically. These results were unexpected, as recent reports have demonstrated involvement of ErbB4 receptors in the excitatory recruitment of interneurons in the CA1 str. oriens and suggested a role of NRG1tyI/ErbB4 signalling in the synaptic wiring of interneurons, particularly of PV+ ones (Fazzari et al., 2010; Ting et al., 2011). However, Fazzari and colleagues (2010) did not identify cell types, therefore a different (possibly PV+) interneuron type might have been affected. Consequently, I analysed AMPAR-mediated mEPSCs in AACs of

Table 5.2 Statistical comparison of mEPSC parameters in putative BCs, AACs and CA3 pyramidal cells of Lhx6 and NRG1tyl/Lhx6 mice

		Putative BC			**AAC**			**Pyramidal cell**		
		Lhx6	NRG1tyI/Lhx6	*p*-value	Lhx6	NRG1tyI/Lhx6	*p*-value	Lhx6	NRG1tyI/Lhx6	*p*-value
R_{access} (MΩ)	mean ± SEM	23.89 ± 3.94	19.02 ± 2.25	0.347	26.17 ± 5.09	29.35 ± 3.26	n.a.	16.00 ± 1.01	17.15 ± 2.14	0.670
	median	21.37	17.92		29.67	29.35		16.30	17.70	
R_{input} at -65 mV (MΩ)	mean ± SEM	252.27 ± 46.95	192.75 ± 13.27	0.308	179.63 ± 16.50	145.41 ± 6.10	n.a.	216.90 ± 44.34	166.13 ± 16.84	0.323
	median	210.38	206.59		187.02	145.41		216.11	149.55	
R_{input} at +40 mV (MΩ)	mean ± SEM	144.54 ± 25.98	111.80 ± 16.63	0.330	98.35 ± 4.06	94.11 ± 13.78	n.a.	78.89 ± 12.36	60.27 ± 6.21	0.164
	median	136.94	92.78		97.74	94.11		81.05	57.90	
AMPAR-mediated mEPSCs (V_h=−65 mV)										
n		8	6		4	2		6	8	
frequency (Hz)	mean ± SEM	4.07 ± 0.92	4.03 ± 0.96	0.796[a]	6.14 ± 1.16	5.16 ± 1.74	n.a.	1.46 ± 0.18	1.28 ± 0.33	0.195[a]
	median	3.43	3.28		6.06	5.16		1.31	0.94	
median amplitude (pA)	mean ± SEM	-26.17 ± 2.27	-24.93 ± 1.69	0.689	-23.53 ± 2.07	-18.88 ± 3.63	n.a.	-20.71 ± 2.81	-20.56 ± 1.23	0.245[a]
	median	-26.63	-24.23		-23.64	-18.88		-18.24	-20.75	
median area (pA·ms)	mean ± SEM	-49.89 ± 4.91	-54.41 ± 3.11	0.487	-56.07 ± 2.40	-45.97 ± 5.74	n.a.	-76.28 ± 9.46	-89.48 ± 7.89	0.302
	median	-48.90	-54.86		-55.66	-45.97		-75.22	-92.29	
NMDAR-mediated mEPSCs (V_h =+40 mV)										
n		7[b]	6		4	2		4[b]	7[b]	
frequency (Hz)	mean ± SEM	2.80 ± 1.16	1.73 ± 0.63	0.454	0.16 ± 0.10	0.00	n.a.	1.62 ± 0.61	1.32 ± 0.63	0.345[a]
	median	2.48	1.52		0.09	0.00		1.40	0.86	
median amplitude (pA)	mean ± SEM	26.07 ± 2.22	17.30 ± 3.60	0.032*[a]	19.17 ± 1.17	0.00	n.a.	23.98 ± 3.70	21.40 ± 0.93	0.850[a]
	median	23.25	20.92		18.16	0.00		20.97	21.11	
median area (pA·ms)	mean ± SEM	138.93 ± 25.49	79.23 ± 17.42	0.089	131.92 ± 43.38	0.00	n.a.	132.17 ± 6.02	139.36 ± 18.63	0.785
	median	123.99	90.97		124.69	0.00		135.39	131.33	

*p<0.05

[a] Mann–Whitney U-test **(**non-normal distributions); other *p*-value data: independent samples t test (normal distributions)

[b] One putative BC in Lhx6 mouse could not be analysed at +40 mV due to electrical noise; not all pyramidal cells were recorded at +40 mV

n.a., not applicable due to low *n* numbers of AAC in NRG1tyI mice (*n*=2)

Lhx6 and NRG1tyI/Lhx6 mice: there was no indication of a difference in frequency (Figure 5.3C.i), median amplitude (Figure 5.3C.ii) or median area (Figure 5.3C.iii), although these results should be interpreted with caution since cell numbers were low (n=2 in transgenic mice). Miniature mEPSCs in both cell types of both genotypes were effectively blocked by NBQX, thereby confirming sole involvement of non-NMDARs at this voltage and validating the analysis criteria (Figure 5.3D).

NMDAR-mediated mEPSCs

Given the implication of interneuronal NMDARs in schizophrenia (Lisman et al., 2008) as well as their proposed involvement in setting gamma frequency, both *in vitro* (in conditions of reduced tonic inhibition; Mann & Mody, 2010) and *in vivo* (Korotkova et al., 2010), I investigated whether NRG1tyI over-expression altered the properties of NMDAR-mediated mEPSC in CA3 putative BCs and AACs. Event detection was optimised for reliable automatic detection of visually verifiable mEPSCs (Methods 2.6.3): the occurrence of mEPSCs was effectively eliminated (to <4%) in the presence of AP5 across all putative BCs and in one AAC (Figure 5.4D).

When voltage clamped at +40 mV, putative BCs exhibited clear albeit small amplitude quantal mEPSCs with slower kinetics than AMPAR-mediated events (traces in Figure 5.4A). NMDAR-mediated miniature events were detected at lower frequencies than AMPAR-mediated events, but, importantly, there was no frequency difference between BCs of the two genotypes (p=0.454; Figure 5.4C.i and Table 5.2). However, NMDAR-mediated mEPSCs in putative BCs of NRG1tyI mice had smaller median amplitudes than events in putative BCs of Lhx6 littermates. The amplitude distributions in the two genotypes were significantly different (p=0.032, Mann-Whitney U test; Figure 5.4C.ii and Table 5.2). Interestingly, in one NRG1tyI/Lhx6 mouse BC, no mEPSCs were detected at a voltage-clamping potential of +40 mV with the standard

threshold criteria. Visual inspection of the trace also revealed no prominent mEPSC events. However, in most recordings, application of AP5 typically reduced background noise (see traces during application of AP5 in Figure 5.4A). A similar observation has previously been made (McBain & Dingledine, 1992: see particularly Figure 7 and discussion), and might indicate the existence of a population of mEPSCs that are not clearly visually evident (or difficult to resolve at this voltage), yet are distinct AP5-sensitive events. Therefore, I re-analysed the data using a lower amplitude threshold (5 pA instead of 7 pA): mEPSCs were still effectively blocked (to <5%) in the presence of AP5, although not all events were visually evident (Figure A3). This analysis yielded a similar number of events in each genotype (frequency comparison: p=0.596; Table A6) but the detected events were again of significantly smaller amplitude in BCs of NRG1tyI mice, consistent with the earlier analysis (p=0.015; Table A6 and Figure A3).

The overall smaller amplitudes of NMDAR-mediated mEPSC in NRG1tyI putative BCs are unlikely to be attributable to a difference in input resistance of BCs at +40 mV (Lhx6: 144.54 ± 25.98 MΩ, n=7; NRG1tyI/Lhx6: 111.80 ± 16.63 MΩ, n=6; p=0.330; Table 5.2). Notably, the median mEPSC areas (indicative of the quantal charge per event) were not significantly different in putative BCs of NRG1tyI compared to Lhx6 mice (p=0.089, Figure 5.4C.iii and Table 5.2). Due to higher background noise at +40 mV and small amplitude of miniature NMDAR-mediated currents, automatic analysis of mEPSC kinetics was not feasible. Thus, it remains unresolved whether smaller mEPSCs exhibit slower kinetics, thereby balancing the total charge of events (see discussion). The findings indicate that NRG1tyI over-expression leads to selective changes in the postsynaptic NMDAR function at glutamatergic synapses of putative BCs (e.g. receptor density or conductance) without affecting the function of their postsynaptic AMPARs or the density or efficiency of presynaptic glutamatergic

terminals (given both the unaltered AMPAR- and NMDAR-mediated mEPSC frequencies).

Interestingly, the proposed down-regulation of phasic NMDAR-mediated transmission appeared not to be restricted to PV-expressing BCs but might also occur in AACs. Indeed, I found that NMDAR-mediated mEPSCs in AACs tended to be smaller in NRG1tyI mice. Generally, AACs in Lhx6 mice contained very few detectable miniature events (0.01–0.44 Hz, *n*=4), but both AACs recorded in NRG1tyI littermates did not contain any detectable, visually verifiable mEPSCs with the standard detection criteria (Figure 5.4C). With reduced threshold detection (5 pA, see above), few events were detected in both AACs of NRG1tyI mice, and they had smaller amplitudes [12.59 ± 0.60 pA (mean ± SEM), *n*=2] than mEPSC in AACs of Lhx6 mice (16.69 ± 0.98 pA, *n*=4; Table A6 and Figure A3). With these settings (5 pA threshold), the frequencies of detectable mEPSCs varied greatly across Lhx6 AACs (0.02–1.61 Hz), and NRG1tyI/Lhx6 AACs were similarly low (0.07 and 0.10 Hz). From this observation and the evidence of unaltered quantal synaptic AMPAR-mediated excitation in AACs of transgenic mice, I propose that the smaller mEPSCs in AACs at +40 mV reflect altered postsynaptic NMDAR function, rather than differences in presynaptic glutamate release.

In summary, the results indicate a significant and specific reduction of spontaneous NMDAR-mediated transmission at glutamatergic synapses of both types of CB1R− (probably PV+) PTIs (putative BCs and AACs) in NRG1tyI mice. Because the change was specific to NMDAR-mediated synaptic activity and did not occur in AMPAR-mediated synaptic activity, it is unlikely to be caused by NRG1tyI-induced differences at presynaptic terminals (e.g. quantal size; efficiency of glutamate release), but rather implicates postsynaptic NMDAR-related changes.

5.3.3 Unchanged excitatory transmission at pyramidal cells of NRG1tyI mice

The fact that both AACs and putative BCs had smaller NMDAR-mediated mEPSCs at +40 mV raises the question as to whether NRG1tyI over-expression selectively affects PV+ interneurons. Recent reports that have highlighted the importance of NRG1tyI/ErbB4 signalling specifically in PV+ interneurons (Fazzari et al., 2010; Ting et al, 2011) support this hypothesis; however, it was important to investigate whether this also applies with enhanced NRG1tyI expression. Given the role of pyramidal cells in maintaining gamma oscillations and their altered excitation/inhibition charge ratio after cholinergic activation in NRG1tyI mice, I recorded AMPAR- and NMDAR-mediated synaptic transmission in 16 anatomically identified CA3 pyramidal cells of both genotypes.

From 16 anatomically identified pyramidal cells, two cells had to be excluded from analysis because they exhibited too much noise for analysis with the selected detection criteria. A third cell was identified as an anatomical and electrophysiological outlier, because its soma was located in str. lucidum (the somata of the other CA3 pyramidal cells were located within str. pyramidale or at the border to str. oriens) and its AMPAR-mediated mEPSC frequency was unusually high (5 Hz; identified as an 'extreme outlier' in SPSS box plots). I suggest that the unusual soma location might reflect different afferents into the dendrites of this cell. Therefore, the final mEPSC analysis examined six pyramidal cells from four Lhx6 mice (an additional pyramidal cell in a WT mouse was recorded by Ms Linda Avena, Department of Pharmacology), and eight pyramidal cells from three NRG1tyI/Lhx6 and three NRG1tyI mice (Figure 5.5). Access resistances across all cells were similar (p=0.670, Table 5.2), thus justifying between-genotype comparison of mEPSC parameters. For this analysis, I maintained the same detection criteria as for PTIs, and confirmed that these were

suitable for detection of mEPSCs (event detection was reduced to <22% in NBQX and <7% in AP5; Figures 5.5C and D).

Importantly, neither AMPAR- (Figure 5.5C) nor NMDAR-mediated mEPSCs (Figure 5.5D) differed across all pyramidal cells recorded in the two genotypes: AMPAR-mediated mEPSCs were detected over a larger range of frequencies in pyramidal cells of NRG1tyI mice (0.54 –3.25 Hz) than of Lhx6 mice (1.11–2.16 Hz), but the distributions were not significantly different (p=0.195; Figure 5.5C.i and Table 5.2). Similarly, mEPSC amplitudes (Figure 5.5C.ii) and areas (Figure 5.5C.iii) were equally distributed in both genotypes (p=0.245 and p=0.302, respectively; Table 5.2). Detected quantal miniature NMDAR-mediated synaptic activity occurred at frequencies akin to AMPAR-mediated events in pyramidal cells (Figure 5.5D.i, but note lower n number because not all pyramidal cells were recorded at +40 mV; Table A4). Also, detected NMDAR-mediated mEPSCs in pyramidal cells of both genotypes did not vary in their distributions of median amplitude (p=0.850; Figure 5.5D.ii and Table 5.2) or median areas (p=0.785; Figure 5.5D.iii and Table 5.2). Lastly, input resistances at −65 mV and +40 mV did not vary significantly (Table 5.2), thus showing that passive membrane properties for the recording of mEPSCs were similar between genotypes.

In summary, in CA3 pyramidal cells, NRG1tyI over-expression interfered with neither passive membrane properties nor the function of glutamatergic synapses. Two conclusions may be drawn: firstly, the reduction of NMDAR-mediated glutamatergic current amplitude in NRG1tyI mice is cell type-specific (occurring in CB1R− PTIs but not in CA3 pyramidal cells) and secondly, these postsynaptic receptor- and cell type-specific changes in the CA3 hippocampal network occur at an early age (1 month), by which time oscillatory network activity has been found to be already altered.

5.3.4 Cell type-specific properties of AMPAR- and NMDAR-mediated quantal synaptic activity

AMPAR- and NMDAR-mediated mEPSCs differed between the identified cell types, specifically between interneurons and pyramidal cells (Figure 5.6). It was also important to distinguish between putative BCs and AACs in this study, because they tend to receive different levels of spontaneous NMDAR-mediated excitation. Pooling BCs and AACs might have masked the subtle effect on NMDAR-mediated amplitude in NRG1tyI mice.

Cell type had a significant overall effect on AMPAR-mediated mEPSCs: Putative BCs and AACs receive significantly more AMPAR-mediated mEPSCs than pyramidal cells (Figure 5.6A.i; results of two-way ANOVAs and *post hoc* pairwise comparisons in Table 5.3; note, cell types were pooled across genotypes for statistical comparison because NRG1tyI over-expression failed to have a significant overall effect on any AMPAR-mediated mEPSC parameters). This is consistent with reports that PV+ dendrites in CA1 have more glutamatergic synapses than pyramidal cells (Gulyas et al., 1999), and some (neurochemically unidentified) CA3 interneurons have higher AMPA content than pyramidal cells (Baude et al., 1995). The mean frequency of mEPSCs across all BCs and AACs was highly variable, which may result from varying contributions of the different afferents across the CA3 subfields and/or along the dorso-ventral hippcampal axis. Despite this variability within cell types, overall, the distribution of amplitudes of AMPAR-mediated mEPSCs did not differ between the three cell types (Figure 5.6A.ii). Yet, AMPAR mEPSCs at glutamatergic synapses of CA3 pyramidal cells transferred a significantly larger median quantal charge across the membrane than mEPSCs in putative BCs (Figure 5.6A.iii; Table 5.3). This likely reflects the slower kinetics of pyramidal cell AMPARs; a previous study reported faster

Table 5.3 Statistical comparisons of AMPAR- and NMDAR-mediated mEPSC parameters across cell types

Parameter	Two-way ANOVA with fixed factors: genotype and cell type	*Post hoc* pairwise comparison					
AMPAR-mediated mEPSCs: V_h=-65 mV		BC vs AAC	BC vs pyr cell	AAC vs pyr cell			
frequency (Hz)	genotype: $F_{(1,28)}$=0.295, p=0.591 cell type: $F_{(2,28)}$=11.767, p<0.001*** interaction: $F_{(2,28)=}$0.118, p=0.889	p=0.216	p=0.003**	p<0.001***			
median amplitude (pA)	genotype: $F_{(1,28)}$=0.993, p=0.328 cell type: $F_{(2,28)}$=3.291, p=0.052 interaction: $F_{(2,28)}$=0.353, p=0.706	p=0.494	p=0.052	p=1.000			
median area (pA·ms)	genotype: $F_{(1,28)}$=0.153, p=0.698 cell type: $F_{(2,28)}$=13.544, p<0.001*** interaction: $F_{(2,28)}$=0.935, p=0.405	p=1.000	p<0.001***	p=0.002 **			
NMDAR-mediated mEPSCs: V_h=+40 mV in 25 µM NBQX		**Lhx6**			**NRG1tyI/Lhx6**		
		BC vs AAC	BC vs pyr cell	AAC vs pyr cell	BC vs AAC [a]	BC vs pyr cell	AAC vs pyr cell [a]
frequency (Hz)	genotype: $F_{(1,24)}$=0.434, p=0.516 cell type: $F_{(2,24)}$=2.466, p=0.106 interaction: $F_{(2,24)}$=0.163, p=0.850						
median amplitude (pA)	genotype: $F_{(1,24)}$=18.968, p<0.001*** [b] cell type: $F_{(2,24)}$=10.159, p=0.001*** interaction: $F_{(2,24)}$=3.565, p=0.044*	p=0.211	p=1.000	p=0.761	p=0.004**	p=0.652	p<0.001***
median area (pA·ms)	genotype: $F_{(1,24)}$=7.597, p=0.011* cell type: $F_{(2,24)}$=2.774, p=0.082 interaction: $F_{(2,24)}$=2.850, p=0.078						

* p<0.05; ** p<0.01; *** p<0.001. Significant overall effects of cell type (p<0.05) were further examined using *post hoc* pairwise comparisons (with Bonferroni correction) across genotypes (if effect of genotype p>0.05), or within each genotype (if effect of genotype p<0.05).

[a] Caution is required in the interpretation of these p-values given low n numbers of AAC in NRG1tyI mice (n=2). Hence, not included in Figure 5.6

[b] *Post hoc* pairwise comparison (Bonferroni) between genotypes: BCs in Lhx6 vs BC in Lhx6/NRG1tyI, p=0.012*; AACs, p=0.001*; pyr cells, p=0.486

kinetics in CA3 str. radiatum interneurons compared to pyramidal cells (McBain & Dingledine, 1993). Faster kinetics in CA3 interneurons might be achieved through expression of different glutamatergic receptor subunits (Geiger et al., 1995; Freund & Buzsaki, 1996) or of AMPAR auxiliary proteins (Jackson and Nicoll, 2011). Importantly, NRG1tyI over-expression had no significant overall effect on any of the parameters that quantify AMPAR-mediated mEPSCs in any cell type (Table 5.3).

NMDAR-mediated miniature currents in both PTI types were on average less frequent than those mediated through AMPARs. This difference was most pronounced in AACs that received very few detectable (<0.5 Hz) mEPSCs at +40 mV (Figure 5.6B.i). There was no significant overall effect of cell type on the frequency of NMDAR-mediated mEPSCs (Table 5.3), but NMDA currents in AACs appeared to be less frequent than those in either putative BCs or pyramidal cells. Whether glutamatergic synapses at CA3 AACs contain few NMDARs altogether, or NMDARs preferentially localise extrasynaptically on the postsynaptic membrane of AACs is not known (see below). The frequency of NMDAR-mediated events in pyramidal cells was in the range of AMPAR-mediated mEPSCs. This was unexpected because pyramidal cells have a high NMDA/AMPA ratio in stimulus-evoked responses. However, the preferred extrasynaptic location of high-affinity NMDARs might contribute to the lower NMDA/AMPA ratio in mEPSC measurements, because these receptors are more likely to be recruited by glutamate spill-over during evoked stimulation than by individual quanta (Rusakov & Kullmann, 1998; Scimemi et al., 2004). Furthermore, NMDAR-mediated events are probably received at more distal synapses (not mossy fibre synapses; McBain & Dingledine, 1992; Weisskopf & Nicholls, 1995), and might therefore be more attenuated to unresolvable somatic amplitudes. Unlike frequency, the amplitudes of NMDAR-mediated events in all three cell types of Lhx6 mice were

comparable (Figure 5.6B.ii). As outlined above, this was the only parameter affected by NRG1tyI over-expression in PTIs (significant overall effect of genotype, Table 5.3). The median quantal mEPSC charge mediated through NMDARs was found to be highly variable in putative BCs and AACs in WT mice, but, on average, not significantly different across all three cell types ('area', Figure 5.6B.iii). Interestingly, genotype had an overall effect on mEPSC area, which may be due to the lack of NMDAR-mediated input into AACs in NRG1tyI mice, and the tendency towards a reduced excitatory drive of BCs (see above and Table 5.3).

5.4 Discussion

Using Lhx6-eGFP reporter mice, this section of the study has explored quantal miniature neurotransmission at glutamatergic synapses in three identified cell types of NRG1tyI mice and control littermates: Lhx6-eGFP+ CB1R− BCs, AACs and CA3 pyramidal cells. This study served to elucidate whether the excitatory drive of identified PV+ PTIs or of pyramidal cells was changed concomitant with the slower CCh-induced gamma oscillations, the altered excitation/inhibition ratio and longer decay times of compound IPSCs during oscillatory network activity (Chapter 3).

Identification of BCs and AACs in area CA3 was based on their distinct axonal pattern inside str. pyramidale. Furthermore, AACs were shown to be form tight appositions with Ankyrin-G-containing AISs.

The main findings of this chapter are:

1. Putative BCs and AACs in NRG1tyI/Lhx6 transgenic mice exhibited qualitatively similar axo-dendritic structures to the corresponding cell types in Lhx6 reporter mice. All putative BCs and AACs were immunonegative for CB1R.

2. TTX-insensitive quantal synaptic currents were altered in NRG1tyI mice in a postsynaptic receptor type- and cell type-specific manner:
   a. The modulation was dependent on the postsynaptic receptor type, as AMPAR- and NMDAR-mediated frequency was unaffected in NRG1tyI mice.
   b. NMDAR-mediated but not AMPAR-mediated quantal currents were decreased in amplitude.
   c. The change was cell type-specific, occurring in putative BCs and (qualitatively) in AACs but not in CA3 pyramidal cells.

Importantly, these alterations occurred at an early age (1–2 months old), at which oscillatory network activity was shown to be altered (Chapter 3). Furthermore, quantal glutamatergic synaptic transmission was noted to differ greatly between identified cell types in CA3 hippocampus. Most strikingly, AACs tended to receive fewer NMDAR-mediated mEPSCs than both putative BCs and pyramidal cells.

5.4.1 Anatomical identification of Lhx6+ PTIs

5.4.1.1 Patching PTIs in slices from Lhx6-eGFP mice

Based on the success of an earlier study (Sauer & Bartos, 2010), I utilised Lhx6-eGFP reporter mice to improve the yield of PV-containing PTIs. I focussed on patching Lhx6-eGFP-expressing somata within or close to CA3 str. pyramidale, where somata of BCs and AACs have been reported to often reside (Freund & Buzsaki, 1996). Yet, the yield was only 22%: only 16 of 73 patched Lhx6-eGFP-containing interneurons were identified *post hoc* as PTIs (one additional AAC was patched in a non-reporter NRG1tyI mouse). Many cells with somata inside or close to str. pyramidale had axon arborisations in layers other than str. pyramidale (data not shown), and were thus

classified as dendritic-targeting interneurons (Somogyi & Klausberger, 2005). This finding emphasises the importance of not relying on soma location (or shape) to infer cell type; *post hoc* analysis of axon arborisation is essential for cell type identification. Surprisingly, and in contrast to my success rate in CA3 hippocampus, Sauer and Bartos (2010) reported that 80% of recorded Lhx6-eGFP neurons in the DG of Lhx6-eGFP mice were PTIs. The reason for this discrepancy remains unclear, but may reflect a greater abundance of PV+ PTIs among Lhx6-containing interneurons in the DG. Future studies of CA3 PV+ interneurons require optimised PV reporter mice that express sufficiently high levels of fluorescent markers in adult heterozygous mice to ensure sufficient fluorescence in acute hippocampal slices. A novel ai9/PV-Cre transgenic mouse strain that expresses tdTomato fluorescence under the strong CAG promoter inserted into the Rosa26 locus might be suited for selective visualisation of PV+ interneurons (Madisen et al., 2010). This mouse strain became available at the University of Oxford in Spring 2012.

5.4.1.2 Variability in axon arborisation of PTIs in area CA3

Interestingly, axon arbours of CB1R− PTIs in area CA3 were often less confined to str. pyramidale than CA1 PV+ BCs in rat hippocampus (Nissen et al., 2010). Similarly less confined and variable axon arborisation has been reported among BCs in guinea pig CA3 hippocampus (Gulyas et al, 1993a; but note that BCs were not neurochemically identified in this study), and among rat CA3 PV+ BCs (Figure 2 in Szabadics & Soltesz, 2009). Further, axon arborisation was often biased towards str. oriens (rather than str. lucidum), which was also noted in the distribution of ChR2-eYFP fluorescence in virus-injected mice. This might reflect a more diffuse laminar arrangement of deep (possibly later developed) pyramidal cells in area CA3, particularly in ventral hippocampus (Slomianka et al., 2011).

5.4.1.3 Recovering immunopositivity for PV

Although I patched specifically Lhx6-eGFP+ somata, and Lhx6 expression has been correlated with PV+ and SOM+ but not CCK+/CB1R+ interneurons (Liodis et al., 2007), immunopositivity for cytosolic PV could only be recovered in some AACs, but not in any whole-cell recorded BCs. After retraction of the pipette and prior to fixation, I allowed a ~30–45 min period for recovery of endogenous protein expression; however, this did not restore immunopositivity for PV in recorded cells. It is noteworthy that unpatched interneurons in the same slice were strongly immunopositive for PV so technical difficulties related to immunoreactivity can be ruled out. These results are again in contrast to those of Sauer and Bartos (2010), who reported successful recovery of immunopositivity for PV in most whole-cell recorded, Lhx6-eGFP-containing PTIs in the DG (10 of 11 cells tested were reported to co-express PV and Lhx6; Sauer & Bartos, 2010). Region-specific differences in PV levels might again explain this discrepancy, even though DG BCs were recently shown to have a fairly low PV concentration compared to cerebellar BCs (Eggermann & Jonas, 2012). Yet, the PV concentration or PV protein turnover in CA3 BCs might be even lower than that in DG BCs. Importantly, though, I confirmed that all BCs are immunonegative for axonal CB1Rs. This has previously served as a sufficient criterion to discriminate between the two populations of hippocampal BCs (Glickfeld & Scanziani, 2006).

5.4.2 NMDAR-mediated postsynaptic currents in PTIs

In line with the general finding of lower NMDAR levels in hippocampal BCs and PV+ interneurons (Section 5.1), I observed that quantal synaptic currents in BCs and AACs were preferentially mediated by AMPARs over NMDARs (Figure 5.6). Furthermore, my data reveal that the physiological contribution of NMDARs to

excitation may be different between the two CB1R− perisomatic interneuron subtypes: AACs tend to receive fewer NMDAR-mediated quantal currents than CB1R− BCs (albeit there was no significant overall effect of cell type on NMDA current frequency, see Table 5.3). The lack of miniature NMDAR-mediated transmission might be an additional hallmark of AACs, possibly distinguishing them electrophysiologically from CB1R−/PV+ BCs. It is not currently known whether AACs in general contain fewer NMDARs than PV+ BCs, or, for instance, if their NMDARs preferentially locate to extrasynaptic loci on the postsynaptic membrane of AACs. Generally, PV+ interneurons are proposed to preferentially express GluN2D-containing NMDARs (Monyer et al., 1994; Standaert et al., 1996) that locate to the extrasynaptic membrane (Misra et al., 2000; Lozovaya et al., 2004). Therefore, NMDARs on PV+ interneurons may be more likely to be recruited by glutamate spill-over during evoked stimulation than by individual quanta. This was indeed reported in neurochemically unidentified BCs in the DG (Kneisler & Dingledine, 1995b). Yet, in CA1 PV+ PTIs, extracellular stimulation (of str. oriens or Schaffer collaterals) still predominately evoked AMPA synaptic currents (over NMDA: mean AMPA/NMDA ratio ~4:1; Fuchs et al., 2007; Korotkova et al., 2010).

It is currently unclear what the functional consequences of little NMDAR-mediated calcium influx could be, especially in AACs. Long-term potentiation of glutamatergic synapses at both AACs and PV+ BCs in CA1 hippocampus were shown to be independent of NMDARs (Nissen et al., 2010). However, NMDARs may serve functions in PV+ BCs and AACs other than mediating plasticity or phasic excitatory synaptic transmission (see Chapter 6). Experiments with repetitive activation of synapses e.g. by electrical stimulation, are required to estimate the physiological role of NMDAR-mediated excitation in both PV+ BCs and AACs during oscillatory activity.

My findings do not reveal if NMDARs are preferentially recruited at specific input pathways, for example at mossy fibre synapses (Section 5.1; Sambandan et al., 2010). Pharmacological manipulation (e.g. by group II mGluR agonists) would have been instructive to examine the contribution of mossy fibre inputs (Toth and McBain, 1998), although this can also modulate perforant pathway synapses on CA3 interneurons to some extent. The contribution of NMDARs in PV+ BCs and AACs might be not only input- but also brain region-dependent. Extracellular stimulation in EC has been reported to evoke pronounced NMDAR-mediated responses in fast-spiking interneurons (some with BC-like axon arborisations) that add to the initial fast-onset AMPAR/kainateR-mediated components (Jones & Buhl, 1993). In general, the difficulty with interpreting many previous studies lies in the incomplete classification of interneurons which is mainly based on electrophysiological criteria. Although BCs and AACs are both fast-spiking interneurons (Freund & Buzsaki, 1996), my study shows that (in area CA3) they may contain quite variable amounts of functional NMDARs. Hence, electrophysiological classification of interneurons may not be sufficient to discriminate between AACs and BCs. Pooling data from a heterogeneous population of interneurons can easily result in over-estimation of the NMDAR-mediated contribution (Sah et al., 1990).

5.4.3 Postsynaptic changes in glutamate receptor-mediated currents in PTIs of NRG1tyI mice

The finding that NMDAR-mediated but not AMPAR-mediated quantal currents are smaller in CB1R− BCs and AACs of NRG1tyI mice is exciting, because it ties together the role of NRG1 in controlling synaptic wiring of PV+ interneurons (Fazzari et al., 2010) with the observation that NRG1 globally suppresses NMDAR activation (in human prefrontal cortex; Hahn et al., 2006). These results are also consistent with the

NMDAR hypofunction hypothesis of schizophrenia, which specifically implicates GABAergic (in particular PV+) interneurons at the core of the disease (Introduction 1.1.5). In line with this, quantal synaptic currents in pyramidal cells of NRG1tyI mice in this study were unaltered at the same developmental stage (see below). It is important to note that NRG1tyI over-expression reduced NMDAR-mediated synaptic currents in both CB1R− BCs and AACs. Because these two cell types tend to receive physiologically different levels of spontaneous NMDAR-mediated excitation, it has been (and will be for future studies) crucial to discriminate between them in order to prevent masking a subtle effect of NRG1tyI over-expression.

Nonetheless, these findings still need to be interpreted with caution. Quantal miniature currents generate only small NMDAR-mediated postsynaptic currents (mean amplitude ~20 pA) which makes analysis of current kinetics difficult. I cannot exclude, for instance, the possibility that more sustained current kinetics in PTIs of NRG1tyI mice might compensate for the smaller current amplitudes. Such a compensation would render the overall current charge per event (and hence the transmembrane calcium and sodium influx) unchanged in transgenic mice. The median area was not significantly different in putative BCs of the two genotypes, but it can only serve as a rough indicator for the median charge per mEPSC. To confirm my results and investigate current kinetics with improved accuracy, future experiments should employ evoked stimulation. As outlined above, this is important for two reasons: firstly, to increase glutamate release and enhance activation of extrasynaptic NMDARs (Rusakov & Kullmann, 1998); and secondly, to achieve more selective activation of afferent glutamatergic pathways (Somogyi, 2010). With regards to the slower gamma oscillations, the input mediated by associational fibres in area CA3 is of particular interest for future studies. Their evoked NMDA/AMPA current ratios needs be determined in CB1R−/PV+ BCs

and in AACs of NRG1tyI mice, and compared to those of identified cell types in WT mice.

5.4.3.1 Interaction of NRG1 with NMDAR-mediated glutamatergic signalling

NMDAR-mediated signalling is known to be modulated by NRG1/ErbB4 signalling but the effects described in the literature are diverse, and often contradictory. Length of the exposure to NRG1 (as discussed in Chapter 3) and other experimental variables might contribute to the diversity of the effects. Generally, acute treatment with NRG1 peptide has been most extensively investigated, and this is possibly the closest model to the elevated NRG1 expression investigated here. Reported effects include: inducing expression of certain NMDAR subunits such as GluN2C in cerebellar granule cells (Ozaki et al., 1997; but see Rieff et al., 1999 and Okada & Corfas, 2004), modulating the phosphorylation of distinct NMDAR subunits (Hahn et al., 2006; Bjarnadottir et al., 2007; Pitcher et al., 2011) and regulating the trafficking of NMDARs (Gu et al., 2005) or AMPARs (Kwon et al., 2005; Li et al., 2007; Kwon et al., 2008). Many of these studies have implicated NRG1 in stabilising or destabilising proteins of the postsynaptic density (PSD), particularly because NRG1's receptor (ErbB4) associates with PSD-95 (Garcia et al., 2000, Huang et al., 2000). Because NMDARs are also anchored in the PSD and associated with PSD-95 (reviewed in Lau & Zukin, 2007), it is conceivable that the down-modulation of NMDAR-mediated mEPSCs that I observed in CB1R− BCs and AACs may be mediated by destabilisation of NMDARs. Indeed, NRG1-induced changes in the phosphorylation state of GluN2 NMDAR subunits were observed after acute treatment with NRG1 (human prefrontal cortex: Hahn et al., 2006; rodent hippocampus and prefrontal cortex: Pitcher et al., 2011) or transgenic reduction of NRG1 (hippocampus of $NRG1^{+/-}$ mice: Bjarnadottir et al., 2007). This is of particular interest because GluN2 subunits of NMDARs are generally

associated with regulating endocytosis, in a mechanism by which dephosphorylation promotes endocytosis (Lau & Zukin, 2007). Taken together, it may be speculated that increased NRG1 signalling results in selective internalisation of NMDARs. Gu et al. (2005) reported that NRG1-mediated reduction of NMDAR currents in the prefrontal cortex is mediated through an actin-dependent mechanism; albeit the effect was observed in pyramidal cells (Section 5.4.4). Further studies need to determine if NRG1 over-expression affects NMDAR subunit expression, phosphorylation state or NMDAR-associated proteins.

5.4.3.2 AMPAR-mediated glutamatergic signalling and presynaptic glutamate release

Remarkably, NRG1tyI over-expression selectively affected postsynaptic NMDAR function without significantly altering AMPAR-mediated postsynaptic current or frequency. Unaltered miniature frequency indicates no change in the number of presynaptic release sites. In contrast to my findings, disrupted NRG1/ErbB4 signalling was recently shown to reduce the frequency of quantal glutamatergic currents in CA1 hippocampal interneurons (Fazzari et al., 2010) and prefrontal cortex (Ting et al., 2011). Neither of these two studies investigated the pharmacology of mEPSC, but the fast quantal synaptic currents were probably mediated by AMPARs/kainateRs (V_h=-65 mV). Based on their evidence, one might have expected increased NRG1tyI expression to augment glutamate release and quantal synaptic currents in PV+ interneurons. However, four aspects need to be considered when comparing my results with those of these two studies.

Firstly, hippocampal interneurons in area CA1 were not anatomically identified by Fazzari et al. (2010), so their recorded cell population might contain several interneuron types (e.g. CCK+ BCs; CR+ interneuron-specific interneurons; O-LM cells;

projection interneurons). Glutamatergic inputs to some of those interneuron types, specifically those expressing ErbB4 receptors such as CCK+ and CR+ interneurons (Neddens & Buonanno, 2010; Neddens et al., 2011), could have been modulated by NRG1/ErbB4 signalling. This will be further discussed in Chapter 6.

Secondly, NRG1 might exert distinct effect in prefrontal cortex fast-spiking interneurons (Ting et al., 2011), particularly if they contain a higher proportion of functional NMDARs (see above).

Thirdly, the effects of tonically increased NRG1 signalling would not necessarily be expected to oppose those that result from genomic lack of ErbB4 signalling (Section 5.1; Role & Talmage, 2007). It is interesting, though, that longer-term increased peripheral NRG1β1 signalling in newborn mice augmented mEPSC amplitude and frequency in fast spiking cortical interneurons (Abe et al., 2011). Their finding is consistent with predictions from Fazzari et al. (2010) and Ting et al. (2011), and they reported sustained increases in protein levels and immunoreactivity for AMPAR subunit GluA1, while levels of NMDAR subunits GluN1 and GluN2B were unchanged (Abe et al., 2011).

Lastly, the impact of altered NRG1/ErbB4 signalling probably depends on the developmental phase during which it first occurs, particularly because of NRG1's role in early embryonic development (Introduction 1.1.4). In the study by Fazzari and colleagues (2010), ErbB4 receptor was ablated from interneurons at embryonic age (~E12.5). Thus, their study might shed light on the impact of NRG1/ErbB4 signalling at the early phase of synapse formation and maturation. In contrast, NRG1tyI over-expression presumably only starts at around P6-10 (Introduction 1.4.1), which corresponds to the period critical for both synapse maturation (Ben-Ari et al., 1997) and interneuronal NMDAR signalling (Monyer et al., 1994; Belforte et al., 2010). The

model of Ting et al. (2011) addressed a later developmental phase, because ErbB4 ablation from PV+ interneurons in their model is likely to commence only well after P10, when PV expression starts (Nitsch et al., 1990; Bergmann et al., 1991).

Thus, it seems that the diversity of NRG1 effects reflect differences in isoform, cell type, brain region, duration of exposure and developmental stage. Although I only observed altered NMDAR signalling under my experimental conditions, AMPAR-mediated synaptic transmission may well be affected under other conditions.

5.4.4 Glutamatergic signalling in pyramidal cells of NRG1tyI mice

Quantal synaptic transmission in CA3 pyramidal cells was unaltered, consistent with recent conclusions that ErbB4 is not expressed in pyramidal cells in adult rodent hippocampus (Vullhorst et al., 2009; Fazzari et al., 2010; but see Fox & Kornblum, 2005 for transient ErbB4 mRNA expression in developing mouse cortex). It is also in agreement with the recent demonstration that acute (2 days) exposure to NRG1 fails to increase the number and size of PSD-95-containing synapses in glutamatergic neurons (Ting et al., 2011). Similarly, in neocortex, transiently augmented NRG1 signalling in newborn mice did not alter mEPSC frequency or amplitude in layer V pyramidal cells (Abe et al., 2011). In contrast to my findings, others report that NRG1 signalling affects pyramidal cell function (Gu et al., 2005; Kwon et al., 2005, Li et al., 2007; Pitcher et al., 2011). Some of these effects may be indirect, like the NRG1-mediated reversal of LTP at Schaffer collateral's CA1 synapses through internalisation of AMPARs (Kwon et al., 2005) that was later shown to be mediated by a direct effect of NRG1 on dopaminergic release (Kwon et al., 2008).

5.4.5 Perspective

Enhanced NRG1 expression (Hashimoto et al., 2004; Law et al., 2006) and interneuronal NMDAR hypofunction (Pilowsky et al., 2006; Lisman et al., 2008) are two independent observations in human schizophrenia but the neurobiological association (first reported by Hahn et al., 2006) is not understood. Here I provide preliminary evidence that postnatal NRG1tyI over-expression can result in selective hypofunction of NMDARs in CB1R− PTIs. Several questions remain; among these are the role of NMDARs in evoked stimulation from distinct afferents, and the underlying molecular mechanisms. Yet, the most pertinent questions to arise from this study are arguably: what are the functional consequences of reduced NMDAR-mediated excitation? Could they contribute to the slower gamma oscillations in NRG1tyI mice? Chapter 6 will address these questions.

Figure 5.1 Anatomical and neurochemical identification of interneurons innervating the perisomatic domain of CA3 pyramidal cells.

(A) Visualisation of two sample PTIs in CA3 hippocampus by digital rendering of epifluorescent image stacks (axon, blue; dendrites, red; from two merged 60 µm sections). Note that axons (blue) arborise primarily inside the str. pyramidale, but some axon collaterals also loosely project into neighbouring layers. Note also the absence of the radial axonal pattern typical of AAC (cf. Figure 5.2), suggesting that these cells are BCs. Scalebars 100 µm. Below: structured illumination microscopy images of neurobiotin-labelled somata (visualised with Cy3-conjugated Streptavidin) and immunopositivity for GFP (visualised with Al 488-conjugated secondary antibody), indicative of cellular Lhx6 expression. Axons of both cells were immunonegative for CB1R (arrows; visualized with Cy5-conjugated secondary antibody). Scalebars 10 µm.

(B) Normalised laminar distribution of axon pixels, measured in at least two digitally reconstructed 50–60 µm sections of each cell (Methods 2.7.2.1 and Table A2). The counted axon pixels of individual cells were divided into eight horizontal bins as proportions, and pixels in similar laminar bins were summed (laminar bin 1–3, str. oriens; bin 4, str. pyramidale; bin 5, str. lucidum; bin 6–8, str. radiatum). This confirms that the majority of the *in vitro* recovered axon arborised inside the str. pyramidale across all 8 interneurons recorded in Lhx6 mice (42.7 ± 3.2% of normalized axon pixels), and across all 6 interneurons of NRG1tyI/Lhx6 mice (46.1 ± 4.8%).

Three lines of evidence suggest these cells are PV+ BCs. Axons arborise primarily in str. pyramidale but lack the radial axonal pattern within the pyramidal cell layer that is typical of AAC (evidence for the latter is the absence of co-labelling of rows of neurobiotin-filled boutons with Ankyrin-G-positive AISs in two randomly tested cells; Figure A2). Cells were identified by Lhx6-GFP fluorescence prior to whole-cell recording, and *post hoc* most cells were shown to be immunopositive for GFP (Table 5.1), both lines indicative of PV expression. Finally, all cells were immunonegative for CB1R, excluding the possibility that they are CCK/CB1R+ BCs. Given PV and CB1R are mutually exclusive markers for BCs, the evidence speaks for these cells being PV+ BCs.

Abbreviations: g.l., granule layer of DG; s.o., stratum oriens; s.p., stratum pyramidale; s.l., stratum lucidum; s.r., stratum radiatum.

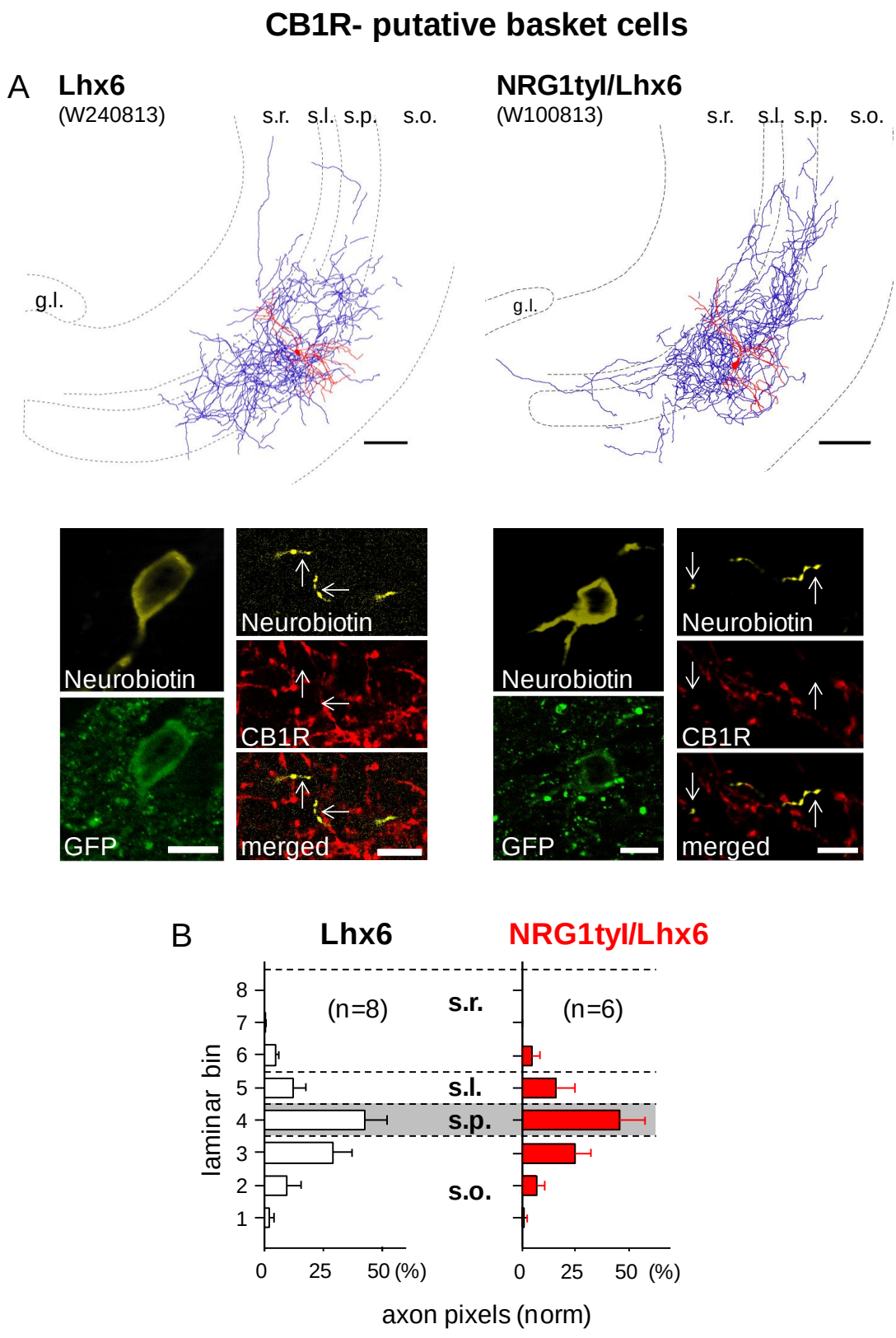

CB1R- putative basket cells
A
Lhx6
(W240813)
s.r. s.l. s.p. s.o.
g.l.
NRG1tyl/Lhx6
(W100813)
s.r. s.l. s.p. s.o.
g.l.
Neurobiotin
GFP
Neurobiotin
CB1R
merged
Neurobiotin
GFP
Neurobiotin
CB1R
merged
B
Lhx6
NRG1tyl/Lhx6
(n=8)
(n=6)
s.r.
s.l.
s.p.
s.o.
laminar bin
8
7
6
5
4
3
2
1
0 25 50 (%)
0 25 50 (%)
axon pixels (norm)

Figure 5.1

Figure 5.2 Anatomical and neurochemical identification of AACs.

(A) Visualisation of two recorded AACs. Left: AAC in area CA3b of an Lhx6 mouse, showing axon (blue) from one 60 µm section, and dendrite (red) from two merged 60 µm sections (scalebars 100 µm). Right: AAC in area CA3c/b of an NRG1tyI/Lhx6 mouse, showing axon and dendrite from one 50 µm thick section (note: apical dendrites were not recovered; axon in the vicinity of the soma could not be reconstructed due to fluorescent background). Note the characteristic radial axonal pattern inside str. pyramidale, unlike the arborisation pattern of a BC (Figure 5.1). Bottom right: structured illumination microscopy images of neurobiotin-filled somata (visualised *post hoc* with Cy3-conjugated streptavidin) and immunopositivity for PV (visualised with Cy5-conjugated secondary antibody). Scalebars 20 µm. Bottom left: rows of neurobiotin-labelled boutons closely followed Ankyrin-G-positive AISs of CA3 pyramidal cells, indicative of axo-axonic synapses. Images of Ankyrin-G immunoreactivity are z-projected stacks, taken with confocal laser-scanning microscopy. Scalebars 5 µm. Abbreviations as in Figure 5.1.

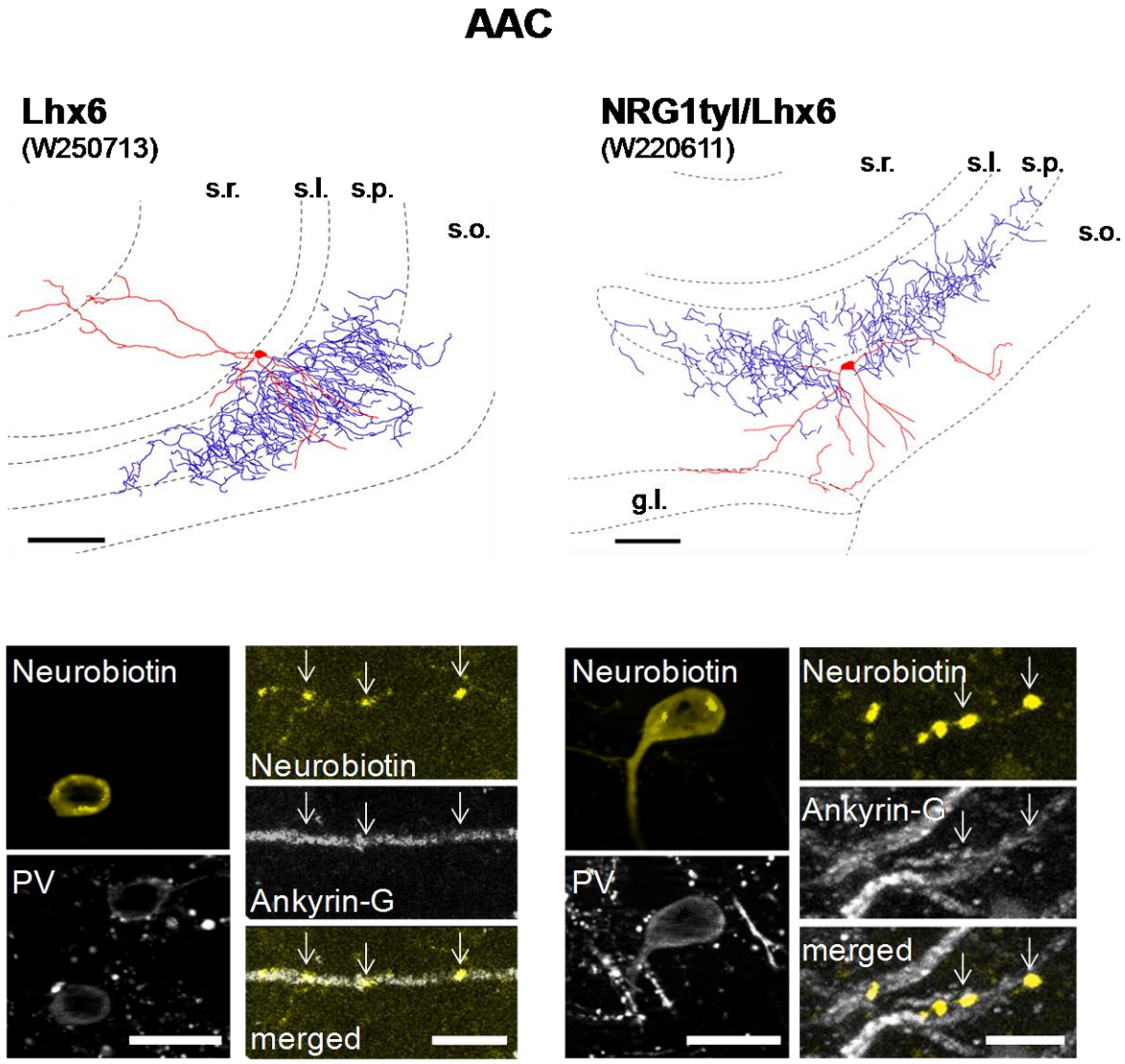

AAC
Lhx6
(W250713)
s.r.
s.l.
s.p.
s.o.
NRG1tyl/Lhx6
(W220611)
s.r.
s.l.
s.p.
s.o.
g.l.
Neurobiotin
PV
Neurobiotin
Ankyrin-G
merged
Neurobiotin
PV
Neurobiotin
Ankyrin-G
merged

Figure 5.2

Figure 5.3 AMPAR-mediated quantal synaptic EPSCs in identified CB1R− putative BCs and AACs.

(A) Band-pass filtered (4 Hz–6 kHz) sample traces (45 s) of mEPSCs in two putative BCs (left, Lhx6; right, NRG1tyI/Lhx6). Cells were voltage clamped at −65 mV. Scalebars 10 s, 50 pA. Wash-in of 25 μM NBQX (incremental grey bar) blocked mEPSCs in cells of both genotypes. Thus, quantal currents are mediated through AMPA/kainate receptors. Insets: 15 superimposed mEPSCs, illustrating fast kinetics at −65 mV and variability in amplitude. Scalebars 5 ms, 50 pA.

(B) Normalised occurrence of all threshold-detected mEPSC amplitudes of cells in (A) (120 s recording). Note the skewed, non-normal distribution of threshold-detected mEPSC amplitudes. Insets: Correlation between time to peak (ms) and amplitude of mEPSCs. Positive correlations were observed in both BCs, indicating that factors other than dendritic filtering are responsible for the amplitude variability.

(C) Scatter plots of (i) mEPSC frequency, (ii) median amplitude and (iii) median area across all identified putative BCs show AMPAR-mediated mEPSCs are unchanged in NRG1tyI over-expressing mice ($p>0.05$, independent samples t tests and non-parametric equivalents); n.s., not significant. Miniature EPSCs in AACs also appear not to be altered.

(D) mEPSCs are effectively blocked by 25 μM NBQX in putative BCs and AACs. With the standard criteria for automatic threshold-detection (amplitude threshold >5 pA; event duration above threshold: 0.5–100 ms; noise rejection: 0.5 ms) no events are detected in 25 μM NBQX. Note that not all cells recorded at +40 mV were exposed to AP5 at the end of the recording.

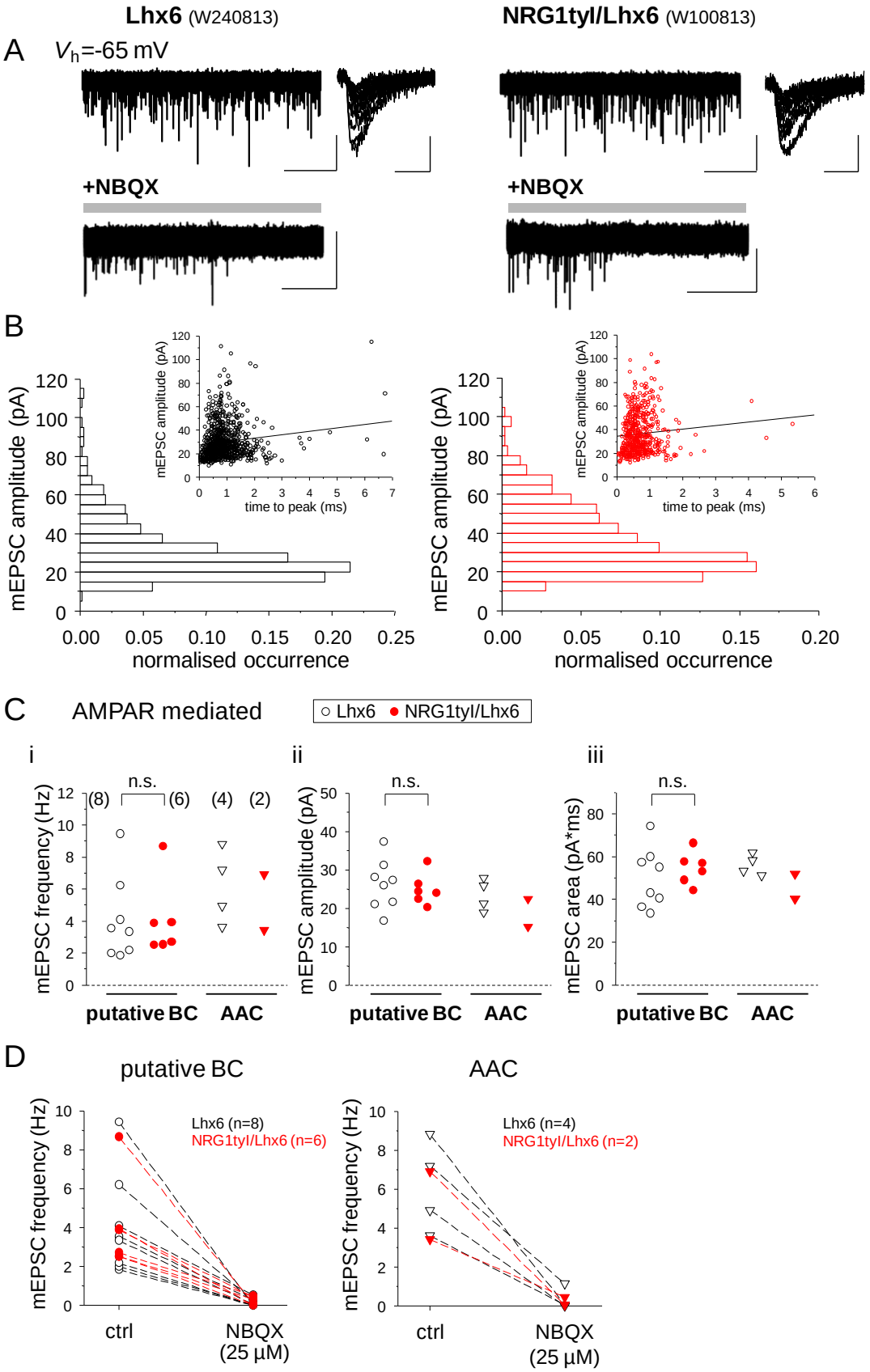

Lhx6 (W240813)
NRG1tyl/Lhx6 (W100813)
A
Vh=-65 mV
+NBQX
+NBQX
B
mEPSC amplitude (pA)
normalised occurrence
mEPSC amplitude (pA)
time to peak (ms)
C
AMPAR mediated
Lhx6
NRG1tyl/Lhx6
i
ii
iii
mEPSC frequency (Hz)
mEPSC amplitude (pA)
mEPSC area (pA*ms)
n.s.
(8)
(6)
(4)
(2)
putative BC
AAC
D
putative BC
AAC
Lhx6 (n=8)
NRG1tyl/Lhx6 (n=6)
Lhx6 (n=4)
NRG1tyl/Lhx6 (n=2)
ctrl
NBQX
(25 µM)

Figure 5.3

Figure 5.4 NMDAR-mediated mEPSCs in identified CB1R− putative BCs and AACs of NRG1tyI mice.

(A) Band-pass filtered (4 Hz–6 kHz), 45 s-long traces of mEPSCs in putative BCs. Cells were voltage-clamped at +40 mV, and mEPSCs recorded in 25 µM NBQX to block AMPARs/kainateRs. Miniature EPSCs are blocked by 100 µM AP5 (wash-in is represented by incremental grey bar), proving they are mediated by NMDARs. Scalebars 10 s, 40 pA. Insets: 20–25 superimposed mEPSCs, illustrating kinetics and amplitude variability of NMDAR-mediated mEPSCs at V_h=+40 mV. Scalebars 20 ms, 40 pA.

(B) Traces from two AACs (band-pass filtered, 4 Hz–6 kHz, 45 s) voltage-clamped at +40 mV, in the presence of 25 µM NBQX. Note small and few mEPSCs (asterisks) detected in Lhx6 cell. Centre left: no mEPSCs were detectable with the same threshold settings when NMDARs were blocked by AP5. Scalebars 10 s, 20 pA. Inset: Superimposed mEPSCs, illustrating kinetics and small amplitude in AACs. Scalebars 20 ms, 20 pA.

(C) NMDAR-mediated mEPSCs in putative BCs of NRG1tyI mice (red dots, n=6) had smaller amplitudes (ii) than those in putative BCs of Lhx6 mice (open dots, n=7; p=0.032, Mann–Whitney U test), although they occurred at similar frequencies (i; p>0.05, independent samples t test). The area (i.e. median charge per event) did not significantly differ between genotypes (iii, p=0.089, independent samples t test). Note that one putative BC of an NRG1tyI mouse did not receive any detectable mEPSCs at +40 mV. Similarly, no mEPSCs could be detected in the two AACs of NRG1tyI mice (i, red triangles). In contrast, AACs of Lhx6 mice received detectable mEPSC at low frequency (i, white triangles, n=4; frequency is >0). The currents had comparable median amplitudes (ii), but variable median areas (iii). Scatter plots present values of individual experiments; n.s., not significant.

(D) The frequency of mEPSCs is reduced to <4% in 100 µM AP5. Criteria for threshold detection were amplitude >7 pA; event duration: 0.8–200 ms (noise rejection: 0.8 ms). Note that only a subset of cells was exposed to AP5 at the end of the recording.

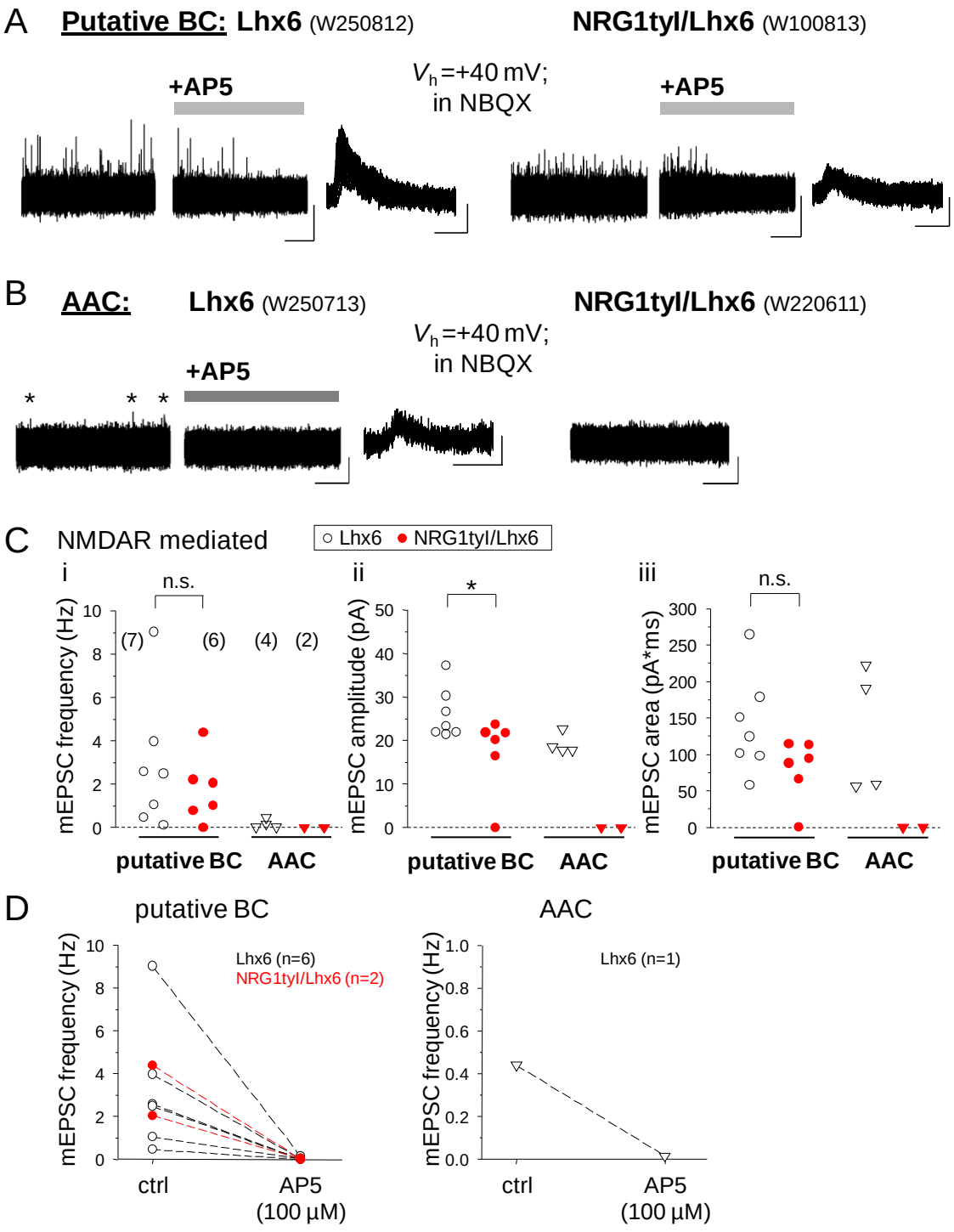

A
Putative BC: Lhx6 (W250812)
NRG1tyI/Lhx6 (W100813)
+AP5
Vh=+40 mV;
in NBQX
+AP5
B
AAC:
Lhx6 (W250713)
NRG1tyI/Lhx6 (W220611)
Vh=+40 mV;
in NBQX
+AP5
C
NMDAR mediated
Lhx6
NRG1tyI/Lhx6
i
n.s.
mEPSC frequency (Hz)
(7)
(6)
(4)
(2)
putative BC
AAC
ii
*
mEPSC amplitude (pA)
putative BC
AAC
iii
n.s.
mEPSC area (pA*ms)
putative BC
AAC
D
putative BC
Lhx6 (n=6)
NRG1tyI/Lhx6 (n=2)
mEPSC frequency (Hz)
ctrl
AP5
(100 µM)
AAC
Lhx6 (n=1)
mEPSC frequency (Hz)
ctrl
AP5
(100 µM)

Figure 5.4

Figure 5.5 AMPAR- and NMDAR-mediated mEPSCs in CA3 pyramidal cells.

(A) Schematic of CA3 pyramidal cell whole-cell recording with major glutamatergic input pathways: PP, perforant pathway; MF, mossy fibres; assoc. fibres, association recurrent fibres; comm. fibres, commissural fibres arising from contralateral hippocampus. Bottom: Somatodendritic structure (one 60 µm section) of a CA3 pyramidal cell recorded in a NRG1tyI/Lhx6 mouse, taken with structured illumination microscope (scalebar, 50 µm). Inset: Confocal stack image of spiny dendrite. Scalebar 5 µm.

(B) Band-pass filtered (4 Hz–6 kHz, 45 s) traces of mEPSCs in two pyramidal cells at two voltage-clamp potentials: (i) −65 mV, top panel; (ii) +40 mV, bottom panel. (i) At −65 mV, mEPSCs are blocked by 25 µM NBQX (incremental grey bar symbolises wash-in), indicating they are mediated by AMPARs/kainateRs. Scalebars for all long traces at −65 mV: 10 s, 40 pA. Insets: 6 superimposed consecutive mEPSCs illustrate kinetics and amplitude variability. Scalebars 10 ms, 40 pA. (ii) At +40 mV, mEPSCs are mediated by NMDAR, because they are antagonised by 100 µM AP5 (incremental grey bar). Scalebars for all long traces at +40 mV: 10 s, 40 pA. Insets: 8 superimposed mEPSCs demonstrate the slow kinetics and amplitude variability (scalebars: 10 ms, 30 pA).

(C) AMPAR-mediated mEPSCs did not differ in (i) frequency, (ii) median amplitude or (iii) median area across pyramidal cells of both genotypes (n.s, not significant, $p>0.05$). Scatter plots present values of individual experiments. (iv) Application of NBQX effectively blocked events at −65 mV. The same detection criteria were used as in PTIs (Figures 5.3 and 5.4).

(D) NMDAR-mediated mEPSC (recorded at +40 mV in the presence of NBQX) did not differ in (i) frequency, (ii) median amplitude or (iii) median area across pyramidal cells of both genotypes ($p>0.05$). (iv) Block of NMDAR-mediated mEPSCs by AP5.

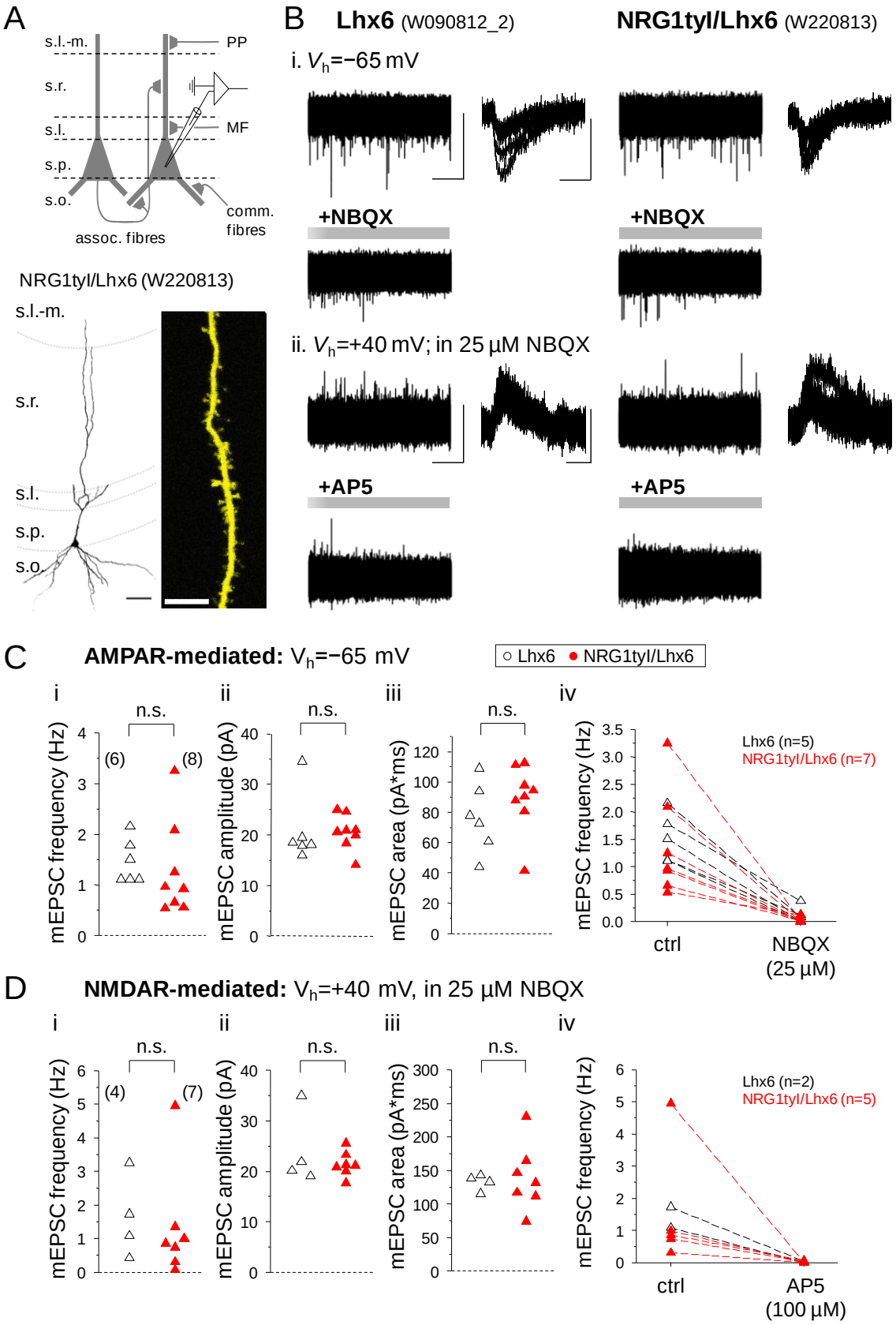

A
s.l.-m.
s.r.
s.l.
s.p.
s.o.
PP
MF
comm. fibres
assoc. fibres
NRG1tyl/Lhx6 (W220813)
B
Lhx6 (W090812_2)
NRG1tyl/Lhx6 (W220813)
i. Vh=−65 mV
+NBQX
ii. Vh=+40 mV; in 25 µM NBQX
+AP5
C
AMPAR-mediated: Vh=−65 mV
Lhx6
NRG1tyl/Lhx6
mEPSC frequency (Hz)
mEPSC amplitude (pA)
mEPSC area (pA*ms)
n.s.
(6)
(8)
Lhx6 (n=5)
NRG1tyl/Lhx6 (n=7)
ctrl
NBQX (25 µM)
D
NMDAR-mediated: Vh=+40 mV, in 25 µM NBQX
(4)
(7)
Lhx6 (n=2)
NRG1tyl/Lhx6 (n=5)
AP5 (100 µM)

Figure 5.5

Figure 5.6 Cell-type specific differences in AMPAR-and NMDAR-mediated quantal synaptic currents.

(A) AMPAR-mediated mEPSCs in putative BCs (dots), AACs (downward triangle) or CA3 pyramidal cells (upward triangle) of Lhx6-reporter mice (white) and NRG1tyI over-expressing mice (red). BCs and AACs exhibited (i) higher frequency of AMPAR-mediated mEPSCs than CA3 pyramidal cells, but (ii) median amplitudes were not significantly different. However, (iii) median current integrals (area) were largest across pyramidal cells, indicating cell type-specific current kinetics (section 5.3.4). NRG1tyI over-expression did not have a significant overall effect on frequency, amplitude or area of AMPAR-mediated mEPSCs ($p>0.05$); therefore, differences between cell types were investigated across genotypes.

(B) NMDAR-mediated mEPSCs tended to be (i) of lower frequency in AACs (<0.5 Hz) than in BCs or pyramidal cells of control Lhx6 mice whereas (ii) median amplitudes and (iii) areas were not different. Notably, NRG1tyI over-expression significantly reduced the median amplitude of NMDAR-mediated mEPSCs (ii) in BCs but not in pyramidal cells. The median area of mEPSCs (iii) was smaller in NRG1tyI mice compared to Lhx6 mice across all three cell types (effect of genotype, $p<0.05$) but there was no overall effect of cell type ($p=0.082$; Table 5.3). Note that AACs of NRG1tyI mice did not receive any detectable mEPSCs (with the standard threshold detection criteria). Note also the variability of glutamate receptor-mediated mEPSC parameters, particularly in interneurons. *$p<0.05$, **$p<0.01$; for statistical comparisons and *p*-values, refer to Tables 5.2 and 5.3.

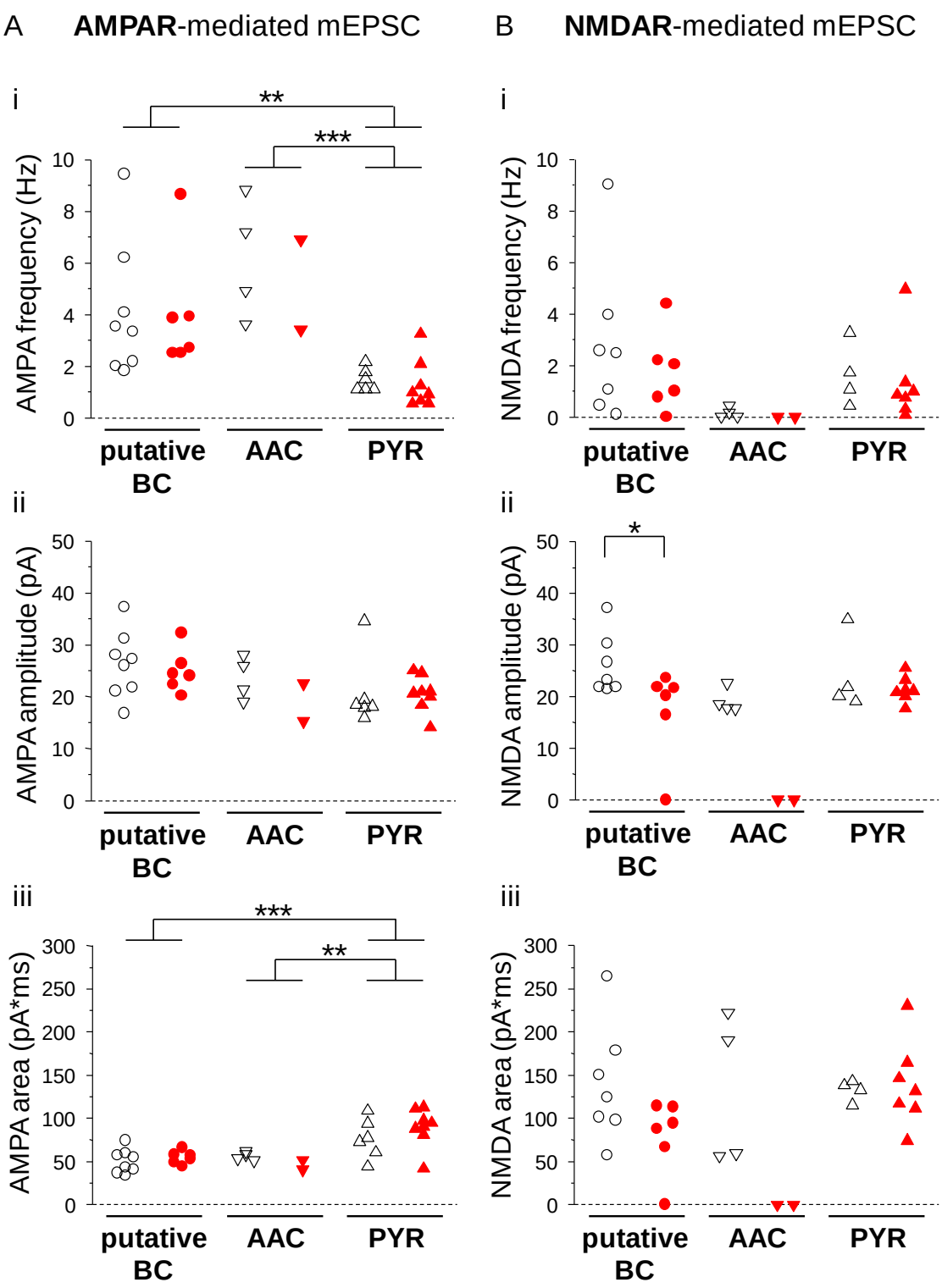

A AMPAR-mediated mEPSC
B NMDAR-mediated mEPSC
i
ii
iii
AMPA frequency (Hz)
NMDA frequency (Hz)
AMPA amplitude (pA)
NMDA amplitude (pA)
AMPA area (pA*ms)
NMDA area (pA*ms)
putative BC
AAC
PYR
**
***
*

Figure 5.6

6 General discussion

6.1 Summary of findings

In this work, I have investigated the effects of NRG1tyI over-expression on hippocampal circuit functioning. Because NRG1tyI over-expressing mice were previously reported to be impaired in spatial working memory (Deakin et al., 2012), I studied gamma-frequency hippocampal network oscillations — a proposed physiological basis of cognitive processing. I demonstrated that CCh-induced gamma oscillations were slower in NRG1tyI mice as young as one month (i.e. much earlier than working memory impairment; Deakin et al., 2012). In line with slower rhythmic field potential activity, compound inhibitory synaptic currents were more sustained in CA3 pyramidal cells, but the functioning of the GABAergic synapse between PV+ PTIs and CA3 pyramidal cells was not significantly altered. Rather, I obtained evidence of a selective down-regulation of the NMDAR-mediated excitatory transmission in CB1R− (putative PV+) BCs and AACs in NRG1tyI mice, as revealed by quantal synaptic current analysis. The analysis further suggested that, under physiological conditions, BCs and AACs exhibit variable quantal current activity, and that AMPAR-mediated transmission did not differ between NRG1tyI and WT mice. Excitatory recruitment of CA3 pyramidal cells was unaffected by NRG1 levels, at least in quantal current analysis. Together, the results suggest that increased NRG1 expression might impair (NMDAR-mediated) excitatory recruitment of those GABAergic interneurons that are directly implicated in the generation of gamma oscillations. Indeed, the increased excitation/inhibition charge transfer in pyramidal cells implies that increased excitatory

input might be necessary to effectively recruit the same number of PV+ interneurons in the NRG1tyI network (compared to the WT network) during cholinergic activation. Together with putative secondary changes in the disynaptic GABAergic inhibition, this might also explain why the CA3 network of transgenic mice was more prone to develop epileptiform discharges upon cholinergic activation.

6.2 Functional implications of NMDAR hypofunction

These findings, together with related previous results, illustrate that NRG1 over-expression causes detectable changes in the function of the hippocampus on at least three levels: the system (cognitive functions; Deakin et al., 2012), neuronal network (gamma oscillations and epileptiform activity; Chapter 3) and cellular level (excitatory input to CB1R− PTIs; Chapter 5). The question that remains is whether these observations are causally linked. Could selective down-modulation of NMDAR-mediated transmission in PTIs contribute to the effects observed at the system and network levels? And, could it influence the input-output function in PV+ cells?

6.2.1 Cognitive functions

Both pharmacological inhibition of NMDARs and genomic ablation of the obligatory GluN1 subunit have demonstrated the essential role of NMDARs in the formation of hippocampal-dependent memories (Morris et al., 1986; Mohn et al., 1999; Nakazawa et al., 2002; Nakazawa et al., 2003; Niewoehner et al., 2007). However, none of these studies addressed the differential contribution of interneuronal NMDARs. Transgenic mouse strains deficient in NMDAR (knockout of NR1 subunit) in PV+ cells (Korotkova et al., 2010; Carlen et al., 2012) or in a heterogeneous subset of cortical interneurons (among them, PV+; Belforte et al., 2010) were developed only recently.

Assessment of their cognitive behaviour and hippocampus function demonstrated selective impairment of their spatial working memory (Belforte et al., 2010; Korotkova et al., 2010; Carlen et al., 2012). In contrast, spatial reference learning was unaltered compared to controls (Korotkova et al., 2010; Carlen et al., 2012). Remarkably, this phenotype of transgenic $NR1^{PVCre-/-}$ mice is similar to that of old NRG1tyI mice (deficient spatial working memory but intact spatial reference memory, Deakin et al., 2012). It is therefore tempting to speculate that down-modulation of NMDARs in CB1R− PTIs might contribute to the cognitive phenotype in NRG1tyI mice. One has to bear in mind, though, that in the $NR1^{PVCre-/-}$ mice NR1 was removed from *all* PV+ interneuron types. However, it is not known how NRG1 over-expression affects NMDARs on dendritic-targeting PV+ interneurons (see below). Furthermore, the temporal discrepancy discussed in Chapter 3 remains unsolved, because both NMDAR hypofunction and altered gamma oscillations were already evident in 1–2-month-old transgenic mice, while the behavioural phenotype only emerges at 10 months (Deakin et al., 2012). How might this be explained? Emergence of the cognitive deficit might involve contributions from other brain regions and/or other factors (possibly age-related). Besides the hippocampus, the prefrontal cortex is also implicated in working memory function (Introduction 1.3.3; Castner et al., 2004), so impaired hippocampal network functioning might be initially (at the younger age) compensated for by improved prefrontal cortex functioning in NRG1tyI mice. This is, however, speculative, because fast oscillations have not been investigated *in vivo*, and it also remains elusive how *in vivo* oscillatory activity in area CA3 relates to prefrontal cortex oscillations. Oscillatory theta–gamma coupling between CA1 hippocampus and prefrontal cortex has been well described (e.g. Hartwich et al., 2009; Sigurdsson et al., 2010) and it is

implicated in working memory operations (Introduction 1.3.3), but the explicit role of direct or indirect CA3 hippocampus–prefrontal cortex coupling is unclear.

It is worth noting that female NRG1tyI mice (2–5 months old) also demonstrated increased anxiety in selected behavioural tests, although this was not a consistent phenotype across all behavioural tests (Deakin et al., 2009). Interestingly, knocking out NMDAR in a subset of cortical interneurons also revealed an anxiety-like behaviour (Belforte et al., 2010). The partial (albeit not complete) overlap in phenotype might suggest that altered NMDAR function in PV+ interneurons contributes, at least partly, to the NRG1tyI phenotype. Processes associated with anxiety-related behaviour have been attributed to the ventral (rather than dorsal) hippocampus (Bannerman et al., 2004), and it is noteworthy that most of my field potential recordings (albeit not stringent) were taken from ventral hippocampal slices. To further elucidate the link between system phenotypes (spatial working memory, anxiety) and neuronal networks in NRG1tyI mice, one must analyse *in vivo* electrophysiological recordings in conjunction with behavioural testing.

6.2.2 Neuronal network function

At the level of neuronal networks, interference with NMDAR function appears to affect gamma-frequency oscillations under certain circumstances: acute treatment with ketamine or AP5 did not change hippocampal gamma oscillations *in vitro* (induced by carbachol: Dickinson et al., 1993; Fisahn et al., 1998; Mann & Mody, 2010; induced by kainate: Cunningham et al., 2006) unless tonic GABAergic inhibitory currents were genomically ablated (Mann & Mody, 2010). In the latter study, application of AP5 slowed high frequency CCh-induced gamma oscillations (>60 Hz) that occurred in mice lacking δ-subunit-containing GABA-A receptors. GluN2D-containing NMDARs

located on (unidentified) interneurons were implicated in this, but it only affected faster gamma oscillations in the absence of tonic inhibition, not the CCh-induced ~40 Hz rhythm in WT mice (Mann & Mody, 2010). Therefore, it is difficult to reconcile this finding with the observed change in slower (~28 Hz) gamma oscillations in my study.

Possibly more relevant to my work are recent reports on *in vivo* gamma oscillations in mice deficient of NR1 subunit selectively in PV+ cells (Korotkova et al., 2010; Carlen et al., 2012). Freely moving mutant mice showed significantly augmented spontaneous gamma oscillations in CA1 hippocampus (Korotkova et al., 2010) and in the somatosensory cortex (Carlen et al., 2012) compared control mice. In contrast, gamma-band activity was *reduced* in power in mutant mice (PV-Cre/NR1f/f mice) when externally entrained through ChR2-mediated activation of PV+ interneurons (Carlen et al., 2012). This finding is interesting because it points to an explicit role of NMDARs in direct PV+ cell recruitment during oscillations (see below). It is striking that both studies reported alterations primarily in oscillation *power*, rather than frequency, upon genomic interference with interneuronal NMDARs (although hippocampal gamma oscillations in $NR1^{PV\text{-}Cre\text{-}/\text{-}}$ mice were also reported to be slightly faster; Korotkova et al., 2010). In contrast, I observed a consistent shift in oscillation frequency, together with a tendency towards larger field power, in slices from NRG1tyI mice. Interestingly, Carlen et al. (2012) reported that the cortical network of PV+ cell-selective NR1-deficient mice (PV-Cre/NR1f/f) could be driven to oscillate at lower gamma frequencies (~25–30 Hz) as efficiently as the network in control mice. Yet, remarkably, the transgenic network failed to reach the power of the control oscillations when it was driven at higher frequencies (30–60 Hz; see Figure 2D in Carlen et al., 2012). Thus, NMDAR may be more necessary for driving higher frequency oscillations. This conclusion is supported by the above-mentioned findings on gamma oscillations in

mice deficient of δ-subunit-containing GABA-A receptors (Mann & Mody, 2010). Furthermore, an NMDAR-dependent switch between fast (here: ~40 Hz) and low (~30 Hz) gamma rhythms has also been found in EC but this could not be replicated in hippocampus (Middleton et al., 2008). From all this evidence, it is not clear whether the observed frequency modulation of 'slow' (~28 Hz) hippocampal gamma oscillations by NRG1tyI over-expression could be due to the suggested down-modulation of NMDARs in PV+ PTIs.

6.2.3 Input and output function of PV+ interneurons

A question that remains to be answered is whether dysfunction of NMDARs in PV+ PTIs could account for the observed sustained compound inhibitory output during CCh-induced network activity in NRG1tyI mice. As shown in Chapter 5, NMDAR-mediated quantal currents in PV+ interneurons are generally small — and even smaller when NRG1 is over-expressed. Despite the small currents, ablation of NMDAR from PV+ interneurons is reported to change the output of fast-spiking interneuron. More specifically, spike synchrony in NMDAR-lacking fast-spiking units is diminished when driven by external (light) activation (Carlen et al., 2012). Thus, excitation of PV+ interneuron types might be less reliable in the absence of NMDAR function. In line with this, pyramidal cell spiking is less synchronised *in vivo* (Belforte et al., 2010), and lacks spatial and temporal precision during hippocampal gamma oscillations when PV+ interneurons are deficient in NMDAR (Korotkova et al., 2010). This suggests impaired inhibitory entraining (Cobb et al., 1995). Yet, my data are not fully consistent with these observations, because pyramidal cell firing during gamma oscillations in NRG1tyI mice was as efficient and temporally precise as in WT mice, although it tended to occur in a higher proportion of gamma cycles, which might point to less stringent inhibitory control.

Due to the Mg^{2+} block of NMDARs, NMDAR-mediated synaptic excitation is unlikely to contribute to the initial subthreshold depolarisation of PV+ interneurons (application of NBQX effectively blocked all mEPSCs at −65 mV; Figure 5.3). Rather, they likely add to the later phase of excitation, when the Mg^{2+} block is partially released. This would prolong excitation and enable temporal integration of different inputs. EPSP kinetics are a major contributor to the precision of EPSP–spike coupling (Fricker & Miles, 2000; Maccaferri & Dingledine, 2002). Tight and faithful EPSP–spike coupling is associated with fast AMPAR-mediated excitation (Miles, 1990; Maccaferri & Dingledine, 2002), particularly in BCs (Geiger et al., 1997; Hu et al., 2010), whereas NMDAR-mediated excitation reduces EPSP–spike-coupling precision and prolongs latencies between EPSPs and the occurrence of postsynaptic spikes (Maccaferri & Dingledine, 2002). Therefore, NMDAR-mediated excitation in BCs, if relevant, would be expected to cause somewhat asynchronous GABA release, thereby prolonging compound IPSCs during gamma oscillations and decreasing gamma power (modelled in Rotaru et al., 2011). In turn, NMDAR hypofunction should improve synchronised spike output and GABA release (Rotaru et al., 2011; review in Gonzalez-Burgos & Lewis, 2012). As a result, gamma power would be expected to be higher, and compound IPSCs to be faster during rhythmic oscillations. This is contrary to my findings, and also to the finding that spike synchrony in fast-spiking units is reduced in transgenic mice in which NR1 is ablated from PV+ interneurons (Carlen et al., 2012).

Yet, NMDARs in BCs might have roles other than mediating phasic excitation. Tonic excitation via NMDAR, for example, may modulate gamma oscillations (Mann & Mody, 2010). In this study, exogenous application of NMDA was shown to increase the frequency of CCh-induced oscillation in juvenile CA3 hippocampus, by increasing tonic GluN2D-containing NMDAR currents associated with interneurons. Interestingly, fast-

spiking interneurons in prefrontal cortex were very recently shown to have pronounced tonic NMDAR currents, similar in magnitude to those in pyramidal cells (Povysheva & Johnson, 2012). It is conceivable that, in NRG1tyI mice, reduced tonic activation of PV+ BCs by NMDARs decreases their excitability, ultimately reducing their spike output. However, application of AP5 did not affect the firing frequency of fast-spiking neurons in prefrontal cortex (Povysheva & Johnson, 2012).

NMDARs were also proposed to act as 'activity sensors' for pyramidal cell activity (Lisman et al., 2008). If NRG1, like BDNF, acted as an indicator of general neuronal activity (Introduction 1.2.2) during early postnatal stages of interneuron maturation, excess NRG1 expression might alter the intrinsic excitability of PV+ interneurons. This might be mediated by changes in postsynaptic NMDAR levels or phosphorylation states (Chapter 5). This would imply: (i) that NRG1 levels control the expression of voltage-gated channels governing PV+ interneurons excitability; and (ii) that NMDARs in these interneurons contribute less to synaptic excitation but, instead, are more involved in interneuron maturation. As such, a balanced expression of NMDARs might be more central to PV+ cell function at the juvenile rather than mature stage. With regards to (i), acute NRG1 treatment has recently been shown to increase the excitability of fast-spiking interneurons through a direct, ErbB4-mediated inhibitory effect on the voltage-gated potassium channel Kv1.1 (Li et al., 2012). With regards to (ii), the strength of NMDAR currents is reported to gradually weaken with maturation of fast-spiking interneurons in rat prefrontal cortex (Wang & Gao, 2009). NMDAR currents were found to be stronger in juveniles (P15–P28) than adolescents (P31–P49). Thus, NRG1 signalling and NMDAR-mediated transmission might indeed both be critical during early postnatal maturation (~4 weeks) and set the intrinsic excitability of PV+ cells. Further studies are required to clarify whether (and in which direction) PV+

interneuron output is altered by NRG1 over-expression. Remarkably, their impaired spiking (i.e. loss of ability to sustain spiking at high frequency) is associated with experimental models of epilepsy (Lau et al., 2000; Ogiwara et al., 2007), and thus could partially cause the epileptiform activity I observed in NRG1tyI mice.

Finally, the contribution of (possibly) reduced NMDAR-mediated excitation in AACs to the altered network activity in NRG1tyI mice needs to be analysed. GABA release from AACs may only be a minor contributor to the physiological generation of CCh-induced gamma oscillations in area CA3 (Gulyas et al., 2010). Nevertheless, AACs are well suited to control pyramidal cell output (Miles et al., 1996). As such, impaired (NMDAR-mediated) excitatory drive of AACs in NRG1tyI mice could predispose the network to epileptiform discharges, assuming that the effect in pyramidal cells is predominantly inhibitory (Glickfeld et al., 2009). However, this requires further investigation, especially as the postsynaptic inhibitory effect of AACs, as well as their role in models of epilepsy or human epilepsy, is controversial (Howard et al., 2005; Glickfeld et al., 2009; Woodruff et al., 2011).

6.3 Neurobiological effects of NRG1tyI over-expression: Is there a link with the pathophysiology of schizophrenia?

The NRG1tyI mouse has strong construct validity with respect to schizophrenia: first, it mimics the increased NRG1 type I expression reported in hippocampus of human schizophrenic patients; and second, the early onset of NRG1tyI over-expression (starting at P6–P10) is consistent with a role for NRG1 in early postnatal development and thus the neurodevelopmental aspect of schizophrenia. It is noteworthy, though, that the level of over-expression in mice is much higher than that observed in humans. NRG1tyI mice have 8- to 10-fold elevated mRNA levels in hippocampus (Deakin,

2009), whereas a relatively moderate (0.34-fold) increase has been reported in human post-mortem brain tissue (Law et al., 2006). Nevertheless, NRG1tyI mice represent a useful model to study the effects of increased postnatal expression of NRG1tyI on brain circuits.

My results provide evidence that enhanced NRG1tyI expression alters the functioning of the hippocampal network in ways similar to that observed in patients with schizophrenia. Specifically, NMDAR down-regulation and altered gamma oscillations in NRG1tyI mice parallel observations in patients (Uhlhaas & Singer, 2010; Gonzalez-Burgos & Lewis, 2012). The finding that NRG1tyI over-expression might lead to smaller NMDAR-mediated phasic responses in CB1R− PTIs is very exciting, because it reconciles three independent findings in human schizophrenia: the involvement of excessive NRG1 transcript levels (Law et al., 2006), impaired NMDAR function (Pilowsky et al., 2006) and alterations in PV+ interneurons (Hashimoto et al., 2003). Specifically, my study extends the initial observation by Hahn et al. (2006) that NRG1 treatment suppresses NMDAR activity to CB1R− (possibly PV+) PTIs but not to pyramidal cells. The preliminary implication of a NMDAR hypofunction in AACs is of particular interest, given that this cell type might play a critical role in the pathophysiology of schizophrenia (Woo et al., 1998; Lewis et al., 2004). Confirmation of the findings in AACs would, however, require independent experiments (see discussion in Chapter 5).

Despite the increasing evidence for involvement of aberrant NRG1tyI/ErbB4 signalling in the neurobiology of the disorder, some aspects remain inconclusive. For example, the function of the GABAergic synapse between PV+ PTIs and CA3 pyramidal cells was not directly affected by NRG1 (Chapter 4), even though reduced GABA metabolism (e.g. decreased GAD67 GABA transporter-1 expression) is

implicated with NMDAR hypofunction (Keilhoff et al., 2004; Kinney et al., 2006; Wang et al., 2008) and schizophrenia (Volk et al., 2000; Volk et al., 2001). Moreover, in addition to the temporal discrepancy between the onset of a cognitive deficit and gamma oscillations discussed above, the direction in which gamma oscillations are altered in NRG1tyI mice (reduced frequency, trend to enlarged power) conflicts with that observed in schizophrenic patients (reduced power; review in Uhlhaas & Singer, 2010).

6.4 Other mechanisms potentially contributing to changed network function in NRG1tyI mice

NRG1 over-expression is also likely to cause changes in other cellular components unidentified in my study. In light of my data and recent published evidence, alterations in three parameters, in particular, could be involved in the observed changes in network activity.

Intrinsic changes in PV+ PTIs. As outlined above, acute NRG1 was recently found to increase the excitability of fast-spiking interneurons (Li et al., 2012). Further experiments should investigate whether NRG1tyI over-expression has similar direct effects and alters PV+ output. NRG1 might also indirectly affect resting membrane potential and resistance of fast-spiking BCs, possibly through interference with the mitochondrial respiratory chain, or oxidative stress. Both were found to change hippocampal gamma oscillations *in vitro* (Steullet et al., 2010; Whittaker et al., 2011). Interestingly, oxidative stress resulting from inhibition of NMDARs *in vivo* (Behrens et al., 2007) selectively reduced the power of kainate-induced beta/gamma oscillations in ventral but not dorsal hippocampus (Steullet et al., 2010). This is noteworthy, because I probed gamma oscillations predominantly in ventral/mid-ventral hippocampal slices.

Inhibition of PV+ PTIs. Computational simulations suggest that mutual inhibition between BCs might contribute to gamma oscillations in the DG network by synchronising interneuron firing (Bartos et al., 2001; Vida et al., 2006; Introduction 1.3.2). However, reducing reciprocal phasic inhibition between PV+ interneurons genetically had little effect on the frequency of *in vivo* hippocampal gamma oscillations (Wulff et al., 2009). Besides phasic inhibition, tonic inhibition via GABA-B receptors might modulate hippocampal gamma oscillations. In fact, block of GABA-B receptors was shown to prolong stimulus-evoked gamma oscillations, suggesting that they contribute to the synaptic control of fast oscillations driven solely by inhibition (Whittington et al., 1995). As outlined above, lack of tonic inhibition makes CA3 hippocampal gamma oscillations, induced by recurrent feedback (PING, Introduction 1.3.2), particularly sensitive to NMDAR antagonism (see above; Mann & Mody, 2010). Thus, it is conceivable that NRG1tyI over-expression might alter tonic inhibitory control and synchronisation of PV+ interneurons via alterations in GABA-B receptor-mediated signalling.

Other interneuron types. Despite the evidence for PV+ interneurons at the heart of the network alteration in NRG1tyI mice, NRG1/ErbB4 signalling probably also interferes with the function of other distinct interneuron types. In fact, immunohistochemical studies found that ErbB4 co-localises not only with PV but also with CCK and nNOS (Introduction 1.1.3; Neddens & Buonanno, 2010). These two markers characterise GABAergic cell types that are distinct from PV+ ones (Somogyi, 2010). I propose future research should focus on two additional interneuron types: CCK+ PTIs and NPY+ dendritic-targeting interneurons.

The evidence for involvement of CCK+ BCs is strong for three reasons. Firstly, a subset of CCK+ GABAergic terminals is immunopositive for ErbB4 (Vullhorst et al.,

2009) and therefore may be subject to NRG1/ErbB4 signalling, although possibly to a lesser degree than PV cells (Neddens & Buonanno, 2010). Secondly, CCK+ BCs have been proposed to 'fine-tune' gamma oscillations (Freund & Katona, 2007; Armstrong & Soltesz, 2012). Thirdly, their biophysical properties give rise to asynchronous GABA release (Hefft & Jonas, 2005; Glickfeld & Scanziani, 2006). This might contribute to the slower-decaying compound IPSCs in pyramidal cells of transgenic mice during gamma oscillations, especially in light of the evidence that the α2 subunit of the GABA-A receptor, which has been associated with PV-negative BC synapses (Nyiri et al., 2001), may confer slower decay kinetics (Lavoie et al., 1997; see Introduction). In anaesthetised rats, CCK+ BCs are only weakly coupled to fast (>50 Hz) CA3 gamma oscillation (Lasztoczi et al., 2011). Yet, their contribution to gamma oscillations might increase with subcortical inputs, given that CCK+ BCs express mAChRs and nAChRs (Introduction 1.2.3). Cholinergic activation was indeed shown to increase the excitability and extend the intrinsic oscillatory activity of CCK+ BCs into the beta-frequency range (Ceo-del Rio et al., 2010; Ceo-del Rio et al., 2011). Thus, they might be more easily recruited in transgenic mice if NRG1tyI over-expression increased expression of their mAChRs (see Chapter 3). On the other hand, GABA release from CCK-containing regular spiking BCs was reported to be suppressed via endocannabinoids in CCh-induced gamma oscillations (Gulyas et al., 2010) so their contribution in my recordings remains to be quantified.

Besides CCK+ BCs, dendritic-targeting interneurons might be compromised in function by aberrant NRG1 levels. In light of the detected upregulation of NPY mRNA in NRG1tyI mouse hippocampus (Chapter 3; Deakin, 2009) NPY-expressing dendritic-targeting interneurons are of particular interest. Indeed, NPY-, SOM- and PV-expressing bistratified cells in area CA1 (Somogyi, 2010) are strongly coupled to CA1

gamma oscillations *in vivo* (Tukker et al., 2007). Dendritic inhibition mediated by SOM-expressing interneurons (including bistratified cells) has recently also been shown to effectively control input–output transformations in CA1 pyramidal cells (Lovett-Barron et al., 2012) and regulate pyramidal cell burst discharge during theta oscillations (Royer et al., 2012). Hence, altered bistratified cell function may contribute to the altered network activity in NRG1tyI mice, even though application of CCh was reported to reduce IPSC amplitude in bistratified cell–CA3 pyramidal cell pairs (Gulyas et al., 2010).

Additionally, NRG1tyI over-expression could exert other effects, including interference with the dopaminergic system (Kwon et al., 2008; Kato et al., 2010).

6.5 Future directions

Further research is required to strengthen the preliminary evidence that increased NRG1tyI expression interferes with NMDAR function in CB1R− (PV+) interneurons, in particular BCs and AACs, and to explore their contribution to abnormal network and system function in NRG1tyI mice. Three questions will be addressed.

1) Are NMDAR-mediated currents, elicited by stimulation of CA3 recurrent fibres, similarly reduced in PV+ BCs and AACs of NRG1tyI mice?

   Electrical stimulation studies will ensure a better signal-to-noise ratio in measuring NMDAR-mediated current amplitudes (and the NMDA/AMPA amplitude ratio). In addition, larger NMDA currents elicited by stimulation will enable reliable measurements of the current kinetics and charge. These parameters are important in elucidating which postsynaptic mechanisms underlie the selective reduction of the NMDAR-mediated current component (see Chapter 5).

2) Is the rate or temporal precision of PV+ BC spiking altered during CCh-induced network activity in NRG1tyI mice?

   Cell-attached and subsequent whole-cell recordings (for filling with neurobiotin to enable *post hoc* identification) from PV+ BCs would reveal their spiking activity during CCh-induced network activity. Impaired precision of individual BC spiking would be expected to reduce BC synchrony and to prolong compound IPSCs. Alternatively, doublet firing of PV+ BCs may also cause longer IPSCs.

3) Does selective pharmacological or pharmacogenetic enhancement of NMDAR activity in PV+ interneurons accelerate gamma oscillations in NRG1tyI mice?

   According to the theory of NMDAR hypofunction in PV+ cells, CCh-induced gamma oscillations in NRG1tyI mice should become faster if boosted selectively in PV+ cells. Selective activation of interneuronal (presumable GluN2D-containing) NMDARs would be required.

Testing the above hypotheses will further our understanding of the role of long-lasting NMDAR-mediated excitation in PV+ interneurons, and establish whether NRG1 over-expression interferes with this component in the hippocampal network. This study is currently ongoing in our lab, and an optimised PV reporter mouse line holds considerable promise for a better yield in patching PV+ PTIs (Chapter 5). Availability of an optimised reporter mouse line would also allow addressing other open questions that could not be clearly addressed with the optogenetic approach or the Lhx6 reporter mouse line:

Does NRG1tyI over-expression cause PV+ PTI-specific differences in the inhibition of pyramidal cells?

As discussed in Chapter 4, the ChR2 construct available enabled optical stimulation of PV+ axons within str. pyramidale but did not allow the identification of presynaptic interneuron types (specifically the discrimination between AACs and BCs). An optimised reporter mouse line would enable paired recordings from *post hoc* identified presynaptic PV+ cells to CA3 pyramidal cells to explore any cell type-specific differences between BCs and AACs.

Is phasic or tonic inhibition in identified PV+ PTIs reduced in NRG1tyI mice (compared to WT littermates)? Altered tonic inhibition might make the network particularly sensitive to NMDAR dysfunction (see 6.2.2).

As discussed above and by others (Rotaru et al., 2012), altered functioning of PV+ PTIs may not completely account for the changed gamma oscillations and the altered excitation/inhibition balance in NRG1tyI mice. Investigating CCK+ cell-mediated inhibition during CCh-induced gamma oscillations is therefore of particular interest. Pharmacological or pharmacogenetic suppression of CCK+ cell-mediated inhibition might affect CCh-induced gamma oscillations to a greater extend in NRG1tyI mice than in WT littermates.

6.6 Final conclusions

The results of this thesis, together with previous findings (Deakin et al., 2012) demonstrate that a postnatal enhancement of NRG1 expression affects the functioning of the hippocampal network similarly to some observations in schizophrenic patients. It will be instructive to explore NMDAR-related cell type-specific effects in more detail, and to establish whether altered NMDAR-mediated synaptic transmission changes PV+ cell functioning during gamma oscillations. Finally, to what extend do slower hippocampal gamma oscillations contribute to working memory deficit, particular in view of the temporal discrepancy? A detailed understanding of the neurobiological changes induced by NRG1tyI over-expression in this animal model promises to shed further light on the involvement of NRG1 in the pathophysiology of schizophrenia.

7 Appendix

Table A1 Peak frequency and field power following CCh-mediated induction

		Peak frequency		Power	
Old mice (3–6 months)					
Two-way ANOVA with fixed factors: genotype and time windows					
genotype		$F_{(1,55)}$=19.163, p<0.001 ***		$F_{(1,55)}$=15.296, p<0.001 ***	
time windows		$F_{(3,55)}$=0.664, p=0.578		$F_{(3,55)}$=0.358, p=0.783	
interaction		$F_{(3,55)}$=0.531, p=0.663		$F_{(3,55)}$=0.315, p=0.815	
Post hoc simple main effects analysis					
Time window	**Genotype (slices)**	**Hz (mean ± SEM)**	**F and *p*-values**	**μV^2/Hz (mean ± SEM)**	**F and *p*-values**
<10 min	wt (10) NRG1tyI (4)	27.22 ± 1.49 19.53 ± 3.63	$F_{(1,55)}$=8.757, p=0.005 **	50.24 ± 7.93 208.40 ± 108.77	$F_{(1,55)}$=4.416, p=0.040 *
10–30 min	wt (16) NRG1tyI (10)	26.70 ± 1.23 22.34 ± 1.21	$F_{(1,55)}$=6.073, p=0.017 *	66.90 ± 8.51 179.08 ± 53.83	$F_{(1,55)}$=4.785, p=0.033 *
30–50 min	wt (8) NRG1tyI (6)	26.55 ± 1.36 20.55 ± 1.59	$F_{(1,55)}$=6.401, p=0.014 *	69.94 ± 13.64 254.03 ± 95.34	$F_{(1,55)}$=7.180, p=0.010 *
>50 min	wt (5) NRG1tyI (4)	23.93 ± 1.13 20.45 ± 0.58	$F_{(1,55)}$=1.394, p=0.243	62.29 ± 13.56 165.05 ± 121.63	$F_{(1,55)}$=1.450, p=0.234

		Peak frequency		Power	
Young mice (1–2 months)					
Two-way ANOVA with fixed factors: genotype and time windows					
genotype		$F_{(1,87)}$=49.820, p<0.001 ***		$F_{(1,87)}$=29.848, p<0.001 ***	
time windows		$F_{(3,87)}$=3.026, p<0.034 *		$F_{(3,87)}$=3.894, p=0.012 *	
interaction		$F_{(3,87)}$=1.035, p=0.381		$F_{(3,87)}$=5.122, p=0.003 **	
Post hoc simple main effects analysis					
Time window	**Genotype (slices)**	**Hz (mean ± SEM)**	**F and *p*-values**	**μV^2/Hz (mean ± SEM)**	**F and *p*-values**
<10 min	wt (18) NRG1tyI (17)	26.72 ± 0.64 22.04 ± 0.64	$F_{(1,87)}$=18.756, p<0.001 ***	140.07 ± 34.00 273.44 ± 78.33	$F_{(1,87)}$=3.254, p=0.075
10–30 min	wt (14) NRG1tyI (11)	25.63 ± 1.03 22.19 ± 0.88	$F_{(1,87)}$=7.159, p=0.009 **	113.54 ± 17.53 198.62 ± 47.37	$F_{(1,87)}$=0.933, p=0.337
30–50 min	wt (12) NRG1tyI (9)	25.63 ± 1.15 18.85 ± 0.93	$F_{(1,87)}$=23.186, p<0.001 ***	117.13 ± 22.11 318.31 ± 80.79	$F_{(1,87)}$=4.356, p=0.040 *
>50 min	wt (7) NRG1tyI (7)	24.41 ± 1.43 19.71 ± 1.05	$F_{(1,87)}$=7.611, p=0.007 **	90.27 ± 19.24 709.66 ± 174.70	$F_{(1,87)}$=28.099, p<0.001 ***

Note that the number of slices varies in each time window because field potential oscillations were not always probed repeatedly. Individual ~60 s long field potential recordings were taken at 1–3 time points for each slice at 5–100 min after bathing in CCh. Two-way ANOVAs were performed to probe whether there was an interaction between genotype and time, and to test the overall effect of genotype as well as time. Simple *post hoc* main effects analyses were performed to investigate significant effects further within each time window. The F- and *p*-values from these analyses are reported here. * p<0.05, ** p<0.01, *** p<0.001

Table A2 Statistical comparison of field potential parameters

	Geno-type	MICE				SLICES			
		n		raw data	*p*-value	n		raw data	*p* -value
FIELD: older mice (3–6 months)									
frequency (Hz)	WT	9	mean±SEM	24.7 ± 1.8	0.269	19	mean	26.3 ± 1.1	0.005 **
			median	25.33			median	26.9	
	NRG1tyI	8	mean±SEM	22.0 ± 1.5		14	Mean±SEM	22.0 ± 0.9	
			median	22.0			median	22.0	
power (μV^2/Hz)	WT	9	mean±SEM	66.02 ± 11.76	0.099	19	Mean±SEM	62.84 ±7.97	0.291 [a]
			median	61.19			median	58.60	
	NRG1tyI	8	mean±SEM	151.24 ± 44.20		14	Mean±SEM	141.45 ±41.33	
			median	125.27			median	65.23	
FIELD: young mice (1–2 months)									
frequency (Hz)	WT	17	mean±SEM	26.8 ± 0.6	<0.0001 ***	27	mean	26.2 ± 0.6	<0.0001 *** [a]
			median	26.9			median	25.6	
	NRG1tyI	10	mean±SEM	22.1 ± 0.5		21	Mean±SEM	22.1 ± 0.6	
			median	22.0			median	23.2	
power (μV^2/Hz)	WT	17	mean±SEM	133.10 ± 25.05	0.079 [a]	27	Mean±SEM	140.16 ±23.35	0.167 [a]
			median	116.85			median	106.96	
	NRG1tyI	10	mean±SEM	228.90 ± 46.91		21	Mean±SEM	245.36 ±65.45	
			median	201.21			median	158.33	
Subset FIRING: young mice (1–2 months)									
frequency (Hz)	WT	7	mean±SEM	24.9 ± 0.9	0.005 **	8	mean	25.0 ± 0.8	0.001 **
			median	25.0			median	25.0	
	NRG1tyI	6	mean±SEM	19.7 ± 1.1		8	Mean±SEM	19.2 ± 1.2	
			median	18.6			median	18.6	
power (μV^2/Hz)	WT	7	mean±SEM	127.50 ± 53.74	0.015 * [a]	8	Mean±SEM	130.20 ±48.19	0.012 * [a]
			median	89.56			median	86.87	
	NRG1tyI	6	mean±SEM	516.50 ± 204.21		8	Mean±SEM	513.20±178.73	
			median	284.67			median	274.74	
Subset WHOLE-CELL RECORDINGS: young mice (1–2 months)									
frequency (Hz)	WT	9	mean±SEM	26.7 ± 0.9	0.002 **	11	mean	26.6 ±1.0	0.002 **
			median	26.9			median	26.9	
	NRG1tyI	5	mean±SEM	21.4 ± 0.7		7	Mean±SEM	20.9 ± 1.1	
			median	22.0			median	22.0	
power (μV^2/Hz)	WT	9	mean±SEM	124.29 ± 24.11	<0.001 ***	11	Mean±SEM	116.21 ± 20.95	0.003 **
			median	79.83			median	90.19	
	NRG1tyI	5	mean±SEM	330.62 ± 22.31		7	Mean±SEM	349.48 ± 77.26	
			median	305.26			Median	305.26	

Statistical comparisons were conducted on the level of mice (by averaging oscillation frequency and power across all slices per mouse) and at the level of slices

* $p<0.05$, ** $p<0.01$, *** $p<0.001$

[a] MW, Mann–Whitney U test; all others, independent samples t test

Table A3 Lower threshold for epileptiform activity in NRG1tyI slices in CCh

	Slices displaying **robust gamma oscillations** in CCh (number of mice)	Slices displaying **epileptiform discharges** in CCh (number of mice)	Slices initially displaying gamma oscillations in CCh, but **develop epileptiform discharges** with time (number of mice)	Total number of slices bathed in CCh (number of mice)
Older Mice				
5 µM CCh				
WT	8 (4 mice)	0	0	8 (4 mice)
NRG1tyI	10 (5 mice)	3 (2 mice)	1 (1 mouse)	14 (5 mice)
10–20 µM CCh				
WT	11 (5 mice)	2 (2 mice)	0	13 (5 mice)
NRG1tyI	3 (3 mice)	19 (5 mice)	0	22 (6 mice)
Younger mice				
5 µM CCh				
WT	9 (6 mice)	0	0	9 (6 mice)
NRG1tyI	12 (6 mice)	3 (3 mice)	1 (1 mouse)	16 (6 mice)
10–2 0µM CCh				
WT	16 (10 mice)	6 (3 mice)	2 (2 mice)	24 (12 mice)
NRG1tyI	4 (4 mice)	9 (7 mice)	4 (2 mice)	17 (8 mice)

Note: Slices that initially displayed gamma oscillations but later presented epileptiform bursts were included in the gamma analysis outlined in Chapter 3, because their properties did not vary from those of slices that remained in gamma oscillation during the entire recording.

Table A4 Overview of anatomical procedures involved in the identification of PTIs

Fixed 250 µm thick slices were resectioned at 50 or 60 µm thickness, resulting in four to five sections. Sections were not kept in a consecutive order; e.g. the numbering (s1–s5) in column 5 is arbitrary. Sections with significant amount of axon (and, if recovered, soma/dendrites) were digitally reconstructed. Sections included in the reconstructions presented in Chapter 5 are underlined. Laminar analysis of CB1R− putative BCs, was carried out on at least two sections (indicated by asterisk; see Figure 5.1B and Methods 2.7.2.1). The computations of axon pixels for laminar analyses were performed by Dr Andras Szabo. Evaluation of immunoreactivity was carried out with Dr Andras Szabo using structured illumination fluorescence microscopy or confocal laser-scanning microscopy. For details refer to Methods 2.7. Cell compartments recovered: s, soma; d, dendrite; ax, axon.

Experimenter initials: AS= Dr Andras Szabo, PL= Petrina Lau, WN= Wiebke Nissen (date of immunoreactions given as day – month - year).

Cell code	Genotype	Compartment recovered	Resectioned by (µm thick)	Sections reconstructed [a]	by	Immunoreactions			
						GFP (chx)	PV (rb)	CB1R (gp)	Ankyrin-G (ms)
Lhx6+, CB1R- putative BCs (*n*=14)									
W180511	Lhx6	ax	WN (50)	s1*, s2*, s3	AS	AS 060611	AS 060611	AS 140611	
W060712	Lhx6	ax, d, s	AS (60)	s1, s2 (s)*, s3, s4*	AS	WN 190711	WN 190711	WN 190711	
W150712	Lhx6	ax	WN (60)	s1*, s2*	AS	AS 020911/ WN 160911	WN 160911	AS 020911	
L150711	Lhx6	ax, d, s	WN (60)	s2*, s3 (s)*, s4*	WN	AS 020911	AS 020911	AS 020911	
L200711	Lhx6	ax (in CA3a)	WN (60)	s1*, s2*, s3*	WN	WN 160911	WN160911	WN 160911	
W240813	Lhx6	ax, d, s	AS (60)	s2 (s)*, s4*, s3	AS	AS 020911	AS 020911	AS 020911	WN 300911
W250812	Lhx6	ax	AS (60)	s1*, s2*, s3	AS	AS 020911/ PL 071011	PL 071011	AS 020911	WN 260911/ WN 300911
M260812	Lhx6	ax	WN (60)	s1, s2*, s3*	WN	AS 020911/ WN 160911	WN 160911	AS 020911	WN 141011
W220612	NRG1tyI/Lhx6	ax	AS (50)	s3, s4*, s6*	WN	AS 010711/ WN 160911	WN 160911	AS 010711	WN 300911
W280612	NRG1tyI/Lhx6	ax, d, s	AS (50)	s2, s3*, s5 (s)*	WN	WN 190711	WN 190711	WN 190711	
W010713	NRG1tyI/Lhx6	ax, d, s	AS (50)	s1*, s2, s3*	AS	WN 190711	WN 190711	WN 190711	
W140711	NRG1tyI/Lhx6	ax	WN (60)	s2*, s4*	AS	AS 020911/ PL 071011	PL 071011	AS 020911	
W100813	NRG1tyI/Lhx6	ax, d, s	WN (60)	s4*, s5 (s)*, s1	AS	AS 020911	AS 020911	AS 020911	
W100815	NRG1tyI/Lhx6	ax, d, s	WN (60)	s2, s4 (s)*, s5*	AS	AS 020911	AS 020911	AS 020911	WN 300911
AACs (*n*=6)									
W120512	Lhx6	ax	WN (50)	s2, s3, s4	AS	WN 030611/ AS 140611	WN 030611	AS 140611	WN 300911
W050712	Lhx6	ax, d, s	AS (60)	s1, s2, s3, s4 (s)	AS	WN 190711	WN 190711	WN 190711	WN 300911/ WN 141011
W150713	Lhx6	ax, d, s	WN (60)	s2 (s), s3, s4	AS	AS 020911	AS 020911	AS 020911	WN 300911
W250713	Lhx6	ax, d, s	WN (60)	s5 (s), s4 (s), s2	WN	AS 020911	AS 020911	AS 020911	WN 300911
W220611	NRG1tyI/Lhx6	ax, d, s	AS (50)	s3 (s)	WN	AS 010711	AS 010711	AS 010711	WN 300911
W150812	NRG1tyI	ax, d, s	AS (60)	s2 (s)	AS	AS 020911	AS 020911	AS 020911	WN 300911/ WN 141011

[a] underlined, presented in reconstruction; * laminar analysis

Table A5 CB1R− BCs, AACs, CA3 pyramidal cells included in mEPSCs analysis

Cell code	Genotype	V_h=−65 mV	V_h=−65 mV in 25 µM NBQX	V_h=+40 mV in 25 µM NBQX	V_h=+40 mV in 25 µM NBQX + 100 µM AP5
Lhx6+, CB1R− putative BCs (n=14)					
W180511	Lhx6	Y	Y	N	N
W060712	Lhx6	Y	Y	Y	Y
W150712	Lhx6	Y	Y	Y	Y
L150711	Lhx6	Y	Y	Y	Y
L200711	Lhx6	Y	Y	Y	N
W240813	Lhx6	Y	Y	Y	Y
W250812	Lhx6	Y	Y	Y	Y
M260812	Lhx6	Y	Y	Y	Y
W220612	NRG1tyI/Lhx6	Y	Y	Y	N
W280612	NRG1tyI/Lhx6	Y	Y	Y	N
W010713	NRG1tyI/Lhx6	Y	Y	Y	N
W140711	NRG1tyI/Lhx6	Y	Y	Y	N
W100813	NRG1tyI/Lhx6	Y	Y	Y	Y
W100815	NRG1tyI/Lhx6	Y	Y	Y	Y
AACs (n=6)					
W120512	Lhx6	Y	Y	Y	N
W050712	Lhx6	Y	Y	Y	N
W150713	Lhx6	Y	Y	Y	N
W250713	Lhx6	Y	Y	Y	Y
W220611	NRG1tyI/Lhx6	Y	Y	Y	N
W150812	NRG1tyI	Y	Y	Y	N
CA3 pyramidal cells (n=14)					
L130611	WT[a]	Y	Y	Y	N
W270713	Lhx6	Y	Y	N	N
W090812_cell1	Lhx6	Y	N	N	N
W090812_cell2	Lhx6	Y	Y	Y	Y
W110811	Lhx6	Y	Y	Y	N
W110814	Lhx6	Y	Y	Y	Y
W100611	NRG1tyI	Y	Y	Y	N
W100612	NRG1tyI	Y	N	N	N
W210712	NRG1tyI/Lhx6	Y	Y	Y	N
W150813	NRG1tyI	Y	Y	Y	Y
W170813	NRG1tyI	Y	Y	Y	Y
W220812	NRG1tyI/Lhx6	Y	Y	Y	Y
W220813	NRG1tyI/Lhx6	Y	Y	Y	Y
W230811	NRG1tyI/Lhx6	Y	Y	Y	Y

[a] NRG1tyI littermate

Y, yes (recorded in this configuration); N, not recorded in this configuration

Table A6 NMDAR-mediated mEPSCs in CB1R− BCs, AACs and CA3 pyramidal cells detected by lower amplitude threshold

		Putative BC			AAC			Pyramidal cell		
		Lhx6	NRG1tyI/ Lhx6	*p*-value	Lhx6	NRG1tyI/ Lhx6	*p*-value	Lhx6	NRG1tyI/ Lhx6	*p*-value
NMDAR-mediated mEPSCs (V_h=+40 mV) – detected with decreased amplitude threshold										
n		7	6		4	2		4	7	
frequency (Hz)	mean ± SEM	4.58 ± 1.88	3.34 ± 1.03	0.596	0.60 ± 0.38	0.09 ± 0.01	n.a.	2.99 ± 0.79	2.56 ± 0.90	0.756
	median	3.58	2.90		0.38	0.09		2.91	1.94	
median amplitude (pA)	mean ± SEM	23.87 ± 2.06	18.11 ± 0.83	0.015*	16.69 ± 0.98	12.59 ± 0.60	n.a.	21.75 ± 3.87	19.18 ± 0.73	0.559
	median	20.32	18.17		16.00	12.59		18.57	19.09	
median area (pA*ms)	mean ± SEM	116.73 ± 22.85	80.14 ± 12.42	0.208	94.15 ± 30.29	25.50 ± 3.42	n.a.	106.04 ± 8.65	100.94 ± 17.14	0.797
	median	106.38	72.92		80.97	25.50		108.66	84.68	

*p<0.05; Mann–Whitney U-test **(**non-normal distributions); other *p*-value data: independent samples t test (normal distributions)
n.a., not applicable, due to low *n* numbers of AAC in NRG1tyI mice (*n*=2)

Table A7 NMDAR-mediated mEPSCs detected by lower amplitude threshold: effect of cell type and genotype

Parameter	**Two-way ANOVA with fixed factors:** genotype and cell type	***Post hoc* pairwise comparison**					
NMDAR-mediated mEPSCs: V_h=+40 mV in 25 µM NBQX		**Lhx6**			**NRG1tyI/Lhx6**		
		BC vs AAC	BC vs pyr cell	AAC vs pyr cell	BC vs AAC [a]	BC vs pyr cell	AAC vs pyr cell [a]
frequency (Hz)	genotype: $F_{(1,24)}$=0.349, p=0.560 cell type: $F_{(2,24)}$=2.647, p=0.091 interaction: $F_{(2,24)}$=0.057, p=0.945						
median amplitude (pA)	genotype: $F_{(1,24)}$=6.161, p=0.020* [b] cell type: $F_{(2,24)}$=4.751, p=0.018* interaction: $F_{(2,24)}$=0.425, p=0.659	p=0.033*	p=1.000	p=0.293	p=0.350	p=1.000	p=0.178
median area (pA·ms)	genotype: $F_{(1,24)}$=3.960, p=0.058 cell type: $F_{(2,24)}$=1.741, p=0.197 interaction: $F_{(2,24)}$=0.873, p=0.430						

The significant overall effect of cell type (*p<0.05) and genotype (*p<0.05) was further examined using *post hoc* pairwise comparisons (with Bonferroni correction) within each genotype.

[a] Caution is required in the interpretation of these p-values given low n numbers of AAC in NRG1tyI mice (n=2).

[b] *Post hoc* pairwise comparison (Bonferroni) between genotypes: BCs in Lhx6 vs BC in Lhx6/NRG1tyI, p=0.020*; AACs, p=0.266; pyr cells, p=0.334

Figure A1 Reconstructions of putative BCs and AACs.

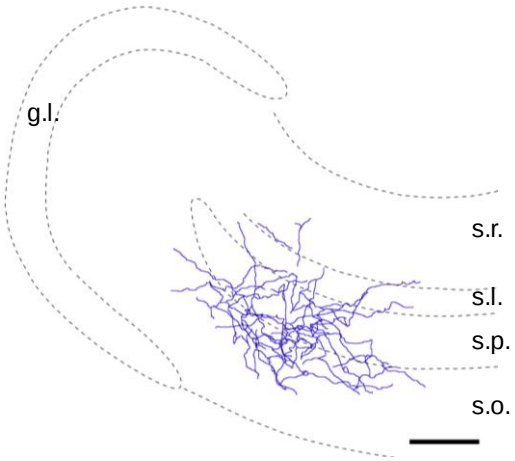
Reconstructions of all putative BCs recorded in Lhx6 mice (*n*=8) and NRG1tyI/Lhx6 mice (*n*=6), and of all AACs recorded in Lhx6 mice (*n*=4) and NRG1tyI/Lhx6 mice (*n*=2). For each cell, one to four 50–60 µm thick sections were reconstructed digitally (Methods 2.7.2.1). The number of sections depended on axon content of each section and variability of axon arborisation between sections. Somatodendritic compartments could not always be recovered, possibly because they were irreversibly damaged when removing the recording electrodes at the end of the experiments. For presentation of putative BCs, sections (up to three) that contained most recovered axon were merged. Sections were digitally aligned using dendrites, main axons and hippocampal strata as landmarks. For AACs, one reconstructed axon section is shown for each cell to clearly illustrate the characteristic radial rows of boutons. Apart from W050712, all AACs had neurobiotin-labelled boutons forming close appositions with Ankyrin-G-labelled AISs.

Laminar borders are indicated, and represent the strata in one section (either the soma section or the section containing most axon) as seen in epifluorescence (using Cy3 filter for Cy3-Streptavidin-labelled Neurobiotin) with 5× magnification. Note, however, that individual CA3 pyramidal cells are often loosely located outside the compact str. pyramidale (more so than in CA1), in particular in ventral CA3a. This may explain why many putative BCs also heavily arborise at the border to str. oriens (not only inside compact str. pyramidale). Note also that in ventral horizontal slices the location of str. pyramidale may be discernibly shifted between adjacent sections. In those cases, only one section is shown, or two individual sections (L200711 and W140711).

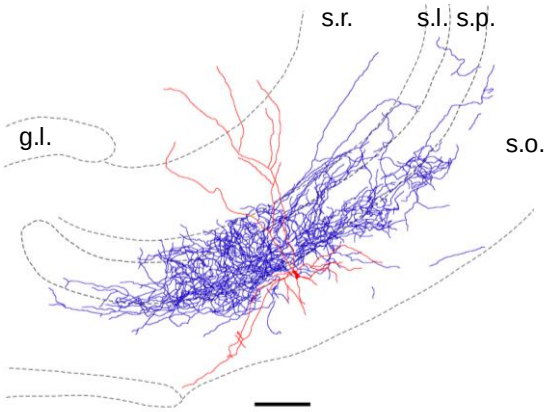
Abbreviations: g.l., granule layer; s.o., stratum oriens; s.p., stratum pyramidale; s.l., stratum lucidum; s.r., stratum radiatum. Scalebars 100 um

Putative BCs recorded in Lhx6 mice (n=8)

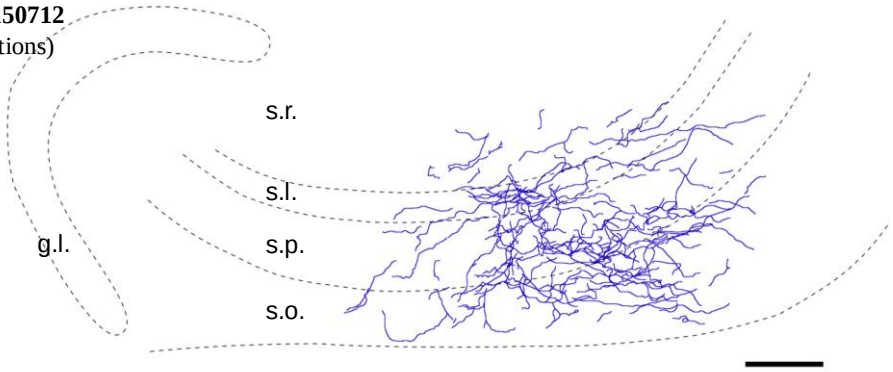
1. W180511
(2 sections)



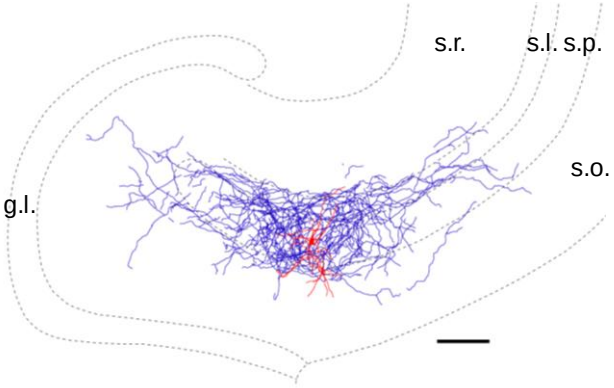
2. W060712
(2 sections)



3. W150712
(2 sections)



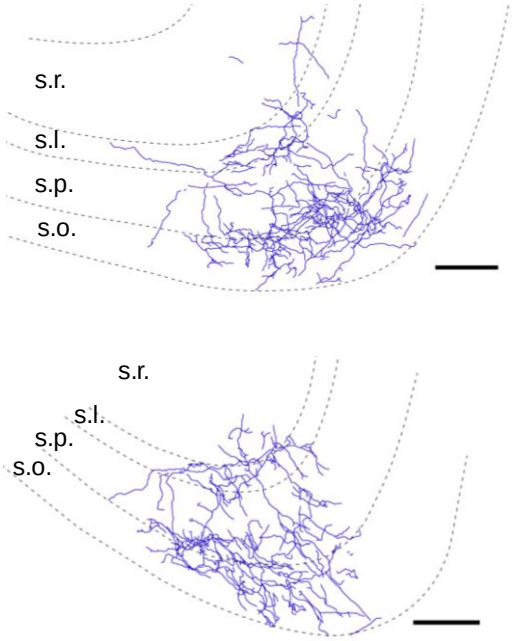
4. L150711
(3 sections)



Putative BCs recorded in Lhx6 mice: continued

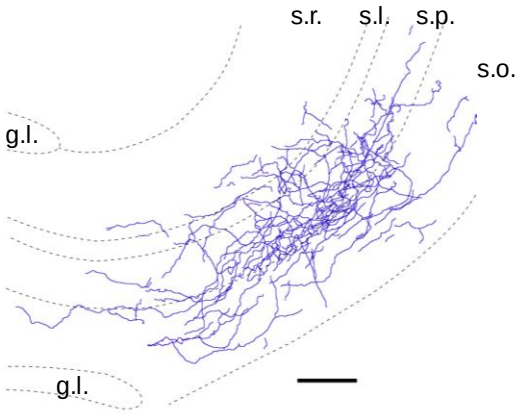
5. L200711
(2 separate sections)

Note: cell is located
in ventral hippocampus

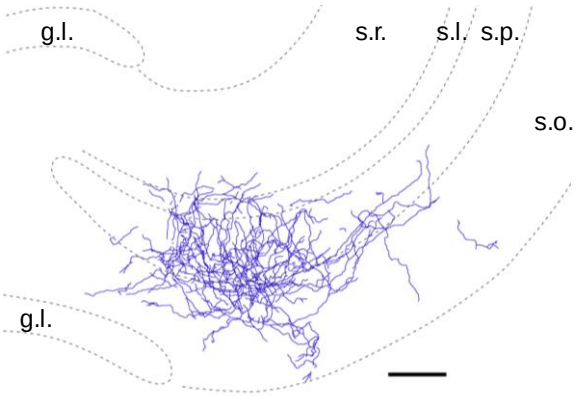


6. W240813 (2 sections) ***see Figure 5.1***

7. W250812
(1 section)

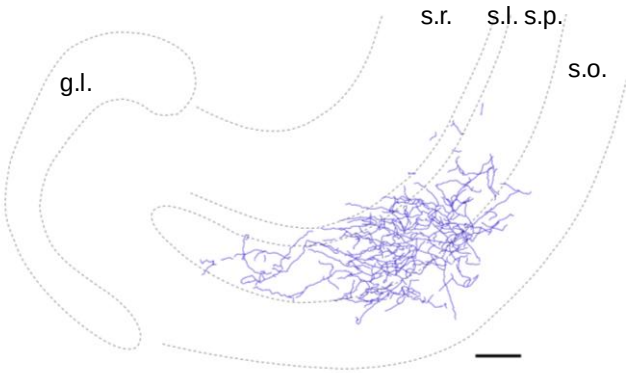


8. M260812
(2 sections)

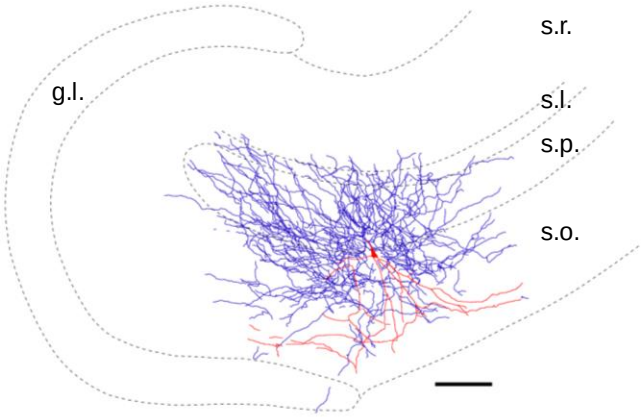


Putative BCs recorded in NRG1tyI/Lhx6 mice (n=6)

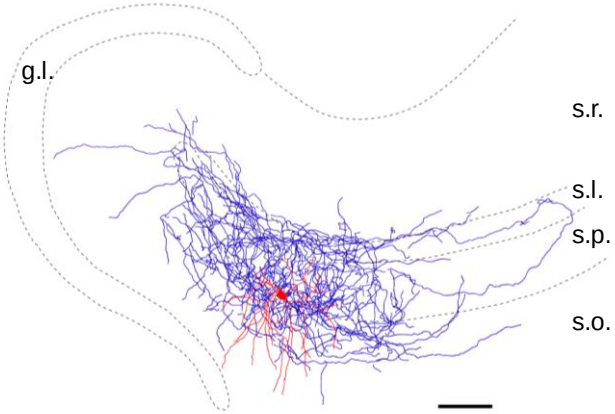
1. W220612
(1 section)



2. W280612
(2 sections)

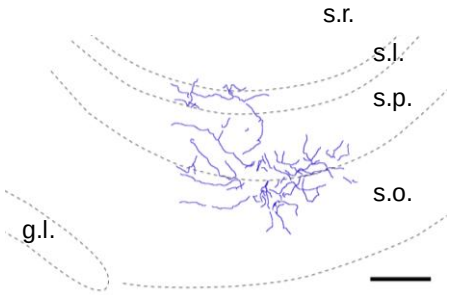


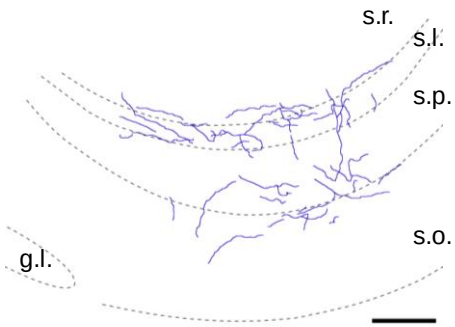
3. W010713
(2 sections)



Putative BCs recorded in NRG1tyI/Lhx6 mice: continued

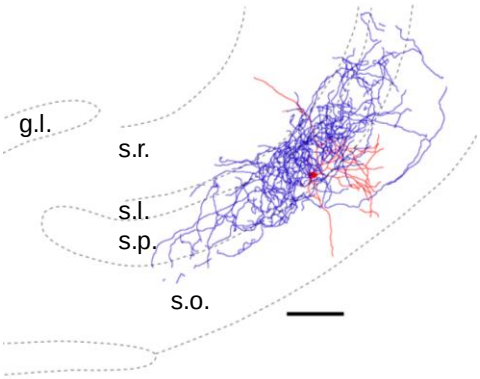
4. W140711
(2 separate sections)





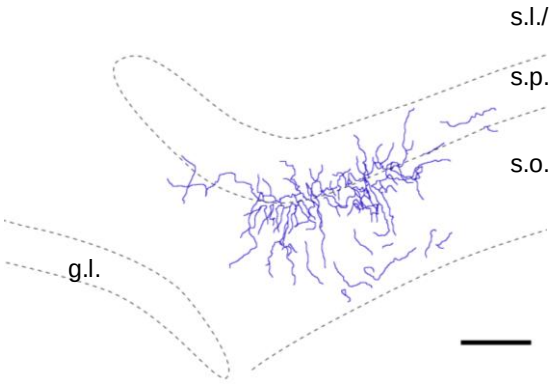
5. W100813 (2 sections) ***see Figure 5.1***

6. W100815
(2 sections)

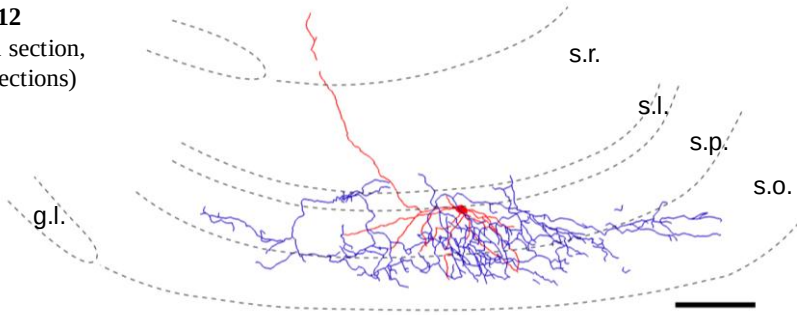


Putative AACs recorded in Lhx6 mice (n=4)

1. W120512
(1 section)

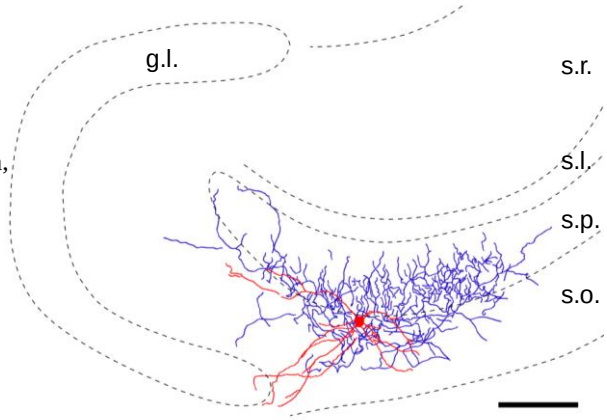


2. W050712
(ax from 1 section,
d from 2 sections)



Note :ventral slice with loose str. pyramidale. The strata are indicated for the section containing axon. Ankyrin-G immunostaining was not successful on any section.

3. W150713
(ax from 1 section,
d from 2 sections)



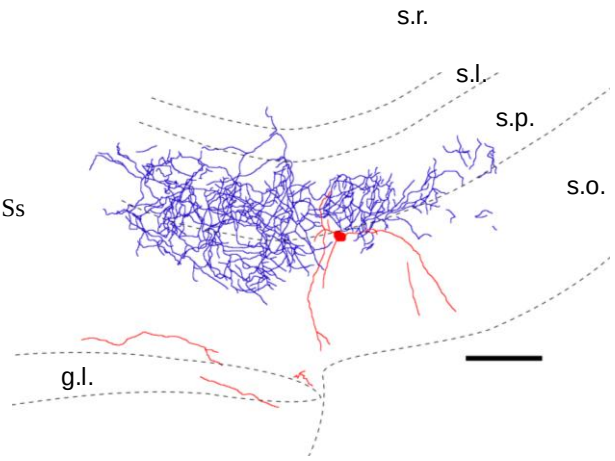
4. W250713 (ax from 1 section, d from 2 sections) ***see Figure 5.2***

Putative AACs recorded in NRG1tyI/Lhx6 mice (n=2)

1. W220611 (1 section) ***see Figure 5.2***

2. W150812
(1 section)

Tight appositions
to Ankyrin-G+ AISs



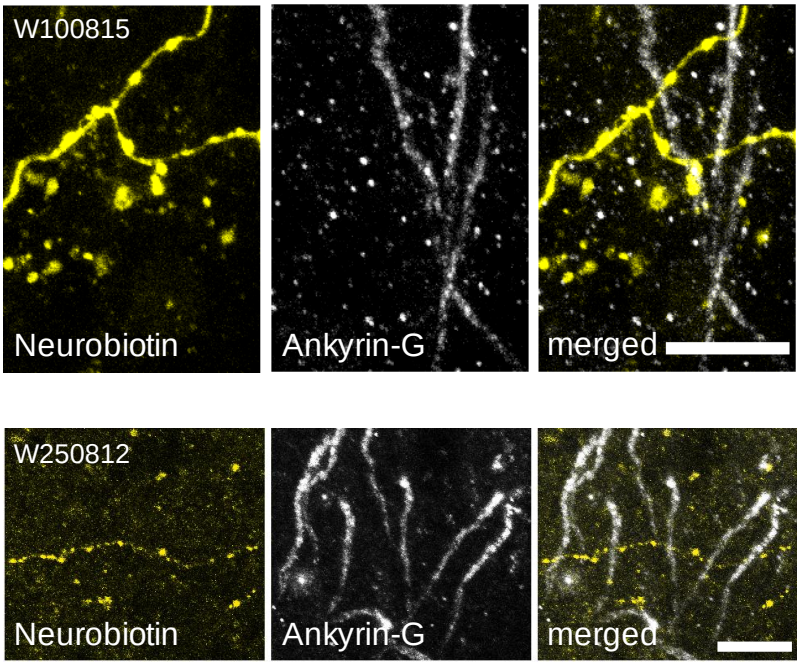


Figure A2 Putative BCs do not form synapses on AIS.

In these two examples, rows of neurobiotin-labelled boutons (yellow) were not observed to follow Ankyrin-G-positive AISs, nor to form tight appositions with them. Scalebars, 10 µm.

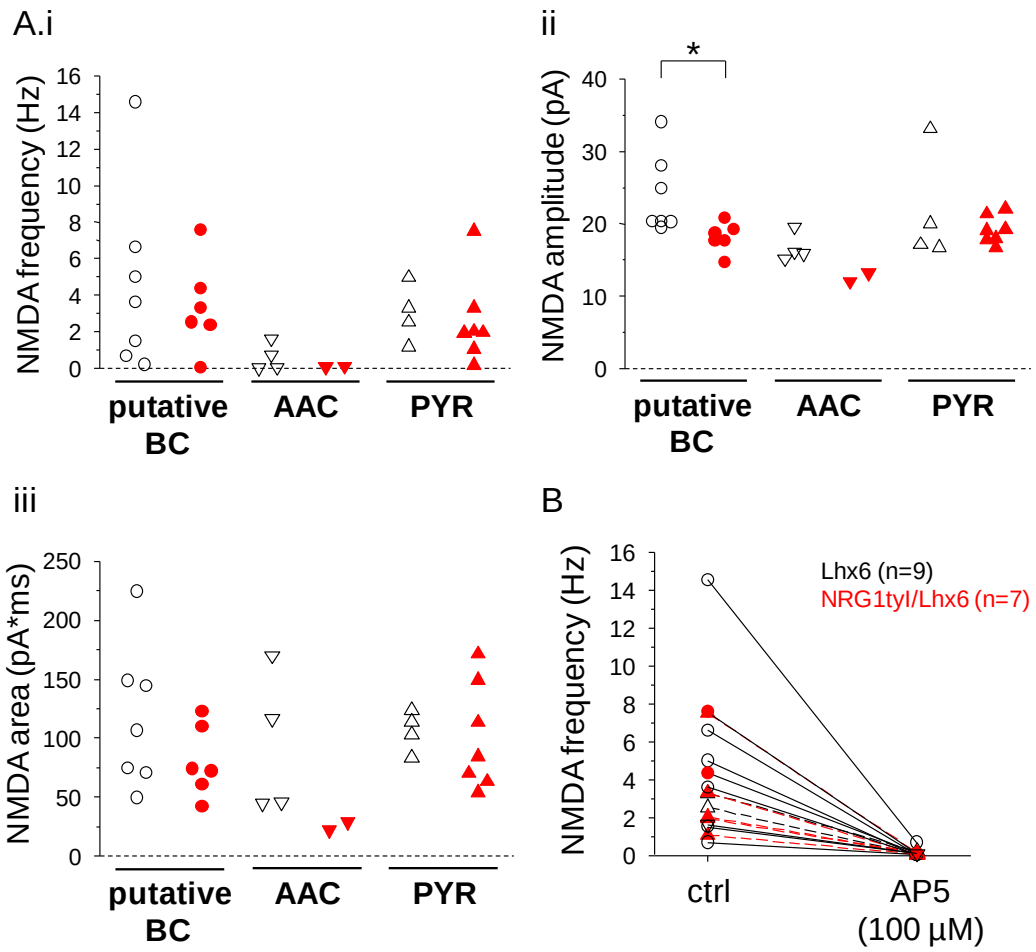


Figure A3 Detection of NMDAR-mediated mEPSCs with lower amplitude threshold.

Decreased amplitude threshold (5 pA, instead of 7 pA) was chosen to include events that were AP5-sensitive (B) but not clearly visually evident among background noise (see Section 5.3.2 NMDAR-mediated mEPSCs). (A) Scatter plots of: (i) frequency, (ii) median amplitudes, and (iii) median areas of NMDAR-mediated mEPSCs in putative BCs (circles), AACs (downward triangles) and pyramidal cells (upward triangles) of Lhx6 (white) and NRG1tyI/Lhx6 (red) mice. Results are qualitatively similar to those reported with higher detection threshold (see Section 5.3.2 and Figure 5.4). All values and statistical comparisons of low threshold results are presented in Tables A6 and A7. Statistical significance: *$p<0.05$. (B) In 100 µM D/L-AP5, automatic event detection using this lowered amplitude threshold is effectively reduced to <13% of the control frequency across all cells (<5% in putative BCs and AACs; <13% in pyramidal cells). This confirms that detected events were NMDAR-mediated, even though they could not be easily verified visually. Note that AP5 was applied for only a subset of experiments.

7 References

Abe Y, Namba H, Kato T, Iwakura Y, Nawa H (2011). Neuregulin-1 signals from the periphery regulate AMPA receptor sensitivity and expression in GABAergic interneurons in developing neocortex. *J Neurosci,* 31 (15): 5699-5709.

Acsady L, Gorcs TJ, Freund TF (1996). Different populations of vasoactive intestinal polypeptide-immunoreactive interneurons are specialized to control pyramidal cells or interneurons in the hippocampus. *Neuroscience,* 73 (2): 317-334.

Amaral DG, Witter MP (1989). The three-dimensional organization of the hippocampal formation: a review of anatomical data. *Neuroscience,* 31 (3): 571-591.

Alger BE, Nicoll RA (1982). Feed-forward dendritic inhibition in rat hippocampal pyramidal cells studied in vitro. *J Physiol,* 328: 105-123.

Andersen P, Bliss TV, Lomo T, Olsen LI, Skrede KK (1969). Lamellar organization of hippocampal excitatory pathways. *Acta Physiol Scand,* 76 (1): 4A-5A.

Andersen P, Soleng AF, Raastad M (2000). The hippocampal lamella hypothesis revisited. *Brain Res,* 886 (1-2): 165-171.

Andersen P, Morris R, Amaral D, Bliss T, O'Keefe J, eds (2007). *The Hippocampus Book*. Oxford University Press, Oxford.

Armstrong C, Soltesz I (2012). Basket cell dichotomy in microcircuit function. *J Physiol,* 590 (Pt 4): 683-694.

Ascoli GA, Alonso-Nanclares L, Anderson SA, Barrionuevo G, Benavides-Piccione R, Burkhalter A, Buzsaki G, Cauli B, Defelipe J, Fairen A, Feldmeyer D, Fishell G, Fregnac Y, Freund TF, Gardner D, Gardner EP, Goldberg JH, Helmstaedter M, Hestrin S, Karube F, et al. (2008). Petilla terminology: nomenclature of features of GABAergic interneurons of the cerebral cortex. *Nat Rev Neurosci,* 9 (7): 557-568.

Atallah BV, Scanziani M (2009). Instantaneous modulation of gamma oscillation frequency by balancing excitation with inhibition. *Neuron,* 62 (4): 566-577.

Autere AM, Lamsa K, Kaila K, Taira T (1999). Synaptic activation of GABAA receptors induces neuronal uptake of Ca2+ in adult rat hippocampal slices. *J Neurophysiol,* 81 (2): 811-816.

Avoli M (2001). Do interictal discharges promote or control seizures? Experimental evidence from an in vitro model of epileptiform discharge. *Epilepsia,* 42 Suppl 3: 2-4.

Baddeley A (2010). Working memory. *Curr Biol,* 20 (4): R136-140.

Banerjee A, Macdonald ML, Borgmann-Winter KE, Hahn CG (2010). Neuregulin 1-erbB4 pathway in schizophrenia: From genes to an interactome. *Brain Res Bull,* 83 (3-4): 132-139.

Bannerman DM, Rawlins JN, McHugh SB, Deacon RM, Yee BK, Bast T, Zhang WN, Pothuizen HH, Feldon J (2004). Regional dissociations within the hippocampus–memory and anxiety. *Neurosci Biobehav Rev,* 28 (3): 273-283.

Bao J, Wolpowitz D, Role LW, Talmage DA (2003). Back signaling by the Nrg-1 intracellular domain. *J Cell Biol,* 161 (6): 1133-1141.

Barros CS, Calabrese B, Chamero P, Roberts AJ, Korzus E, Lloyd K, Stowers L, Mayford M, Halpain S, Muller U (2009). Impaired maturation of dendritic spines without disorganization of cortical cell layers in mice lacking NRG1/ErbB signaling in the central nervous system. *Proc Natl Acad Sci U S A,* 106 (11): 4507-4512.

Barry PH (1994). JPCalc, a software package for calculating liquid junction potential corrections in patch-clamp, intracellular, epithelial and bilayer measurements and for correcting junction potential measurements. *J Neurosci Methods,* 51 (1): 107-116.

Bartlett JS, Samulski RJ, McCown TJ (1998). Selective and rapid uptake of adeno-associated virus type 2 in brain. *Hum Gene Ther,* 9 (8): 1181-1186.

Bartos M, Vida I, Frotscher M, Geiger JR, Jonas P (2001). Rapid signaling at inhibitory synapses in a dentate gyrus interneuron network. *J Neurosci,* 21 (8): 2687-2698.

Bartos M, Vida I, Frotscher M, Meyer A, Monyer H, Geiger JR, Jonas P (2002). Fast synaptic inhibition promotes synchronized gamma oscillations in hippocampal interneuron networks. *Proc Natl Acad Sci U S A,* 99 (20): 13222-13227.

Bartos M, Vida I, Jonas P (2007). Synaptic mechanisms of synchronized gamma oscillations in inhibitory interneuron networks. *Nat Rev Neurosci,* 8 (1): 45-56.

Batista-Brito R, Fishell G (2009). The developmental integration of cortical interneurons into a functional network. *Curr Top Dev Biol,* 87: 81-118.

Baude A, Nusser Z, Molnar E, McIlhinney RA, Somogyi P (1995). High-resolution immunogold localization of AMPA type glutamate receptor subunits at synaptic and non-synaptic sites in rat hippocampus. *Neuroscience,* 69 (4): 1031-1055.

Beasley CL, Zhang ZJ, Patten I, Reynolds GP (2002). Selective deficits in prefrontal cortical GABAergic neurons in schizophrenia defined by the presence of calcium-binding proteins. *Biol Psychiatry,* 52 (7): 708-715.

Behrens MM, Ali SS, Dao DN, Lucero J, Shekhtman G, Quick KL, Dugan LL (2007). Ketamine-induced loss of phenotype of fast-spiking interneurons is mediated by NADPH-oxidase. *Science,* 318 (5856): 1645-1647.

Bekkers JM, Richerson GB, Stevens CF (1990). Origin of variability in quantal size in cultured hippocampal neurons and hippocampal slices. *Proc Natl Acad Sci U S A,* 87 (14): 5359-5362.

Belforte JE, Zsiros V, Sklar ER, Jiang Z, Yu G, Li Y, Quinlan EM, Nakazawa K (2010). Postnatal NMDA receptor ablation in corticolimbic interneurons confers schizophrenia-like phenotypes. *Nat Neurosci,* 13 (1): 76-83.

Ben-Ari Y, Khazipov R, Leinekugel X, Caillard O, Gaiarsa JL (1997). GABAA, NMDA and AMPA receptors: a developmentally regulated 'ménage à trois'. *Trends Neurosci,* 20 (11): 523-529.

Ben-Ari Y (2002). Excitatory actions of gaba during development: the nature of the nurture. *Nat Rev Neurosci,* 3 (9): 728-739.

Bergmann I, Nitsch R, Frotscher M (1991). Area-specific morphological and neurochemical maturation of non-pyramidal neurons in the rat hippocampus as revealed by parvalbumin immunocytochemistry. *Anat Embryol (Berl),* 184 (4): 403-409.

Bertram I, Bernstein HG, Lendeckel U, Bukowska A, Dobrowolny H, Keilhoff G, Kanakis D, Mawrin C, Bielau H, Falkai P, Bogerts B (2007). Immunohistochemical evidence for impaired neuregulin-1 signaling in the prefrontal cortex in schizophrenia and in unipolar depression. *Ann N Y Acad Sci,* 1096: 147-156.

Bi GQ, Poo MM (1998). Synaptic modifications in cultured hippocampal neurons: dependence on spike timing, synaptic strength, and postsynaptic cell type. *J Neurosci,* 18 (24): 10464-10472.

Biro AA, Holderith NB, Nusser Z (2006). Release probability-dependent scaling of the postsynaptic responses at single hippocampal GABAergic synapses. *J Neurosci,* 26 (48): 12487-12496.

Bischofberger J, Engel D, Frotscher M, Jonas P (2006). Timing and efficacy of transmitter release at mossy fiber synapses in the hippocampal network. *Pflugers Arch,* 453 (3): 361-372.

Bjarnadottir M, Misner DL, Haverfield-Gross S, Bruun S, Helgason VG, Stefansson H, Sigmundsson A, Firth DR, Nielsen B, Stefansdottir R, Novak TJ, Stefansson K, Gurney ME, Andresson T (2007). Neuregulin1 (NRG1) signaling through Fyn modulates NMDA receptor phosphorylation: differential synaptic function in NRG1+/- knock-outs compared with wild-type mice. *J Neurosci,* 27 (17): 4519-4529.

Blasco-Ibanez JM, Freund TF (1995). Synaptic input of horizontal interneurons in stratum oriens of the hippocampal CA1 subfield: structural basis of feed-back activation. *Eur J Neurosci,* 7 (10): 2170-2180.

Blatow M, Caputi A, Monyer H (2005). Molecular diversity of neocortical GABAergic interneurones. *J Physiol,* 562 (Pt 1): 99-105.

Boyden ES, Zhang F, Bamberg E, Nagel G, Deisseroth K (2005). Millisecond-timescale, genetically targeted optical control of neural activity. *Nat Neurosci,* 8 (9): 1263-1268.

Bragin A, Jando G, Nadasdy Z, Hetke J, Wise K, Buzsaki G (1995). Gamma (40-100 Hz) oscillation in the hippocampus of the behaving rat. *J Neurosci,* 15 (1 Pt 1): 47-60.

Brinkmann BG, Agarwal A, Sereda MW, Garratt AN, Muller T, Wende H, Stassart RM, Nawaz S, Humml C, Velanac V, Radyushkin K, Goebbels S, Fischer TM, Franklin RJ, Lai C, Ehrenreich H, Birchmeier C, Schwab MH, Nave KA (2008). Neuregulin-1/ErbB signaling serves distinct functions in myelination of the peripheral and central nervous system. *Neuron,* 59 (4): 581-595.

Buhl EH, Szilagyi T, Halasy K, Somogyi P (1996). Physiological properties of anatomically identified basket and bistratified cells in the CA1 area of the rat hippocampus in vitro. *Hippocampus,* 6 (3): 294-305.

Buonanno A (2010). The neuregulin signaling pathway and schizophrenia: from genes to synapses and neural circuits. *Brain Res Bull,* 83 (3-4): 122-131.

Burglen F, Marczewski P, Mitchell KJ, van der Linden M, Johnson MK, Danion JM, Salame P (2004). Impaired performance in a working memory binding task in patients with schizophrenia. *Psychiatry Res,* 125 (3): 247-255.

Butt SJ, Fuccillo M, Nery S, Noctor S, Kriegstein A, Corbin JG, Fishell G (2005). The temporal and spatial origins of cortical interneurons predict their physiological subtype. *Neuron,* 48 (4): 591-604.

Buzsaki G, Leung LW, Vanderwolf CH (1983). Cellular bases of hippocampal EEG in the behaving rat. *Brain Res,* 287 (2): 139-171.

Buzsaki G, Draguhn A (2004). Neuronal oscillations in cortical networks. *Science,* 304 (5679): 1926-1929.

Buzsaki G (2006). *Rhythms of the Brain.* 1st Edition. Oxford University Press, New York.

Buzsaki G, Kaila K, Raichle M (2007). Inhibition and brain work. *Neuron,* 56 (5): 771-783.

Buzsaki G (2010). Hippocampal microcircuits - physiology. In: *Handbook of Brain Microcircuits* (Shepherd GM, Grillner S, eds), pp 165-174. Oxford University Press, New York.

Caillard O, Moreno H, Schwaller B, Llano I, Celio MR, Marty A (2000). Role of the calcium-binding protein parvalbumin in short-term synaptic plasticity. *Proc Natl Acad Sci U S A*, 97 (24): 13372-13377.

Capogna M (2011). Neurogliaform cells and other interneurons of stratum lacunosum-moleculare gate entorhinal-hippocampal dialogue. *J Physiol*, 589 (Pt 8): 1875-1883.

Cardin JA, Carlen M, Meletis K, Knoblich U, Zhang F, Deisseroth K, Tsai LH, Moore CI (2009). Driving fast-spiking cells induces gamma rhythm and controls sensory responses. *Nature*, 459 (7247): 663-667.

Cardin JA, Carlen M, Meletis K, Knoblich U, Zhang F, Deisseroth K, Tsai LH, Moore CI (2010). Targeted optogenetic stimulation and recording of neurons in vivo using cell-type-specific expression of Channelrhodopsin-2. *Nat Protoc*, 5 (2): 247-254.

Carlen M, Meletis K, Siegle JH, Cardin JA, Futai K, Vierling-Claassen D, Ruhlmann C, Jones SR, Deisseroth K, Sheng M, Moore CI, Tsai LH (2012). A critical role for NMDA receptors in parvalbumin interneurons for gamma rhythm induction and behavior. *Mol Psychiatry*, 17 (5): 537-548.

Caroni P (1997). Overexpression of growth-associated proteins in the neurons of adult transgenic mice. *J Neurosci Methods*, 71 (1): 3-9.

Castner SA, Goldman-Rakic PS, Williams GV (2004). Animal models of working memory: insights for targeting cognitive dysfunction in schizophrenia. *Psychopharmacology (Berl)*, 174 (1): 111-125.

Catania MV, Tolle TR, Monyer H (1995). Differential expression of AMPA receptor subunits in NOS-positive neurons of cortex, striatum, and hippocampus. *J Neurosci*, 15 (11): 7046-7061.

Cea-del Rio CA, Lawrence JJ, Tricoire L, Erdelyi F, Szabo G, McBain CJ (2010). M3 muscarinic acetylcholine receptor expression confers differential cholinergic modulation to neurochemically distinct hippocampal basket cell subtypes. *J Neurosci*, 30 (17): 6011-6024.

Cea-del Rio CA, Lawrence JJ, Erdelyi F, Szabo G, McBain CJ (2011). Cholinergic modulation amplifies the intrinsic oscillatory properties of CA1 hippocampal cholecystokinin-positive interneurons. *J Physiol*, 589 (Pt 3): 609-627.

Chang Q, Fischbach GD (2006). An acute effect of neuregulin 1 beta to suppress alpha 7-containing nicotinic acetylcholine receptors in hippocampal interneurons. *J Neurosci*, 26 (44): 11295-11303.

Charpak S, Pare D, Llinas R (1995). The entorhinal cortex entrains fast CA1 hippocampal oscillations in the anaesthetized guinea-pig: role of the monosynaptic component of the perforant path. *Eur J Neurosci,* 7 (7): 1548-1557.

Chattopadhyaya B, Di Cristo G, Higashiyama H, Knott GW, Kuhlman SJ, Welker E, Huang ZJ (2004). Experience and activity-dependent maturation of perisomatic GABAergic innervation in primary visual cortex during a postnatal critical period. *J Neurosci,* 24 (43): 9598-9611.

Chen MS, Bermingham-McDonogh O, Danehy FT, Jr., Nolan C, Scherer SS, Lucas J, Gwynne D, Marchionni MA (1994). Expression of multiple neuregulin transcripts in postnatal rat brains. *J Comp Neurol,* 349 (3): 389-400.

Cho RY, Konecky RO, Carter CS (2006). Impairments in frontal cortical gamma synchrony and cognitive control in schizophrenia. *Proc Natl Acad Sci U S A,* 103 (52): 19878-19883.

Chong VZ, Thompson M, Beltaifa S, Webster MJ, Law AJ, Weickert CS (2008). Elevated neuregulin-1 and ErbB4 protein in the prefrontal cortex of schizophrenic patients. *Schizophr Res,* 100 (1-3): 270-280.

Cobb SR, Buhl EH, Halasy K, Paulsen O, Somogyi P (1995). Synchronization of neuronal activity in hippocampus by individual GABAergic interneurons. *Nature,* 378 (6552): 75-78.

Cobb SR, Halasy K, Vida I, Nyiri G, Tamas G, Buhl EH, Somogyi P (1997). Synaptic effects of identified interneurons innervating both interneurons and pyramidal cells in the rat hippocampus. *Neuroscience,* 79 (3): 629-648.

Cobos I, Calcagnotto ME, Vilaythong AJ, Thwin MT, Noebels JL, Baraban SC, Rubenstein JL (2005). Mice lacking Dlx1 show subtype-specific loss of interneurons, reduced inhibition and epilepsy. *Nat Neurosci,* 8 (8): 1059-1068.

Cobos I, Long JE, Thwin MT, Rubenstein JL (2006). Cellular patterns of transcription factor expression in developing cortical interneurons. *Cereb Cortex,* 16 Suppl 1: i82-88.

Colgin LL, Denninger T, Fyhn M, Hafting T, Bonnevie T, Jensen O, Moser MB, Moser EI (2009). Frequency of gamma oscillations routes flow of information in the hippocampus. *Nature,* 462 (7271): 353-357.

Colgin LL, Moser EI (2010). Gamma oscillations in the hippocampus. *Physiology (Bethesda),* 25 (5): 319-329.

Corfas G, Rosen KM, Aratake H, Krauss R, Fischbach GD (1995). Differential expression of ARIA isoforms in the rat brain. *Neuron,* 14 (1): 103-115.

Cossart R, Dinocourt C, Hirsch JC, Merchan-Perez A, De Felipe J, Ben-Ari Y, Esclapez M, Bernard C (2001). Dendritic but not somatic GABAergic inhibition is decreased in experimental epilepsy. *Nat Neurosci,* 4 (1): 52-62.

Cossart R, Epsztein J, Tyzio R, Becq H, Hirsch J, Ben-Ari Y, Crepel V (2002). Quantal release of glutamate generates pure kainate and mixed AMPA/kainate EPSCs in hippocampal neurons. *Neuron,* 35 (1): 147-159.

Coyle JT, Tsai G, Goff D (2003). Converging evidence of NMDA receptor hypofunction in the pathophysiology of schizophrenia. *Ann N Y Acad Sci,* 1003: 318-327.

Csicsvari J, Jamieson B, Wise KD, Buzsaki G (2003). Mechanisms of gamma oscillations in the hippocampus of the behaving rat. *Neuron,* 37 (2): 311-322.

Cunningham MO, Hunt J, Middleton S, LeBeau FE, Gillies MJ, Davies CH, Maycox PR, Whittington MA, Racca C (2006). Region-specific reduction in entorhinal gamma oscillations and parvalbumin-immunoreactive neurons in animal models of psychiatric illness. *J Neurosci,* 26 (10): 2767-2776.

Danglot L, Triller A, Marty S (2006). The development of hippocampal interneurons in rodents. *Hippocampus,* 16 (12): 1032-1060.

Deakin IH (2009). *Phenotypic characterisation of mice over-expressing neuregulin 1 type I.* DPhil thesis. Keble College, University of Oxford, Oxford.

Deakin IH, Law AJ, Oliver PL, Schwab MH, Nave KA, Harrison PJ, Bannerman DM (2009). Behavioural characterization of neuregulin 1 type I overexpressing transgenic mice. *Neuroreport,* 20 (17): 1523-1528.

Deakin IH, Nissen W, Law AJ, Lane T, Kanso R, Schwab MH, Nave KA, Lamsa KP, Paulsen O, Bannerman DM, Harrison PJ (2012). Transgenic overexpression of the type I isoform of neuregulin 1 affects working memory and hippocampal oscillations but not long-term potentiation. *Cereb Cortex,* 22 (7): 1520-1529.

Dickinson R, Awaiz S, Whittington MA, Lieb WR, Franks NP (2003). The effects of general anaesthetics on carbachol-evoked gamma oscillations in the rat hippocampus in vitro. *Neuropharmacology,* 44 (7): 864-872.

Du J, Zhang L, Weiser M, Rudy B, McBain CJ (1996). Developmental expression and functional characterization of the potassium-channel subunit Kv3.1b in parvalbumin-containing interneurons of the rat hippocampus. *J Neurosci,* 16 (2): 506-518.

Dzhala VI, Staley KJ (2003). Transition from interictal to ictal activity in limbic networks in vitro. *J Neurosci,* 23 (21): 7873-7880.

Ecker C, Suckling JM, Paulsen O (2001). Temperature dependence of cholinergically induced network oscillations in the CA1 region of the hippocampus. *Society for Neuroscience Abstracts,* 27: Program No. 27.1.

Eggermann E, Jonas P (2012). How the 'slow' Ca^{2+} buffer parvalbumin affects transmitter release in nanodomain-coupling regimes. *Nat Neurosci,* 15 (1): 20-22.

Eilam R, Pinkas-Kramarski R, Ratzkin BJ, Segal M, Yarden Y (1998). Activity-dependent regulation of Neu differentiation factor/neuregulin expression in rat brain. *Proc Natl Acad Sci U S A,* 95 (4): 1888-1893.

Engel AK, Fries P, Singer W (2001). Dynamic predictions: oscillations and synchrony in top-down processing. *Nat Rev Neurosci,* 2 (10): 704-716.

Falls DL (2003). Neuregulins: functions, forms, and signaling strategies. *Exp Cell Res,* 284 (1): 14-30.

Fazzari P, Paternain AV, Valiente M, Pla R, Lujan R, Lloyd K, Lerma J, Marin O, Rico B (2010). Control of cortical GABA circuitry development by Nrg1 and ErbB4 signalling. *Nature,* 464 (7293): 1376-1380.

Field A (2009). *Discovering Statistics Using SPSS.* 3rd Edition. SAGE Publications Ltd, London.

Fisahn A, Pike FG, Buhl EH, Paulsen O (1998). Cholinergic induction of network oscillations at 40 Hz in the hippocampus in vitro. *Nature,* 394 (6689): 186-189.

Fisahn A, Yamada M, Duttaroy A, Gan JW, Deng CX, McBain CJ, Wess J (2002). Muscarinic induction of hippocampal gamma oscillations requires coupling of the M1 receptor to two mixed cation currents. *Neuron,* 33 (4): 615-624.

Fisahn A, Contractor A, Traub RD, Buhl EH, Heinemann SF, McBain CJ (2004). Distinct roles for the kainate receptor subunits GluR5 and GluR6 in kainate-induced hippocampal gamma oscillations. *J Neurosci,* 24 (43): 9658-9668.

Fisahn A, Neddens J, Yan L, Buonanno A (2009). Neuregulin-1 modulates hippocampal gamma oscillations: implications for schizophrenia. *Cereb Cortex,* 19 (3): 612-618.

Flames N, Long JE, Garratt AN, Fischer TM, Gassmann M, Birchmeier C, Lai C, Rubenstein JL, Marin O (2004). Short- and long-range attraction of cortical GABAergic interneurons by neuregulin-1. *Neuron,* 44 (2): 251-261.

Flames N, Marin O (2005). Developmental mechanisms underlying the generation of cortical interneuron diversity. *Neuron,* 46 (3): 377-381.

Foffani G, Uzcategui YG, Gal B, Menendez de la Prida L (2007). Reduced spike-timing reliability correlates with the emergence of fast ripples in the rat epileptic hippocampus. *Neuron,* 55 (6): 930-941.

Foldy C, Lee SH, Morgan RJ, Soltesz I (2010). Regulation of fast-spiking basket cell synapses by the chloride channel ClC-2. *Nat Neurosci,* 13 (9): 1047-1049.

Fox IJ, Kornblum HI (2005). Developmental profile of ErbB receptors in murine central nervous system: implications for functional interactions. *J Neurosci Res,* 79 (5): 584-597.

Frerking M, Malenka RC, Nicoll RA (1998). Synaptic activation of kainate receptors on hippocampal interneurons. *Nat Neurosci,* 1 (6): 479-486.

Freund TF, Antal M (1988). GABA-containing neurons in the septum control inhibitory interneurons in the hippocampus. *Nature,* 336 (6195): 170-173.

Freund TF (1989). GABAergic septohippocampal neurons contain parvalbumin. *Brain Res,* 478 (2): 375-381.

Freund TF, Buzsaki G (1996). Interneurons of the hippocampus. *Hippocampus,* 6 (4): 347-470.

Freund TF, Katona I (2007). Perisomatic inhibition. *Neuron,* 56 (1): 33-42.

Fricker D, Miles R (2000). EPSP amplification and the precision of spike timing in hippocampal neurons. *Neuron,* 28 (2): 559-569.

Fries P (2005). A mechanism for cognitive dynamics: neuronal communication through neuronal coherence. *Trends Cogn Sci,* 9 (10): 474-480.

Fuchs EC, Zivkovic AR, Cunningham MO, Middleton S, Lebeau FE, Bannerman DM, Rozov A, Whittington MA, Traub RD, Rawlins JN, Monyer H (2007). Recruitment of parvalbumin-positive interneurons determines hippocampal function and associated behavior. *Neuron,* 53 (4): 591-604.

Fuentealba P, Begum R, Capogna M, Jinno S, Marton LF, Csicsvari J, Thomson A, Somogyi P, Klausberger T (2008). Ivy cells: a population of nitric-oxide-producing, slow-spiking GABAergic neurons and their involvement in hippocampal network activity. *Neuron,* 57 (6): 917-929.

Fukuda T, Kosaka T (2000). Gap junctions linking the dendritic network of GABAergic interneurons in the hippocampus. *J Neurosci,* 20 (4): 1519-1528.

Garcia RA, Vasudevan K, Buonanno A (2000). The neuregulin receptor ErbB-4 interacts with PDZ-containing proteins at neuronal synapses. *Proc Natl Acad Sci U S A,* 97 (7): 3596-3601.

Geiger JR, Melcher T, Koh DS, Sakmann B, Seeburg PH, Jonas P, Monyer H (1995). Relative abundance of subunit mRNAs determines gating and Ca2+ permeability of AMPA receptors in principal neurons and interneurons in rat CNS. *Neuron,* 15 (1): 193-204.

Geiger JR, Lubke J, Roth A, Frotscher M, Jonas P (1997). Submillisecond AMPA receptor-mediated signaling at a principal neuron-interneuron synapse. *Neuron,* 18 (6): 1009-1023.

Gerecke KM, Wyss JM, Karavanova I, Buonanno A, Carroll SL (2001). ErbB transmembrane tyrosine kinase receptors are differentially expressed throughout the adult rat central nervous system. *J Comp Neurol,* 433 (1): 86-100.

Gerecke KM, Wyss JM, Carroll SL (2004). Neuregulin-1beta induces neurite extension and arborization in cultured hippocampal neurons. *Mol Cell Neurosci,* 27 (4): 379-393.

Gittis AH, Nelson AB, Thwin MT, Palop JJ, Kreitzer AC (2010). Distinct roles of GABAergic interneurons in the regulation of striatal output pathways. *J Neurosci,* 30 (6): 2223-2234.

Glass GV, Peckham PD, Sanders JR (1972). Consequences of failure to meet assumptions underlying the fixed effects analyses of variance and covariance. *Review of Educational Research,* 42 (3): 237-288.

Glickfeld LL, Scanziani M (2006). Distinct timing in the activity of cannabinoid-sensitive and cannabinoid-insensitive basket cells. *Nat Neurosci,* 9 (6): 807-815.

Glickfeld LL, Atallah BV, Scanziani M (2008). Complementary modulation of somatic inhibition by opioids and cannabinoids. *J Neurosci,* 28 (8): 1824-1832.

Glickfeld LL, Roberts JD, Somogyi P, Scanziani M (2009). Interneurons hyperpolarize pyramidal cells along their entire somatodendritic axis. *Nat Neurosci,* 12 (1): 21-23.

Gloveli T, Dugladze T, Saha S, Monyer H, Heinemann U, Traub RD, Whittington MA, Buhl EH (2005). Differential involvement of oriens/pyramidale interneurones in hippocampal network oscillations in vitro. *J Physiol,* 562 (Pt 1): 131-147.

Goldin M, Epsztein J, Jorquera I, Represa A, Ben-Ari Y, Crepel V, Cossart R (2007). Synaptic kainate receptors tune oriens-lacunosum moleculare interneurons to operate at theta frequency. *J Neurosci,* 27 (36): 9560-9572.

Goldman-Rakic PS (1995). Cellular basis of working memory. *Neuron,* 14 (3): 477-485.

Goldstein PA, Elsen FP, Ying SW, Ferguson C, Homanics GE, Harrison NL (2002). Prolongation of hippocampal miniature inhibitory postsynaptic currents in mice lacking the GABA(A) receptor alpha1 subunit. *J Neurophysiol,* 88 (6): 3208-3217.

Gonzalez-Burgos G, Hashimoto T, Lewis DA (2010). Alterations of cortical GABA neurons and network oscillations in schizophrenia. *Curr Psychiatry Rep,* 12 (4): 335-344.

Gonzalez-Burgos G, Lewis DA (2012). NMDA receptor hypofunction, parvalbumin-positive neurons, and cortical gamma oscillations in schizophrenia. *Schizophr Bull,* 38 (5): 950-957.

Gozlan H, Ben-Ari Y (2003). Interneurons are the source and the targets of the first synapses formed in the rat developing hippocampal circuit. *Cereb Cortex,* 13 (6): 684-692.

Green MF (1996). What are the functional consequences of neurocognitive deficits in schizophrenia? *Am J Psychiatry,* 153 (3): 321-330.

Gu Z, Jiang Q, Fu AK, Ip NY, Yan Z (2005). Regulation of NMDA receptors by neuregulin signaling in prefrontal cortex. *J Neurosci,* 25 (20): 4974-4984.

Guillin O, Abi-Dargham A, Laruelle M (2007). Neurobiology of dopamine in schizophrenia. *Int Rev Neurobiol,* 78: 1-39.

Gulyas AI, Miles R, Hajos N, Freund TF (1993a). Precision and variability in postsynaptic target selection of inhibitory cells in the hippocampal CA3 region. *Eur J Neurosci,* 5 (12): 1729-1751.

Gulyas AI, Miles R, Sik A, Toth K, Tamamaki N, Freund TF (1993b). Hippocampal pyramidal cells excite inhibitory neurons through a single release site. *Nature,* 366 (6456): 683-687.

Gulyas AI, Hajos N, Freund TF (1996). Interneurons containing calretinin are specialized to control other interneurons in the rat hippocampus. *J Neurosci,* 16 (10): 3397-3411.

Gulyas AI, Megias M, Emri Z, Freund TF (1999). Total number and ratio of excitatory and inhibitory synapses converging onto single interneurons of different types in the CA1 area of the rat hippocampus. *J Neurosci,* 19 (22): 10082-10097.

Gulyas AI, Hajos N, Katona I, Freund TF (2003). Interneurons are the local targets of hippocampal inhibitory cells which project to the medial septum. *Eur J Neurosci,* 17 (9): 1861-1872.

Gulyas AI, Buzsaki G, Freund TF, Hirase H (2006). Populations of hippocampal inhibitory neurons express different levels of cytochrome c. *Eur J Neurosci,* 23 (10): 2581-2594.

Gulyas AI, Szabo GG, Ulbert I, Holderith N, Monyer H, Erdelyi F, Szabo G, Freund TF, Hajos N (2010). Parvalbumin-containing fast-spiking basket cells generate the field potential oscillations induced by cholinergic receptor activation in the hippocampus. *J Neurosci,* 30 (45): 15134-15145.

Hahn CG, Wang HY, Cho DS, Talbot K, Gur RE, Berrettini WH, Bakshi K, Kamins J, Borgmann-Winter KE, Siegel SJ, Gallop RJ, Arnold SE (2006). Altered neuregulin 1-erbB4 signaling contributes to NMDA receptor hypofunction in schizophrenia. *Nat Med,* 12 (7): 824-828.

Hajos N, Papp EC, Acsady L, Levey AI, Freund TF (1998). Distinct interneuron types express m2 muscarinic receptor immunoreactivity on their dendrites or axon terminals in the hippocampus. *Neuroscience,* 82 (2): 355-376.

Hajos N, Katona I, Naiem SS, MacKie K, Ledent C, Mody I, Freund TF (2000). Cannabinoids inhibit hippocampal GABAergic transmission and network oscillations. *Eur J Neurosci,* 12 (9): 3239-3249.

Hajos N, Palhalmi J, Mann EO, Nemeth B, Paulsen O, Freund TF (2004). Spike timing of distinct types of GABAergic interneuron during hippocampal gamma oscillations in vitro. *J Neurosci,* 24 (41): 9127-9137.

Hajos N, Ellender TJ, Zemankovics R, Mann EO, Exley R, Cragg SJ, Freund TF, Paulsen O (2009). Maintaining network activity in submerged hippocampal slices: importance of oxygen supply. *Eur J Neurosci,* 29 (2): 319-327.

Hajos N, Mody I (2009). Establishing a physiological environment for visualized in vitro brain slice recordings by increasing oxygen supply and modifying aCSF content. *J Neurosci Methods,* 183 (2): 107-113.

Hajos N, Paulsen O (2009). Network mechanisms of gamma oscillations in the CA3 region of the hippocampus. *Neural Netw,* 22 (8): 1113-1119.

Harrison PJ (2004). The hippocampus in schizophrenia: a review of the neuropathological evidence and its pathophysiological implications. *Psychopharmacology (Berl),* 174 (1): 151-162.

Harrison PJ, Weinberger DR (2005). Schizophrenia genes, gene expression, and neuropathology: on the matter of their convergence. *Mol Psychiatry,* 10 (1): 40-68; image 45.

Harrison PJ, Law AJ (2006). Neuregulin 1 and schizophrenia: genetics, gene expression, and neurobiology. *Biol Psychiatry,* 60 (2): 132-140.

Hartwich K, Pollak T, Klausberger T (2009). Distinct firing patterns of identified basket and dendrite-targeting interneurons in the prefrontal cortex during hippocampal theta and local spindle oscillations. *J Neurosci,* 29 (30): 9563-9574.

Hashimoto R, Straub RE, Weickert CS, Hyde TM, Kleinman JE, Weinberger DR (2004). Expression analysis of neuregulin-1 in the dorsolateral prefrontal cortex in schizophrenia. *Mol Psychiatry,* 9 (3): 299-307.

Hashimoto T, Volk DW, Eggan SM, Mirnics K, Pierri JN, Sun Z, Sampson AR, Lewis DA (2003). Gene expression deficits in a subclass of GABA neurons in the prefrontal cortex of subjects with schizophrenia. *J Neurosci,* 23 (15): 6315-6326.

Hefft S, Jonas P (2005). Asynchronous GABA release generates long-lasting inhibition at a hippocampal interneuron-principal neuron synapse. *Nat Neurosci,* 8 (10): 1319-1328.

Heinrichs RW (2005). The primacy of cognition in schizophrenia. *Am Psychol,* 60 (3): 229-242.

Heistek TS, Jaap Timmerman A, Spijker S, Brussaard AB, Mansvelder HD (2010). GABAergic synapse properties may explain genetic variation in hippocampal network oscillations in mice. *Front Cell Neurosci,* 4: 18.

Hille B (1992). *Ionic Channels of Excitable Membranes.* 2nd Edition, Sinauer, Sunderland, MA.

Hippenmeyer S, Vrieseling E, Sigrist M, Portmann T, Laengle C, Ladle DR, Arber S (2005). A developmental switch in the response of DRG neurons to ETS transcription factor signaling. *PLoS Biol,* 3 (5): e159.

Howard A, Tamas G, Soltesz I (2005). Lighting the chandelier: new vistas for axo-axonic cells. *Trends Neurosci,* 28 (6): 310-316.

Hu H, Martina M, Jonas P (2010). Dendritic mechanisms underlying rapid synaptic activation of fast-spiking hippocampal interneurons. *Science,* 327 (5961): 52-58.

Huang YZ, Won S, Ali DW, Wang Q, Tanowitz M, Du QS, Pelkey KA, Yang DJ, Xiong WC, Salter MW, Mei L (2000). Regulation of neuregulin signaling by PSD-95 interacting with ErbB4 at CNS synapses. *Neuron,* 26 (2): 443-455.

Ishizuka N, Cowan WM, Amaral DG (1995). A quantitative analysis of the dendritic organization of pyramidal cells in the rat hippocampus. *J Comp Neurol,* 362 (1): 17-45.

Jackson AC, Nicoll RA (2011). The expanding social network of ionotropic glutamate receptors: TARPs and other transmembrane auxiliary subunits. *Neuron,* 70 (2): 178-199.

Jensen O, Lisman JE (1996). Novel lists of 7 +/- 2 known items can be reliably stored in an oscillatory short-term memory network: interaction with long-term memory. *Learn Mem,* 3 (2-3): 257-263.

Jensen O (2006). Maintenance of multiple working memory items by temporal segmentation. *Neuroscience,* 139 (1): 237-249.

Jones JT, Akita RW, Sliwkowski MX (1999). Binding specificities and affinities of egf domains for ErbB receptors. *FEBS Lett,* 447 (2-3): 227-231.

Jones RS, Buhl EH (1993). Basket-like interneurones in layer II of the entorhinal cortex exhibit a powerful NMDA-mediated synaptic excitation. *Neurosci Lett,* 149 (1): 35-39.

Kaila K, Voipio J (1987). Postsynaptic fall in intracellular pH induced by GABA-activated bicarbonate conductance. *Nature,* 330 (6144): 163-165.

Kaila K, Voipio J, Paalasmaa P, Pasternack M, Deisz RA (1993). The role of bicarbonate in GABAA receptor-mediated IPSPs of rat neocortical neurones. *J Physiol,* 464: 273-289.

Kann O, Huchzermeyer C, Kovacs R, Wirtz S, Schuelke M (2011). Gamma oscillations in the hippocampus require high complex I gene expression and strong functional performance of mitochondria. *Brain,* 134 (Pt 2): 345-358.

Kao WT, Wang Y, Kleinman JE, Lipska BK, Hyde TM, Weinberger DR, Law AJ (2010). Common genetic variation in Neuregulin 3 (NRG3) influences risk for schizophrenia and impacts NRG3 expression in human brain. *Proc Natl Acad Sci U S A,* 107 (35): 15619-15624.

Kato T, Kasai A, Mizuno M, Fengyi L, Shintani N, Maeda S, Yokoyama M, Ozaki M, Nawa H (2010). Phenotypic characterization of transgenic mice overexpressing neuregulin-1. *PLoS One,* 5 (12): e14185.

Kehrer C, Dugladze T, Maziashvili N, Wojtowicz A, Schmitz D, Heinemann U, Gloveli T (2007). Increased inhibitory input to CA1 pyramidal cells alters hippocampal gamma frequency oscillations in the MK-801 model of acute psychosis. *Neurobiol Dis,* 25 (3): 545-552.

Keilhoff G, Becker A, Grecksch G, Wolf G, Bernstein HG (2004). Repeated application of ketamine to rats induces changes in the hippocampal expression of parvalbumin, neuronal nitric oxide synthase and cFOS similar to those found in human schizophrenia. *Neuroscience,* 126 (3): 591-598.

Kerber G, Streif R, Schwaiger FW, Kreutzberg GW, Hager G (2003). Neuregulin-1 isoforms are differentially expressed in the intact and regenerating adult rat nervous system. *J Mol Neurosci,* 21 (2): 149-165.

Keri S, Kiss I, Kelemen O (2009). Effects of a neuregulin 1 variant on conversion to schizophrenia and schizophreniform disorder in people at high risk for psychosis. *Mol Psychiatry,* 14 (2): 118-119.

Kinney JW, Davis CN, Tabarean I, Conti B, Bartfai T, Behrens MM (2006). A specific role for NR2A-containing NMDA receptors in the maintenance of parvalbumin and GAD67 immunoreactivity in cultured interneurons. *J Neurosci,* 26 (5): 1604-1615.

Kiernan JA (1981). *Histological & Histochemical Methods: Theory & Practice.* 1st Edition. Pergamon Press Ltd., Oxford.

Klausberger T, Roberts JD, Somogyi P (2002). Cell type- and input-specific differences in the number and subtypes of synaptic GABA(A) receptors in the hippocampus. *J Neurosci,* 22 (7): 2513-2521.

Klausberger T, Magill PJ, Marton LF, Roberts JD, Cobden PM, Buzsaki G, Somogyi P (2003). Brain-state- and cell-type-specific firing of hippocampal interneurons in vivo. *Nature,* 421 (6925): 844-848.

Klausberger T, Marton LF, Baude A, Roberts JD, Magill PJ, Somogyi P (2004). Spike timing of dendrite-targeting bistratified cells during hippocampal network oscillations in vivo. *Nat Neurosci,* 7 (1): 41-47.

Klausberger T, Marton LF, O'Neill J, Huck JH, Dalezios Y, Fuentealba P, Suen WY, Papp E, Kaneko T, Watanabe M, Csicsvari J, Somogyi P (2005). Complementary roles of cholecystokinin- and parvalbumin-expressing GABAergic neurons in hippocampal network oscillations. *J Neurosci,* 25 (42): 9782-9793.

Klausberger T, Somogyi P (2008). Neuronal diversity and temporal dynamics: the unity of hippocampal circuit operations. *Science,* 321 (5885): 53-57.

Kleinman JE, Law AJ, Lipska BK, Hyde TM, Ellis JK, Harrison PJ, Weinberger DR (2011). Genetic neuropathology of schizophrenia: new approaches to an old question and new uses for postmortem human brains. *Biol Psychiatry,* 69 (2): 140-145.

Kneisler TB, Dingledine R (1995a). Synaptic input from CA3 pyramidal cells to dentate basket cells in rat hippocampus. *J Physiol,* 487 (Pt 1): 125-146.

Kneisler TB, Dingledine R (1995b). Spontaneous and synaptic input from granule cells and the perforant path to dentate basket cells in the rat hippocampus. *Hippocampus,* 5 (3): 151-164.

Koh DS, Geiger JR, Jonas P, Sakmann B (1995). Ca(2+)-permeable AMPA and NMDA receptor channels in basket cells of rat hippocampal dentate gyrus. *J Physiol,* 485 (Pt 2): 383-402.

Kohl MM, Paulsen O (2010). The roles of GABAB receptors in cortical network activity. *Adv Pharmacol,* 58: 205-229.

Kohl MM, Shipton OA, Deacon RM, Rawlins JN, Deisseroth K, Paulsen O (2011). Corrigendum: Hemisphere-specific optogenetic stimulation reveals left-right asymmetry of hippocampal plasticity. *Nat Neurosci,* 14 (12): 1617.

Korotkova T, Fuchs EC, Ponomarenko A, von Engelhardt J, Monyer H (2010). NMDA receptor ablation on parvalbumin-positive interneurons impairs hippocampal synchrony, spatial representations, and working memory. *Neuron,* 68 (3): 557-569.

Kramer R, Bucay N, Kane DJ, Martin LE, Tarpley JE, Theill LE (1996). Neuregulins with an Ig-like domain are essential for mouse myocardial and neuronal development. *Proc Natl Acad Sci U S A,* 93 (10): 4833-4838.

Kraushaar U, Jonas P (2000). Efficacy and stability of quantal GABA release at a hippocampal interneuron-principal neuron synapse. *J Neurosci,* 20 (15): 5594-5607.

Krenz I, Kalkan D, Wevers A, de Vos RA, Steur EN, Lindstrom J, Pilz K, Nowacki S, Schutz U, Moser N, Witter B, Schroder H (2001). Parvalbumin-containing interneurons of the human cerebral cortex express nicotinic acetylcholine receptor proteins. *J Chem Neuroanat,* 21 (3): 239-246.

Krivosheya D, Tapia L, Levinson JN, Huang K, Kang Y, Hines R, Ting AK, Craig AM, Mei L, Bamji SX, El-Husseini A (2008). ErbB4-neuregulin signaling modulates synapse development and dendritic arborization through distinct mechanisms. *J Biol Chem,* 283 (47): 32944-32956.

Kwon OB, Longart M, Vullhorst D, Hoffman DA, Buonanno A (2005). Neuregulin-1 reverses long-term potentiation at CA1 hippocampal synapses. *J Neurosci,* 25 (41): 9378-9383.

Kwon OB, Paredes D, Gonzalez CM, Neddens J, Hernandez L, Vullhorst D, Buonanno A (2008). Neuregulin-1 regulates LTP at CA1 hippocampal synapses through activation of dopamine D4 receptors. *Proc Natl Acad Sci U S A,* 105 (40): 15587-15592.

Lasztoczi B, Tukker JJ, Somogyi P, Klausberger T (2011). Terminal field and firing selectivity of cholecystokinin-expressing interneurons in the hippocampal CA3 area. *J Neurosci,* 31 (49): 18073-18093.

Lau CG, Zukin RS (2007). NMDA receptor trafficking in synaptic plasticity and neuropsychiatric disorders. *Nat Rev Neurosci,* 8 (6): 413-426.

Lau D, Vega-Saenz de Miera EC, Contreras D, Ozaita A, Harvey M, Chow A, Noebels JL, Paylor R, Morgan JI, Leonard CS, Rudy B (2000). Impaired fast-spiking, suppressed cortical inhibition, and increased susceptibility to seizures in mice lacking Kv3.2 K+ channel proteins. *J Neurosci,* 20 (24): 9071-9085.

Lavoie AM, Tingey JJ, Harrison NL, Pritchett DB, Twyman RE (1997). Activation and deactivation rates of recombinant GABA(A) receptor channels are dependent on alpha-subunit isoform. *Biophys J,* 73 (5): 2518-2526.

Law AJ, Shannon Weickert C, Hyde TM, Kleinman JE, Harrison PJ (2004). Neuregulin-1 (NRG-1) mRNA and protein in the adult human brain. *Neuroscience,* 127 (1): 125-136.

Law AJ, Lipska BK, Weickert CS, Hyde TM, Straub RE, Hashimoto R, Harrison PJ, Kleinman JE, Weinberger DR (2006). Neuregulin 1 transcripts are differentially expressed in schizophrenia and regulated by 5' SNPs associated with the disease. *Proc Natl Acad Sci U S A,* 103 (17): 6747-6752.

Leao RN, Tan HM, Fisahn A (2009). Kv7/KCNQ channels control action potential phasing of pyramidal neurons during hippocampal gamma oscillations in vitro. *J Neurosci,* 29 (42): 13353-13364.

LeBeau FE, Towers SK, Traub RD, Whittington MA, Buhl EH (2002). Fast network oscillations induced by potassium transients in the rat hippocampus in vitro. *J Physiol,* 542 (Pt 1): 167-179.

Lei S, McBain CJ (2002). Distinct NMDA receptors provide differential modes of transmission at mossy fiber-interneuron synapses. *Neuron,* 33 (6): 921-933.

Lewis DA, Volk DW, Hashimoto T (2004). Selective alterations in prefrontal cortical GABA neurotransmission in schizophrenia: a novel target for the treatment of working memory dysfunction. *Psychopharmacology (Berl),* 174 (1): 143-150.

Lewis DA, Hashimoto T, Volk DW (2005). Cortical inhibitory neurons and schizophrenia. *Nat Rev Neurosci,* 6 (4): 312-324.

Lewis DA, Gonzalez-Burgos G (2006). Pathophysiologically based treatment interventions in schizophrenia. *Nat Med,* 12 (9): 1016-1022.

Lewis DA, Fish KN, Arion D, Gonzalez-Burgos G (2011). Perisomatic inhibition and cortical circuit dysfunction in schizophrenia. *Curr Opin Neurobiol,* 21 (6): 866-872.

Lewis DA, Curley AA, Glausier JR, Volk DW (2012). Cortical parvalbumin interneurons and cognitive dysfunction in schizophrenia. *Trends Neurosci,* 35 (1): 57-67.

Lewis TL, Jr., Mao T, Svoboda K, Arnold DB (2009). Myosin-dependent targeting of transmembrane proteins to neuronal dendrites. *Nat Neurosci,* 12 (5): 568-576.

Li B, Woo RS, Mei L, Malinow R (2007). The neuregulin-1 receptor erbB4 controls glutamatergic synapse maturation and plasticity. *Neuron,* 54 (4): 583-597.

Li D, Collier DA, He L (2006). Meta-analysis shows strong positive association of the neuregulin 1 (NRG1) gene with schizophrenia. *Hum Mol Genet,* 15 (12): 1995-2002.

Li KX, Lu YM, Xu ZH, Zhang J, Zhu JM, Zhang JM, Cao SX, Chen XJ, Chen Z, Luo JH, Duan S, Li XM (2012). Neuregulin 1 regulates excitability of fast-spiking neurons through Kv1.1 and acts in epilepsy. *Nat Neurosci,* 15 (2): 267-273.

Li XG, Somogyi P, Tepper JM, Buzsaki G (1992). Axonal and dendritic arborization of an intracellularly labeled chandelier cell in the CA1 region of rat hippocampus. *Exp Brain Res,* 90 (3): 519-525.

Liodis P, Denaxa M, Grigoriou M, Akufo-Addo C, Yanagawa Y, Pachnis V (2007). Lhx6 activity is required for the normal migration and specification of cortical interneuron subtypes. *J Neurosci,* 27 (12): 3078-3089.

Lisman JE (1999). Relating hippocampal circuitry to function: recall of memory sequences by reciprocal dentate-CA3 interactions. *Neuron,* 22 (2): 233-242.

Lisman J (2005). The theta/gamma discrete phase code occuring during the hippocampal phase precession may be a more general brain coding scheme. *Hippocampus,* 15 (7): 913-922.

Lisman J, Buzsaki G (2008). A neural coding scheme formed by the combined function of gamma and theta oscillations. *Schizophr Bull,* 34 (5): 974-980.

Lisman JE, Coyle JT, Green RW, Javitt DC, Benes FM, Heckers S, Grace AA (2008). Circuit-based framework for understanding neurotransmitter and risk gene interactions in schizophrenia. *Trends Neurosci,* 31 (5): 234-242.

Liu Y, Ford B, Mann MA, Fischbach GD (2001). Neuregulins increase alpha7 nicotinic acetylcholine receptors and enhance excitatory synaptic transmission in GABAergic interneurons of the hippocampus. *J Neurosci,* 21 (15): 5660-5669.

Liu Y, Ford BD, Mann MA, Fischbach GD (2005). Neuregulin-1 increases the proliferation of neuronal progenitors from embryonic neural stem cells. *Dev Biol,* 283 (2): 437-445.

Lopez-Bendito G, Sturgess K, Erdelyi F, Szabo G, Molnar Z, Paulsen O (2004). Preferential origin and layer destination of GAD65-GFP cortical interneurons. *Cereb Cortex,* 14 (10): 1122-1133.

Lopez-Bendito G, Cautinat A, Sanchez JA, Bielle F, Flames N, Garratt AN, Talmage DA, Role LW, Charnay P, Marin O, Garel S (2006). Tangential neuronal migration controls axon guidance: a role for neuregulin-1 in thalamocortical axon navigation. *Cell,* 125 (1): 127-142.

Lovett-Barron M, Turi GF, Kaifosh P, Lee PH, Bolze F, Sun XH, Nicoud JF, Zemelman BV, Sternson SM, Losonczy A (2012). Regulation of neuronal input transformations by tunable dendritic inhibition. *Nat Neurosci,* 15 (3): 423-430.

Lozovaya NA, Grebenyuk SE, Tsintsadze T, Feng B, Monaghan DT, Krishtal OA (2004). Extrasynaptic NR2B and NR2D subunits of NMDA receptors shape 'superslow' afterburst EPSC in rat hippocampus. *J Physiol,* 558 (Pt 2): 451-463.

Maccaferri G, Roberts JD, Szucs P, Cottingham CA, Somogyi P (2000). Cell surface domain specific postsynaptic currents evoked by identified GABAergic neurones in rat hippocampus in vitro. *J Physiol,* 524 Pt 1: 91-116.

Maccaferri G, Dingledine R (2002). Control of feedforward dendritic inhibition by NMDA receptor-dependent spike timing in hippocampal interneurons. *J Neurosci,* 22 (13): 5462-5472.

MacIver MB (2009). Abused inhalants enhance GABA-mediated synaptic inhibition. *Neuropsychopharmacology,* 34 (10): 2296-2304.

Madisen L, Zwingman TA, Sunkin SM, Oh SW, Zariwala HA, Gu H, Ng LL, Palmiter RD, Hawrylycz MJ, Jones AR, Lein ES, Zeng H (2010). A robust and high-throughput Cre reporting and characterization system for the whole mouse brain. *Nat Neurosci,* 13 (1): 133-140.

Mann EO, Suckling JM, Hajos N, Greenfield SA, Paulsen O (2005). Perisomatic feedback inhibition underlies cholinergically induced fast network oscillations in the rat hippocampus in vitro. *Neuron,* 45 (1): 105-117.

Mann EO, Paulsen O (2007). Role of GABAergic inhibition in hippocampal network oscillations. *Trends Neurosci,* 30 (7): 343-349.

Mann EO, Mody I (2010). Control of hippocampal gamma oscillation frequency by tonic inhibition and excitation of interneurons. *Nat Neurosci,* 13 (2): 205-212.

Markram H, Lubke J, Frotscher M, Sakmann B (1997). Regulation of synaptic efficacy by coincidence of postsynaptic APs and EPSPs. *Science,* 275 (5297): 213-215.

Martinou JC, Falls DL, Fischbach GD, Merlie JP (1991). Acetylcholine receptor-inducing activity stimulates expression of the epsilon-subunit gene of the muscle acetylcholine receptor. *Proc Natl Acad Sci U S A,* 88 (17): 7669-7673.

McBain C, Dingledine R (1992). Dual-component miniature excitatory synaptic currents in rat hippocampal CA3 pyramidal neurons. *J Neurophysiol,* 68 (1): 16-27.

McBain CJ, Dingledine R (1993). Heterogeneity of synaptic glutamate receptors on CA3 stratum radiatum interneurones of rat hippocampus. *J Physiol,* 462: 373-392.

McNaughton BL, Morris RGM (1987). Hippocampal synaptic enhancement and information storage within a distributed memory system. *Trends Neurosci,* 10 (10): 408-415.

McQuiston AR, Colmers WF (1996). Neuropeptide Y2 receptors inhibit the frequency of spontaneous but not miniature EPSCs in CA3 pyramidal cells of rat hippocampus. *J Neurophysiol,* 76 (5): 3159-3168.

Mei L, Xiong WC (2008). Neuregulin 1 in neural development, synaptic plasticity and schizophrenia. *Nat Rev Neurosci,* 9 (6): 437-452.

Meyer AH, Katona I, Blatow M, Rozov A, Monyer H (2002). In vivo labeling of parvalbumin-positive interneurons and analysis of electrical coupling in identified neurons. *J Neurosci,* 22 (16): 7055-7064.

Meyer D, Birchmeier C (1995). Multiple essential functions of neuregulin in development. *Nature,* 378 (6555): 386-390.

Meyer D, Yamaai T, Garratt A, Riethmacher-Sonnenberg E, Kane D, Theill LE, Birchmeier C (1997). Isoform-specific expression and function of neuregulin. *Development,* 124 (18): 3575-3586.

Michailov GV, Sereda MW, Brinkmann BG, Fischer TM, Haug B, Birchmeier C, Role L, Lai C, Schwab MH, Nave KA (2004). Axonal neuregulin-1 regulates myelin sheath thickness. *Science,* 304 (5671): 700-703.

Middleton S, Jalics J, Kispersky T, Lebeau FE, Roopun AK, Kopell NJ, Whittington MA, Cunningham MO (2008). NMDA receptor-dependent switching between different gamma rhythm-generating microcircuits in entorhinal cortex. *Proc Natl Acad Sci U S A,* 105 (47): 18572-18577.

Miles R (1990). Synaptic excitation of inhibitory cells by single CA3 hippocampal pyramidal cells of the guinea-pig in vitro. *J Physiol,* 428: 61-77.

Miles R, Toth K, Gulyas AI, Hajos N, Freund TF (1996). Differences between somatic and dendritic inhibition in the hippocampus. *Neuron,* 16 (4): 815-823.

Misra C, Brickley SG, Farrant M, Cull-Candy SG (2000). Identification of subunits contributing to synaptic and extrasynaptic NMDA receptors in Golgi cells of the rat cerebellum. *J Physiol,* 524 (Pt 1): 147-162.

Miyoshi G, Butt SJ, Takebayashi H, Fishell G (2007). Physiologically distinct temporal cohorts of cortical interneurons arise from telencephalic Olig2-expressing precursors. *J Neurosci,* 27 (29): 7786-7798.

Mizuseki K, Diba K, Pastalkova E, Buzsaki G (2011). Hippocampal CA1 pyramidal cells form functionally distinct sublayers. *Nat Neurosci,* 14 (9): 1174-1181.

Mohn AR, Gainetdinov RR, Caron MG, Koller BH (1999). Mice with reduced NMDA receptor expression display behaviors related to schizophrenia. *Cell,* 98 (4): 427-436.

Monyer H, Burnashev N, Laurie DJ, Sakmann B, Seeburg PH (1994). Developmental and regional expression in the rat brain and functional properties of four NMDA receptors. *Neuron,* 12 (3): 529-540.

Moran LV, Hong LE (2011). High vs low frequency neural oscillations in schizophrenia. *Schizophr Bull,* 37 (4): 659-663.

Morozov YM, Torii M, Rakic P (2009). Origin, early commitment, migratory routes, and destination of cannabinoid type 1 receptor-containing interneurons. *Cereb Cortex,* 19 Suppl 1: i78-89.

Morris RG, Anderson E, Lynch GS, Baudry M (1986). Selective impairment of learning and blockade of long-term potentiation by an N-methyl-D-aspartate receptor antagonist, AP5. *Nature,* 319 (6056): 774-776.

Murray AJ, Sauer JF, Riedel G, McClure C, Ansel L, Cheyne L, Bartos M, Wisden W, Wulff P (2011). Parvalbumin-positive CA1 interneurons are required for spatial working but not for reference memory. *Nat Neurosci,* 14 (3): 297-299.

Nakashiba T, Young JZ, McHugh TJ, Buhl DL, Tonegawa S (2008). Transgenic inhibition of synaptic transmission reveals role of CA3 output in hippocampal learning. *Science,* 319 (5867): 1260-1264.

Nakazawa K, Quirk MC, Chitwood RA, Watanabe M, Yeckel MF, Sun LD, Kato A, Carr CA, Johnston D, Wilson MA, Tonegawa S (2002). Requirement for hippocampal CA3 NMDA receptors in associative memory recall. *Science,* 297 (5579): 211-218.

Nakazawa K, Sun LD, Quirk MC, Rondi-Reig L, Wilson MA, Tonegawa S (2003). Hippocampal CA3 NMDA receptors are crucial for memory acquisition of one-time experience. *Neuron,* 38 (2): 305-315.

Neddens J, Vullhorst D, Paredes D, Buonanno A (2009). Neuregulin links dopaminergic and glutamatergic neurotransmission to control hippocampal synaptic plasticity. *Commun Integr Biol,* 2 (3): 261-264.

Neddens J, Buonanno A (2010). Selective populations of hippocampal interneurons express ErbB4 and their number and distribution is altered in ErbB4 knockout mice. *Hippocampus,* 20 (6): 724-744.

Neddens J, Fish KN, Tricoire L, Vullhorst D, Shamir A, Chung W, Lewis DA, McBain CJ, Buonanno A (2011). Conserved interneuron-specific ErbB4 expression in frontal cortex of rodents, monkeys, and humans: implications for schizophrenia. *Biol Psychiatry,* 70 (7): 636-645.

Newbern J, Birchmeier C (2010). Nrg1/ErbB signaling networks in Schwann cell development and myelination. *Semin Cell Dev Biol*, 21 (9): 922-928.

Niewoehner B, Single FN, Hvalby O, Jensen V, Meyer zum Alten Borgloh S, Seeburg PH, Rawlins JN, Sprengel R, Bannerman DM (2007). Impaired spatial working memory but spared spatial reference memory following functional loss of NMDA receptors in the dentate gyrus. *Eur J Neurosci*, 25 (3): 837-846.

Nissen W, Szabo A, Somogyi J, Somogyi P, Lamsa KP (2010). Cell type-specific long-term plasticity at glutamatergic synapses onto hippocampal interneurons expressing either parvalbumin or CB1 cannabinoid receptor. *J Neurosci*, 30 (4): 1337-1347.

Nitsch R, Bergmann I, Kuppers K, Mueller G, Frotscher M (1990). Late appearance of parvalbumin-immunoreactivity in the development of GABAergic neurons in the rat hippocampus. *Neurosci Lett*, 118 (2): 147-150.

Nusser Z, Sieghart W, Benke D, Fritschy JM, Somogyi P (1996). Differential synaptic localization of two major gamma-aminobutyric acid type A receptor alpha subunits on hippocampal pyramidal cells. *Proc Natl Acad Sci U S A*, 93 (21): 11939-11944.

Nyiri G, Freund TF, Somogyi P (2001). Input-dependent synaptic targeting of alpha(2)-subunit-containing GABA(A) receptors in synapses of hippocampal pyramidal cells of the rat. *Eur J Neurosci*, 13 (3): 428-442.

Nyiri G, Stephenson FA, Freund TF, Somogyi P (2003). Large variability in synaptic N-methyl-D-aspartate receptor density on interneurons and a comparison with pyramidal-cell spines in the rat hippocampus. *Neuroscience*, 119 (2): 347-363.

O'Keefe J, Nadel L (1978). *The Hippocampus as a Cognitive Map*. Clarendon Press, Oxford.

O'Keefe J (1993). Hippocampus, theta, and spatial memory. *Curr Opin Neurobiol*, 3 (6): 917-924.

Ogden DC, ed (1994). *Microelectrode Techniques, The Plymouth Workshop Handbook.*, 2nd Edition. The Company of Biologists Limited, Cambridge.

Ogiwara I, Miyamoto H, Morita N, Atapour N, Mazaki E, Inoue I, Takeuchi T, Itohara S, Yanagawa Y, Obata K, Furuichi T, Hensch TK, Yamakawa K (2007). Nav1.1 localizes to axons of parvalbumin-positive inhibitory interneurons: a circuit basis for epileptic seizures in mice carrying an Scn1a gene mutation. *J Neurosci*, 27 (22): 5903-5914.

Okada M, Corfas G (2004). Neuregulin1 downregulates postsynaptic GABAA receptors at the hippocampal inhibitory synapse. *Hippocampus*, 14 (3): 337-344.

Olney JW, Farber NB (1995). Glutamate receptor dysfunction and schizophrenia. *Arch Gen Psychiatry,* 52 (12): 998-1007.

Olton DS, Becker JT, Handelmann GE (1979). Hippocampus, space and memory. . *Behavioral and Brain Sciences,* 2 (3): 313-365.

Oren I, Mann EO, Paulsen O, Hajos N (2006). Synaptic currents in anatomically identified CA3 neurons during hippocampal gamma oscillations in vitro. *J Neurosci,* 26 (39): 9923-9934.

Oren I, Hajos N, Paulsen O (2010). Identification of the current generator underlying cholinergically induced gamma frequency field potential oscillations in the hippocampal CA3 region. *J Physiol,* 588 (Pt 5): 785-797.

Ozaki M, Sasner M, Yano R, Lu HS, Buonanno A (1997). Neuregulin-beta induces expression of an NMDA-receptor subunit. *Nature,* 390 (6661): 691-694.

Ozaki M, Itoh K, Miyakawa Y, Kishida H, Hashikawa T (2004). Protein processing and releases of neuregulin-1 are regulated in an activity-dependent manner. *J Neurochem,* 91 (1): 176-188.

Palhalmi J, Paulsen O, Freund TF, Hajos N (2004). Distinct properties of carbachol- and DHPG-induced network oscillations in hippocampal slices. *Neuropharmacology,* 47 (3): 381-389.

Park S, Holzman PS (1992). Schizophrenics show spatial working memory deficits. *Arch Gen Psychiatry,* 49 (12): 975-982.

Parlapani E, Schmitt A, Wirths O, Bauer M, Sommer C, Rueb U, Skowronek MH, Treutlein J, Petroianu GA, Rietschel M, Falkai P (2010). Gene expression of neuregulin-1 isoforms in different brain regions of elderly schizophrenia patients. *World J Biol Psychiatry,* 11 (2 Pt 2): 243-250.

Pawelzik H, Hughes DI, Thomson AM (2002). Physiological and morphological diversity of immunocytochemically defined parvalbumin- and cholecystokinin-positive interneurones in CA1 of the adult rat hippocampus. *J Comp Neurol,* 443 (4): 346-367.

Petreanu L, Huber D, Sobczyk A, Svoboda K (2007). Channelrhodopsin-2-assisted circuit mapping of long-range callosal projections. *Nat Neurosci,* 10 (5): 663-668.

Pike FG, Goddard RS, Suckling JM, Ganter P, Kasthuri N, Paulsen O (2000). Distinct frequency preferences of different types of rat hippocampal neurones in response to oscillatory input currents. *J Physiol,* 529 (Pt 1): 205-213.

Pilowsky LS, Bressan RA, Stone JM, Erlandsson K, Mulligan RS, Krystal JH, Ell PJ (2006). First in vivo evidence of an NMDA receptor deficit in medication-free schizophrenic patients. *Mol Psychiatry,* 11 (2): 118-119.

Pinault D (2008). N-methyl d-aspartate receptor antagonists ketamine and MK-801 induce wake-related aberrant gamma oscillations in the rat neocortex. *Biol Psychiatry,* 63 (8): 730-735.

Pitcher GM, Kalia LV, Ng D, Goodfellow NM, Yee KT, Lambe EK, Salter MW (2011). Schizophrenia susceptibility pathway neuregulin 1-ErbB4 suppresses Src upregulation of NMDA receptors. *Nat Med,* 17 (4): 470-478.

Pouille F, Scanziani M (2001). Enforcement of temporal fidelity in pyramidal cells by somatic feed-forward inhibition. *Science,* 293 (5532): 1159-1163.

Poulsen FR, Jahnsen H, Blaabjerg M, Zimmer J (2002). Pilocarpine-induced seizure-like activity with increased BNDF and neuropeptide Y expression in organotypic hippocampal slice cultures. *Brain Res,* 950 (1-2): 103-118.

Povysheva NV, Johnson JW (2012). Tonic NMDA receptor-mediated current in prefrontal cortical pyramidal cells and fast-spiking interneurons. *J Neurophysiol,* 107 (8): 2232-2243.

Rall W (1969). Time constants and electrotonic length of membrane cylinders and neurons. *Biophys J,* 9 (12): 1483-1508.

Ramamoorthi K, Lin Y (2011). The contribution of GABAergic dysfunction to neurodevelopmental disorders. *Trends Mol Med,* 17 (8): 452-462.

Rapoport JL, Addington AM, Frangou S, Psych MR (2005). The neurodevelopmental model of schizophrenia: update 2005. *Mol Psychiatry,* 10 (5): 434-449.

Reynolds GP, Zhang ZJ, Beasley CL (2001). Neurochemical correlates of cortical GABAergic deficits in schizophrenia: selective losses of calcium binding protein immunoreactivity. *Brain Res Bull,* 55 (5): 579-584.

Rico B, Marin O (2011). Neuregulin signaling, cortical circuitry development and schizophrenia. *Curr Opin Genet Dev,* 21 (3): 262-270.

Rieff HI, Raetzman LT, Sapp DW, Yeh HH, Siegel RE, Corfas G (1999). Neuregulin induces GABA(A) receptor subunit expression and neurite outgrowth in cerebellar granule cells. *J Neurosci,* 19 (24): 10757-10766.

Role LW, Talmage DA (2007). Neurobiology: new order for thought disorders. *Nature,* 448 (7151): 263-265.

Roopun AK, Cunningham MO, Racca C, Alter K, Traub RD, Whittington MA (2008). Region-specific changes in gamma and beta2 rhythms in NMDA receptor dysfunction models of schizophrenia. *Schizophr Bull,* 34 (5): 962-973.

Rotaru DC, Yoshino H, Lewis DA, Ermentrout GB, Gonzalez-Burgos G (2011). Glutamate receptor subtypes mediating synaptic activation of prefrontal cortex neurons: relevance for schizophrenia. *J Neurosci,* 31 (1): 142-156.

Royer S, Zemelman BV, Losonczy A, Kim J, Chance F, Magee JC, Buzsaki G (2012). Control of timing, rate and bursts of hippocampal place cells by dendritic and somatic inhibition. *Nat Neurosci,* 15 (5): 769-775.

Rund BR, Melle I, Friis S, Larsen TK, Midboe LJ, Opjordsmoen S, Simonsen E, Vaglum P, McGlashan T (2004). Neurocognitive dysfunction in first-episode psychosis: correlates with symptoms, premorbid adjustment, and duration of untreated psychosis. *Am J Psychiatry,* 161 (3): 466-472.

Rusakov DA, Kullmann DM (1998). Extrasynaptic glutamate diffusion in the hippocampus: ultrastructural constraints, uptake, and receptor activation. *J Neurosci,* 18 (9): 3158-3170.

Rutecki PA, Yang Y (1998). Ictal epileptiform activity in the CA3 region of hippocampal slices produced by pilocarpine. *J Neurophysiol,* 79 (6): 3019-3029.

Sah P, Hestrin S, Nicoll RA (1990). Properties of excitatory postsynaptic currents recorded in vitro from rat hippocampal interneurones. *J Physiol,* 430: 605-616.

Sambandan S, Sauer JF, Vida I, Bartos M (2010). Associative plasticity at excitatory synapses facilitates recruitment of fast-spiking interneurons in the dentate gyrus. *J Neurosci,* 30 (35): 11826-11837.

Sanderson DJ, Bannerman DM (2012). The role of habituation in hippocampus-dependent spatial working memory tasks: Evidence from GluA1 AMPA receptor subunit knockout mice. *Hippocampus*. 22(5): 981-994.

Sauer JF, Bartos M (2010). Recruitment of early postnatal parvalbumin-positive hippocampal interneurons by GABAergic excitation. *J Neurosci,* 30 (1): 110-115.

Scimemi A, Fine A, Kullmann DM, Rusakov DA (2004). NR2B-containing receptors mediate cross talk among hippocampal synapses. *J Neurosci,* 24 (20): 4767-4777.

Senior TJ, Huxter JR, Allen K, O'Neill J, Csicsvari J (2008). Gamma oscillatory firing reveals distinct populations of pyramidal cells in the CA1 region of the hippocampus. *J Neurosci,* 28 (9): 2274-2286.

Shinohara Y, Hirase H, Watanabe M, Itakura M, Takahashi M, Shigemoto R (2008). Left-right asymmetry of the hippocampal synapses with differential subunit allocation of glutamate receptors. *Proc Natl Acad Sci U S A,* 105 (49): 19498-19503.

Sigurdsson T, Stark KL, Karayiorgou M, Gogos JA, Gordon JA (2010). Impaired hippocampal-prefrontal synchrony in a genetic mouse model of schizophrenia. *Nature,* 464 (7289): 763-767.

Sik A, Penttonen M, Ylinen A, Buzsaki G (1995). Hippocampal CA1 interneurons: an in vivo intracellular labeling study. *J Neurosci,* 15 (10): 6651-6665.

Slomianka L, Amrein I, Knuesel I, Sorensen JC, Wolfer DP (2011). Hippocampal pyramidal cells: the reemergence of cortical lamination. *Brain Struct Funct,* 216 (4): 301-317.

Sohal VS, Zhang F, Yizhar O, Deisseroth K (2009). Parvalbumin neurons and gamma rhythms enhance cortical circuit performance. *Nature,* 459 (7247): 698-702.

Somogyi P (1977). A specific 'axo-axonal' interneuron in the visual cortex of the rat. *Brain Res,* 136 (2): 345-350.

Somogyi P, Nunzi MG, Gorio A, Smith AD (1983). A new type of specific interneuron in the monkey hippocampus forming synapses exclusively with the axon initial segments of pyramidal cells. *Brain Res,* 259 (1): 137-142.

Somogyi P, Klausberger T (2005). Defined types of cortical interneurone structure space and spike timing in the hippocampus. *J Physiol,* 562 (Pt 1): 9-26.

Somogyi P (2010). Hippocampus: intrinsic organization In: *Handbook of Brain Microcircuits* (Shepherd GM, Grillner S, eds), pp 148-164. Oxford University Press, New York.

Sorensen AT, Nikitidou L, Ledri M, Lin EJ, During MJ, Kanter-Schlifke I, Kokaia M (2009). Hippocampal NPY gene transfer attenuates seizures without affecting epilepsy-induced impairment of LTP. *Exp Neurol,* 215 (2): 328-333.

Spencer KM, Nestor PG, Niznikiewicz MA, Salisbury DF, Shenton ME, McCarley RW (2003). Abnormal neural synchrony in schizophrenia. *J Neurosci,* 23 (19): 7407-7411.

Spencer KM, Nestor PG, Perlmutter R, Niznikiewicz MA, Klump MC, Frumin M, Shenton ME, McCarley RW (2004). Neural synchrony indexes disordered perception and cognition in schizophrenia. *Proc Natl Acad Sci U S A,* 101 (49): 17288-17293.

Srinivas S, Watanabe T, Lin CS, William CM, Tanabe Y, Jessell TM, Costantini F (2001). Cre reporter strains produced by targeted insertion of EYFP and ECFP into the ROSA26 locus. *BMC Dev Biol,* 1: 4.

Standaert DG, Landwehrmeyer GB, Kerner JA, Penney JB, Jr., Young AB (1996). Expression of NMDAR2D glutamate receptor subunit mRNA in neurochemically identified interneurons in the rat neostriatum, neocortex and hippocampus. *Brain Res Mol Brain Res,* 42 (1): 89-102.

Stefansson H, Sigurdsson E, Steinthorsdottir V, Bjornsdottir S, Sigmundsson T, Ghosh S, Brynjolfsson J, Gunnarsdottir S, Ivarsson O, Chou TT, Hjaltason O, Birgisdottir B, Jonsson H, Gudnadottir VG, Gudmundsdottir E, Bjornsson A, Ingvarsson B, Ingason A, Sigfusson S, Hardardottir H, Harvey et al. (2002). Neuregulin 1 and susceptibility to schizophrenia. *Am J Hum Genet,* 71 (4): 877-892.

Steinthorsdottir V, Stefansson H, Ghosh S, Birgisdottir B, Bjornsdottir S, Fasquel AC, Olafsson O, Stefansson K, Gulcher JR (2004). Multiple novel transcription initiation sites for NRG1. *Gene,* 342 (1): 97-105.

Steullet P, Cabungcal JH, Kulak A, Kraftsik R, Chen Y, Dalton TP, Cuenod M, Do KQ (2010). Redox dysregulation affects the ventral but not dorsal hippocampus: impairment of parvalbumin neurons, gamma oscillations, and related behaviors. *J Neurosci,* 30 (7): 2547-2558.

Stone JM, Morrison PD, Pilowsky LS (2007). Glutamate and dopamine dysregulation in schizophrenia — a synthesis and selective review. *J Psychopharmacol,* 21 (4): 440-452.

Stuart GJ, Dodt HU, Sakmann B (1993). Patch-clamp recordings from the soma and dendrites of neurons in brain slices using infrared video microscopy. *Pflugers Arch,* 423 (5-6): 511-518.

Swanson LW, Wyss JM, Cowan WM (1978). An autoradiographic study of the organization of intrahippocampal association pathways in the rat. *J Comp Neurol,* 181 (4): 681-715.

Szabadics J, Varga C, Molnar G, Olah S, Barzo P, Tamas G (2006). Excitatory effect of GABAergic axo-axonic cells in cortical microcircuits. *Science,* 311 (5758): 233-235.

Szabadics J, Soltesz I (2009). Functional specificity of mossy fiber innervation of GABAergic cells in the hippocampus. *J Neurosci,* 29 (13): 4239-4251.

Szabo A, Somogyi J, Cauli B, Lambolez B, Somogyi P, Lamsa K (2012). Calcium-permeable AMPA receptors provide a common mechanism for LTP in glutamatergic synapses of distinct hippocampal interneuron types. *J Neurosci.* [in press]

Szabo GG, Holderith N, Gulyas AI, Freund TF, Hajos N (2010). Distinct synaptic properties of perisomatic inhibitory cell types and their different modulation by cholinergic receptor activation in the CA3 region of the mouse hippocampus. *Eur J Neurosci,* 31 (12): 2234-2246.

Talmage DA, Role LW (2004). Multiple personalities of neuregulin gene family members. *J Comp Neurol,* 472 (2): 134-139.

Tan GH, Liu YY, Hu XL, Yin DM, Mei L, Xiong ZQ (2012). Neuregulin 1 represses limbic epileptogenesis through ErbB4 in parvalbumin-expressing interneurons. *Nat Neurosci,* 15 (2): 258-266.

Tan W, Wang Y, Gold B, Chen J, Dean M, Harrison PJ, Weinberger DR, Law AJ (2007). Molecular cloning of a brain-specific, developmentally regulated neuregulin 1 (NRG1) isoform and identification of a functional promoter variant associated with schizophrenia. *J Biol Chem,* 282 (33): 24343-24351.

Thomson AM, Bannister AP, Hughes DI, Pawelzik H (2000). Differential sensitivity to Zolpidem of IPSPs activated by morphologically identified CA1 interneurons in slices of rat hippocampus. *Eur J Neurosci,* 12 (2): 425-436.

Tiesinga P, Sejnowski TJ (2009). Cortical enlightenment: are attentional gamma oscillations driven by ING or PING? *Neuron,* 63 (6): 727-732.

Ting AK, Chen Y, Wen L, Yin DM, Shen C, Tao Y, Liu X, Xiong WC, Mei L (2011). Neuregulin 1 promotes excitatory synapse development and function in GABAergic interneurons. *J Neurosci,* 31 (1): 15-25.

Toth K, Borhegyi Z, Freund TF (1993). Postsynaptic targets of GABAergic hippocampal neurons in the medial septum-diagonal band of broca complex. *J Neurosci,* 13 (9): 3712-3724.

Toth K, Freund TF, Miles R (1997). Disinhibition of rat hippocampal pyramidal cells by GABAergic afferents from the septum. *J Physiol,* 500 (Pt 2): 463-474.

Toth K, McBain CJ (1998). Afferent-specific innervation of two distinct AMPA receptor subtypes on single hippocampal interneurons. *Nat Neurosci,* 1 (7): 572-578.

Traub RD, Jefferys JG, Whittington MA (1997). Simulation of gamma rhythms in networks of interneurons and pyramidal cells. *J Comput Neurosci,* 4 (2): 141-150.

Traub RD, Bibbig A, Fisahn A, LeBeau FE, Whittington MA, Buhl EH (2000). A model of gamma-frequency network oscillations induced in the rat CA3 region by carbachol in vitro. *Eur J Neurosci,* 12 (11): 4093-4106.

Tukker JJ, Fuentealba P, Hartwich K, Somogyi P, Klausberger T (2007). Cell type-specific tuning of hippocampal interneuron firing during gamma oscillations in vivo. *J Neurosci,* 27 (31): 8184-8189.

Uhlhaas PJ, Singer W (2010). Abnormal neural oscillations and synchrony in schizophrenia. *Nat Rev Neurosci,* 11 (2): 100-113.

Usdin TB, Fischbach GD (1986). Purification and characterization of a polypeptide from chick brain that promotes the accumulation of acetylcholine receptors in chick myotubes. *J Cell Biol,* 103 (2): 493-507.

van Hooft JA, Giuffrida R, Blatow M, Monyer H (2000). Differential expression of group I metabotropic glutamate receptors in functionally distinct hippocampal interneurons. *J Neurosci,* 20 (10): 3544-3551.

Varoqueaux F, Jamain S, Brose N (2004). Neuroligin 2 is exclusively localized to inhibitory synapses. *Eur J Cell Biol,* 83 (9): 449-456.

Vida I, Frotscher M (2000). A hippocampal interneuron associated with the mossy fiber system. *Proc Natl Acad Sci U S A,* 97 (3): 1275-1280.

Vida I, Bartos M, Jonas P (2006). Shunting inhibition improves robustness of gamma oscillations in hippocampal interneuron networks by homogenizing firing rates. *Neuron,* 49 (1): 107-117.

Volk D, Austin M, Pierri J, Sampson A, Lewis D (2001). GABA transporter-1 mRNA in the prefrontal cortex in schizophrenia: decreased expression in a subset of neurons. *Am J Psychiatry,* 158 (2): 256-265.

Volk DW, Austin MC, Pierri JN, Sampson AR, Lewis DA (2000). Decreased glutamic acid decarboxylase67 messenger RNA expression in a subset of prefrontal cortical gamma-aminobutyric acid neurons in subjects with schizophrenia. *Arch Gen Psychiatry,* 57 (3): 237-245.

Volman V, Behrens MM, Sejnowski TJ (2011). Downregulation of Parvalbumin at Cortical GABA Synapses Reduces Network Gamma Oscillatory Activity. *J Neurosci,* 31 (49): 18137-18148.

Vreugdenhil M, Jefferys JG, Celio MR, Schwaller B (2003). Parvalbumin-deficiency facilitates repetitive IPSCs and gamma oscillations in the hippocampus. *J Neurophysiol,* 89 (3): 1414-1422.

Vreugdenhil M, Toescu EC (2005). Age-dependent reduction of gamma oscillations in the mouse hippocampus in vitro. *Neuroscience,* 132 (4): 1151-1157.

Vullhorst D, Neddens J, Karavanova I, Tricoire L, Petralia RS, McBain CJ, Buonanno A (2009). Selective expression of ErbB4 in interneurons, but not pyramidal cells, of the rodent hippocampus. *J Neurosci,* 29 (39): 12255-12264.

Walsh T, McClellan JM, McCarthy SE, Addington AM, Pierce SB, Cooper GM, Nord AS, Kusenda M, Malhotra D, Bhandari A, Stray SM, Rippey CF, Roccanova P, Makarov V, Lakshmi B, Findling RL, Sikich L, Stromberg T, Merriman B, Gogtay N et al. (2008). Rare structural variants disrupt multiple genes in neurodevelopmental pathways in schizophrenia. *Science,* 320 (5875): 539-543.

Wang CZ, Yang SF, Xia Y, Johnson KM (2008). Postnatal phencyclidine administration selectively reduces adult cortical parvalbumin-containing interneurons. *Neuropsychopharmacology,* 33 (10): 2442-2455.

Wang HX, Gao WJ (2009). Cell type-specific development of NMDA receptors in the interneurons of rat prefrontal cortex. *Neuropsychopharmacology,* 34 (8): 2028-2040.

Weisskopf MG, Nicoll RA (1995). Presynaptic changes during mossy fibre LTP revealed by NMDA receptor-mediated synaptic responses. *Nature,* 376 (6537): 256-259.

Wen D, Suggs SV, Karunagaran D, Liu N, Cupples RL, Luo Y, Janssen AM, Ben-Baruch N, Trollinger DB, Jacobsen VL, et al. (1994). Structural and functional aspects of the multiplicity of Neu differentiation factors. *Mol Cell Biol,* 14 (3): 1909-1919.

Wen L, Lu YS, Zhu XH, Li XM, Woo RS, Chen YJ, Yin DM, Lai C, Terry AV, Jr., Vazdarjanova A, Xiong WC, Mei L (2010). Neuregulin 1 regulates pyramidal neuron activity via ErbB4 in parvalbumin-positive interneurons. *Proc Natl Acad Sci U S A,* 107 (3): 1211-1216.

Whittaker RG, Turnbull DM, Whittington MA, Cunningham MO (2011). Impaired mitochondrial function abolishes gamma oscillations in the hippocampus through an effect on fast-spiking interneurons. *Brain,* 134 (Pt 7): e180.

Whittington MA, Traub RD, Jefferys JG (1995). Synchronized oscillations in interneuron networks driven by metabotropic glutamate receptor activation. *Nature,* 373 (6515): 612-615.

Whittington MA, Traub RD, Kopell N, Ermentrout B, Buhl EH (2000). Inhibition-based rhythms: experimental and mathematical observations on network dynamics. *Int J Psychophysiol,* 38 (3): 315-336.

Whittington MA (2008). Can brain rhythms inform on underlying pathology in schizophrenia? *Biol Psychiatry,* 63 (8): 728-729.

Wondolowski J, Frerking M (2009). Subunit-dependent postsynaptic expression of kainate receptors on hippocampal interneurons in area CA1. *J Neurosci,* 29 (2): 563-574.

Woo RS, Li XM, Tao Y, Carpenter-Hyland E, Huang YZ, Weber J, Neiswender H, Dong XP, Wu J, Gassmann M, Lai C, Xiong WC, Gao TM, Mei L (2007). Neuregulin-1 enhances depolarization-induced GABA release. *Neuron,* 54 (4): 599-610.

Woo TU, Miller JL, Lewis DA (1997). Schizophrenia and the parvalbumin-containing class of cortical local circuit neurons. *Am J Psychiatry,* 154 (7): 1013-1015.

Woo TU, Whitehead RE, Melchitzky DS, Lewis DA (1998). A subclass of prefrontal gamma-aminobutyric acid axon terminals are selectively altered in schizophrenia. *Proc Natl Acad Sci U S A,* 95 (9): 5341-5346.

Woodruff A, Xu Q, Anderson SA, Yuste R (2009). Depolarizing effect of neocortical chandelier neurons. *Front Neural Circuits,* 3: 15.

Woodruff AR, Anderson SA, Yuste R (2011). The enigmatic function of chandelier cells. *Front Neurosci,* 4: 201.

Wulff P, Ponomarenko AA, Bartos M, Korotkova TM, Fuchs EC, Bahner F, Both M, Tort AB, Kopell NJ, Wisden W, Monyer H (2009). Hippocampal theta rhythm and its coupling with gamma oscillations require fast inhibition onto parvalbumin-positive interneurons. *Proc Natl Acad Sci U S A,* 106 (9): 3561-3566.

Xu Q, Cobos I, De La Cruz E, Rubenstein JL, Anderson SA (2004). Origins of cortical interneuron subtypes. *J Neurosci,* 24 (11): 2612-2622.

Yau HJ, Wang HF, Lai C, Liu FC (2003). Neural development of the neuregulin receptor ErbB4 in the cerebral cortex and the hippocampus: preferential expression by interneurons tangentially migrating from the ganglionic eminences. *Cereb Cortex,* 13 (3): 252-264.

Zhang Y, Behrens MM, Lisman JE (2008). Prolonged exposure to NMDAR antagonist suppresses inhibitory synaptic transmission in prefrontal cortex. *J Neurophysiol,* 100 (2): 959-965.

Zheng K, An JJ, Yang F, Xu W, Xu ZQ, Wu J, Hokfelt TG, Fisahn A, Xu B, Lu B (2011). TrkB signaling in parvalbumin-positive interneurons is critical for gamma-band network synchronization in hippocampus. *Proc Natl Acad Sci U S A,* 108 (41): 17201-17206.

Zhong C, Du C, Hancock M, Mertz M, Talmage DA, Role LW (2008). Presynaptic type III neuregulin 1 is required for sustained enhancement of hippocampal transmission by nicotine and for axonal targeting of alpha7 nicotinic acetylcholine receptors. *J Neurosci,* 28 (37): 9111-9116.

Zucker RS, Regehr WG (2002). Short-term synaptic plasticity. *Annu Rev Physiol,* 64: 355-405.